Semiconductors, Vol. 38, No. 6, 2004, pp. 615–638. Translated from Fizika i Tekhnika Poluprovodnikov, Vol. 38, No. 6, 2004, pp. 641–664.

REVIEW

Magnetic Properties of Carbon Structures

T. L. Makarova

Ioffe Physicotechnical Institute, Russian Academy of Sciences, Politekhnicheskaya ul. 26, St. Petersburg, 194021 Russia
e-mail: Tatiana.Makarova@physics.umu.se

Submitted October 21, 2003; accepted for publication December 1, 2003

Abstract—Magnetic properties of the main allotropic modifications of carbon (diamond, graphite, nanographite, nanotubes, and fullerenes) are described. Properties of nanocarbon are considered from the standpoint of the interrelation between structural imperfection and magnetic ordering. Experimental data on high-temperature ferromagnetism in carbon structures and some theoretical models of magnetic carbon are reported. © *2004 MAIK "Nauka/Interperiodica"*.

1. INTRODUCTION

Silicon and germanium are traditionally and primarily assigned to the elements in the periodic table that are semiconductors in the solid state. Carbon, the element neighboring silicon and germanium, is rarely included in the list of semiconductors.

A silicon or germanium ingot looks like a gray crystal with a metallic luster. However, the use of the term "ingot" in reference to carbon is debatable. A substance consisting of carbon atoms can be transparent (like diamond), silvery (like graphite), black (like soot), or yellow (like a defect-free fullerite crystal). No element offers such a diversity of electronic structure as carbon. Carbon with a tetrahedral spatial structure is an insulator. Carbon with a planar structure is a semimetal with an insignificant overlap of bands (about 30 meV) and a low concentration of charge carriers; the resistivity of this material is measured in μΩ cm in the layer plane and μΩ cm in the direction perpendicular to the layers.

The linear structural form of carbon is a semiconductor. Carbon allotropic modifications with a spherical structure are semiconductors with a band gap of 1.3–2.5 eV. Polymerized structures based on these carbon modifications are also semiconductors with a narrower band gap. Cylindrical forms of carbon can be either semiconductors or metals, depending on their geometric structure ("zigzag–armchair" and chirality–achirality). The entire range of materials with electrical conductivity varying from that of undoped insulating diamond to that of metallic graphite is covered by soot, carbon black, carbyne, fullerenes, single- and multiple-wall nanotubes (SWNTs and MWNTs), graphite nanofibers and filaments (GNFs), nanoribbons, "herring-bone" GNFs, platelet-type GNFs, bundles, ropes, fibers, conical layer nanotubes (GLNTs), nanohoops, toroids, nanocones, single-wall nanohorns (SWNHs), "onion bulbs", "Russian matryoshka dolls", "peapods", and other carbon modifications known under the common (not quite correct) name of "amorphous carbon." This features various ratios between the numbers of *sp*-, sp^2-, and sp^3-hybridized atoms. Apparently, it is appropriate to consider carbon in general as a semiconductor.

I wrote this review in response to the following circumstances. Recently, a number of publications appeared in which observations of the ferromagnetic behavior of various materials based on fullerenes was reported. These observations concern fullerenes polymerized under the effects of pressure [1–4] or illumination [5, 6] and fullerene hydrides [7]. I am confident that the above behavior is only a manifestation of a more general phenomenon: the ferromagnetic properties of carbon. Over the last three decades, a number of theoretical studies have appeared that showed that specific features of the electronic structure of carbon could give rise to ferromagnetic or superconducting correlations retained at high temperatures [8]. These theoretical results are also confirmed by experimental data, e.g., obtained for such a classical structure as graphite [9].

The ferromagnetism of compounds that contain only *p* and *s* electrons is a fast-developing branch of science [10]. The ferromagnetic chemical compounds that have been synthesized so far, which are composed of light elements, have a Curie temperature no higher than 35 K (up to 65 K under pressure). At the same time, reports regularly appear in the literature on the synthesis of organic materials that feature a magnetic hysteresis that is retained even at high temperatures (up to 800 K) [11]. The weak ferromagnetic signal and low reproducibility of the results give rise to reasonable skepticism and doubt that the above effect has a carbon-related origin, although an analysis of the metallic impurities is mentioned in each publication. However, the term "impurity" is just a label that cannot be used to explain either the value of magnetization or the various dependences of magnetic properties on the degree of amorphism of the material and the conditions of synthesis or subsequent annealing.

This review is an attempt to combine the data on the magnetism of carbon structures. These data cannot be assigned to molecular magnetism since the structural

unit (molecule) responsible for ferromagnetism was not identified in any of the cases considered. In my opinion, in the case of polymerized rhombohedral fullerene, the structural unit is a certain set of specifically arranged carbon atoms formed at the threshold of the fullerene-cage collapse, rather than the C_{60} cluster itself and the unit cell of the rhombohedral structure. The mechanism of the origination of ferromagnetism in carbon structures has not been clarified so far.

This review is organized in the following way. The magnetic properties of the main modifications of carbon (diamond, graphite, nanographite, nanotubes, and fullerenes) are briefly described first. The properties of nanocarbon are considered from the standpoint of the interrelation between structural imperfection and magnetic ordering. Numerous experimental data (published from 1986 to 2003) on high-temperature ferromagnetism in carbon structures are then reported. In almost none of the cases can we use the term pure carbon, since the carbon structure is inevitably contaminated with oxygen and hydrogen (sometimes, with nitrogen). This contamination is not critical from the standpoint of the existence of π-electron magnetism but can significantly affect the identification of the mechanism of this magnetism. The question of whether magnetic impurities are a feasible mechanism of initiation of carbon-related magnetism is considered separately. The main trends encountered in the experimental studies published so far are combined in the last section of this review, which, hopefully, forms the basis for further theoretical studies in the field under consideration.

In the entire text, the term *ferromagnetism* is used *in sensu maiore*, unless otherwise specified.

2. MAGNETIC PROPERTIES OF ALLOTROPIC CARBON MODIFICATIONS

The magnetic properties of carbon (like all its other properties) depend on the carbon allotropic modification. The diamagnetism of molecules is typically evaluated using the Pascal–Langevin formula and taking into account the combined contribution of several components with correction for the chemical bonding [12]. In contrast, we have to accept chemical bonds as diamagnetism components in the case of carbon. The diamagnetism of a C^{4+} ion amounts to -1.2×10^{-8} emu/g [13]. The magnetic moment of molecules that form a carbon material is mainly controlled by the total spin magnetic moment of electrons and the van Vleck term of opposite sign. This term accounts for the admixture of excited energy levels to the ground state of the molecule due to deformation of the atom's electronic shell by an applied magnetic field. The contribution of the paramagnetism of van Vleck polarization to the magnetic susceptibility of solid-state carbon phases is quite significant in some cases [14, 15].

2.1. Diamond

According to the van Vleck formula [16], the magnetic susceptibility χ of diamond includes two diamagnetic contributions (from the core electrons χ_{core} and from valent electrons χ_v) and the paramagnetic term χ_{vv}, which originates from virtual magnetic dipole transitions between the valence and conduction bands:

$$\chi = \chi_{core} + \chi_v + \chi_{vv}. \quad (1)$$

The paramagnetic (van Vleck) term is proportional to the interband magnetic dipole matrix element and is sensitive to the symmetry of chemical bonds; this term vanishes in the case of spherical electron distribution. The other term that is indicative of spatial electron distribution is related to the diamagnetism of valent electrons. The value of this term is governed by the arrangement of the charge distributed at a distance of the valence radius r and varies with temperature in inverse proportion to the square of this distance. The temperature dependence of diamagnetic susceptibility of diamond was analyzed and used to determine the following partial contributions of each term to the molar susceptibility: $\chi_{core} = -0.3 \times 10^{-6}$ cm^3/mol, $\chi_v = -24.7 \times 10^{-6}$ cm^3/mol, and $\chi_{vv} = -13.2 \times 10^{-6}$ cm^3/mol [17]. The value of χ_v was used to determine the mean diamagnetic valence radius $r_L = (\Sigma\langle r^2\rangle)^{1/2} = 1.04$ Å; for comparison, the valence-bond length in diamond is 1.548 Å. The total molar susceptibility $\chi = -11.8 \times 10^{-6}$ cm^3/mol on the assumption that the unit cell consists of two atoms; the specific susceptibility is equal to about -0.5×10^{-6} emu/g.

2.2. Graphite

The magnetic properties of graphite are primarily governed by circular currents that circulate above and beneath the planar graphite layers. Bulk graphite is a semimetal with a Fermi energy of 20 meV; the Fermi level is located near a sharp minimum in the density of states. As a result, Pauli paramagnetism χ_P in ideal graphite should be absent. However, in actual graphite, $\chi_P \approx 10^{-8}$ emu/g [18]. The term χ_v, which is responsible for the orbital contribution of valence electrons, is large and anisotropic. The theoretical study [19] shows that the value of χ_v is caused by the following specific features of the energy-band structure: (i) a very narrow energy gap and (ii) a high density of states due to an insignificant dispersion of the energy bands in the k_z direction. Interband interactions make a major contribution to $\chi_{v\perp}$ and a negligible contribution to $\chi_{v\parallel}$. The contribution of the core electrons χ_{core} is believed to be isotropic since the spin–orbit interaction is negligible.

As a result of delocalization of electrons, graphite has the largest diamagnetic susceptibility (second only to that of superconductors): $\chi_\perp = -(22–50) \times 10^{-6}$ emu/g for a field directed along the c axis. In the majority of publications, it is pointed out that graphite is also diamagnetic in the situation where the magnetic-field vec-

tor is in the basal plane; values on the order of $\chi_{\parallel} = -0.5 \times 10^{-6}$ emu/g are reported. Careful measurements show that experimental values of $\chi_{\parallel}$ inevitably include a diamagnetic contribution of $\chi_{\perp}$, which is caused not only by incorrect alignment of the sample but mainly by the natural corrugation of graphene planes even in highly oriented graphite. Thus, it is possible that the true value of $\chi_{\parallel}$ is several orders of magnitude smaller or even has the opposite sign [20]. Graphite paramagnetism $\chi_{\parallel}$ was observed at low magnetic fields [15, 21]. The data of electron spin resonance (ESR) are indicative of the complex behavior of the *g*-factor, which suggests the existence of an internal field in graphite [22, 23].

2.3. An Intermediate Graphite–Diamond Structure

The existence of carbon structures in which spin ordering and magnetic interactions take place was predicted in the 1960s [24–26]. One of the models [27] implies the idea of ferromagnetism in pure carbon. If some carbon atoms in a graphene sheet are replaced by trivalent atoms (for example, by B, N, or Al; see closed circles in Fig. 1), the resulting magnetic moment can be very large. This idea can be also realized in a purely carbon structure if sp^2- and sp^3-hybridized carbon atoms are used as the atoms with differing valence. This structural model cannot be planar since tetrahedrally coordinated carbon forms a three-dimensional (3D) structure. The requirements of the valence are satisfied if the sp^3 atoms in the odd-numbered lines (Fig. 1; lines *1*, *3*, and so on) are linked to the atoms in lower graphite-like layers and the atoms in the even-numbered layers (*2*, *4*, *6*, …) are bonded to the atoms in the upper layers. Calculation shows that such an intermediate graphite–diamond (IGD) structure, which has a monoclinic cell of the *P*2/*m* group with parameters $a = 3.99$ Å, $b = 5.08$ Å, $c = 2.59$ Å, and $\beta = 82.1°$, is stable and features a spontaneous magnetic moment equal to 230 emu/g. This value was obtained for the case of an equal number of sp^2 and sp^3 atoms, which corresponds to the highest concentration (50%) of the carriers of unpaired spins (i.e., sp^2-hybridized atoms) [28].

It is technologically difficult to form a structure in which carbon atoms with differing hybridization alternate. Using high temperatures and pressures, one can obtain nongraphitized nanocarbon with a mixture of sp^2- and sp^3-hybridized atoms. This class of carbon materials includes nanodiamond, tetrahedrally bonded nanocarbon, and vitreous carbon. One modification of tetrahedrally bonded carbon (carbon nanofoam) has a very high concentration of spins, which gives rise to a paramagnetic susceptibility on the order of 0.01 of that of transition metals. This result is in sharp contrast to the data for other known carbon phases [29].

2.4. Nanosized Graphite

Nanographite has attracted the attention of both theoreticians and experimentalists owing to the unique behavior of its π-electron system, which is different from that in molecules and solids. The electronic structure is completely controlled by geometric factors: primarily by the width, packing, and shape of the edge of the planes; the presence of voids; and the defects in curvature. A complex energy-band structure gives rise to unusual optical [30, 31], magnetic, transport [32, 33], and thermal [34] properties, as well as special features in the spectrum of collective electronic excitations [35]. Two-dimensional (2D) graphite structures do not belong to the class of imaginary model objects. Graphite images obtained using a scanning electron microscope include a number of periodic superstructures caused by the interference of the wave functions. Some of these structures are attributed to the moiré patterns that are caused by a mismatch between the inner and surface regions, stresses, and the difference between the processes of 3D tunneling on the nanometer and atomic scales. It is shown that, in the case of graphite flakes, oscillations with a large period are added to the aforementioned pattern; these oscillations are caused by electrons whose distribution reproduces the energy-band structure of 2D graphene [36].

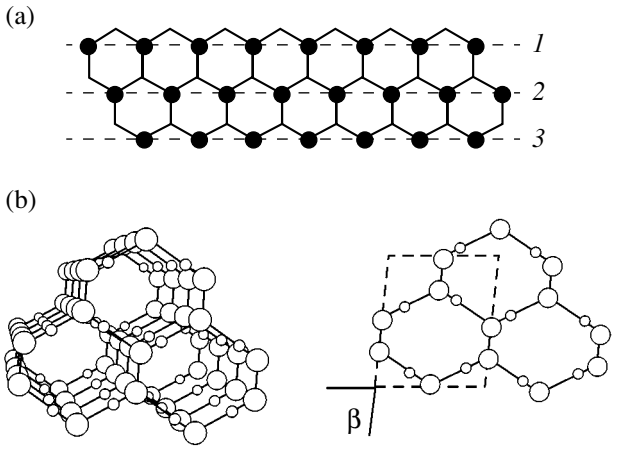

Fig. 1. Theoretical models of organic ferromagnets: (a) graphite network in which 50% of atoms are replaced by trivalent elements and (b) an intermediate graphite–diamond structure [27].

The electronic properties of graphene planes of finite size differ radically from those of bulk graphite. In order to describe the magnetic susceptibility of quasi-2D graphites, one has to take into account the contributions of the atomic-core diamagnetism χ_{core}, the Pauli paramagnetism and Landau diamagnetism of conduction electrons χ_P and χ_L, the orbital diamagnetism χ_{orb}, the Curie paramagnetism χ_C, and the orbital paramagnetic van Vleck contribution χ_{vv}:

$$\chi_{total} = \chi_{core} + \chi_P + \chi_L + \chi_{orb} + \chi_C + \chi_{vv}. \quad (2)$$

The diamagnetic susceptibility of graphene planes of a finite size is primarily controlled by the charge-carrier concentration related to structural defects. The

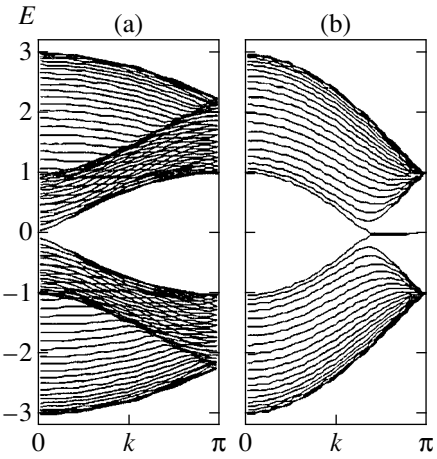

Fig. 2. Energy-band structure of graphite ribbons with a width amounting to 20 cells and with (a) "armchair" and (b) "zigzag" edges [40].

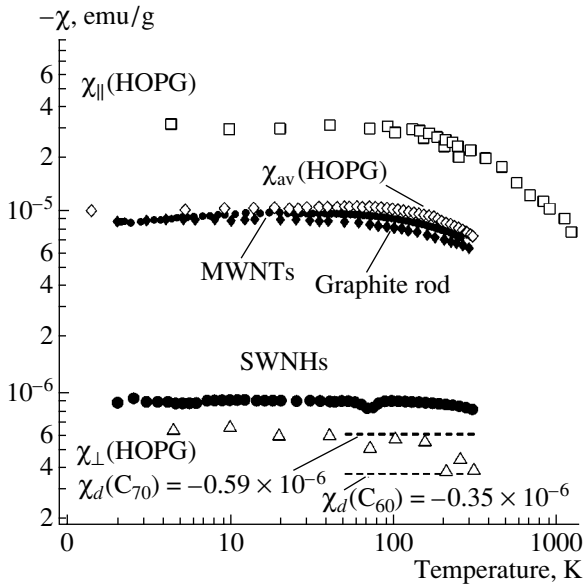

Fig. 3. Experimental values of magnetic susceptibility of highly oriented pyrolytic graphite (HOPG) in the longitudinal ($\chi_{\parallel}$) and transverse ($\chi_{\perp}$) directions, powdered HOPG (χ_{av}), a graphite rod, multiple-wall nanotubes (MWNTs), single-wall nanohorns (SWNHs), and C_{60} and C_{70} fullerenes [48].

main parameters of the model (the spread in the density of states at the Fermi level as a result of charge-carrier scattering by structural defects and the temperature corresponding to the degeneracy of charge carriers) used to calculate the susceptibility are governed by this concentration [37].

If graphite has a steplike surface, localized states appear at the Fermi level [38]; these states are of primary importance in the case of nanosized graphite [39]. Graphite ribbons have an extremely high density of states at the Fermi level, which leads to paramagnetism and (for a certain packing) to antiferromagnetism. An arbitrary boundary of a graphene plane can be described by a combination of two types of edges: "armchair" and "zigzag." A nanographite ribbon can be characterized by the type of the long edge and by the number of cells N that fit between the edges. Zigzag-type strips are always metallic, whereas the armchair strips are metallic only if $N = 3m - 1$, where m is an integer. A specific feature of the zigzag strips is the appearance of a sharp peak in the density of states localized at the Fermi level in the region where the π and π^* bands of 2D graphite contact each other [40]. Since the boundary states give rise to a peak in the density of states at the Fermi level, these states contribute to the Pauli susceptibility that balances the orbital diamagnetism. The response of the strips with zigzag edges remains diamagnetic at high temperatures. As temperature decreases, this response is replaced by the temperature (T) dependence of magnetic susceptibility in the form $\chi_C = C/T$, where C is the Curie constant [41]. This type of $\chi(T)$ dependence was observed experimentally for graphitized diamond [42] and activated carbon fibers; in the latter case, the dangling bonds were localized in 10-Å-sized microvoids [43].

One of the specific features of the graphite electronic structure with zigzag edges is the presence of flat energy bands near the Fermi level (Fig. 2). A consideration of the effects of electron–electron interactions in the context of the Hubbard model shows that there can be a spontaneous magnetic ordering in nanographite. In the case of the zigzag-type strips, a ferrimagnetic structure is possible; the appearance of magnetic ordering is controlled by the magnitude of the surface deformation caused by the electron–phonon interaction [44].

2.5. Nanotubes

It was verified both experimentally and theoretically that the model in [37], which was originally suggested for quasi-2D graphites is applicable to the case of multiple-wall carbon nanotubes [45]. The magnetic properties of single-wall nanotubes are mainly governed by the spin polarization and ring currents that surround a nanotube if the field is directed along the nanotube axis [46]. The experimental value of diamagnetic susceptibility for multiple-wall nanotubes is close to that for misoriented graphite [47]; reliable data for single-wall nanotubes are so far lacking because of the inevitable presence of the catalyst's ferromagnetic particles. Nanohorns, i.e., short single-wall nanotubes closed on one side, are similar in magnetic properties to fullerenes [48]. In Fig. 3, the available experimental data on the magnetic susceptibility of highly oriented graphite, disordered graphite, graphite rods, multiple-wall nanotubes, nanohorns, and fullerenes are summed up [48].

A theoretical study revealed an unusually high paramagnetism of nanotubes that are closed upon themselves to form toroids if the radius of the toroid is equal to a certain "magic" number [49].

2.6. Fullerenes

Fullerenes are classified as aromatic compounds [50], although the term aromaticity imposes several requirements, not all of which are fully met by fullerenes. The term "superaromaticity" was suggested 15 years before the discovery of fullerenes and was introduced to describe diamagnetic currents around a hypothetical 3D molecule composed of carbon atoms and shaped like a truncated icosahedron [51]. One of the main indicators of aromaticity is the presence of ring currents. Circular currents represent a typical response of an atom or a molecule to an external magnetic field: a current loop is formed around the atomic nucleus. Ring currents are different because the loop in this case encompasses several atoms. Cyclic delocalization of electrons in aromatic compounds directly affects the magnetic properties by varying the diamagnetic susceptibility: an external magnetic field induces a diamagnetic ring current. This gives rise to a magnetic field within the aromatic ring; the direction of this field is opposite to that of the external magnetic field. In contrast, the external magnetic field is enhanced outside the aromatic ring. Therefore, the value of diamagnetic susceptibility is larger in aromatic hydrocarbons than in other unsaturated compounds. An increase in diamagnetic susceptibility as a result of ring currents is not an isotropic effect; this increase manifests itself only if the ring plane is oriented perpendicularly to an external magnetic field. Thus, aromaticity can be recognized from anisotropy. However, this criterion cannot be applied to the case of fullerenes.

Even in the first publication dedicated to the discovery of fullerenes, it was mentioned that spheroidal clusters should have unusual magnetic properties. However, calculations using the London method showed that the addition to the magnetic susceptibility due to π-electron circular currents was unusually small [52] and was controlled by the relative strength of two nonequivalent molecular bonds. If all the bonds were equivalent, the susceptibility would be equal to –0.21 of the susceptibility in benzene (the field is applied perpendicularly to the six-membered ring). It is sufficient to vary the relative values of the bond strength by 2% for the susceptibility to change its sign.

In subsequent publications, the question of the negligible contribution of the π-electron currents to the magnetic susceptibility of fullerene C_{60} was considered again. It turned out the fact that the π-electron system does not contribute to dielectric susceptibility cannot be used as an indicator of the absence of ring currents [53]. The paramagnetic currents flowing in pentagonal fullerene rings are nearly equal to currents in the benzene ring. However, the paramagnetic contribution of currents in pentagons is completely compensated by the diamagnetic contribution of hexagons [54]. It has been shown that paramagnetic currents in five-membered rings are generated by active motion electrons around double bonds that are adjacent to the vertices of pentagons. The current flowing in a five-membered ring can be perceived using a model of a toothed wheel driven by five uniformly arranged gears. Paratropic currents near the pentagon plane are generated owing to the combined efforts of these five gears that rotate in phase [55]. Calculations of chemical shifts at the centers of faces for the series of fullerenes C_{32}–C_{180} confirmed that the regions of aromaticity and antiaromaticity in fullerenes are in fact related to hexagons and pentagons, respectively [56].

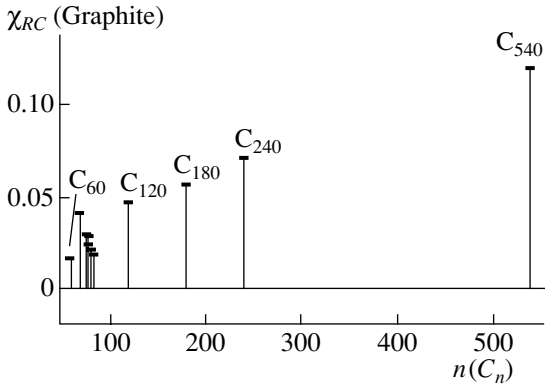

Fig. 4. Calculated values of magnetic susceptibility caused by circular currents for fullerenes C_n with number of carbon atoms *n*. The values are normalized to the susceptibility of an infinite graphene plane [57].

Once the hexagons are responsible for the diamagnetic contribution to susceptibility and pentagons are responsible for the paramagnetic contribution, it is reasonable to assume that, as the fullerene size increases (i.e., as the number of hexagons increases and the number of pentagons remains unchanged), the compensating paramagnetic contribution decreases. This means that diamagnetic susceptibility should increase steadily with cluster size and ultimately approach that of graphite. However, this tendency is observed only for giant fullerenes; as expected, the fullerene C_{5000} has a susceptibility equal to that of graphite (Fig. 4) [57]. The diamagnetic susceptibility of clusters with a number of atoms less than 100 varies randomly, which is attributed to the dependence of the characteristics of bonds in pentagons and hexagons on the structure [58]. It is interesting that electric polarizability increases steadily in the sequence C_{60}–C_{70}–C_{84}, whereas the magnetic susceptibility increases drastically when C_{60} is replaced by C_{70} and then decreases with a further increase in the fullerene size [59].

Adding electrons to a fullerene has a significant effect on the magnetic susceptibility: the hexaanion C_{60}^{6-} features a much larger diamagnetism than the neutral molecule. This circumstance is caused by the fact that currents in five-membered rings become diamagnetic; thus, a large diamagnetic current becomes dominant in the entire system [52]. C_{70} behaves in the opposite way. The neutral fullerene C_{70} is diamagnetic to a

greater extent than C_{60}; however, the magnetic properties of the hexaanion are poorly pronounced. This behavior is attributed to the fact that, in the case of C_{60}, additional electrons are localized in the region of five-membered rings, whereas C_{70} has nonequivalent pentagons and hexagons, so the additional charge is distributed nonuniformly [60].

Experiments confirmed both the small value of magnetic susceptibility of C_{60} and the much larger value for C_{70}; these values are $\chi = -0.35 \times 10^{-6}$ and -0.59×10^{-6} emu_χ/g for C_{60} and C_{70}, respectively. The temperature dependences of magnetic susceptibility are typically expressed as the sum of diamagnetic and paramagnetic terms; the paramagnetism is related to intercalated oxygen. There is no paramagnetic contribution to susceptibility in single crystals that were grown under special conditions and were never in contact with oxygen [63]. At the same time, there is evidence that paramagnetism is related not only to oxygen but also to intrinsic defects, for example, C_{60}^- ions. A drastic change (jump) in susceptibility is observed at the point of orientational phase transition. This jump is attributed to a change in the shape of the molecule, which is caused by intermolecular collective interaction. It was also reported that high-resolution measurements of magnetization in C_{60} and C_{70} powders revealed additional phase transitions interpreted as transitions to the state of magnetic glass [64].

2.7. Magnetic Compounds Based on Fullerenes

Despite their almost negligible magnetism in the initial state, closed carbon clusters became the first members of a new class of magnetic materials [65]. The intercalation of alkali metals (*A*) in A_3C_{60} stoichiometry gives rise to superconductivity; it is worth noting that the critical temperature increases as the ion radius and the lattice constant increase. Antiferromagnetic intercalational compounds of fullerenes have the highest Néel temperature (76 K) for molecular structures without magnetic atoms. It is interesting that intercalation of a neutral ammonium molecule in K_3C_{60} transforms the crystal structure from face-centered cubic into orthorhombic. As a result, the superconducting ground state is changed to the antiferromagnetic state [66]. These and numerous other experimental data indicate that there is a strong correlation between the orientation of the nearest neighbors of C_{60} and intermolecular magnetic exchange interactions.

The compound TDAE–C_{60} was the second ever compound with a magnetic molecule composed only of light atoms; it was also the first substance in which π-electron ferromagnetism could be realized at a relatively high temperature (16 K) [67]. TDAE–C_{60} is a magnetic material of the donor–acceptor type. The ion–radical is formed as a result of charge transfer from the π orbitals of a donor molecule. Experimental data indicate that tetrakis(dimethylamino)ethylene (TDAE) $C_2N_4(CH_3)_8$ in itself is not so important for the origination of ferromagnetism. Replacing TDAE with another efficient donor (cobaltacene) gives rise to similar ferromagnetism at a temperature below 19 K [68]; replacing C_{60} with C_{70} does not produce a ferromagnetic compound.

There are two modifications of the compound under consideration: the ferromagnetic α-TDAE–C_{60} phase and the paramagnetic α'-TDAE–C_{60} phase; the α' phase transforms into the α phase as a result of heat treatment at 300–370 K. The heat treatment affects the mutual orientation of the nearest-neighbor C_{60} molecules; this orientation plays a decisive role in the origination of magnetic order [69]. The maximum value of saturation magnetization in high-quality crystals is 6 emu/g, which corresponds to $\sim 1\mu_B/C_{60}$. The isolating electrical properties of these crystals and the absence of low-frequency absorption exclude any models based on energy-band magnetism. The data of ferromagnetic resonance were used to exclude superparamagnetism and spin glass from consideration. All the experimental data taken together tends to indicate isotropic or almost isotropic Heisenberg ferromagnetism [70].

3. STRUCTURAL IMPERFECTION AND MAGNETIC ORDERING

Bulk graphite with a perfect structure is a diamagnetic material whose magnetic susceptibility is second only to that of superconductors. Graphite containing certain defects can exhibit spontaneous magnetization. This behavior is caused not only by carbon atoms but mainly by its “honeycomb” structure. Certain defects in this structure give rise to a sharp asymmetric peak in the density of states at the Fermi level. In order for ferromagnetism to arise in a system of itinerant electrons, it is necessary that the density of states at the Fermi level be fairly high. This specific feature of the energy-band structure gives grounds to discuss the possibility of observing band-related magnetism in an organic material. The reasoning is based on the Hubbard model, since the latter is the simplest model for considering the band-related magnetism in a π-electron system with standard parameters: electron transitions between the lattice sites, the interaction between electrons, and the average number of electrons at the site are characterized by the kinetic energy *t*, the Coulomb energy *U*, and the electron concentration *n*, respectively. It has been reliably established that there are not many mechanisms of ordering. Graphite can become magnetic as a result of Lieb ferrimagnetism [71], which is a modification of antiferromagnetism in a two-sublattice system with a disbalance of sites in sublattices. Another possibility is the ferromagnetism of flat bands according to the Mielke–Tasaki mechanism [72].

If the energy-band structure includes a flat band at the Fermi level, an infinite number of states corresponds to a specific value of energy; such a situation is

favorable for the origination of band-related ferromagnetism. If the flat band is half-filled, repulsive electron–electron interaction leads to a completely spin-polarized ground state [72]. The presence of flat bands does not in itself ensure ferromagnetism: the flat band in the models under consideration should satisfy certain special conditions (e.g., the condition for connectivity [72]). If the condition for connectivity is satisfied, the neighboring localized orbitals overlap and the spins are aligned according to Pauli's exclusion principle. The Lieb theorem [71] is applicable to two-sublattice systems; according to this theorem, the effect of short-range electron–electron repulsive interactions leads to the fact that the ground state of a half-filled system with flat bands becomes ferromagnetic with total spin $S = N(n_a - n_b)/2$, where N is the total number of unit cells and n_a and n_b are the number of sites in the A and B sublattices of the two-sublattice structure. Nevertheless, reliable data on whether the ferromagnetism related to flat bands can arise in actual systems are lacking. The ferromagnetism related to flat bands is often discussed in the context of possible organic magnetism, because it is precisely organic substances that can form the required energy-band pattern, which will be illustrated below by considering various types of defects in graphite.

3.1. Porous Graphite

Three types of defects in graphite can be recognized provisionally: porosity, edges of the planes, and so-called topological defects. The "honeycomb" structure, i.e., an ideal infinite network of hexagons composed of light-element atoms, has the energy-band structure of a semimetal. The same plane, but porous and studded with hexagonal holes, becomes semiconductive, semimetallic, or metallic, depending on the size and arrangement of the holes, and flat bands appear systematically in the electronic structure [73]. On the basis of the Lieb theorem, it is predicted that organic ferromagnetism can appear in a "superhoneycomb" two-sublattice structure. Another porous-graphite model that takes into account the ordered structure of the plane edges also reveals the presence of flat bands in the electronic structure [74]. The energy-band pattern of porous graphite is governed not only by the shape of voids but mainly by the symmetry; in some cases, the energy gap is a periodic function of the distance between voids. It is shown theoretically that the energy-band structure of porous graphite allows for the separation of spin and charge [75].

3.2. The Curvature of the Graphene Plane

The magnetic properties of bulk graphite can be changed radically owing to the Stone–Wales reaction [76]: the rotation of two neighboring carbon bonds by an angle $\pi/2$ transforms four hexagons into two pentagons and two hexagons. As a result, flat bands appear in the energy-band structure. Variations in the curvature due to the appearance of hexagons and pentagons instead of hexagons are referred to as topological defects, Stone–Wales defects, or 5/7 defects. The periodic system of these defects completely changes the energy-band structure of graphite; a nondispersive band is formed along one of the directions, while the peak in the density of states caused by defects is located near the Fermi level [77].

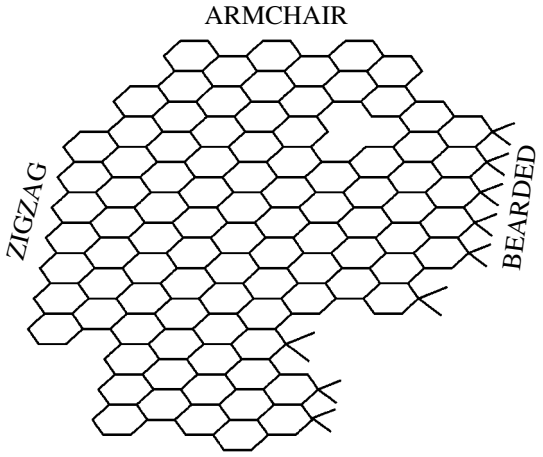

Fig. 5. A graphene structure of finite size. The "zigzag" (acene), "armchair" (phenanthrene), and "bearded" (suggested by Klein) edges are shown.

3.3. Edges of the Planes

Bounded graphite structures (Fig. 5) have specific boundary states. Two types of edges of a graphene plane are recognized when considering the electronic structure of micrographite: a phenanthrene (or "armchair") edge and an acene (or "zigzag") edge. Unsaturated valence bonds at the boundaries of graphene flakes are filled with stabilizing elements; these stabilizers are theoretically considered to be hydrogen atoms. It is typically assumed that a zigzag-type edge is stabilized by a single hydrogen atom. A "bearded" edge (considered by Klein and Bytautas [78] and referred to as the Klein edge) differs from a zigzag-type edge in that, in the former, each edge carbon atom is bonded to two hydrogen atoms. There is a sharp distinction between the electronic states with different shapes of edges. Narrow and long graphene ribbons with zigzag edges feature a sharp peak in the density of states at the Fermi energy; such a peak is not observed in the case of bulk graphite. The corresponding energy bands exhibit almost no dispersion at the Fermi level. The wave functions are mainly localized at the zigzag edge. Fujita *et al.* [40] used the Hubbard model in the mean-field approximation and assumed that the π electrons at a zigzag-type edge could give rise to a ferrimagnetic system of spins. Localized states do not appear in graphite structures with an armchair-type edge. The graphene perimeter of an arbitrary shape can be described as a combination of

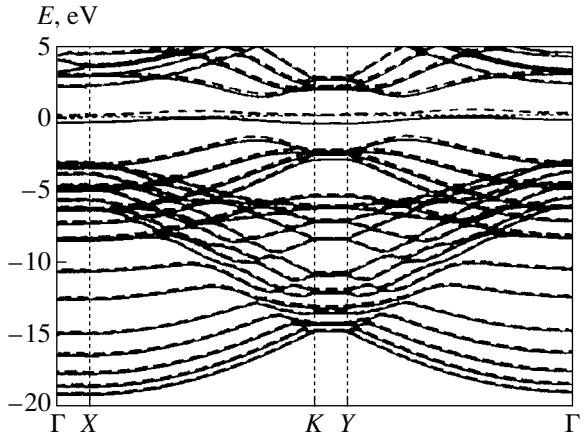

Fig. 6. Electronic band structure of a hydrogenated graphite ribbon. The solid and dashed lines represent dispersion curves for electrons with spins directed up and down, respectively. There is a completely spin-polarized dispersionless band at the Fermi level [82].

zigzag- and armchair-type edges. The boundary states, which cannot be disregarded, appear even in graphene planes with a poorly pronounced zigzag structure: three to four jags in the edge are sufficient to cause appreciable changes in the electronic structure [79].

If both edges of the graphene tape are of the zigzag or bearded type, the total spin moment is equal to zero, since a π-electron system forms a two-sublattice structure with an equal number of sites in the sublattices. Using a simplified approach, one may state that local magnetic moments interact antiferromagnetically at the edges. The spin-wave mode of this magnetic state was studied in the random-phase approximation using the Hubbard model. If the spin polarization is taken into account in the Heisenberg model, an energy gap is formed. However, analysis shows that the gap is narrow and the tendency towards ferrimagnetic correlations at the edges is pronounced [80]. The use of the Möbius boundary conditions for a graphene ribbon with zigzag-type edges leads to destruction of the two-sublattice system and suppresses the spin polarization, which gives rise to a magnetic domain wall. The magnetic-domain width is governed by the Coulomb interaction and decreases as the ratio U/t increases [81].

The entrapment of hydrogen by dangling bonds at the nanographite perimeter can induce a finite magnetization. A theoretical study of a graphene ribbon in which each carbon atom is bonded to two hydrogen atoms at one edge (the Klein edge) and to a single hydrogen atom at the other edge (the zigzag-type edge) shows that the structure has a finite total magnetic moment: a two-sublattice structure with a different number of sites in each sublattice is formed. The two-sublattice system is stable and features a spin-polarized flat band. The magnetism obtained using the local spin-density approximation (LSDA) calculations is interpreted as an appearance of ferrimagnetism in the Hubbard model with flat bands (Fig. 6) [82]. The same mechanism is operative in the case of hypergraphites, i.e., structures with edges where completely degenerate states appear [83].

3.4. Packing of the Planes

Unusual magnetism was predicted theoretically and observed experimentally in nanocrystals of carbon material that were formed as stacks of graphene layers. There is a sharp dependence of the magnetic behavior of nanographite systems on the order of alternation of graphene planes. The Hubbard model was used by Harigaya [84, 85] to consider the simplest packing *A–A* (where the sites of carbon atoms were identical for all layers) and the packing *A–B* (where every other layer was shifted by half the cell width, so that the layers alternated as in hexagonal graphite). Harigaya considered the situation where the number of atomic sites and the number of electrons is the same for all graphene planes. The matrix element for hopping between the layers is larger in the case of the *A–B* sequence, which gives rise to a finite magnetization of the structure. For an ideal *A–B* packing [84] and also for a structure with smaller values of interplanar spacing due to a slight shift of the *B* layers with respect to the *A* layers [85], an antiferromagnetic solution was obtained. The *A–B* packing is characteristic of the most abundant hexagonal graphite modification and is apparently typical of nanographite systems, since nontrivial magnetic properties (the state of the spin glass [86, 87] and the variation in the ESR line as a result of adsorption of gases [88]) were discovered experimentally.

3.5. An Open Electron Shell

A model of a closed electron shell cannot account for the experimental fact that the magnetic moment decreases as the interplanar spacing decreases as a result of adsorption of water molecules [89]. Calculations for systems with an open electron shell in an isolated nanographite layer were performed [90–92]. An open electron shell can be formed either by changing the geometric parameters or by adding active side groups that supply nanographite with electrons or holes. Effective potential was used to simulate the charge that comes from the side functional groups [90–92]; it was shown that absolute values of the total magnetic moment in nanographite with an open electron shell decreased with decreasing interplanar spacing, which was completely consistent with experimental data. Ferromagnetism is stable in the regions with an intense interlayer hopping interaction and a strong Coulomb repulsion of electrons at the lattice sites.

3.6. A Defect Consisting of a Carbon Atom and a Carbon Vacancy

The energies of adsorption and diffusion of carbon adatoms on the graphene plane were calculated from first principles. These calculations show that a defect consisting of a carbon vacancy and a carbon adatom features both high mobility and magnetism [93]. In the equilibrium state, the carbon adatom forms a bridge between two carbon atoms at the surface (Fig. 7). Calculations performed using the density-functional method show that this carbon adatom should have a magnetic moment equal to $0.45\mu_B$. The magnetism of the adatom is explained by the fact that the atoms of the substrate and the adatom are hybridized differently. The surface atoms are transformed into sp^3 hybridization, whereas the adsorbed atoms remain in the sp^2 state. The adatom electrons are distributed in the following way: two electrons are involved in the covalence bonding with the atoms of the graphene plane. One of the remaining electrons forms the dangling sp^2 bond, whereas the second electron is distributed between the sp^2 bond and the p_z orbital. This p_z orbital is (according to the symmetry) orthogonal to the surface π orbitals and cannot form a band if it remains localized and, consequently, spin-polarized. Apparently, the dangling sp^2 bond is partially spin-polarized; however, this effect is negligible.

A carbon atom diffuses mainly over the plane (the barrier for diffusion between the planes is four times higher). In the course of diffusion, the magnetic moment decreases and vanishes at a quarter of the diffusion path. Why does the magnetic moment vanish? At the transitional point during the diffusion, the atom has only a single bond with the surface, so the hybridization changes to the *sp* type. Thus, two free *p* orbitals appear and accept an excess electron; these orbitals can be found at the same level as the π orbitals at the surface and, thus, form bands. The spin density becomes delocalized, and the magnetism first vanishes and then reappears when the atom approaches the next stable state. Consequently, the atoms diffuse as nonmagnetic particles and become magnetic at equilibrium sites. Their high mobility leads to frequent collisions of adatoms and to their annihilation as a result of recombination. However, the pinning and combination of adatoms into clusters should be expected; the aforementioned clusters have remanent magnetization even at high temperatures. The Curie temperature was estimated to be 100–200 K using the difference between the energies of the paramagnetic ($S = 0$) and ferromagnetic states.

3.7. Structures with Elements from the First Row of the Periodic Table

The ability to form flat bands is not only a property of carbon atoms; this property is inherent to planes that are composed of atoms bonded hexagonally to each other and feature zigzag-type edges or zigzag-type

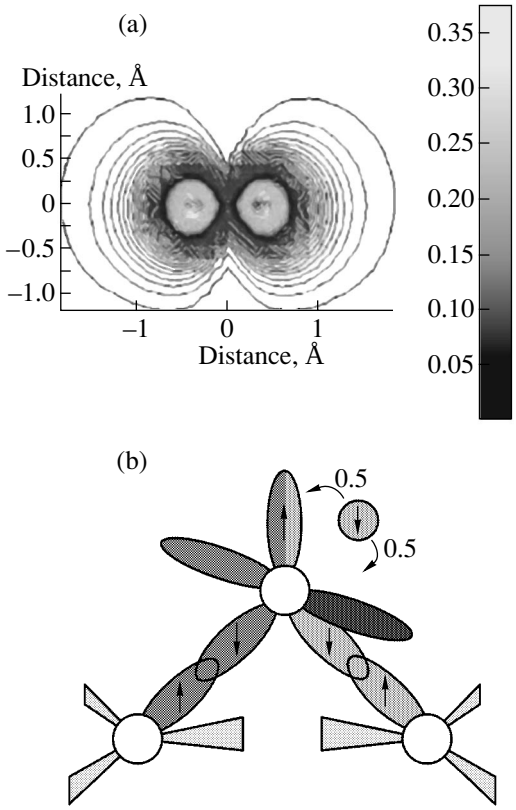

Fig. 7. (a) Spin density in the plane that goes through an adatom in the equilibrium state and is perpendicular to the graphite surface; (b) a schematic representation of the arrangement of orbitals in the plane that goes through an adatom and two atoms on the surface. The drawing is a projection and the *p* orbital depicted by the dark gray circle is in fact perpendicular to the drawing plane [93].

boundaries between chemically different elements. The origination of magnetic ordering is caused by the edge or interface states that are characteristic of tubular structures and hexagonally bonded structures. Heteronanotubes and heteroplanes composed of boron and nitrogen (like those composed of carbon) are nanodimensional ferromagnets [94]. The presence of two factors is sufficient to attain ferromagnetic or ferrimagnetic states: a zigzag-type boundary between the chemically differing elements and a disbalance between the number of carbon atoms in each sublattice. The electronic structure of the planes composed of hexagonally coordinated B, N, and C atoms was calculated from first principles; the calculations show that the ground state of BNC planes with a certain stoichiometry is ferromagnetic. Magnetic and nonmagnetic solutions were derived for two types of lattices; in both cases, the ferromagnetic ground state was found to be lower in terms of energy. As the level of doping becomes higher, the ferromagnetic correlations are reduced; however, calculations by the LSDA method show quite clearly that ferromagnetic solutions are stable with respect to the doping level. The transition from ferromagnetic to nonmagnetic states

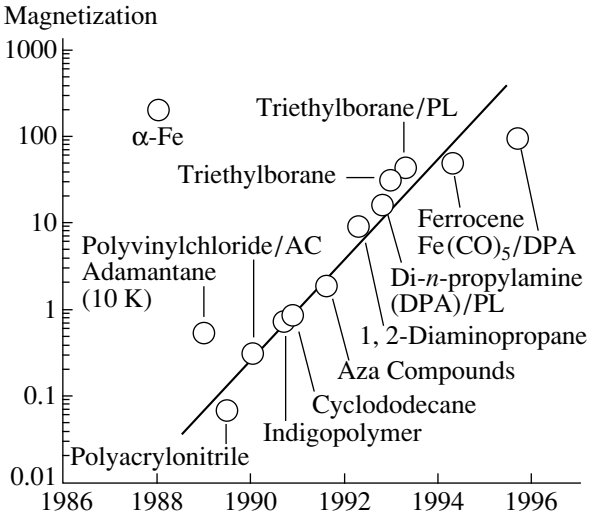

Fig. 8. Values of magnetization of magnetic carbon obtained from various starting materials in the National Institute for Materials Science and Chemical Reactions (Japan). The data for iron and iron-containing carbon are also shown for comparison [100].

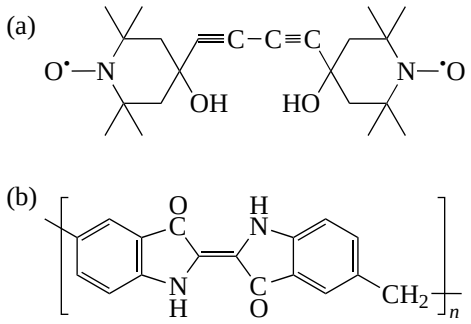

Fig. 9. (a) A BIPO monomer and (b) a unit of indigo polymer.

occurs when we have from 0.02 to 0.05 electrons per unit cell for two different lattice types [95].

3.8. Open Nanotubes

Most of the reasoning concerned with graphite edges is applicable to nanotubes. The electronic structure of finite-length nanotubes implies the feasibility of magnetic ordering, which depends heavily on the radius and length of the nanotubes [96]. It follows from the analysis of the energy levels and spin densities that the origin of magnetic ordering is related to the boundary states. Effective spins at the zigzag-type edge of nanotubes have almost free mobility [97]. Spin polarization develops at the ends of a nanotube; as a result, a nanotube can be used as a spin injector [94]. Calculations [98] show that, in the case of (8, 0) and (10, 0) nanotubes, ferromagnetic ordering is more energetically favorable (by 71 and 49 meV) than antiferromagnetic ordering. These results indicate that these nanotubes can be considered as nanosized magnets at room temperature. The magnetic moment per dangling bond in an (8, 0) nanotube is equal to $1.25\mu_B$. The appearance of magnetic instabilities in nanotubes with a periodic porous structure is also predicted [99].

4. EXPERIMENTAL DATA ON HIGH-TEMPERATURE MAGNETISM IN CARBON STRUCTURES

4.1. Unidentified Ferromagnetic Organic Compounds

Over the last two decades, a large number of publications have appeared that report on carbon structures that exhibit ferromagnetic behavior at room temperature. It was stated in review paper [100] that "among all magnetic materials, carbon is the most promising since it exhibits spontaneous magnetization at room temperature; magnetic carbon can be readily produced, it is physically and chemically stable and is easily workable." Pyrolytic carbon prepared at relatively moderate temperatures (900–1500 K) has a highly oriented structure and contains a large number of unpaired spins in the graphite skeleton, which interact with each other [101]. The material is a 3D structure that is composed of an approximately equal number of sp^2- and sp^3-hybridized carbon atoms. Figure 8 [100] shows the values of room-temperature magnetization obtained after pyrolysis of various substances. For comparison, the values of magnetization for α-Fe and magnetic carbon synthesized from iron-containing organic substances are also given.

When analyzing the publications concerned with the synthesis of high-temperature ferromagnets, one can recognize five main types of structure: (i) chains of interacting radicals; (ii) carbon structures containing trivalent elements, for example, P, N, and B; (iii) structures composed of sp^2- and sp^3-coordinated carbon atoms; (iv) graphite and nanographite; and (v) fullerenes. Let us consider several compounds that belong to the first three types of structure. A more complete list of relevant papers and patents can be found in the recent review [11].

A chain of interacting radicals was obtained by polymerization of a BIPO polydiacetylene crystal (Fig. 9a) [102, 103]. Poly-BIPO featured spontaneous magnetization $M = 0.02$ emu/g that vanished at a temperature of 420–460 K. Separation of phases using a permanent magnet made it possible to isolate the particles of an anisotropic substance whose magnetization is severalfold greater than that of the surrounding material. In subsequent publications [104, 105], a higher magnetization after phase separation was reported: $M = 0.5$ emu/g; however, no differences in structural units and chemical properties were detected. The absence of transition-metal impurities was ensured to within 10^{-5} wt % according to the data of inductively coupled plasma (ICP) emission spectroscopy.

A linear polymer based on indigo (Fig. 9b) is magnetic at temperatures as high as 200°C [106]. If the content of iron is 26–28 ppm and of cobalt and nickel is less than 1 ppm, the substance features saturation magnetization, remanent magnetization, and coercivity equal to M_s = 0.7 emu · G/g, M_r = 0.08 emu · G/g, and H_c = 120 Oe, respectively. If it is assumed that the effect is related to impurities and the organic matrix is nonmagnetic, an amount of 3200 ppm of Fe should be introduced in order to attain the above values of magnetization. The infrared spectra generally correspond to those of indigo; however, additional lines inherent in unordered structures with hydrogen bonds are also observed. The ESR spectrum includes a narrow line with parameters g = 2.0048 and ΔH_{pp} = 7 G and also a broad band in the high-spin region.

Torrance *et al.* [107] used the reaction of *s*-triaminobenzene with iodine to obtain a black insoluble polymer with ferromagnetic properties that were retained up to a temperature of 700 K but did not recover when cooled owing to thermal decomposition of the sample. The triarylmethane resin is a diamagnetic material. However, when this material is synthesized in a magnetic field, a ferromagnet is obtained; this apparently happens owing to radicals that are formed in the course of dehydrogenation [108].

A 3D PIRO-pan structure was obtained by pyrolytic decomposition of polyacrylonitrile [109]. The material was distinguished by a high concentration of spins (10^{23} cm^{-3}), and various samples had a saturation magnetization of 6–15 emu · G/g; the separated magnetic phase was more crystalline than the nonmagnetic phase. Analysis of the impurities using laser-assisted mass microanalysis (LAMMA), secondary-ion mass spectroscopy (SIMS), and electron-emission spectroscopy showed that there were no correlations between the impurity content and magnetization. The majority impurities in ferromagnetic carbon are nitrogen (2.3 at %) and oxygen (4.7 at %).

The magnetic properties of pyrolytic carbon are of particular interest. Pyrolysis of organic compounds at relatively low temperatures (600–1300°C) yields a highly oriented graphite-like material with a high concentration of unpaired spins. Exchange interaction between spins was observed in some cases.

Adamantane is recognized for its ability to graphitize easily. Using pyrolysis of adamantane at 1000°C in an argon atmosphere, one can obtain a substance that exhibits a pronounced ferromagnetic hysteresis. The parameters M_s = 0.5 emu · G/g, M_r = 0.35 emu · G/g, and H_c = 600 Oe are the results of measurements at 10 K; however, the values of magnetization at 400 K are approximately 1/3 of those given above [110]. According to the ESR data, the concentration of spins amounts to about 10^{21} spin/g at room temperature and with a content of transition metals no higher than 25 ppm. Ferromagnetic carbon based on adamantane was reproducibly obtained by several research teams. However, the following general rule for unidentified ferromagnetic compounds was confirmed: if two samples are prepared under identical conditions, one of them is found to be ferromagnetic and the other is not [111]. Studies of the structure show that two special features are characteristic of samples with nonlinear magnetization: a highly oriented structure of the material and a high concentration of unpaired electrons. The diffraction pattern includes peaks at 2Θ = 9°, 17.5°, and 25.5°, which corresponds to an interplanar spacing of 3.49 Å [112].

Pyrolysis at 1000°C was used to obtain magnetic structures from other starting materials as well, i.e., polyvinyl chloride, phenol resins, and a pyren-benzaldehyde polymer [113]. Pronounced magnetic properties (M_s = 1.07 emu/g, M_r = 0.21 emu/g, and H_c = 163 Oe at 4 K) were observed in pyrolitic carbon obtained by heating cyclodecane to 950°C [114]. The above values of magnetization can be interpreted in two ways: either 0.2% of carbon atoms have unpaired interacting spins or the material contains 4800 ppm of iron. ICP emission and the X-ray characteristic radiation indicate that there is no more than 50 ppm of iron in the material and the amount of other metals is below the sensitivity of the methods. The values of magnetization and coercivity at room temperature amounted to 80% of those at 4 K; the material completely lost its magnetic properties after exposure to air for about one month. The ESR spectra of this material were typical of a carbon magnetic structure: a broad line located at about 2940 G and a narrow line with g = 2.0014 and ΔH_{pp} = 6.3 G. The relative contribution of the paramagnetic signal increases with decreasing temperature, and the intensity of the broad-line signal is almost directly proportional to the saturation magnetization.

Good results are obtained using pyrolysis of nitrogen-containing compounds. The latter exhibit a clearly pronounced isomeric effect: stronger magnets are obtained from branched starting components. In other words, the geometric arrangement of radicals is important for attaining an ordered spin structure. Ferromagnetic molecules $(–CH_2–CH–CN–)_n$ were obtained by pyrolysis of polyacrylonitrile [115]. The magnetic properties of substances obtained by decomposition of a mixture of phenyldiamine and melamine are very sensitive to the decomposition temperature; the best results obtained as a result of decomposition at 600°C are M_s = 0.624 emu/g, $M_r = 6.65 \times 10^{-2}$ emu/g, and H_c = 125 Oe [116]. A substance obtained by pyrolysis of guanine (one of the amino acids of DNA) has similar properties [117]. A dark-red substance with an unusually high saturation magnetization M_s = 10.4 emu/g can be obtained by treating a mixture of triphenoxytriazine TPTA and melamine at 950°C in an argon atmosphere with a certain amount of dry air [118]. The ESR spectrum consists of a very broad line and indicates that the spin concentration amounts to 4.7×10^{23} spin/g. The intensity of peaks decreases with temperature; however, the inte-

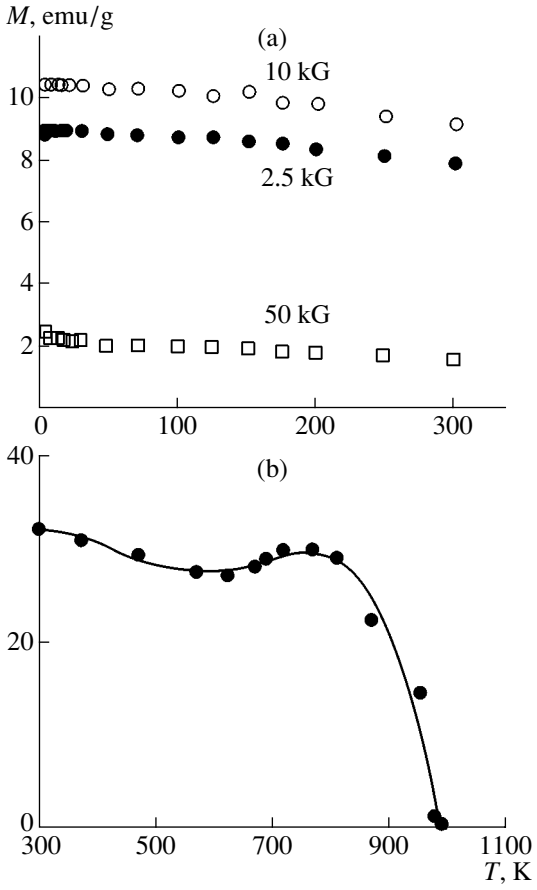

Fig. 10. Temperature dependences of magnetization in magnetic carbon obtained by pyrolysis of (a) diaminopropane ($C_3H_{10}N_2$) at 950°C [101] and (b) triethylborane ($C_6H_{15}B$) at 810°C [100].

grated intensity remains unchanged owing to an increase in the line breadth ΔH_{pp}. Temperature dependences of the g-factor and ΔH_{pp} are nontrivial. Both parameters decrease with temperature, whereas ΔH_{pp} increases with temperature and the g-factor is temperature-independent in conventional 3D ferromagnets. The temperature dependence of magnetic susceptibility determined from the ESR data is also unconventional.

The temperature dependences of saturation magnetization in magnetic carbon deserve attention: the magnetic properties are temperature-independent up to temperatures that are much higher than 295 K (Fig. 10). Similar dependences were later obtained for polymerized fullerenes.

The technological conditions and starting organic compounds are extremely important for preparation of ferromagnetic carbon from nitrogen-containing organic compounds. The ratio between the concentrations of hydrogen and carbon [H] and [C] in the starting material is particularly critical [119]. As soon as this ratio exceeds 1.5, a sharp increase in the saturation magnetization of the reaction product is observed. Several dozens of substances were studied [119]; it is believed that atomic hydrogen generated during thermal decomposition is very important from the structural standpoint, since this hydrogen prevents graphitization of the material.

Diaminopropane has the largest value [H]/[C] = 3.3 of all the starting materials studied; the product of pyrolysis features a saturation magnetization of 10.5 emu/g or $0.022\mu_B$ per carbon atom [11]. The temperature dependence of magnetization does not obey the Curie–Weiss law. The Curie point is at a temperature higher than 500 K; however, it is impossible to determine this temperature owing to thermal decomposition of the material (Fig. 10a). Some structure-related information can be gained from Fourier IR spectroscopy of frustrated total internal reflection: absorption in the region 2850–3000 cm^{-1} and the large number of lines in the range of 850–1750 cm^{-1} are related to various degrees of freedom of carbon bonds in the sp^3 and sp^2 hybridizations and also to aromatic and heterocyclic links. Rings that resemble those of benzene are observed using tunneling and atomic-force microscopes. The electrical conductivity of the material is much lower than that of graphite. It is assumed that the material has a 3D sp^2/sp^3 structure.

Studies of a large number of ferromagnetic materials obtained from various nitrogen-containing substances showed that the structure of these materials is most often amorphous and disordered. In order to reveal the structural–magnetic correlations, samples of ferromagnetic carbon were subjected to various doses of plasma treatment, after which the percentage of amorphous carbon and the value of magnetization were measured. A one-to-one correspondence between the above two parameters was observed: the higher the content of amorphous carbon, the higher the spontaneous magnetization [120]. A second tendency was observed in studying ferromagnetic carbon obtained by pyrolysis of plyacrylonitrile: the magnetic properties are closely related to the presence of various radicals, which are mainly nitroxides that exist at the edges of graphite-like structures [121]. Apparently, a ferromagnetic carbon substance has been never separated, but a ferromagnetic phase is typically present in the form of inclusions in the nonmagnetic matrix (Fig. 11).

There is a general difficulty in producing organic magnetic materials: complex chemical processes involve a large number of reactions, and the results are hard to reproduce. Despite the fact that the mechanism of origination of ferromagnetism in carbon structures that do not contain metal atoms remains unclear, several dozens of patents for methods of producing these structures have been granted [11]. The common feature of these patents is the recommendation to heat organic substances in a complex (steplike) way, sometimes in the presence of a magnetic field, and to stop the processes halfway to graphitization. Another group of patents describes the carbon structures that contain nitrogen, boron, or phosphorus and feature values of magne-

tization as large as 60 emu/g. Figure 12 illustrates hypothetical processes that occur in the production of magnetic carbon [100].

Thus, there are publications that describe technological processes that make it possible to obtain magnetic carbon structures where the ferromagnetic ordering is attained at the π-delocalized spins caused by the presence of a trivalent element in the carbon skeleton. In addition, structures in which alternating sp^2- and sp^3-hybridized carbon atoms that act as elements of different valence can be obtained.

4.2. Ferromagnetic Graphite

There are both theoretical estimates and experimental proofs of the fact that electronic instabilities in graphite can give rise to superconducting and ferromagnetic correlations at high temperatures. The magnetic ordering can be caused by the appearance of curvature in the surface, structural disorder, and grain boundaries in graphene planes. It is predicted that, in the case of a highly developed topological disorder, ferromagnetism is preferable to antiferromagnetism since the presence of pentagons and hexagons destroys the antiferromagnetic ordering. However, it may happen that ferromagnetism would be suppressed by other instabilities of a different kind (superconducting), which would be governed by the relation between short-range spin-dependent interactions and long-range spin-independent links [8].

Experimentally, a hysteresis curve of superconductivity type against the background of a strong diamagnetic signal is observed in a field applied along the *c* axis (**H** || **c**). If the field is applied parallel to the basal plane of graphite (**H** ⊥ **c**), the dependences *M*(*H*) of ferromagnetic type are observed; in this case, magnetization is proportional to the sample volume [9]. Annealing in a helium atmosphere increases the magnetization severalfold. Measurements of ferromagnetic characteristics in various well-characterized graphite samples have verified the carbon origin of the signal. The mechanism of the phenomenon is related either to topological defects, such as grain boundaries and edge states, or to the energy-band magnetism of an electron gas that features a strong electron–electron interaction [20].

Studies of meteorite graphite [122] that contained iron-containing minerals showed that the total experimental magnetization exceeded the calculated magnetization by a factor of 1.5 even if overestimated values of the iron contribution were used. It is believed [122] that the above effect can be attributed only to ferromagnetic graphite, which constitutes more than half the material of the meteorite and has an average magnetic moment equal to $0.05\mu_B$ per carbon atom. The temperature dependence of saturation magnetization indicates that there are several phase transitions related to iron and iron oxides; however, the phase transition at 570 K is interpreted as corresponding to the Curie temperature

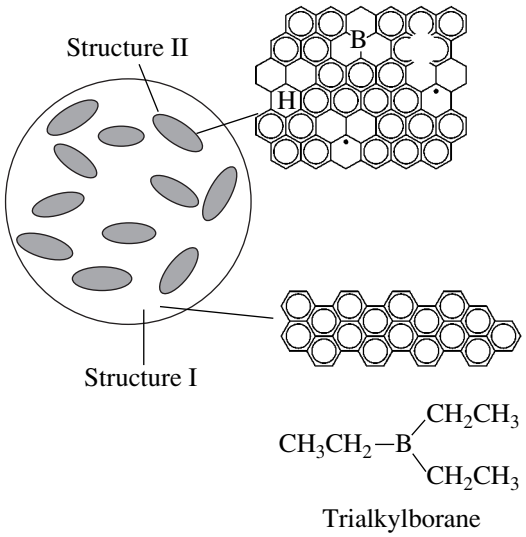

Fig. 11. Assumed structure of pyrolytic carbon prepared from trialkylboranes. Structure I is an sp^2-hybridized carbon plane; structure II includes both a mixture of sp^2- and sp^3-hybridized carbon atoms and boron atoms [100].

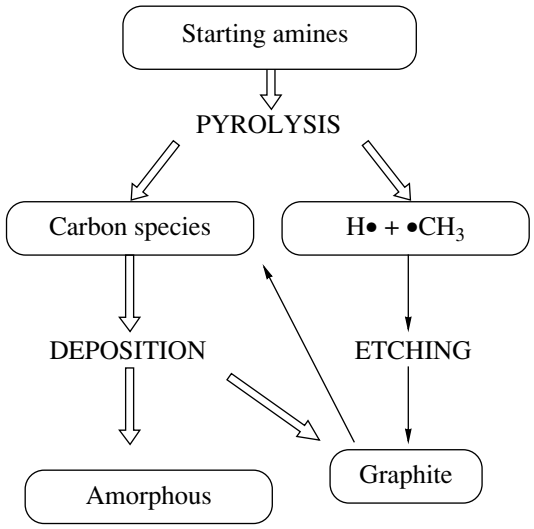

Fig. 12. Assumed mechanism of formation of amorphous carbon from a nitrogen-containing starting material [100]: starting amines ⟶ pyrolysis ⟶ (the left-hand branch) carbon substances ⟶ deposition ⟶ amorphous carbon; ⟶ (the right-hand branch) ($H^{\bullet}$ + $^{\bullet}CH_3$) ⟶ etching ⟶ graphite.

of extraterrestrial graphite. This effect can have its origin in special features of formation, chemical doping, and impact effects that give rise to a large number of interacting defects in carbon. It is believed [122] that the most plausible version of magnetic ordering is the inducement of a magnetic moment by ferromagnetic inclusions.

Irradiation with protons can be used to produce ferromagnetic spots on samples of highly oriented pyro-

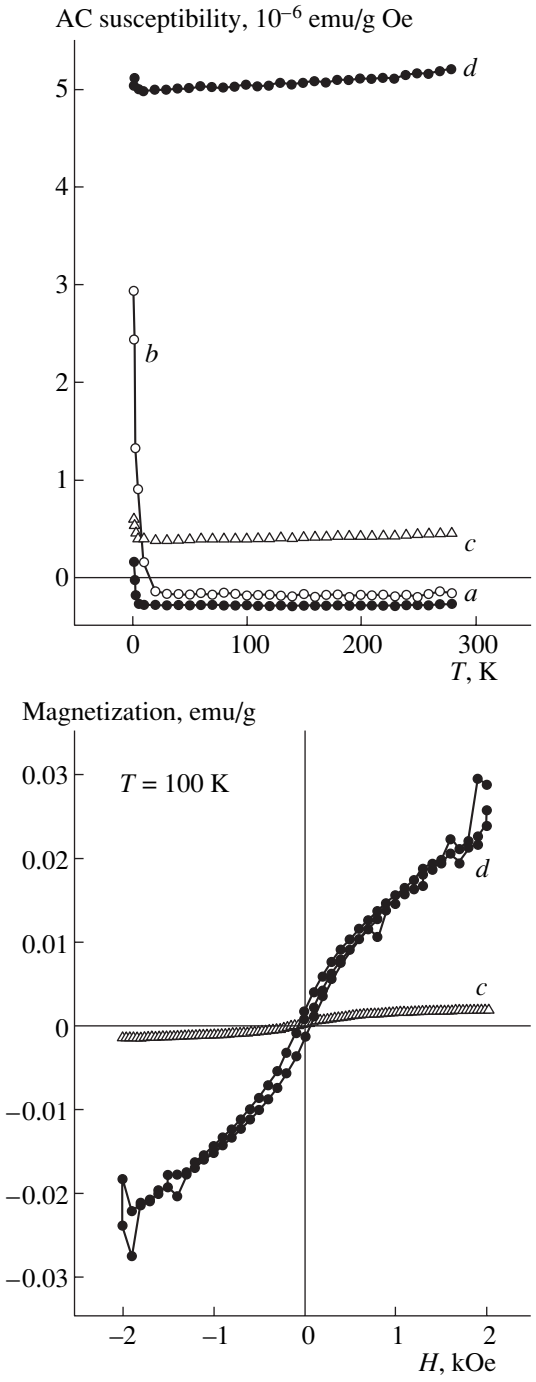

Fig. 13. Magnetic properties of phototransformed fullerenes. Upper panel: magnetic susceptibility of (*a*) the starting C_{60} powder and the C_{60} powder exposed to light (*b*) in the absence of oxygen and (*c*, *d*) in the presence of oxygen for (*c*) 48 and (*d*) 720 h. Magnetization loops for samples (*c*) and (*d*) are shown in the lower panel [6].

lytic graphite [123]. Atomic-force microscope studies showed that a magnetic signal appeared in an irradiated region; this signal varied in an applied external field. The extremely high reproducibility of the results obtained for special impurity-free samples indicate that the origin of the above signal is related to carbon. Presumably [123], this effect is caused by induced disorder with a partial change of hybridization from the sp^2 type to the sp^3 type. In addition, it suggested [123] that the presence of hydrogen is important for the inducement of ferromagnetism as similar experiments with irradiation with helium ions do not yield a magnetic contrast.

4.3. Fullerenes Polymerized by Radiation

The ferromagnetism of polymerized fullerenes was reported for the first time in 1996. The exposure of C_{60} crystals to high-intensity light from a xenon lamp in the presence oxygen gives rise to a nonlinear field dependence of magnetization with a pronounced hysteresis [5]. A similar result was obtained in a repeat experiment: the samples were exposed to radiation from a xenon lamp with intensity $I = 10$ mW/cm^2 for 30 days. The control powder was irradiated in a sealed evacuated cell; changes in the magnetic properties were not detected to within the measurement accuracy [6].

A starting van der Waals fullerene crystal is diamagnetic (Fig. 13, curve *a*). The susceptibility is almost temperature-independent, except at low temperatures, where the paramagnetic term $\chi_P \propto 1/T$ becomes important. The exposure of fullerene to oxygen in the dark increases the magnitude of the Curie paramagnetism, which is most likely caused by intercalated oxygen; a certain paramagnetic contribution can be made by defects in fullerene (Fig. 13, curve *b*).

The temperature dependence of magnetic susceptibility is changed radically if the crystals under investigation are exposed to visible light in the presence of oxygen. In this case, magnetic susceptibility changes its sign and becomes positive in the entire temperature range (Fig. 13, curve *c*). The susceptibility increases with the exposure time (Fig. 13, curve *d*).

Fullerenes irradiated in the presence of oxygen feature a nonlinear magnetization curve. The saturation magnetization increases with the irradiation time (see Fig. 13, the lower panel).

A C_{60} crystal containing oxygen in interfullerene voids can be returned to the initial state: intercalated oxygen is removed by heating to 450 K in a dynamic vacuum. Polymerized C_{60} that does not contain oxygen can also be returned to the initial state by heating to 480–560 K for various types of polymerization. However, the crystal is not brought back to the initial state if oxygen diffusion is accompanied by exposure to visible or ultraviolet light (or, which amounts to the same, if polymerization is performed in the presence of oxygen). Only intercalated oxygen can be removed by annealing phototransformed fullerene in vacuum; chemically bonded oxygen remains intact. It was shown [5] that the sample prepared in an oxygen atmosphere and then heated retained the nonlinear magnetization curve, although the paramagnetic background

was replaced by a diamagnetic background as a result of heating.

Plots of magnetization as a function of magnetic field are almost identical at 5 K and at room temperature. At still higher temperatures, magnetization begins to decrease but remains finite at temperatures as high as 800 K.

The amount of polymerized material that can be obtained by photopolymerization is inevitably small. Photons with energies in the range of band-to-band transitions are required for polymerization. A strong absorption corresponds to band-to-band transitions; as a result, the penetration depth of radiation is very small and amounts to 100–500 fullerene layers for different wavelengths. If C_{60} powder with a grain size of ~10 μm is irradiated, phototransformation affects only 1% of the fullerene volume. The values of the magnetic moment reported previously [5, 6] are very small and are no larger than $0.001\mu_B$ per fullerene. One can enhance the magnetization by dissolving the crystal in toluene [5]. As a result, an unreacted part of the fullerenes is removed and the value of magnetization is increased by two orders of magnitude (to $0.1\mu_B$ per fullerene molecule). X-ray and Raman studies show that the concentrated ferromagnetic phase is the orthorhombic phase of polymerized C_{60}.

4.4. Fullerene Films

Studies aimed at visualizing the magnetic response have been carried out. C_{60} films were subjected to radiation from an argon laser with photon energy $h\omega$ = 2.4 eV and a power density of $I = 1$ W/cm^2; the radiation dose amounted to 10^5 photons per C_{60} molecule. There were no magnetic domains in the starting C_{60} films. Several topographic inhomogeneities were detected within the unirradiated area. However, these inhomogeneities did not produce any signal in the magnetic microscopy. In contrast, a weak (but nontrivial) magnetic signal from the laser-irradiated area was detected; the amplitude of this signal was larger at the grain boundaries (Fig. 14).

Photochemical reactions proceed in the surface layers of films and crystals. The combined effect of laser radiation and oxygen on the surface of fullerene films initiates the following processes: (i) fullerenes are combined into one-dimensional polymerized structures; (ii) partial oxidation of fullerenes occurs; (iii) the film that consists of covalent-bonded fullerenes and is formed at the surface becomes cracked so that the previously formed interfullerene bonds are split; and (iv) a small amount of disordered sp^2-hybridized carbon can be formed as a result of the destruction of the molecules' skeleton.

The largest magnetic-field gradient is attained at the grain center and at the grain boundary; evidently, magnetism of the layers is caused by some of the structural changes described above. The grain boundaries are imperfect regions that contain dangling interfullerene bonds. It cannot be excluded that imperfect molecules or even fragments of a destroyed fullerene cage are present at the grain boundaries; however, the number of the above fragments is evidently small since they are not detected by spectroscopic methods.

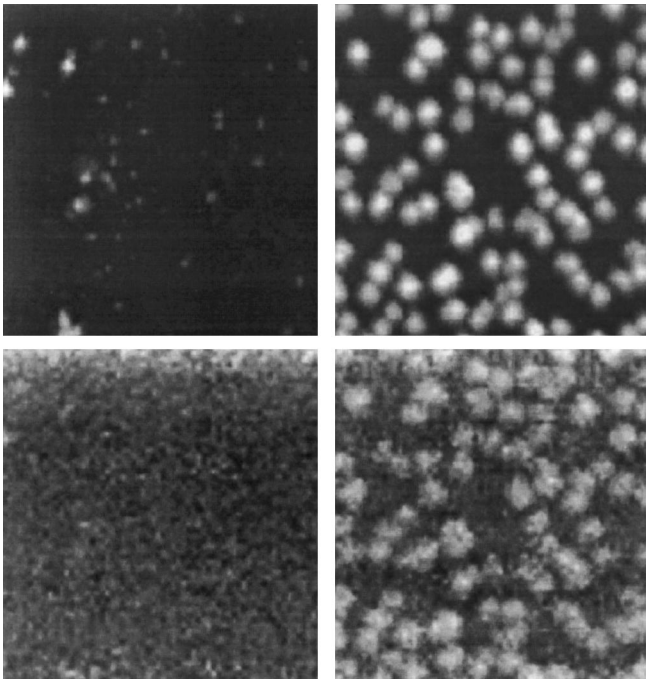

Fig. 14. Topographic (above) and magnetic (below) images of C_{60} films. On the left: the starting film; the surface defects that do not contribute to the magnetic signal can be recognized. On the right: the film exposed to laser radiation; the magnetic image reproduces the topographic image. The area of the images is 5×5 μm^2 and the depth of scanning is 50 nm [6].

4.5. Fullerenes Polymerized Under Pressure

A magnetically ordered phase is also formed in the case of polymers obtained under pressure. This phase was observed for the first time in rhombohedral C_{60} (*Rh*-C_{60}) prepared under a pressure of 6 GPa in a very narrow temperature range (slightly higher than 1000 K). The highest magnetization was obtained for the sample prepared at 1075 K [1]. The magnetization curves measured in the magnetic-field range -2 kOe $< H <$ 2 kOe were practically identical at temperatures of 10 and 300 K. The remanent magnetization in both cases was equal to $M_r = 0.015$ emu/g, and the coercivity was H_c = 300 Oe. Saturation of magnetization is observed in the fields with a strength of $\sim 2 \times 10^4$ Oe. If the experimental value of the spin concentration $n = 5 \times 10^{18}$ cm^{-3} is used, the magnetic moment can be estimated as $0.4\mu_B$ per electron. The temperature dependence of magnetization at a fixed value of magnetic-field strength of 2 kOe and the temperature dependence of remanent magnetization at $H = 0$ after a field of 2 kOe was

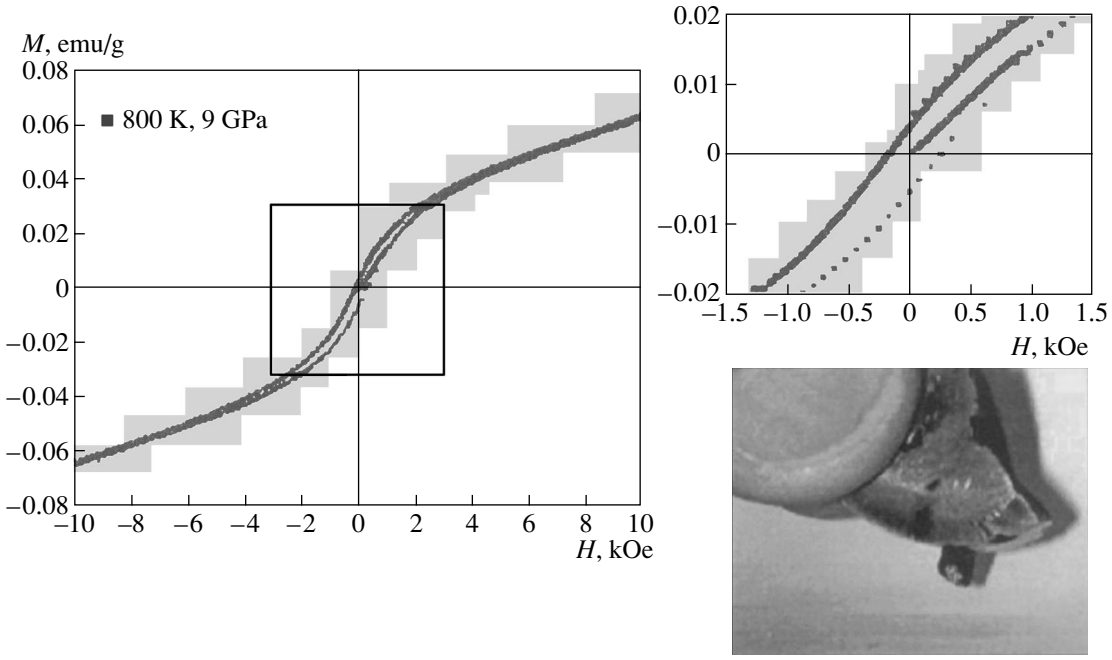

Fig. 15. Nonlinear magnetization curves for C_{60} polymerized at a pressure of 9 GPa and a temperature of 800 K [2]. The photograph on the right at the bottom shows a sample held in place by a magnet (by courtesy of P. Wood, Warwick University).

applied yield the same estimate of the Curie temperature: approximately 500 K.

The results of this study were verified and confirmed by Wood *et al.* [2]. A series of samples were produced under a pressure of 6 GPa and at temperatures of 925–1125 K. Nonlinear magnetization was observed only in five out of eight samples that were prepared in the very narrow temperature range 1000 K < T < 1065 K. One of the samples prepared at 1055 K featured magnetization that exceeded the value given above by a factor of 4; the Curie temperature was T_C = 820 K.

Experiments on the polymerization of fullerenes were also carried out at other pressures. A paramagnetic polymerized fullerene phase is formed at a pressure of 2.5 GPa, which is favorable for the origination of the tetragonal phase (often not alone but mixed with the rhombohedral phase). Evidence of magnetic ordering was observed in the sample prepared in the temperature range 1000 K < T < 1075 K [124]. The largest magnetic signal was obtained in the sample polymerized at 1025 K. The samples prepared at temperatures higher than 1100 K were diamagnetic, much like graphite or nonpolymerized fullerene. It was found that the duration of polymerization considerably affects the possibility of obtaining samples with evidence of ferromagnetism. The number of unpaired spins increases in the course of the first several minutes of treatment under pressure, then attains a maximum, and finally starts to decrease. Consequently, the magnetic properties are very sensitive to the duration of preparing the samples, so that optimal conditions for obtaining the ferromagnetic phase should be sought in the 3D p–T–t space [125].

An increase in the pressure to 9 GPa leads to similar results. The samples are diamagnetic if the polymerization temperature is below 800 K; however, if the temperature exceeds 800 K, a pronounced magnetic hysteresis is superimposed on the paramagnetic signal (Fig. 15). If the polymerization temperature is too high, a sharp transition to diamagnetism is observed; a poorly pronounced hysteresis loop can be recognized against the background of this transition [2]. A sharp decrease in the ferromagnetic contribution to the magnetic response and the transition to diamagnetic behavior are observed when studies of the structure indicate the onset of destruction of fullerene cages [2].

4.6. Magnetic Domains in Polymerized Fullerenes

Polymerized fullerenes were scanned using proton-induced X-ray emission (PIXE); maps of distribution of the elements in the surface regions to a depth of 30 μm were obtained. The main impurities were two elements: calcium that was transferred from the hands of the experimentalist and iron that was introduced from the forceps and tools used in splitting the samples. Nevertheless, there were impurity-free regions with linear dimensions of about 250 μm and with an iron, cobalt, and nickel content that could not be detected by the method used (i.e., the content was less than 1 μg/g). Magnetic-force microscopy (MFM) was used to identify three types of regions in the impurity-free zones; these regions differ in magnetic properties [4].

In region *A* (Fig. 16a), the amplitude of surface roughness does not exceed 60 nm and the presence of

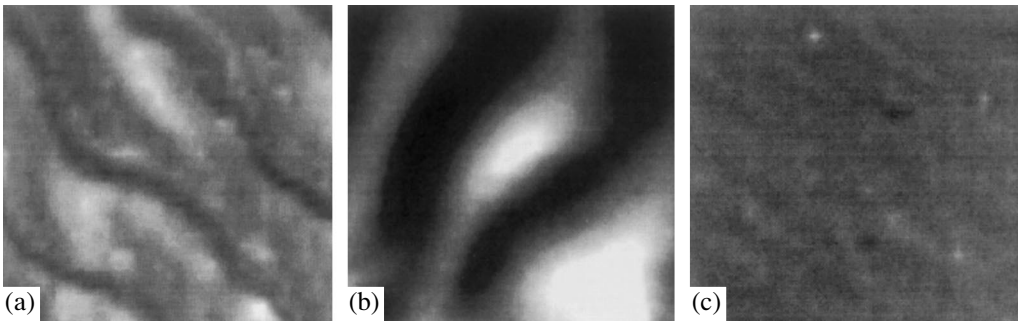

Fig. 16. Images of the magnetic-field gradient in an impurity-free polymerized fullerene. Region *A* (10×10 μm^2) includes parallel magnetic domains on the smooth crystallite surface. Region *B* (2.5×2.5 μm^2) includes the domains at the boundaries of crystallites. In region *C* (10×10 μm^2), there is no magnetic structure.

domains does not correlate with the topography in any respect. The direction of magnetization is inclined to the surface. The domain walls are almost parallel to each other. There are two types of domains: wide (~2 μm) and narrow (~0.6 μm); however, the length of domains is always ~20 μm. Region *B* in the impurity-free zone (Fig. 16b) contains undulatory domains. Here, one can detect a certain correlation between the topology and the magnetism: the main peaks in the topographic and magnetic images coincide with each other. A comparison of the AFM and MFM results shows that the largest gradient of magnetic forces is observed at the crystallite boundaries, where the magnetization direction is nearly perpendicular to the surface. Region *C* occupies 70% of the area of the impurity-free zone; none of the magnetic domains are observed in this region.

If an external magnetic field **B** is applied parallel to the surface in a situation where the direction of domains is inclined or perpendicular to the sample surface, the magnetization direction will change. This behavior is further proof that the origin of the signal is intrinsic. Indeed, an application of a field of 0.01 T radically affects the image in regions *A* and *B*; however, the image contrast is not affected by the field in any way. The images in the regions *A* and *B* are also affected if the magnetic-field direction is changed to the opposite direction.

The area occupied by domains of types *A* and *B* amounts to 30% of the total area of the impurity-free zone studied. Thus, polymerized C_{60} constitutes a mixture of magnetic and nonmagnetic portions, so only a part of the sample makes a contribution to the total magnetization.

4.7. Ferromagnetism in Other Fullerene Structures

The characteristic features of ferromagnetic behavior at room temperature have been observed not only in polymerized fullerenes but also in other fullerene-based structures. The report on a solution of organic polymers into which fullerene was introduced by ultrasonic dispersion was one of the first [126]. After condensation of the solution, there remained a film of a fullerene-containing polymer with ferromagnetic properties that were attributed to the adduct radicals $C_{60}R_n$ (R = H, F, CF_3) [126].

The hybrid fullerenes $C_{60}H_{36}$ obtained by transfer hydrogenation had saturation magnetization M_s = 0.04 emu/g at room temperature; it is noteworthy that all the other compositions were found to be diamagnetic [127]. Ferromagnetism was also observed in the $C_{60}H_{24}$ structure [7]. Twelve samples of $C_{60}H_x$ ($24 \le x \le 32$) were prepared under pressure with an excess of hydrogen; each sample exhibited a nonlinear magnetization curve and a coercivity of about 100 Oe. The saturation magnetization was typically very small; however, three samples exhibited saturation magnetization that was much higher than that in the remaining samples of the batch: 0.046, 0.054, and 0.16 μ_B/C_{60}. These samples were synthesized under identical conditions and had the same composition $C_{60}H_{24}$ and an fcc crystal structure. The ferromagnetic properties of hydrogenated fullerenes become less pronounced with time. The samples are found to be diamagnetic over a period of a year, and analysis of the samples detects no changes either in the composition or in the crystal structure. The curves $\sigma(H)$ are identical in the range 80–300 K, and the Curie point is much higher than room temperature; this behavior (as in the case of polymerized fullerenes) is inconsistent with small values of magnetization. One may consider various models based on ferrimagnetism, the slanting of magnetic moments, or weak ferromagnetism. However, the evolution to the diamagnetic (rather than the antiferromagnetic) state and the appreciable spread in the values of magnetization from sample to sample count in favor of magnetic islands in a nonmagnetic matrix.

5. THE ROLE OF IMPURITIES IN THE MAGNETISM OF CARBON STRUCTURES

The main question arising in studies of magnetism in carbon structures is related to the role of metallic impurities. *Caveat emptor* [128] (caution against error) was first expressed at the early stages of research on

organic magnetic materials and retains its validity to the present day. Iron makes up 5% of the earth's crust and carbon, less than 0.01%. Any household organic material contains several tenths of one percent of iron, although this circumstance does not transform the organic substance into a ferromagnetic material. All the publications cited here include an analysis of impurities and the following basic arguments. If the iron impurity atoms, whose content typically amounts to 20–100 ppm, are distributed uniformly in the material, they cannot make a contribution to the magnetization owing to the large interatomic distances and the resulting impossibility of exchange interactions. If it is assumed that ferromagnetic properties are caused by the clusterization of iron atoms under specific experimental conditions, the calculated resulting magnetic moment (taking into account all metal atoms) is always found to be smaller than the experimental value by one to three orders of magnitude. An impurity-based model cannot explain the dependences of magnetic properties on technology, the concentrations of hydrogen or oxygen, the isomeric composition, crystallinity, and the hybridization of carbon atoms.

In order to maintain objectivity, we note immediately that magnetic properties can be greatly affected by a mechanical effect without any changes in the elemental composition. Effects such as pressure, grinding, and pulverization generate radicals and are conducive to a more uniform distribution of impurity iron clusters. A specially prepared ultradisperse powder will be attracted to a magnet; we verified this effect in coal, glass, aluminum, grass, and peat.

Special additives of iron to activated carbon showed that the effect of iron did not manifest itself if the iron content is lower than 6–8% [129]. Decomposition of a PDA organic substance with various values of iron content (from 3.5 to 2200 ppm) was also studied [130]; magnetic properties of the reaction products were analyzed. A sharp transition from the diamagnetic to paramagnetic states and a nonlinear magnetization curve were observed when the content of iron in the starting material was changed from 2000 to 2100 ppm [130].

The report on ferromagnetism in fragments of the Canyon Diablo giant meteorite [122] makes one reconsider the problem of carbon magnetism. In that study, magnetic properties of graphite with inclusions of magnetite were considered. Graphite is a semimetal, whereas magnetite is a half-metal; equalization of the chemical potential for electrons with differing spin orientations at the interface leads to the complete spin polarization of neighboring carbon atoms. If the spin-related splitting of graphite energy bands amounts to several electronvolts, the Fermi level shifts to the region with a higher density of states and sustains the spin polarization. Thus, the magnetite inclusions are found to be surrounded by a region of spin polarization that is attenuated according to the law $\exp[-(r - r_0)/\lambda_s]$. Measurements of magnetization yield the attenuation constant $\lambda_s = 5$ nm. This value is reasonable taking into account that the Fermi wavelength in graphite is equal to 10.6 nm. The idea of induced magnetism in graphite is very attractive from both the theoretical and the practical standpoints. If the model is correct, one can obtain lightweight, inexpensive, and biocompatible magnetic materials by introducing a small amount of iron into carbon structures.

It is difficult to apply the model under consideration to polymerized fullerenes. Ferromagnetic domains were observed in regions with linear dimensions of about 250 μm, where only carbon atoms were detected to within the measurement accuracy of 1 ppm. The question arises as to whether the source of magnetic contrast in "impurity-free" regions can still be related to impurities. One cannot expect the fields to extend for hundreds of micrometers from iron grains if there are no external fields (the above grains are no more than a micrometer in size). Let us still assume that the distant iron-impurity atoms can give rise to an external field (hypothesis *1*). It is noteworthy that magnetic domains can appear only in a magnetic material; however, elemental analysis shows that the material consists only of carbon to within an accuracy of 1 μg/g. Let us then accept another hypothesis: iron acts as a trigger that transforms carbon into a magnetic material (hypothesis *2*). The effect of magnetic proximity can be observed at distances as large as 100 nm from inclusions of magnetic material. The distance to the nearest impurity cluster exceeds 0.1 mm in the regions occupied by magnetic domains. In the direction perpendicular to the plane, impurities were not detected within the characteristic depth available for analysis by particle-induced X-ray emission (PIXE); this depth is approximately equal to 36 μm. Another hypothesis is based on the assumption that macroscopic magnetism in polymerized C_{60} is ensured by impurities whose amount is smaller than 1 μg/g; if this hypothesis (hypothesis *3*) is not accepted, one then has to state that pure carbon is a magnetic material [4].

6. MODELS OF MAGNETISM IN FULLERENES

As shown above, the models of magnetism in carbon structures are diverse. These models range from those based on calculations of an ideal graphite–diamond structure with ferromagnetic interaction or on ferromagnetism due to topological defects in the graphite structure to those based on the magnetic-proximity effects induced by metallic impurities. Nevertheless, it cannot be stated with confidence which of the models can be applied to the experimental facts described above. Polymerized C_{60} is a comparatively simple structure; it is conceivable that investigation of this structure can furnish insight into the mechanisms of origination of magnetic ordering in carbon.

The first attribute of fullerene polymerization consists in the transformation of $sp^{2.2}$-hybridized fullerenes

into a structure that contains alternating sp^2- and sp^3-hybridized atoms.

The second special feature of polymerization consists in the specific orientation of molecules. It has been shown repeatedly that it is the orientation of C_{60} that plays the most important role in the origination of exchange interaction.

The third special feature is not a characteristic of polymerization but rather is typical of specific processes that occur during experiments. These processes include the formation of a ferromagnetic phase under conditions that are very close to those of the destruction of fullerenes. Two types of defects may be considered: defects of the molecule itself and defects formed as a result of the disruption of interfullerene bonds. Both types of defects are characteristic of both fullerenes polymerized under pressure and the phototransformed phase; therefore, one should not disregard either of these possibilities.

The hypothesis about undamaged fullerenes is supported by the following facts. In the case of fullerenes polymerized under a high pressure, the temperature of formation of the ferromagnetic phase is approximately 100 K lower than that of the collapse of the fullerene cage. Bonds connecting molecules in the polymer phase are much weaker than those of the cage itself. These bonds are considered diamond-like, although they are much weaker than those in diamond, are directed at right angles to each other rather than at 109.45° (as in diamond), and are destroyed as a result of heating to 560 K. It is quite possible that it is these bonds that constitute the weak point in the polymerized structure and can be a source of unpaired spins. Ferromagnetism was observed not only in fullerenes on the verge of collapse but also in structures where the integrity of the cage was unquestionable: in hydrated fullerenes, compounds containing palladium, and disperse C_{60} in the polymer matrix.

The situation where some of the molecules are destroyed or damaged should be also considered. It was initially stated [1] that magnetism ceases to exist completely as a result of depolarization; however, this statement was later corrected [131]. Magnetization decreases irreversibly after annealing; however, this decrease is specific for each sample. One of the samples lost only 2% of magnetization, and the X-ray diffraction patterns remained unchanged after annealing and corresponded as before to the rhombohedral phase of polymerized C_{60}. This result is nontrivial since the rhombohedral phase is typically depolymerized at 560 K. Figure 17 illustrates the results of the relevant studies. Although a sample of polymerized C_{60} annealed for 3 h at a temperature of 800 K lost 20% of magnetization, this sample did not decompose into starting fullerenes. It is likely that the phase formed under critical conditions features enhanced structural stability accompanied by magnetic stability.

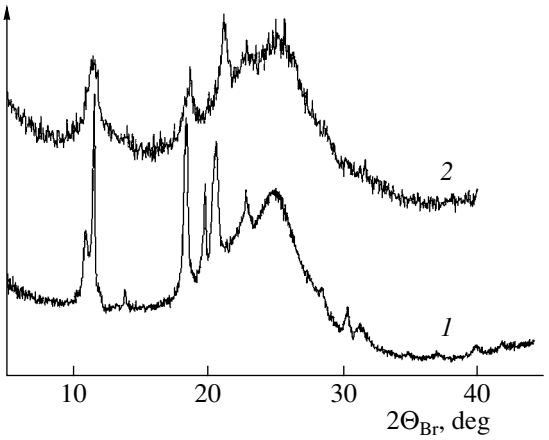

Fig. 17. X-ray diffraction patterns of (*1*) C_{60} polymerized at a temperature close to the limit of thermal stability of the molecule and (*2*) the same sample after annealing for 3 h at a temperature of 800 K.

It seems that the irradiation of fullerenes with visible and ultraviolet light should not affect the integrity of the molecules themselves. However, it has been repeatedly reported that photoexcitation of a C_{60}–O_2 system leads to the formation of carbonyl structures and, if the light intensity is high, to the dissociation of carbon molecules and formation of amorphous carbon.

If it is assumed that the change in magnetic properties of fullerene films is caused by defects, the parallel between the magnetism of fullerenes polymerized by exposure to light and pressure then becomes clear. Let us consider a diagram of the pressures and temperatures required to produce polymerized fullerenes [132]. In this diagram, one can find regions that correspond to the formation of orthorhombic, tetragonal, and hexagonal polymerized phases. It is also possible to determine the conditions under which the fullerene cage is broken with the formation of several postfullerene phases. The closed circles indicating the conditions for observing the ferromagnetic behavior of fullerene materials (2.5 GPa, 1025 K; 6 GPa, 1075 K; 6 GPa, 1045 K; and 9 GPa, 900 K) are located in the critical region. The arrangement of these circles follows the run of the line that separates polymerized fullerenes from destroyed fullerenes [1–3, 124] (Fig. 18).

The observation of poorly pronounced ferromagnetic properties in fullerenes that are photopolymerized in the presence of oxygen suggests that the magnetic properties of fullerenes polymerized under pressure could be improved by intercalating gases into the starting material. We tested the validity of this assumption and obtained the opposite result. The samples were prepared under a pressure of 2.5 GPa and a temperature of 1025 K; the cells were divided into two sections by a vertical partition. A half of the cell was filled with C_{60} powder, while the second half was filled with the same powder but exposed to air for 24 h. The results of magnetic studies showed that the presence of oxygen had a

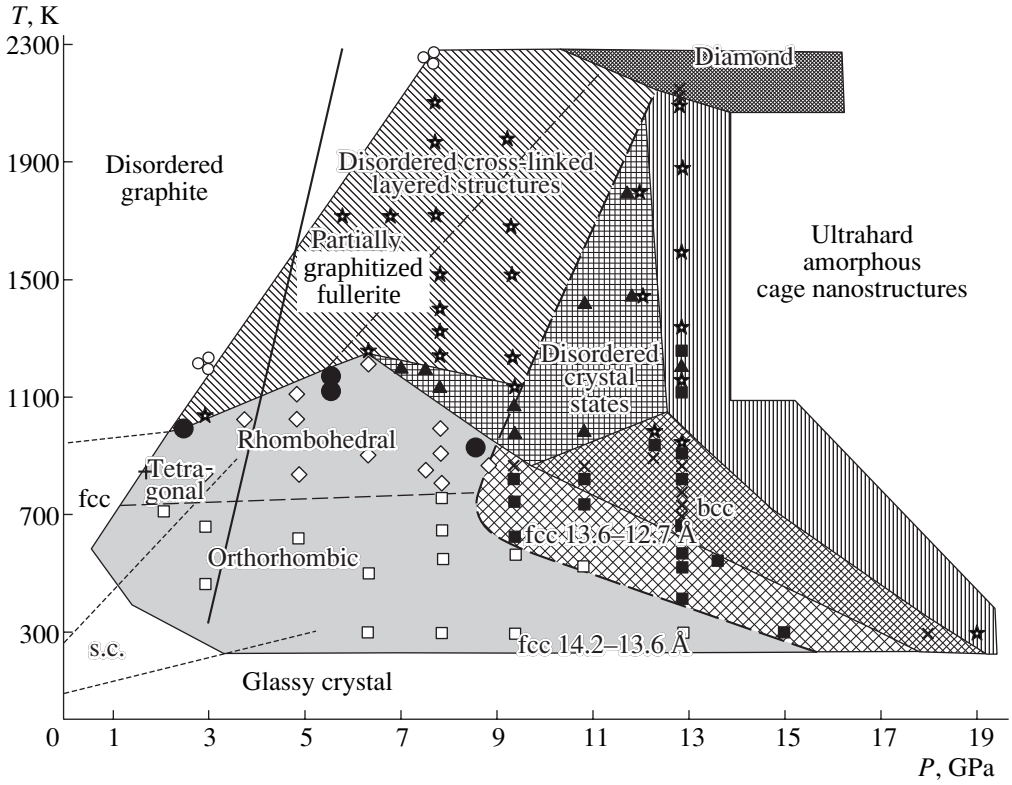

Fig. 18. Diagram of pressures and temperatures required for preparation of various carbon phases from C_{60} fullerenes [132]. Large closed circles indicate the conditions under which the phases exhibiting spontaneous magnetization were obtained.

detrimental effect on the magnetic properties: magnetization in the material saturated with oxygen was found to be equal to a third of that in the material that was not exposed to air.

The apparent contradiction is easily attributed to the fact that oxygen plays opposite roles in the two cases under consideration. Molecular oxygen dissociates in the fullerene lattice exposed to light, interacts with the fullerene, and produces charged radicals. If fullerene is subjected to pressure, oxygen no longer acts as a source of generated spins, because the spins are now generated by the fullerene itself. In contrast, oxygen reacts easily with dangling carbon bonds and cancels out the spins that form.

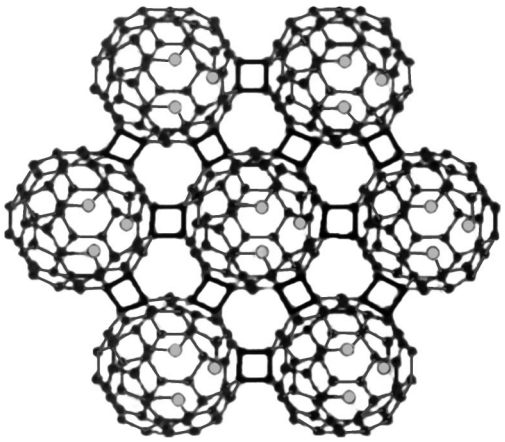

Fig. 19. Model of interaction between defects in rhombohedral C_{60}. The atoms surrounding the defect (a carbon vacancy) are shown as large gray circles. The bonds between the sp^3-coordinated atoms are represented by thick solid lines [134].

In the models of ferromagnetic fullerenes, the following three possibilities are considered: (i) a fraction of the fullerene cages are broken, and, thus, unpaired electrons appear at the dangling bonds; (ii) the shape of the fullerene cage changes as a result of Stone–Wales transformations; and (iii) fullerenes remain intact, but unpaired electrons are formed at interfullerene links. In an alternative approach, a high-spin ground state of charged fullerene polymer is considered; this state arises owing to the contribution of electron correlation to the total energy [133].

In a theoretical paper [134], Andriotis *et al.* suggested a scenario in which structural defects (vacancies) and sp^3-hybridized atoms interact. A correlation should exist between spin moments for magnetic ordering to appear. Since the defects are widely spaced, interaction between them is indirect and needs a mediator. The dipole moment induced by a vacancy can play the role of such a mediator. The Coulomb interaction

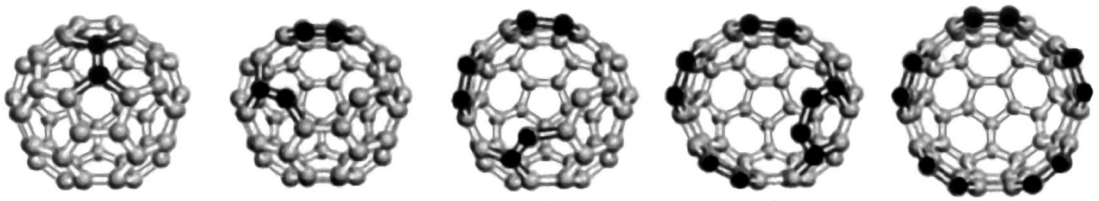

Fig. 20. Models of intermediate metastable structures formed as a result of the transformation of C_{60} into a segment of an open (5, 5) nanotube according to the Stone–Wales reactions. The atoms involved in the reactions are depicted by closed circles. The initial fullerene and the final *SW*-III structure are nonmagnetic; the structure *SW*-I is antiferromagnetic and the structure *SW*-II is ferromagnetic [98].

between localized excess charges and electric dipoles ensures a means for the exchange interaction between magnetic moments (Fig. 19).

The cage of a C_{60} fullerene can be made open by a sequence of Stones–Wales transformations that require lower energies than the breakage of the bonds. As illustrated in Fig. 20, a sequence of five transformations converts fullerene to a fragment of a nanotube. Of the first three intermediate states, referred to as *SW*-I, *SW*-II, and *SW*-III, the first is antiferromagnetic and the second is ferromagnetic. In order to verify this identification, the distribution of spins was considered for various configurations [98]. The spin density is highest at the sites where a zigzag-type edge with dangling bonds is formed. The degree of overlap of electron clouds in the *SW*-II structure is lower than in the *SW*-I structure, so the ferromagnetic ordering in *SW*-II is stabilized. The result of calculations is consistent with previous concepts about the formation of a partially filled flat band that gives rise to magnetic instability. The difference between this and graphite ribbons consists in the fact that the total moment does not attenuate in this structure. It is predicted that, in the case of open nanotubes with a specific configuration, the effect should be much more pronounced than in the case of fullerenes [98].

7. CONCLUSION

The reasons why one cannot expect high-temperature ferromagnetism in carbon are well known [10]: (i) the singlet state leading to antiferromagnetism is energetically more favorable for organic pairs of radicals; (ii) unpaired spins in organic substances practically do not interact with each other, since these spins are separated by large spin-free fragments; and (iii) an attempt to bring together the spins of radicals ultimately results in a chemical reaction.

Nevertheless, about 100 papers and 30 patents have been published in which methods for obtaining structures that either consisted only of carbon or included elements of the first row of the periodic table and had nonlinear magnetization at room temperature are described; these were ferromagnetic *in sensu maiore*. Reproducible results obtained recently for polymerized fullerenes and proton-irradiated graphite suggest that a specific ordering of carbon atoms, which is favorable for spontaneous magnetization, arises under various critical conditions, such as high temperatures and pressures or irradiation. Both small values of total magnetization of the sample and microscopy studies indicate that the ferromagnetic phase originates in the form of magnetic islands in a nonmagnetic matrix.

Several scenarios that account for (or predict) the magnetism of carbon have been suggested: volume magnetism of an ideal structure that contains alternating sp^2- and sp^3-hybridized atoms, induced magnetism, and atomic-scale magnetism caused by structural imperfection.

If it is technologically feasible to produce a bulk carbon magnetic material in a macroscopic amount, one can then expect applications of this material in engineering, as well as in medicine and biology as a unique biocompatible magnetic material.

If the hypothesis about induced magnetism is confirmed, there may be a quicker way to produce bulk carbon magnetic materials: controlled doping.

If the phenomenon of carbon magnetism is basically related to the boundary states, then further development of this effect can be expected in the field of nanotechnology; specifically, it was suggested that open nanotubes be used as nanodimensional magnets. The experimentally observed possibility of changing the magnetic properties of fullerenes and graphite by irradiating these materials can be used to produce magnetic patterns by nanolithography.

New materials have always been a decisive factor in the development of new technologies. The publications cited in this review show that the properties of carbon, which is the main element in all creatures, are far from fully understood.

ACKNOWLEDGMENTS

This study was supported by the Russian Foundation for Basic Research, project no. 02-02-17617.

REFERENCES

1. T. L. Makarova, B. Sundqvist, P. Esquinazi, *et al.*, Nature **413**, 718 (2001).
2. R. A. Wood, M. H. Lewis, M. R. Lees, *et al.*, J. Phys.: Condens. Matter **14**, L385 (2002).
3. V. N. Narozhnyi, K.-H. Müller, D. Eckert, *et al.*, Physica B (Amsterdam) **329**, 537 (2003).
4. K.-H. Han, D. Spemann, R. Höhne, *et al.*, Carbon **41**, 785 (2003).
5. Y. Murakami and H. Suematsu, Pure Appl. Chem. **68**, 1463 (1996).
6. T. L. Makarova, K.-H. Han, P. Esquinazi, *et al.*, Carbon **41**, 1575 (2003).
7. V. E. Antonov, I. O. Bashkin, S. S. Khasanov, *et al.*, J. Alloys Compd. **330**, 365 (2002).
8. J. Gonzalez, F. Guinea, and M. Vozmediano, Phys. Rev. B **63**, 134421 (2001).
9. Y. Kopelevich, P. Esquinazi, J. H. S. Torres, and S. Moehlecke, J. Low Temp. Phys. **119**, 691 (2000).
10. *Magnetism: Molecules to Materials*, Ed. by J. S. Miller and M. Drillon (Weinheim, New York, 2002), Vols. 1–4.
11. T. L. Makarova, in *Studies of High-T_c Superconductivity*, Ed. by A. Narlikar (Nova Sci., Huntington, 2003), Vol. 45, p. 107.
12. *Theory and Applications of Molecular Diamagnetism*, Ed. by L. N. Mulay and E. A. Boudreaux (Wiley, New York, 1976).
13. R. R. Gupta, in *Landolt–Börnstein New Series II*, Ed. by K.-H. Hellwege (Springer, Berlin, 1986), Vol. 16, p. 7.
14. V. Elser and R. C. Haddon, Phys. Rev. A **36**, 4579 (1987).
15. M. F. Ling, T. R. Finlayson, and G. L. Raston, Aust. J. Phys. **52**, 913 (1999).
16. J. H. van Vleck, *The Theory of Electric and Magnetic Susceptibilities* (Oxford Univ. Press, Oxford, 1932).
17. S. Hudgens, M. Kastner, and H. Fritzsche, Phys. Rev. Lett. **33**, 1552 (1974).
18. G. Wagoner, Phys. Rev. **118**, 647 (1960).
19. J. W. McClure, Phys. Rev. **104**, 666 (1956).
20. P. Esquinazi, A. Setzer, R. Höhne, *et al.*, Phys. Rev. B **66**, 024429 (2002).
21. J. Heremans, D. Olk, and T. Morell, Phys. Rev. B **49**, 15122 (1994).
22. M. S. Sercheli, Y. Kopelevich, R. R. da Silva, *et al.*, Solid State Commun. **121**, 579 (2002).
23. M. S. Sercheli, Y. Kopelevich, R. R. da Silva, *et al.*, Physica B (Amsterdam) **320**, 413 (2002).
24. H. M. McConnell, J. Chem. Phys. **39**, 1910 (1963).
25. H. M. McConnell, Proc. Robert A. Welch Found. Chem. Res. **11**, 144 (1967).
26. N. Mataga, Theor. Chim. Acta **10**, 372 (1968).
27. A. A. Ovchinnikov and V. N. Spector, Synth. Met. **27**, B615 (1988).
28. A. A. Ovchinnikov and L. I. Shamovsky, J. Mol. Struct.: THEOCHEM **251**, 133 (1991).
29. A. V. Rode, R. G. Elliman, E. G. Gamaly, *et al.*, Appl. Surf. Sci. **197**, 644 (2002).
30. M.-F. Lin and F.-L. Shyu, J. Phys. Soc. Jpn. **69**, 3529 (2000).
31. C. W. Chiu, F. L. Shyu, C. P. Chang, *et al.*, J. Phys. Soc. Jpn. **72**, 170 (2003).
32. K. Wakabayashi and M. Sigrist, Phys. Rev. Lett. **84**, 3390 (2000).
33. H. Takeda and K. Yoshino, Jpn. J. Appl. Phys., Part 1 **41**, 6436 (2002).
34. C. W. Chiu, M. F. Lin, and F. L. Shyu, Physica E (Amsterdam) **11**, 356 (2001).
35. M. F. Lin, M. Y. Chen, and F. L. Shyu, J. Phys. Soc. Jpn. **70**, 2513 (2001).
36. K. Harigaya, Y. Kobayashi, K. Takai, *et al.*, J. Phys.: Condens. Matter **14**, L605 (2002).
37. A. S. Kotosonov, Pis'ma Zh. Éksp. Teor. Fiz. **43**, 30 (1986) [JETP Lett. **43**, 37 (1986)].
38. K. Kobayashi, Phys. Rev. B **48**, 1757 (1993).
39. K. Yoshizawa, K. Okahara, T. Sato, *et al.*, Carbon **32**, 1517 (1994).
40. M. Fujita, K. Wakabayashi, K. Nakada, and K. Kusakabe, J. Phys. Soc. Jpn. **65**, 1920 (1996).
41. K. Wakabayashi, M. Fujita, H. Ajiki, and M. Sigrist, Physica B (Amsterdam) **280**, 388 (2000).
42. O. E. Andersson, B. L. V. Prasad, H. Sato, *et al.*, Phys. Rev. B **58**, 16387 (1998).
43. A. Nakayama, K. Suzuki, T. Enoki, *et al.*, Synth. Met. **57**, 3736 (1993).
44. K. Wakabayashi, M. Fujita, K. Kusakabe, and K. Nakada, Czech. J. Phys. **46**, 1865 (1996).
45. A. S. Kotosonov and S. V. Kuvshinnikov, Phys. Lett. A **230**, 377 (1997).
46. M. F. Lin and K. W. K. Shung, Phys. Rev. B **52**, 8423 (1995).
47. S. Bandow, J. Appl. Phys. **80**, 1020 (1996).
48. S. Bandow, F. Kokai, K. Takahashi, *et al.*, Appl. Phys. A **73**, 281 (2001).
49. L. Liu, G. Y. Guo, C. S. Jayanthi, and S. Y. Wu, Phys. Rev. Lett. **88**, 217206 (2002).
50. M. Buhl and A. Hirsch, Chem. Rev. **101**, 1153 (2001).
51. E. Osawa, Kagaku (Kyoto) **25**, 843 (1970).
52. V. Elser and R. C. Haddon, Nature **325**, 792 (1987).
53. A. Pasquarello, M. Schlüter, and R. C. Haddon, Science **257**, 1660 (1992).
54. R. C. Haddon, Science **261**, 1545 (1993).
55. R. Zanasi and P. Fowler, Chem. Phys. Lett. **238**, 270 (1995).
56. M. Buhl, Chem. Eur. J. **4**, 734 (1998).
57. R. C. Haddon and A. Pasquarello, Phys. Rev. B **50**, 16459 (1994).
58. M. Saunders, A. Jimenez-Vazquez, R. J. Cross, *et al.*, Am. Chem. Soc. **117**, 9305 (1995).
59. D. Jonsson, P. Norman, K. Ruud, *et al.*, J. Chem. Phys. **109**, 572 (1998).

60. T. Sternfeld, R. E. Hoffman, C. Thilgen, *et al.*, J. Am. Chem. Soc. **122**, 9038 (2000).
61. R. C. Haddon, L. F. Schneemeyer, J. V. Waszczak, *et al.*, Nature **350**, 46 (1991).
62. R. S. Ruoff, D. Beach, J. Cuomo, *et al.*, J. Phys. Chem. **95**, 3457 (1991).
63. W. L. Luo, H. Wang, R. S. Ruoff, *et al.*, Phys. Rev. Lett. **73**, 186 (1994).
64. V. Buntar, H. W. Weber, and M. Ricco, Solid State Commun. **98**, 175 (1996).
65. D. Arčon and K. Prassides, Struct. Bonding (Berlin) **100**, 129 (2002).
66. K. Prassides, S. Margadonna, D. Arcon, *et al.*, J. Am. Chem. Soc. **121**, 11227 (1999).
67. P.-M. Allemand, K. C. Khemani, A. Koch, *et al.*, Science **253**, 301 (1991).
68. A. Mrzel, A. Omerzu, P. Umek, *et al.*, Chem. Phys. Lett. **298**, 329 (1998).
69. B. Narymbetov, A. Omerzu, V. V. Kabanov, *et al.*, Nature **407**, 883 (2000).
70. R. Blinc, P. Cevc, D. Arcon, *et al.*, Phys. Rev. B **58**, 14416 (1998).
71. E. H. Lieb, Phys. Rev. Lett. **62**, 1201 (1989).
72. A. Mielke and H. Tasaki, Commun. Math. Phys. **158**, 341 (1993).
73. N. Shima and H. Aoki, Phys. Rev. Lett. **71**, 4389 (1993).
74. H. Kajii, K. Yoshino, T. Sato, and T. Yamabe, J. Phys. D: Appl. Phys. **33**, 3146 (2000).
75. H. Takeda, H. Kajii, and K. Yoshino, Jpn. J. Appl. Phys., Part 1 **41**, 3782 (2002).
76. A. J. Stone and D. J. Wales, Chem. Phys. Lett. **128**, 501 (1986).
77. M. Igami, K. Nakada, M. Fujita, and K. Kusakabe, Czech. J. Phys. **46**, 2715 (1996).
78. D. J. Klein and L. Bytautas, J. Phys. Chem. A **103**, 5196 (1999).
79. K. Nakada, M. Fujita, G. Dresselhaus, and M. S. Dresselhaus, Phys. Rev. B **54**, 7954 (1996).
80. K. Wakabayashi, M. Sigrist, and M. Fujita, J. Phys. Soc. Jpn. **67**, 2089 (1998).
81. K. Wakabayashi and K. Harigaya, J. Phys. Soc. Jpn. **72**, 998 (2003).
82. K. Kusakabe and M. Maruyama, Phys. Rev. B **67**, 092406 (2003).
83. K. Kusakabe and Y. Takagi, Mol. Cryst. Liq. Cryst. **387**, 231 (2002).
84. K. Harigaya, J. Phys.: Condens. Matter **13**, 1295 (2001).
85. K. Harigaya, Chem. Phys. Lett. **340**, 123 (2001).
86. Y. Shibayama, H. Sato, T. Enoki, and M. Endo, Phys. Rev. Lett. **84**, 1744 (2000).
87. T. Enoki, N. Kawatsu, Y. Shibayama, *et al.*, Polyhedron **20**, 1311 (2001).
88. N. Kobayashi, T. Enoki, C. Ishii, *et al.*, J. Chem. Phys. **109**, 1983 (1998).
89. H. Sato, N. Kawatsu, T. Enoki, *et al.*, Solid State Commun. **125**, 641 (2003).
90. K. Harigaya, Chem. Phys. Lett. **339**, 23 (2001).
91. K. Harigaya and T. Enoki, Mol. Cryst. Liq. Cryst. **386**, 205 (2002).
92. K. Harigaya and T. Enoki, Chem. Phys. Lett. **351**, 128 (2002).
93. P. O. Lehtinen, A. S. Foster, A. Ayuela, *et al.*, Phys. Rev. Lett. **91**, 017202 (2003).
94. A. Oshiyama, S. Okada, and S. Saito, Physica B (Amsterdam) **323**, 21 (2002).
95. S. Okada and A. Oshiyama, Phys. Rev. Lett. **87**, 146803 (2001).
96. S. Okada and A. Oshiyama, J. Phys. Soc. Jpn. **72**, 1510 (2003).
97. T. Hikihara and X. Hu, Physica B (Amsterdam) **329**, 1166 (2003).
98. Y.-H. Kim, J. Choi, K. J. Chang, and D. Tomanek, Phys. Rev. B **68**, 125240 (2003).
99. H. Takeda and K. Yoshino, J. Phys. D: Appl. Phys. **35**, 3225 (2002).
100. K. Murata and H. Ushijima, J. Natl. Inst. Mater. Chem. Res. **4**, 1 (1996).
101. K. Murata, H. Ushijima, and H. J. Ueda, J. Chem. Soc. Chem. Commun. **7**, 567 (1992).
102. Yu. V. Korshak, A. A. Ovchinnikov, A. M. Shapiro, *et al.*, Pis'ma Zh. Éksp. Teor. Fiz. **43**, 309 (1986) [JETP Lett. **43**, 399 (1986)].
103. Yu. V. Korshak, T. V. Medvedeva, A. A. Ovchinnikov, and V. N. Spektor, Nature **326**, 370 (1987).
104. Y. Cao, P. Wang, Z. Hu, *et al.*, Synth. Met. **27**, B625 (1988).
105. Y. Cao, P. Wang, Z. Hu, *et al.*, Solid State Commun. **68**, 817 (1988).
106. H. Tanaka, K. Tokuyama, T. Sato, and T. Ota, Chem. Lett. **10**, 1813 (1990).
107. J. B. Torrance, S. Oostra, and A. Nazzal, Synth. Met. **19**, 70 (1987).
108. M. Ota, M. Otani, and M. Igarashi, Chem. Lett. **7**, 1179 (1989).
109. Y. M. Shulga, A. I. Boldyrev, and A. A. Ovchinnikov, Chem. Phys. Lett. **189**, 577 (1992).
110. K. Kawabata, M. Mizutani, M. Fukuda, and S. Mizogami, Synth. Met. **33**, 399 (1989).
111. K. Tanaka, M. Kobashi, H. Sanekata, *et al.*, J. Appl. Phys. **71**, 836 (1992).
112. S. Mizogami, M. Mizutani, M. Fukuda, and K. Kawabata, Synth. Met. **43**, 3271 (1991).
113. K. Murata, T. Masuda, and H. Ueda, Chem. Express **5**, 597 (1990).
114. K. Murata, H. Ueda, and K. Kawaguchi, Synth. Met. **44**, 357 (1991).
115. Yu. A. Katulevskii, M. A. Magrupov, and A. A. Muminov, Phys. Status Solidi A **127**, 223 (1991).
116. H. Araki, R. Matsuoka, and K. Yoshino, Solid State Commun. **79**, 443 (1991).

117. H. Araki and K. Yoshino, Jpn. J. Appl. Phys., Part 2 **31**, L130 (1992).
118. H. Araki, Y. B. Roh, N. Kuwamura, and K. Yoshino, Jpn. J. Appl. Phys., Part 2 **31**, L337 (1992).
119. K. Murata, H. Ushijima, H. Ueda, and K. Kawaguchi, J. Chem. Soc. Chem. Commun. **18**, 1265 (1991).
120. H. Ushijima, K. Murata, H. Ueda, and K. Kawaguchi, Mol. Cryst. Liq. Cryst. **233**, 351 (1993).
121. R. Setnescu, S. Jipa, T. Setnescu, *et al.*, Carbon **37**, 1 (1999).
122. J. M. D. Coey, M. Venkatesan, C. B. Fitzgerald, *et al.*, Nature **420**, 156 (2002).
123. K.-H. Han, D. Spemann, P. Esquinazi, *et al.*, J. Magn. Magn. Mater. **270** (2004, in press).
124. T. L. Makarova, B. Sundqvist, and Y. Kopelevich, Synth. Met. **137**, 1335 (2003).
125. T. L. Makarova and B. Sundqvist, High Press. Res. **23**, 135 (2003).
126. M. Ata, M. Machida, H. Watanabe, and J. Seto, Jpn. J. Appl. Phys., Part 1 **33**, 1865 (1994).
127. A. S. Lobach, Y. M. Shul'ga, O. S. Roshchupkina, *et al.*, Fullerene Sci. Technol. **6**, 375 (1998).
128. J. S. Miller, Adv. Mater. **4**, 298 (1992).
129. H. Ueda and K. Murata, Nippon Kagaku Kaishi, No. 12855 (1992).
130. A. Ouchi, K. Saito, and Y. Koga, Chem. Lett., No. 12, 1083 (1995).
131. R. Höhne and P. Esquinazi, Adv. Mater. **14**, 753 (2002).
132. V. D. Blank, S. G. Buga, G. A. Dubitsky, *et al.*, Carbon **36**, 319 (1998).
133. O. E. Kvyatkovskii, M. G. Shelyapina, B. F. Shchegolev, *et al.*, in *Abstracts of IWFAC'2003* (St. Petersburg, Russia, 2003), p. 270.
134. A. N. Andriotis, M. Menon, R. M. Sheetz, and L. Chernozatonskii, Phys. Rev. Lett. **90**, 026801 (2003).

Translated by A. Spitsyn

Semiconductors, Vol. 38, No. 6, 2004, pp. 639–643. Translated from Fizika i Tekhnika Poluprovodnikov, Vol. 38, No. 6, 2004, pp. 665–669.

ELECTRONIC AND OPTICAL PROPERTIES OF SEMICONDUCTORS

A Study of Recombination Centers in Irradiated *p*-Si Crystals

T. A. Pagava

Georgian Technical University, ul. Kostaza 77, Tbilisi, 380075 Georgia

e-mail: tpagava@gtu.edu.ge

Submitted October 27, 2003; accepted for publication November 4, 2003

Abstract—*p*-Si samples irradiated with 8-Mev electrons are studied. It is suggested that the multicomponent V_3 + O or V_2 + O_2 complexes are not recombination centers on the basis of an analysis of the dependences of the minority-carrier lifetime τ, the resistivity ρ, the concentration p, and the Hall mobility μ_H on the temperature of isochronous annealing T_{ann}. Deep donors with energy levels at $\Delta E_i = E_v + 0.40$ eV and the V_3 + O_3 and the V_3 + O_2 complexes affect the values of μ_H and τ. The curves of isochronous annealing are used to determine the annealing-activation energies E_{ann} for defects such as *K* centers, interstitial carbon atoms C_i, the *V* + B and V_2 + O_2 complexes, divacancies V_2, and defects with a level at $\Delta E_i = E_V + 0.20$ eV. These energies were found to be equal to E_{ann} = 0.9, 0.25, 1.6, 2, 1.54, and 2.33 eV, respectively. © *2004 MAIK "Nauka/Interperiodica".*

1. INTRODUCTION

Previous publications [1, 2] indicate that the lifetime of minority charge carriers τ in Si crystals is affected appreciably by irradiation. Bolotov *et al.* [3] attributed the observed increase and subsequent decrease in τ in *n*-Si with an increase in the radiation dose (Φ) to a decrease in the number of recombination centers of chemical origin (Au, Cu, and such) due to the radiation-induced transfer of these centers to interstices, an increase in the number of radiation-induced recombination centers, and retrograde dissolution of an active impurity in nonequilibrium vacancies at large values of Φ. The observed increase in τ from 20 to 70 μs in floating-zone *p*-Si crystals as Φ increases from 2×10^{14} to 8×10^{15} cm^{-2} was previously attributed to a decrease in the concentration of free charge carriers *p*. A recovery of τ was not observed in *p*-Si crystals grown by the Czochralski method even after irradiation with doses that resulted in a decrease in the charge-carrier concentration to 10^{11} cm^{-3}. It is believed [5] that, in floating-zone *p*-Si crystals, defects with deep levels are formed, whereas in crystals grown by the Czochralski method, recombination centers with shallow levels that lead to a degradation of τ are formed in addition to the deep-level recombination centers. It was shown [6] that τ decreased even at doses as low as $\Phi \approx 10^{10}$–10^{13} cm^{-2}, in which case ρ remained virtually unchanged. A decrease in τ from 90 to ~20 μs is attributed to a continuous increase in the concentration of recombination-active radiation defects.

In order to gain insight into which center is responsible for the variation in τ, we studied the dependences of τ, ρ, *p*, and the Hall mobility of holes μ_H on the temperature of isochronous annealing T_{ann} of irradiated *p*-Si crystals.

2. EXPERIMENT, RESULTS, AND DISCUSSION

Samples of single-crystal silicon that were grown by the Czochralski method and had a hole concentration of 6×10^{13} cm^{-3}, a density of grown-in dislocations of 10^3–10^4 cm^{-2}, and starting lifetime $\tau_{st} \approx 100$ μs were studied. The samples under investigation were irradiated with 8-MeV electrons at room temperature. The value of the dose ($\Phi \approx 5 \times 10^{15}$ cm^{-2}) was chosen so that the lifetime in irradiated samples was $\tau_{irr} \approx \tau_{st}$; the flux density of electrons was $\varphi = 5 \times 10^{12}$ cm^{-2} s^{-1}. The irradiated samples were annealed isochronously in the temperature range $T_{ann} \approx$ 80–600°C with a step of 10°C; the samples were kept for 10 min at each fixed temperature. The quantities τ, ρ, *p*, and μ_H were measured after each step of isochronous annealing; the lifetime τ was determined from the decay of photoconductivity.

The excess concentration of charge carriers was generated by exposing the sample under study to a pulsed flux of white polychromatic light that was passed through a polished plane-parallel silicon wafer that acted as a filter. In order to eliminate the effects of trapping centers generated in the samples as a result of irradiation, the samples were exposed to a continuous flux of white light in the course of measurements. Measurements of the volume photovoltage in the plane of irradiated samples did not reveal any inhomogeneity that could affect the results of measuring the lifetime τ. The excess-carrier concentrations (Δn and Δp) determined from the variation in the voltage across the load resistance connected in series with the sample did not exceed a few percent of the equilibrium concentration of holes in this sample (p_0); i.e., the lifetime τ was measured under the condition of a low-injection level: $\Delta n = \Delta p \ll p_0$. The parameters τ, ρ, and μ_H were measured at 300 K. The concentration *p* was measured using the Hall method in the temperature range 77–300 K. Ohmic contacts for measurements were formed by rub-

1063-7826/04/3806-0639$26.00 © 2004 MAIK "Nauka/Interperiodica"

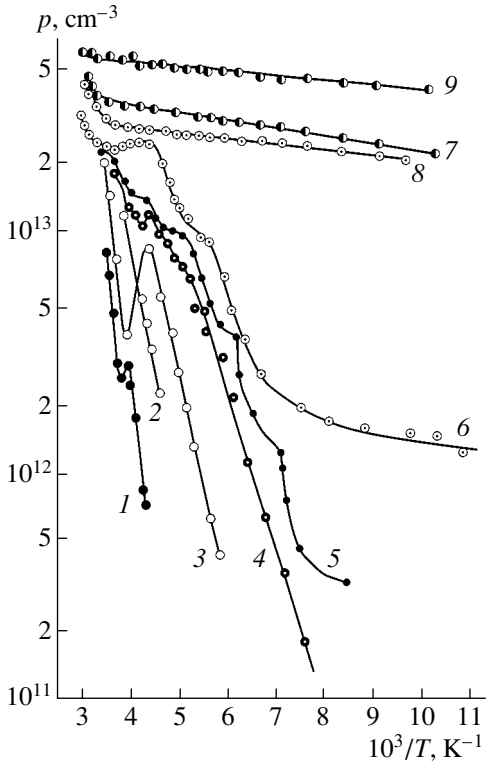

Fig. 1. Temperature dependences of the hole concentration p in a p-Si crystal irradiated with electrons. Curve *1* was obtained before postirradiation annealing. The other curves were obtained after annealing at T_{ann} = (*2*) 100, (*3*) 170, (*4*) 240, (*5*) 270, (*6*) 300, (*7*) 400, (*8*) 500, and (*9*) 600°C.

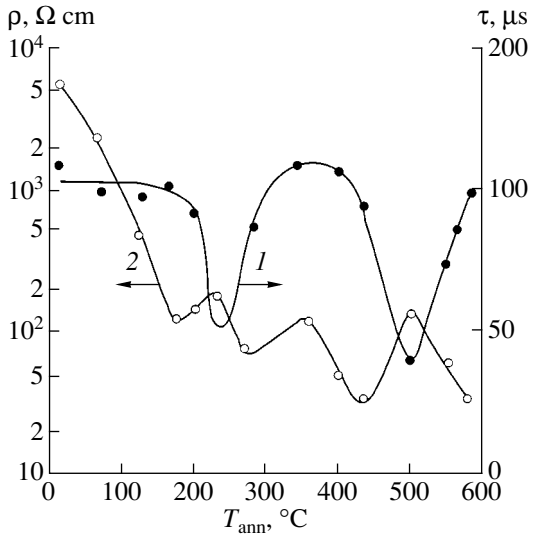

Fig. 2. Dependences of (*1*) the lifetime of minority charge carriers τ and (*2*) the resistivity ρ on the temperature of isochronous annealing T_{ann} for p-Si crystals irradiated with electrons; $T \approx 300$ K.

bing aluminum into the surface of the sample under investigation.

The variation in p as a result of isochronous annealing was determined from the curves $p(10^3/T)$ at T = 260 K. The error in determining p was no larger than 10%. The energy levels of defects ΔE_i were determined on the assumption that $\varepsilon_F = \Delta E_i$, where ε_F is the Fermi level, and the formula

$$p = N_v F_{1/2}\left(\frac{\varepsilon_F}{kT}\right),$$

where N_v is the effective density of states in the valence band and $F_{1/2}$ is the Fermi–Dirac integral. The relevant portions in the plots $p = f(10^3/T)$ were chosen taking into account both the degree of exhaustion of a specific level and the multiplicity of degeneracy of the valence band (Fig. 1, curves *5*, *6*). In heavily compensated samples, the value of ΔE_i was determined from the slope of dependences $p = f(10^3/T)$ (Fig. 1, curves *1–4*). Concentrations of various radiation defects after each stage of isochronous annealing were calculated using the steplike dependences $p = f(10^3/T)$ and $p = f(T_{ann})$ in the temperature ranges 77–300 K and 20–600°C, respectively.

Figure 2 shows variations in τ (curve *1*) and ρ (curve *2*) at 300 K in relation to the isochronous-annealing temperature T_{ann}; similar dependences for the concentration p (curve *1*) and mobility μ_H (curve *2*) are shown in Fig. 3. In Fig. 3, the numbers *3–11* of the curves correspond to various types of defects, as numbered in the table. The parameters of the defects (the energy levels ΔE_i; the temperatures T_{ann} corresponding to annealing of particular defects; the defect-production rates $\eta = dN_{rd}/d\Phi$, where N_{rd} is the concentration of radiation defects; the annealing-activation energy E_{ann}; and the plausible identification of the defect types) are also listed in the table.

As can be seen from Fig. 3, the defects with the energy level $\Delta E = E_v + 0.28$ eV (curve *3*) are annealed out in the range T_{ann} = 20–110°C. These defects have a concentration of $N_3 = 3 \times 10^{12}$ cm^{-3} before annealing and are identified with interstitial carbon atoms C_i [7]. The variation in the hole concentration Δp_1 (curve *1*) in the above temperature range is higher than the concentration of atoms C_i by a factor of 2 ($\Delta p_1 \approx 6 \times 10^{12}$ cm^{-3}). This circumstance indicates that other defects are also annealed out in this temperature range. These defects can include tetravacancies V_4 [8]. Apparently, a sharp increase in the mobility μ_H (Fig. 3, curve *2*) in the annealing-temperature range of 20–160°C is related to the annealing of multivacancy centers V_4. It is noteworthy that rearrangement and annealing of the defect–impurity shell of disordered regions also occur in this temperature range, whereas the value of τ remains virtually unchanged (Fig. 2, curve *1*).

A sharp increase in p in the range $T_{ann} \approx$ 170–200°C is related to the annealing of the defects with energy level $E_v + 0.45$ eV and concentration $N_{rd} \approx 5 \times 10^{12}$ cm^{-3} (Fig. 3, curves *1*, *4*). This level is attributed to the complex V + B [9].

According to our calculations, disordered regions with an effective radius $R_{eff} \approx 5 \times 10^3$ Å are formed in *p*-Si crystals ($p = 6 \times 10^{13}$ cm^{-3}) irradiated with 8-MeV electrons. Vacancies (products of dissociation of complexes *V* + B) are actively adsorbed by disordered regions; as a result, the radius R_{eff} increases. The annealing of disordered regions sets in at $T_{ann} \approx 220$°C [10] and is accompanied by a decrease in R_{eff}. This behavior may account for the presence of the minimum at $T_{ann} \approx 230$°C in the dependence $\mu_H(T_{ann})$ (Fig. 3, curve *2*) and the maximum in the dependence $\rho(T_{ann})$ (Fig. 2, curve *2*).

An increase in the concentration of centers with a level at $E_V + 0.18$ eV is observed in the range $T_{ann} \approx$ 100–160°C (Fig. 3, curve *5*). Apparently, this concentration (we failed to observe variation in the concentration of this center in the range 170–260°C) passes through a maximum at $T_{ann} = 220$°C, whereas the centers under consideration are completely annealed out in the region of $T_{ann} \approx 270$°C. The level $E_V + 0.18$ eV belongs to interstitial boron atoms B_i that are formed in the course of irradiation according to the Watkins reaction: $B_s + I \longrightarrow B_i$ [11, 12]. An increase in the concentration of B_i is apparently related to annealing of complexes *V* + B. The concentration of B_i increases until the onset of annealing of complexes *V* + B; the highest concentration of B_i exceeds the concentration of *V* + B complexes by a factor of 2. This circumstance indicates that there are also other mechanisms of formation of B_i interstitials. Apparently, the complex C + B is the source for B_i prior to annealing of the complex *V* + B; according to the authors of [7], the former complex is annealed out in the region of 90°C. A variation in the concentration of B_i does not affect the hole concentration *p* measured at 300 K but results in an appreciable variation in τ (Fig. 2, curve *1*). The invariability of *p* in the course of annealing of the defects B_i indicates that boron interstitials do not return to the lattice sites, which would increase *p*; they apparently diffuse to other sinks and form shallow-level donors, for example $V + O + B_i$ [13].

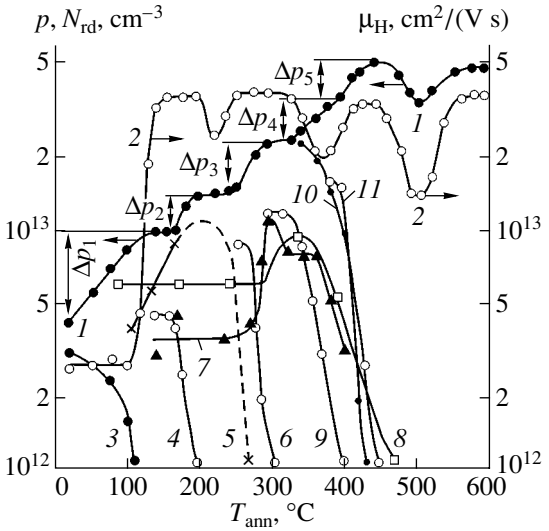

Fig. 3. Variations in (*1*) hole concentration *p*, (*2*) Hall mobility μ_H of majority charge carriers, and (*3–11*) concentrations of some radiation defects N_{rd} in the course of isochronous annealing of *p*-Si crystals irradiated with electrons.

A center with the level $\Delta E_6 = E_V + 0.28$ eV and an initial concentration of $\sim 9 \times 10^{12}$ cm^{-3} is annealed out

Table

Defect no.	ΔE_i, eV	T_{ann}, °C	η, cm^{-1}	E_{ann}, eV	Plausible identification
3	$E_V + 0.28$	20–110	2.2×10^{-3}	0.25	C_i
4	$E_V + 0.45$	170–200	3.3×10^{-3}	1.6	$V + B$
5	$E_V + 0.18$	210–270	3.0×10^{-3}	–	B_i
6	$E_V + 0.28$	260–300 300–330	6.0×10^{-3}	1.54	V_2
7	$E_V + 0.22$	360–400	2.6×10^{-3}	–	V + ?
8	$E_V + 0.20$	340–470	4.4×10^{-3}	2.33	V + ?
9	$E_V + 0.40$	360–400	9.0×10^{-3}	2.0	$V_3 + O$ $V_2 + O_2$
10	$E_V + 0.35$	330–430	18×10^{-3}	0.9	*K* center $V_2 + O + C$
11	$E_V + 0.36$	400–450	11×10^{-3}	–	–
*	$E_V + 0.40$	500–550	–	–	$V_3 + O_3$

Note: The asterisk indicates that this particular defect is formed in the course of isochronous annealing.

in the temperature range $T_{ann} \approx 200$–300°C (Fig. 3, curves *1*, *6*). Judging from the values of T_{ann} and ΔE_i, one can identify these centers with divacancies V_2 [9]. The annealing of divacancies is accompanied by a sharp increase in τ and a decrease in ρ (Fig. 2, curves *1*, *2*). The concentration of annealed-out divacancies is equal to $N_{V_2} \approx \Delta p_3 \approx 9 \times 10^{12}$ cm^{-3} (Fig. 3, curve *1*). This observation indicates that other deep-level donors are not formed as a result of the decomposition of divacancies. The formation of these donors would reduce the value of Δp_3 and disturb the equality between the values of N_{V_2} and Δp_3. An increase in the concentration of defects with a level at $\Delta E_i = E_v + 0.22$ eV is observed in the course of annealing of divacancies; the above defects are annealed out in two stages: at $T_{ann} \approx 300$–330°C and $T_{ann} \approx 360$–400°C. The first stage of annealing of the center under consideration is accompanied by an increase in the concentration of a defect with the energy level at $E_v + 0.20$ eV. This concentration passes through a maximum at 340°C, and the corresponding defects are completely annealed out in the region of 470°C. The origin of these defects is unknown. All that can be said is that they contain vacancies, since their concentration increases as divacancies are annealed out. Taking into account that $E_{ann} \approx 2.33$ eV and $T_{ann} \approx$ 470°C for this defect, we may assume that the center with a level at $E_v + 0.20$ eV is a multicomponent defect [8] (Fig. 3, curves *7*, *8*). These defects do not affect τ, p, ρ, and μ_H at $T \approx 300$ K. The centers with a level at $\Delta E_i = 0.40$ eV (Fig. 3, curve *9*) are annealed out in the same annealing-temperature range as defects with a level at $E_v + 0.20$ eV. Taking into account the values of ΔE_i and T_{ann}, we may assume that these defects are multicomponent complexes of the $V_3 + O$ or $V_2 + O_2$ types [8, 14]. The defects under consideration do not affect μ_H and τ (see Figs. 2, 3). At $T_{ann} \approx 340$°C, the onset of both the annealing of centers with $\Delta E_i = E_v + 0.35$ eV and an increase in the hole concentration p are observed (Fig. 3, curves *1*, *10*). The aforementioned level belongs to the *K* center, which is formed as a result of the attachment of V_2 to the CO center [15]. It is believed that the structure of the *K* center is either $C + O_2 + V$ [16] or $O + C + V$ [17]. However, according to Londos [18], a *K* center comprises only oxygen and carbon (C + O). The concentration of the *K* centers before annealing is equal to $N_K \approx 2.5 \times 10^{13}$ cm^{-3} (Fig. 3, curve *10*).

Defects with a level at $E_v + 0.36$ eV are annealed out in the range of $T_{ann} \approx 400$–450°C. The initial concentration of these defects is equal to $\Delta p_5 \approx 1.5 \times 10^{13}$ cm^{-3} (Fig. 3, curves *1*, *11*). It is impossible to differentiate between the defect levels $E_v + 0.35$ eV and $E_v + 0.36$ eV within the measurement error. However, the annealing of defects with a level at $E_v + 0.36$ eV sets in at a higher temperature; a sharp increase in the hole concentration is observed in the same temperature range (400–440°C) (Fig. 3, curve *1*). The defects under consideration and the *K* centers can efficiently scatter holes, which accounts for the minimum in the dependence $\mu_H(T_{ann})$ (Fig. 3, curve *2*) and the corresponding maximum in the dependence $\rho(T_{ann})$ (Fig. 2, curve *2*) at $T_{ann} \approx 360$°C. The dependence $\tau(T_{ann})$ passes through a maximum at the aforementioned temperature (Fig. 2, curve *1*). The sharp decrease in ρ in the range $T_{ann} \approx 360$–420°C is caused by the increase in μ_H and p. The total concentration of defects that have levels at $E_v + 0.40$, 0.35, and 0.36 eV and are annealed out in the range 340–440°C exceeds the variation in the hole concentration $\Delta p = \Delta p_4 + \Delta p_5$ in this annealing-temperature range (Fig. 3). This circumstance indicates that deep-level centers with a high thermal stability are formed as a result of the annealing of the above defects; the concentration of these centers increases even after the defects are annealed out. In this case, the equality $\Delta N_{rd} = \Delta p + \Delta N'_{rd}$ holds. Here, ΔN_{rd} is the concentration of annealed-out radiation defects, Δp is the increase in the hole concentration, and $\Delta N'_{rd}$ is the concentration of deep-level donors formed as a result of isochronous annealing (taking into account that $p \geqslant N_{rd} + \Delta N'_{rd}$ at any temperature of isochronous annealing). The formation and annealing of the complexes under consideration give rise to a minimum in the dependence $p(T_{ann})$ at $T_{ann} = 500$°C. The hole concentration decreases to 3.5×10^{13} cm^{-3} and at $T_{ann} = 600$°C attains the initial value observed at $T_{ann} \approx 450$°C. By comparing curves *8* and *9* in Fig. 1 at $T = 200$ K, we can determine the concentration of the defects under consideration. The latter is found to be equal to 2.5×10^{13} cm^{-3}. At $T_{ann} \approx 500$°C, the curves $p(T_{ann})$ and $\mu_H(T_{ann})$ feature minima (Fig. 3), which gives rise to a maximum in the dependence $\rho(T_{ann})$ (Fig. 2, curve *2*). As can be seen from Fig. 2 (curve *1*), the dependence $\tau(T_{ann})$ passes through a minimum at $T_{ann} = 500$°C and attains the initial value at $T_{ann} = 600$°C. Judging from the temperatures of formation and annealing of the defects discussed above, we may assume that these defects are multicomponent complexes of the $V_3 + O_3$ or $V_3 + O_2$ types with $\Delta E_i = E_v + 0.40$ eV [8, 19]. These complexes are formed after decomposition of the $V_3 + O$ and $V_2 + O_2$ complexes, the *K* centers, and defects with $\Delta E_i = E_v + 0.36$ eV. The effect of these complexes on the quantities p, μ_H, and τ at 300 K suggests that they are recombination centers with deep levels and can efficiently scatter holes.

It is noteworthy that the value of T_{ann} for the complexes observed in this study is shifted to lower temperatures; this circumstance is apparently related to the presence of disordered regions in the crystal bulk after irradiation with 8-MeV electrons. Disordered regions are efficient sinks for vacancies (products of the decomposition of secondary radiation defects) and reduce the value of T_{ann} for the aforementioned defects. As is well

known [10], isolated disordered regions in silicon crystals are annealed out in the temperature range 200–260°C, while amorphized clusters of disordered regions are annealed out at 570°C. Therefore, disordered regions can affect the value of T_{ann} for all known secondary radiation defects.

Radiation defects in irradiated *p*-Si crystals are diverse. It is therefore difficult to ensure conditions in which recombination process can be completely controlled by the defects of a single type, which would make it possible to determine the parameters of recombination centers from temperature dependences of τ. For the same reason, it is difficult to derive and solve the kinetic equations and determine the quantities ΔE_i, N_{rd}, and T_{ann} for the radiation defects that are formed as a result of irradiation and subsequent isochronous annealing in *p*-Si crystals. Nevertheless, a comparison of the isochronous-annealing curves for τ, ρ, p, and μ_H suggests that the defects B_i and divacancies are responsible the variation in τ at 300 K in the course of isochronous annealing in the range $T_{ann} \approx$ 200–300°C, while multicomponent deep-level donors ($\Delta E_i = E_v + 0.40$ eV) of the $V_3 + O_3$ or $V_3 + O_2$ types are responsible for variations in τ (measured at 300 K) in the region of 500°C; the above donors are also scattering centers. The defects C_i, V_4, $V_3 + O$, and $V_2 + O_2$ are not recombination centers. It was found out that the activation energies for annealing the *K* centers, defects C_i, complexes $V + B$ and $V_2 + O_2$, divacancies V_2, and defects with $\Delta E_i = E_v + 0.20$ eV (as determined from the isochronous-annealing curves for these centers) [20] were equal to E_{ann} = 0.9, 0.25, 1.6, 2.0, 1.54, and 2.33 eV, respectively (see table).

3. CONCLUSION

Thus, we studied variations in the lifetime of minority charge carriers τ, the resistivity ρ, the hole concentration p, and the Hall mobility μ_H of majority charge carriers in electron-irradiated *p*-Si crystals in the course of postirradiation isochronous annealing in the range $T_{ann} \approx$ 80–600°C. An analysis of the dependences of τ, ρ, p, and μ_H on the annealing temperature T_{ann} suggests that interstitial boron atoms B_i and divacancies V_2 are responsible for the variation in the lifetime τ (measured at $T \approx 300$ K) as a result of annealing in the range $T_{ann} \approx$ 200–300°C, while multicomponent deep-level donors with ionization energy $\Delta E_i = E_v + 0.40$ eV of the $V_3 + O_3$ or $V_3 + O_2$ types are responsible for variations in τ at $T_{ann} \approx$ 500°C; these donors are also efficient scattering centers. The defects C_i, $V_3 + O$, and $V_2 + O_2$ are not recombination centers at $T \approx 300$ K. We used the isochronous-annealing curves to determine the activation energies for annealing *K* centers, interstitial carbon atoms C_i, the complexes $V + B$ and $V_2 + O_2$, divacancies V_2, and defects with an energy level at $\Delta E_i = E_v + 0.20$ eV. These energies were found to be equal to 0.9, 0.25, 1.6, 2.0, 1.54, and 2.33 eV, respectively.

REFERENCES

1. V. S. Vavilov, S. I. Vintovkin, A. S. Lyutovich, *et al.*, Fiz. Tverd. Tela (Leningrad) **7**, 502 (1965) [Sov. Phys. Solid State **7**, 399 (1965)].
2. V. S. Vavilov, *Effects of Radiation on Semiconductors* (Fizmatgiz, Moscow, 1963; Consultants Bureau, New York, 1965).
3. V. V. Bolotov, V. A. Korotchenko, A. P. Mamontov, *et al.*, Fiz. Tekh. Poluprovodn. (Leningrad) **14**, 2257 (1980) [Sov. Phys. Semicond. **14**, 1337 (1980)].
4. Z. V. Basheleĭshvili, V. S. Garnyk, S. N. Gorin, and T. A. Pagava, Fiz. Tekh. Poluprovodn. (Leningrad) **18**, 1714 (1984) [Sov. Phys. Semicond. **18**, 1074 (1984)].
5. V. S. Garnyk and Z. V. Basheleĭshvili, Fiz. Tekh. Poluprovodn. (Leningrad) **24**, 1485 (1990) [Sov. Phys. Semicond. **24**, 930 (1990)].
6. G. Tsintsadze, Z. Bashaleishvili, T. Pagava, *et al.*, Bull. Georgian Acad. Sci. **162** (1), 63 (2000).
7. V. N. Gubskaya, P. V. Kuchinskiĭ, and V. M. Lomako, Fiz. Tekh. Poluprovodn. (Leningrad) **20**, 1055 (1986) [Sov. Phys. Semicond. **20**, 664 (1986)].
8. V. V. Emtsev and T. V. Mashovets, *Impurities and Point Defects in Semiconductors* (Radio i Svyaz', Moscow, 1981).
9. I. D. Konozenko, A. K. Semenyuk, and V. I. Khivrich, *Radiation Effects in Silicon* (Naukova Dumka, Kiev, 1974).
10. *Physical Processes in Irradiated Semiconductors*, Ed. by L. S. Smirnov (Nauka, Novosibirsk, 1977).
11. N. V. Kolesnikov, S. E. Mal'khanov, and M. A. Pogarskiĭ, Fiz. Tekh. Poluprovodn. (Leningrad) **12**, 1836 (1978) [Sov. Phys. Semicond. **12**, 1088 (1978)].
12. V. V. Luk'yanitsa, Fiz. Tekh. Poluprovodn. (St. Petersburg) **33**, 921 (1999) [Semiconductors **33**, 842 (1999)].
13. M. Yu. Barabanenkov, A. V. Leonov, V. N. Mordkovich, and N. M. Omel'yanovskaya, Fiz. Tekh. Poluprovodn. (St. Petersburg) **33**, 897 (1999) [Semiconductors **33**, 821 (1999)].
14. J. Bourgoin and M. Lannoo, *Point Defects in Semiconductors*, Vol. 2: *Experimental Aspects* (Springer, New York, 1983; Mir, Moscow, 1985).
15. Y. H. Lee, J. W. Corbett, and K. L. Brover, Phys. Status Solidi A **41**, 637 (1977).
16. L. S. Berman, N. A. Vitkovskiĭ, V. N. Lomasov, and V. N. Tkachenko, Fiz. Tekh. Poluprovodn. (Leningrad) **24**, 2186 (1990) [Sov. Phys. Semicond. **24**, 1354 (1990)].
17. P. M. Mooney, L. J. Cheng, M. Suly, *et al.*, Phys. Rev. B **15**, 3836 (1977).
18. C. A. Londos, Jpn. J. Appl. Phys. **27**, 2089 (1988).
19. Y. H. Lee and J. W. Corbett, Phys. Rev. B **13**, 2653 (1976).
20. A. C. Damask and G. J. Dienes, *Point Defects in Metals* (Gordon and Breach, New York, 1963; Mir, Moscow, 1966).

Translated by A. Spitsyn

Semiconductors, Vol. 38, No. 6, 2004, pp. 644–647. Translated from Fizika i Tekhnika Poluprovodnikov, Vol. 38, No. 6, 2004, pp. 670–673.

ELECTRONIC AND OPTICAL PROPERTIES OF SEMICONDUCTORS

Long-Wavelength Edge of the Spectrum of Hot Electron–Hole Plasma Radiation in Photoexcited Indium Arsenide

E. Shatkovskis* and A. Česnys

Vilnius Gediminas Technical University, Vilnius, 2040 Lithuania

**e-mail: eusat@fm.vtu.lt; eusat@uj.pfi.lt*

Submitted October 27, 2003; accepted for publication November 4, 2003

Abstract—The long-wavelength edge of the radiation spectrum of hot electron–hole plasma induced in indium arsenide by neodymium laser pulses is studied. The shape of the long-wavelength edge is nearly exponential and is independent of the pump power in the range 1–2 MW/cm^2. The constancy of the exponential factor indicates that the filling of LO-phonon states only slightly depends on the excitation power; i.e., the ensemble of LO phonons still does not heat up. The phonon temperature is determined and is shown to coincide with that of the crystal lattice. The absence of phonon heating is explained by strong *e–h* interaction and the screening of the electron energy scattering by LO phonons. © *2004 MAIK "Nauka/Interperiodica".*

High-power laser excitation of semiconductors gives rise to a variety of nonequilibrium processes, which are due to high density and excess energy of photoexcited electron–hole plasma (EHP) [1–3]. Recently, much attention has been given to studying such processes in a system of phonons. The experiments carried out with wide-gap materials showed that, in conditions of high laser-induced excitation of EHP, the electron heating is accompanied by the nonequilibrium overfilling of phonon states. This phenomenon is usually referred to as phonon heating. This effect attracted considerable interest after it was discovered that the nonequilibrium heating of phonons appreciably slows down the rate of energy loss in photoexcited EHP. A corresponding increase in the photoelectron energy relaxation time was observed in a number of wide-gap semiconductors [1–9].

For the first time, phonon heating was discovered in Raman studies when comparing the intensities of Stokes and anti-Stokes components [7–9]. In extreme conditions, when the power density of the pumping laser radiation is on the order of several GW/cm^2, the filling of phonon states can increase by tens of times: it was observed that the equivalent phonon temperature reached 3700 K when the crystal lattice temperature was 290 K [9]. Apart from producing an effect on the Raman spectrum, hot phonons manifest themselves in the EHP radiation spectrum, since they are involved in the formation of the long-wavelength edge of the band-to-band recombination spectrum similar to the situation described by the Urbach rule for fundamental absorption in semiconductors. In this case, phonon heating manifests itself in the exponential falloff of the long-wavelength edge of the emission band. The steepness of this falloff decreases as the phonon temperature rises with the intensity of excitation [10–11]. The influence of hot phonons on EHP radiation has been thoroughly studied for wide-gap semiconductors [1–13]. However, there are almost no data concerning the photoexcited plasma of charge carriers in indium arsenide and other narrow-gap materials. One reason for this is because the radiation of narrow-gap semiconductors falls in the infrared spectral range, which is not easily studied experimentally. However, there are data on the behavior of nonequilibrium phonons in somewhat different conditions. For example, the dynamics of electron heating during intraband absorption in *n*-type indium arsenide was studied in [14, 15]. Pulses of radiation with the same wavelength but different intensities were employed for the excitation and the time-resolved probing of EHP. It is shown that, at a lattice temperature no higher than 70 K, the free electron absorption increases with the electron-gas temperature and this effect is governed by nonequilibrium phonons. The related growth of the electron-energy relaxation time is only small. At room temperature, the contribution of nonequilibrium phonons to absorption is found to be insignificant as compared to that of equilibrium phonons. The analysis of the dynamics of Raman scattering in *n*-type indium arsenide [16] shows that this dynamics can be explained in terms of a model that assumes the presence of a lateral *L* minimum in the conduction band. Within such a model, the generation of nonequilibrium phonons is retarded because of the comparatively large time of the intervalley L–Γ electron transitions that precede the cascading of LO phonons. The intensity of the anti-Stokes component increases for about 8 ps after the excitation; however, no refilling of the phonon states is observed. The characteristic time of such a transition is estimated to be 6 ps, whereas the LO-phonon lifetime is 1.8 ps. Therefore, the relationship of these times is unfavorable for the accumulation of phonons, since their excitation rate is lower than the recombination rate. The study above is concerned with

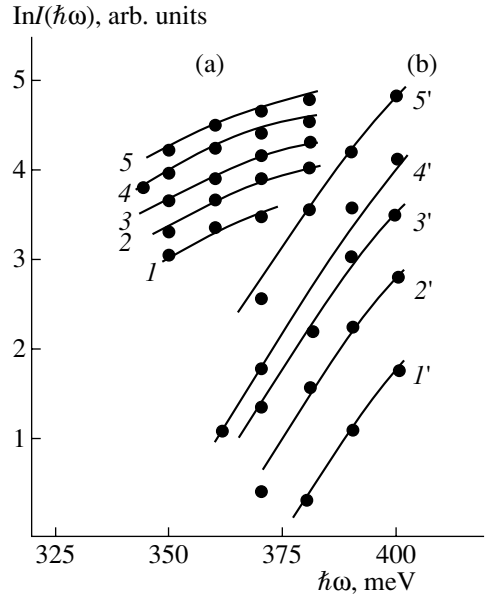

Fig. 1. Long-wavelength wing in the radiation spectrum of hot photoexcited EHP in indium arsenide: (a) T_L = 296 K with excitation intensity I_0 = (*1*) 8×10^{22}, (*2*) 1.7×10^{23}, (*3*) 2.6×10^{23}, (*4*) 5.4×10^{23}, and (*5*) 1.6×10^{24} photon cm^{-2} s^{-1}; (b) T_L = 100 K with I_0 = (*1'*) 1.5×10^{22}, (*2'*) 8×10^{22}, (*3'*) 1×10^{23}, (*4'*) 4×10^{23}, and (*5'*) 2.5×10^{24} photon cm^{-2} s^{-1}.

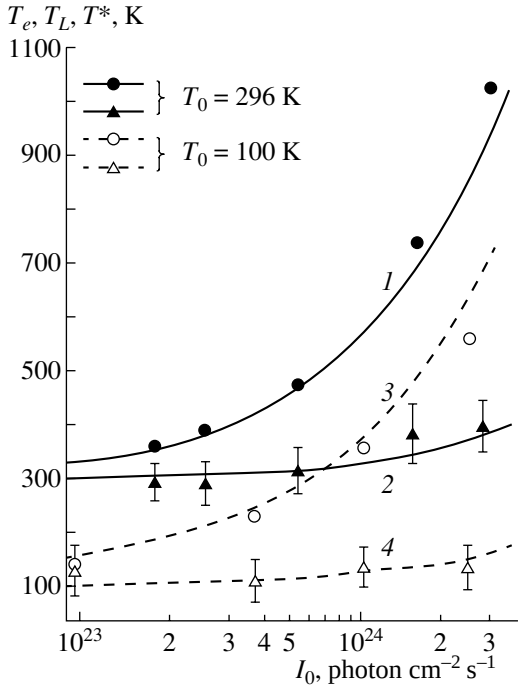

Fig. 2. Characteristic temperatures of hot photoexcited EHP in indium arsenide vs. the excitation intensity I_0 (neodymium laser): (*1*) and (*3*) the electron temperature T_e calculated from the energy balance equations, dots are the experimental values; (*2*) phonon temperature T^*; and (*4*) lattice temperature T_L.

the dynamics of energy relaxation on the picosecond and subpicosecond time scales and presents no direct estimates of the phonon temperature. Thus, the phenomenon of phonon heating was never observed in indium arsenide in the same way that it was observed for wide-gap semiconductor materials in the presence of highly excited EHP. Note, in addition, that the experimental conditions of studying the nonequilibrium concentration of charge carriers in [14–16] correspond to a low excitation or even to the absence of excitation in the case of intraband absorption. Furthermore, Raman studies are not generally efficient for the analysis of phonon heating, since the phonons that are actively involved in the Raman scattering can be heated only slightly. In this case, the method of EHP radiation is more appropriate, since it is precisely the most high-temperature phonon modes that are responsible for the formation of the long-wavelength edge of plasma radiation [10–12]. As far as we know, no data of such studies are available at present.

This study aims to investigate the long-wavelength edge of radiation from highly excited EHP in indium arsenide. Samples of nominally undoped *n*-type material with an equilibrium electron concentration of $n_0 = 1.6 \times 10^{16}$ cm^{-3} are considered. The samples were irradiated with pulses of Q-switched neodymium laser pulses ($h\nu$ = 1.17 eV). The technique used for the detection of hot EHP radiation spectra is basically similar to that described in [17]. The measurements were carried out at 296 and 100 K.

If the intensity of EHP excitation in indium arsenide irradiated with high-power neodymium laser pulses exceeds a particular level, the EHP temperature can be hundreds of absolute degrees higher than the lattice temperature T_L. It is known that, as a result of such heating, the falloff of the short-wavelength edge of EHP radiation becomes less steep [17, 18]. In this study, we consider the long-wavelength edge of the EHP radiation band. The behavior of the long-wavelength portion of the spectrum with an increase in the excitation intensity is illustrated in Fig. 1. There are two following characteristic features to be noted. First, the intensity of radiation increases within the entire spectral range with an increase in the laser pump power. Second, the shape of the long-wavelength wing remains nearly exponential, and the exponent does not change with the pump power. In view of the exponential behavior of the long-wavelength wing, one may introduce and determine the parameter representing the so-called phonon temperature T^* by assuming that the broadening parameter $E_0 = kT^*$ (here, k is the Boltzmann constant) [10–12]. The experimental values of T^* at different excitation intensities are shown by filled and unfilled triangles in Fig. 2. For comparison, the calculated and experimentally determined values of the EHP temperature c and the lattice temperature T_L in the same experimental con-

ditions are also given [17]. It can be seen that the EHP temperature rises considerably with the excitation intensity, whereas the phonon temperature remains nearly the same. At the highest densities of pump power, when the heating of the sample surface becomes significant, the phonon temperature virtually coincides with the lattice temperature.

Thus, the experimental study of the long-wavelength wing in the spectrum of radiation from laser-heated indium arsenide EHP revealed no appreciable phonon heating up to the excitation level ~1 MW/cm^2. This observation differs significantly from the data available for a majority of wide-gap materials. For example, in the experiments performed under the same conditions with cadmium selenide, T^* may reach 400 K or higher [2, 12]. This conclusion is even more unexpected if one recalls that the band-to-band recombination of nonequilibrium electron–hole pairs accounts for more than 90% of the recombination events in indium arsenide. The point is that, in conditions of quasi-stationary photoexcitation in the fundamental-absorption region, the prevalence of band-to-band impact recombination implies that the excitation-photon energy is spent completely on EHP heating [3, 17]. Therefore, the efficiency of heating of EHP in indium arsenide and other narrow-gap semiconductors is higher than that in wide-gap semiconductors, where a noticeable part of EHP energy is carried away by recombination. One should conclude therefore that the energy dissipation mechanism in indium arsenide EHP differs somewhat from that in wide-gap semiconductors; as a result, phonon heating is less efficient for the former. As shown in [16], the cascade emission of nonequilibrium phonons in indium arsenide is preceded by intervalley Γ–L scattering and the reverse transition of electrons to the Γ valley. The time of intervalley transitions (~6 ps) is longer than the lifetime of phonons in indium arsenide (~1.8 ps). Therefore, the relationship between the times of intervalley transitions and the emission of optical phonons is unfavorable for their buildup and the filling of phonon states. This feature makes a considerable difference between the EHP energy dissipation in narrow-gap indium arsenide and in wide-gap indium phosphide, where electron cooling occurs directly in the Γ valley via cascade emission of LO phonons [16]. In our opinion, the short lifetime of phonons and the comparatively long time of the intervalley L–Γ scattering is only one of several factors that hinder the phonon heating. Another possible obstacle for the energy transfer from hot EHP to phonons in indium arsenide is competition with other channels of energy loss, the main one of which is electron–hole (e–h) scattering. When the EHP density is higher than ~10^{18} cm^{-3}, the electron energy loss via ordinary e–h scattering alone exceeds that via LO-phonon scattering [18, 19]. Moreover, in considering indium arsenide, one should take into account another highly efficient channel of e–h scattering, which accompanies the transition of heavy holes to the subband of light holes [20]. In both cases, the amount of energy that is lost by electrons via e–h scattering grows with the number of scattering centers, which in our case coincides with the EHP density. As the excitation power grows, so does the EHP density, thus enhancing the electron energy fraction that is transferred to the hole component of EHP via e–h scattering and, accordingly, reducing the energy fraction that is lost via scattering by LO phonons. Another fact that should be taken into consideration is that the EHP density causes the screening of polar e–LO interaction as this density increases with increasing excitation level [21]. Eventually, the energy transfer to the lattice occurs via the hole–phonon scattering; however, the quasi-momenta of phonons that are excited during this process differ from those of phonons involved in the cascading of photoexcited electrons.

In our opinion, the factors mentioned above explain the absence of considerable phonon heating in indium arsenide irradiated by laser pulses with a power density of up to (1–2) MW/cm^2. In turn, the absence of phonon heating accounts for the undisturbed shape of the long-wavelength edge of the hot EHP radiation spectrum. However, this circumstance does not preclude phonon heating when the excitation power is higher than that considered above. Note also that the conditions realized in this study differ radically from those in [14–15], where the dynamics of nonequilibrium phonons was observed in a heavily doped material and, which is especially important, without the excitation of hot EHP. In this study, we dealt with two-component bipolar EHP and, consequently, the contribution of e–h scattering to the electron energy loss was major.

Thus, it is experimentally established that the long-wavelength edge of the spectrum of radiation from photoexcited indium arsenide EHP retains its shape up to an excitation power density of (1–2) MW/cm^2. The retention of both the exponential shape of the long-wavelength wing and the value of the exponent indicates that the level of phonon heating is low. The absence of considerable phonon heating can be attributed to the fact that the energy of hot photoexcited electrons is lost mainly via electron–hole scattering rather than via scattering by polar optical phonons, which is attenuated by screening.

REFERENCES

1. J. Shah, Solid-State Electron. **12**, 1051 (1989).
2. R. Baltramejūnas, A. Žukauskas, and G. Tamulaĭtis, Zh. Éksp. Teor. Fiz. **91**, 1909 (1986) [Sov. Phys. JETP **64**, 1132 (1986)].
3. E. Shatkovskis, Mater. Sci. Forum **297–298**, 299 (1999).
4. W. Pötz and P. Kocevar, Phys. Rev. B **57**, 7040 (1983).
5. A. Žukauskas, Phys. Rev. B **57**, 15337 (1998).
6. A. S. Vengurlekar, S. S. Prabbu, and S. K. Roy, Phys. Rev. B **50**, 15461 (1994).
7. G. P. Vella-Coleiro, Phys. Rev. Lett. **23**, 697 (1969).

8. J. Shah, R. C. C. Leite, and J. F. Scott, Solid State Commun. **8**, 1089 (1970).
9. E. Gallego Lluesma, G. Mendes, C. A. Arguello, and R. C. C. Leite, Solid State Commun. **14**, 1195 (1974).
10. J. G. Ramos and R. Luzzi, Solid State Commun. **14**, 1275 (1974).
11. E. A. Meneses, N. Jannuzzi, J. G. P. Ramos, *et al.*, Phys. Rev. B **11**, 2213 (1975).
12. R. Baltramejūnas and A. Žukauskas, Phys. Status Solidi B **149**, 337 (1998).
13. A. Žukauskas and S. Juršenas, Phys. Rev. B **51**, 4836 (1995).
14. T. Elsaesser, R. J. Bäuerle, and W. Kaiser, Phys. Rev. B **40**, 2976 (1989).
15. R. J. Bäuerle, T. Elsaesser, and W. Kaiser, Semicond. Sci. Technol. **5**, S176 (1990).
16. E. D. Grann, K. T. Tsen, and D. K. Ferry, Phys. Rev. B **53**, 9847 (1996).
17. G. N. Galkin, J. Jagminas, J. Pozhela, *et al.*, in *Proceedings of International Conference RECON'79* (Praque, 1979), p. 69.
18. G. N. Galkin and E. V. Shatkovskii, Sov. Phys. Collect. **16** (1), 70 (1976).
19. G. Lasene, K. Piragas, and A. Tamashyavichyus, Litov. Fiz. Sb. **24** (2), 26 (1984).
20. M. I. D'yakonov, V. I. Perel', and I. N. Yassievich, Fiz. Tekh. Poluprovodn. (Leningrad) **11**, 1364 (1977) [Sov. Phys. Semicond. **11**, 805 (1977)].
21. E. J. Yoffa, Phys. Rev. B **23**, 1909 (1981).

Translated by A. Sidorova

Semiconductors, Vol. 38, No. 6, 2004, pp. 648–651. Translated from Fizika i Tekhnika Poluprovodnikov, Vol. 38, No. 6, 2004, pp. 674–677.

ELECTRONIC AND OPTICAL PROPERTIES OF SEMICONDUCTORS

A Protrusion in the Absorption Spectra of GaAs Excited by High-Power Picosecond Light Pulses

G. S. Altybaev*, I. L. Bronevoĭ, and S. E. Kumekov*^**

**Kazakh National Technical University, Almaty, 480013 Kazakhstan*

***Institute of Radio Engineering and Electronics, Russian Academy of Sciences, Moscow, 101999 Russia*

^e-mail: kumekov@nursat.kz

Submitted November 3, 2003; accepted for publication November 4, 2003

Abstract—Absorption spectra of GaAs excited by short high-power light pulses are calculated. The appearance of a "protrusion" in the spectra is caused by the deviation of the electron distribution function from the Fermi function. The distortion of the distribution function is related to LO phonon-assisted relaxation of electrons between the states involved in the formation of a "hole" in the gain region and a "protrusion" in the absorption region. It is shown that the temperature of optical phonons responsible for the relaxation of photoexcited electrons differs from the lattice temperature and the time of recovery of the perturbed Fermi distribution via electron–electron collisions is nearly equal to the characteristic time of interaction between electrons and optical phonons. © *2004 MAIK "Nauka/Interperiodica".*

Absorption spectra of GaAs samples excited by picosecond light pulses were measured in [1]. The samples were synchronously irradiated with probe and excitation pulses. The excitation photon energy exceeded the band gap by more than 0.1 eV. The measurements were carried out at room temperature (T_a). The results obtained in [1] are presented in the figure.

In the recorded spectra, shown by dotted lines *2*, *3*, and *5*, there is a region corresponding to the amplification of light (see curve *5*) in the range of probe photon energies near the fundamental absorption edge. The emission that was observed in the same energy range (curve *1*) exhibited features typical of superluminescence, which indicates that the gain band is formed in the course of electron–hole pair generation and in the presence of stimulated emission of recombination radiation.

A difference found between the gain spectrum calculated under the assumption of a Fermi distribution of charge carriers (the long-wavelength portion of curve *4*) and the experimental spectrum *5* was called a "hole" in the gain spectrum [1]. It was suggested that the hole is caused by a reduction of the gain due to superluminescence.

A salient feature in the recorded spectra is the markedly nonmonotonic behavior of absorption, which was called "absorption protrusion" [1]. Comparison of the recorded absorption spectra (dotted curves *2*, *3*) with those calculated under the assumption of a Fermi distribution of electrons and holes generated by the excitation light pulse (the short-wavelength portion of curve *4*) revealed a pronounced difference between them in the region of the protrusion. This fact indicates that the electron distribution function is different from the Fermi function in this region.

The photon energy $\hbar\omega_a$ corresponding to the maximum of the protrusion exceeds the energy $\hbar\omega_r$ corresponding to the peak of the emission spectrum by 0.04 eV. This value matches exactly the difference in interband transition energies for electrons whose energies in the conduction band differ by $\hbar\omega_O$,

$$\Delta = \hbar\omega_a - \hbar\omega_r = \hbar\omega_O\left(1 + \frac{m_c}{m_v}\right),$$

where $\hbar\omega_O$ is the optical-photon energy and m_c and m_v stand for the electron and the heavy-hole effective mass, respectively. This observation suggests the following pattern. An electron created in the conduction band in state 1 with energy ε emits an optical phonon of energy $\hbar\omega_O$, and a transition to state 2 of energy $\varepsilon - \hbar\omega_O$ occurs with subsequent emission of the superluminescence photon $\hbar\omega_r$. The depopulation of states 1 caused by optical-phonon emission results in extra absorption related to interband transitions to these states. Electrons leave state 2 if they emit superluminescence photons, and a quasi-stationary flow of electrons from state 1 to state 2 is maintained.

In this paper, the relationship between the absorption spectrum in the region of the "protrusion" and the gain spectrum in the region of the "hole" is calculated in the framework of a simple model. It is assumed that the distortion of the Fermi distribution of charge carriers is caused by their interaction with optical phonons, and the recovery of this distribution is controlled by electron–electron collisions. The perturbation of the distribution function at an energy ε originates from the depopulation of states with energy $\varepsilon - \hbar\omega_O$ due to radiative transitions of electrons from the bottom of the

conduction band to the valence band; it develops via the processes of phonon emission by electrons with energy ε and phonon absorption by electrons with energy $\varepsilon - \hbar\omega_O$. Since optical-phonon emission by holes in the energy range of interest is forbidden by the energy conservation law, the hole distribution remains close to the Fermi distribution.

To calculate the spectrum of extra absorption of light that determines the shape of the protrusion, it is necessary to find the energy distribution of electrons $f(\varepsilon)$ in the vicinity of state 1. Let us write the kinetic equation for $f(\varepsilon)$ [2]:

$$\frac{\partial f(\varepsilon)}{\partial t} = -\frac{f(\varepsilon) - f_0(\varepsilon)}{\tau_0(\varepsilon)}$$
$$+ \int W(\varepsilon', \varepsilon) N_q [1 - f(\varepsilon)] f(\varepsilon') \rho(\varepsilon') d\varepsilon' \delta(\varepsilon' - \varepsilon + \hbar\omega_O)$$
$$- \int W(\varepsilon, \varepsilon')(N_q + 1)[1 - f(\varepsilon')] f(\varepsilon) \rho(\varepsilon') d\varepsilon' \quad (1)$$
$$\times \delta(\varepsilon' - \varepsilon + \hbar\omega_O).$$

Here, $\tau_0(\varepsilon)$ is the time of the Fermi distribution recovery; $\delta f = f(\varepsilon) - f_0(\varepsilon)$ [2];

$$f_0(\varepsilon) = \{\exp[(\varepsilon - \mu_e)/T_c] + 1\}^{-1};$$
$$N_q = [\exp(\hbar\omega_O/T_q) - 1]^{-1};$$

T_c and T_q are the electron and the optical-phonon temperatures, respectively; and μ_e is the Fermi level.

Disregarding the optical-phonon dispersion and taking into account that the duration of the excitation pulse is considerably longer than the characteristic times of energy relaxation via electron–optical phonon and electron–electron interactions, one can disregard the time derivative in (1). Then we have

$$-\frac{\delta f}{\tau_0(\varepsilon)} + \chi N_q [1 - f(\varepsilon)] f(\varepsilon - \hbar\omega_O)$$
$$- \beta(N_q + 1)[1 - f(\varepsilon - \hbar\omega_O)] f(\varepsilon) = 0, \quad (2)$$

where β is the probability of the emission of an optical phonon by an electron in the absence of other phonons and electrons. It follows from the principle of detailed balance that $\chi = \beta$. Let us set

$$f(\varepsilon) = f_0(\varepsilon) + f_+,$$
$$f(\varepsilon - \hbar\omega_O) = f_0(\varepsilon - \hbar\omega_O) + f_-. \quad (3)$$

The terms f_+ and f_- describe the distortion of the Fermi distribution in the regions of the protrusion and the hole, respectively; from (2) and (3), we obtain the following relationship between these distortions:

$$f_+ = \frac{\delta N_q [f_0(\varepsilon - \hbar\omega_O) - f_0(\varepsilon)] + f_-[f_0(\varepsilon) + N_q]}{[\beta\tau_0(\varepsilon)]^{-1} + N_q + 1 - f_0(\varepsilon - \hbar\omega_O) - f_-}, \quad (4)$$

where $\delta N_q = N_q - N_{qc}$ (here, N_{qc} is the optical-phonon distribution function for $T_q = T_c$). The quantities f_+ and f_- can be related to the values of the absorption coefficient in the photon energy regions corresponding to the protrusion and to the hole, respectively, which are separated by the energy interval Δ.

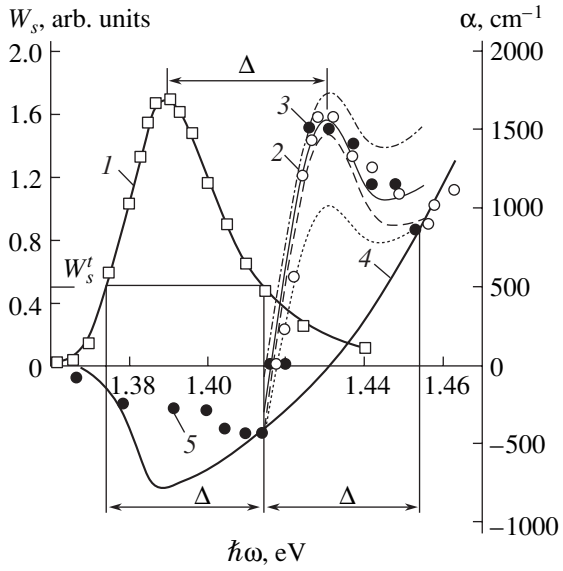

Room-temperature spectra of absorption and superluminescence in GaAs excited by high-power picosecond light pulses. Experimental data (*1–3*, *5*) and curve *4* are reproduced from [1]. Curve *1* represents the experimental superluminescence spectrum (dependence of the superluminescence intensity on the photon energy); circles *2*, *3*, and *5* represent the measured values of the absorption coefficient α of the sample under excitation (here, filled and open circles correspond to two different samples); and curve *4* shows the absorption coefficient calculated on the assumption of a Fermi distribution of electrons and holes [1]. The spectra of the protrusion region were calculated according to formulas (7)–(9) for the following sets of parameters T_q and $(\beta\tau_O(\varepsilon))^{-1}$: 52 meV and 2 (dotted line), 52 meV and 1 (dashed line), 40 meV and 1 (thin solid line), 25 meV and 1 (dash-dotted line).

Before we proceed with the calculations using expression (4), let us discuss the importance of screening the Coulomb interaction between the electrons and holes for the formation of absorption spectra in the energy region under consideration. The concentrations of charge carriers attained in the experiment [1] ($\sim 5 \times 10^{18}$ cm^{-3}) are fairly high and have a significant effect on the shape of the absorption spectra due to exciton screening. The variation of the shape of intrinsic absorption spectra in heavily doped materials is discussed in [3, 4].

The spectra of linear absorption of pure GaAs samples recorded in the absence of excitation were presented in [1]. The shape of these spectra (exhibiting a characteristic step at the absorption edge) indicates that the exciton effect plays an important role.

In the photon-energy range where there are no optical transitions from the spin–orbit split-off valence

band to the conduction band, the absorption coefficient can be expressed as

$$\alpha(\omega) = \alpha_1(\omega) + \alpha_2(\omega), \quad (5)$$

where $\alpha_1(\omega)$ and $\alpha_2(\omega)$ are the absorption coefficients related to the transitions from the heavy-hole and the light-hole bands, respectively, to the conduction band:

$$\alpha_i(\omega) = \frac{\sqrt{\hbar\omega - E_g}}{\hbar\omega} A_i Z(\xi_i)[1 - f(\varepsilon_i) - f_h(\varepsilon_{hi})]. \quad (6)$$

Here, subscripts $i = 1, 2$ denote the transitions that involve heavy-hole and light-hole bands, respectively; $f(\varepsilon_i)$ is the electron distribution function; $f_h(\varepsilon_{hi})$ is the hole distribution function; ε_i and ε_{hi} are the energies of an electron and a hole involved in the absorption of a photon with energy $\hbar\omega$;

$$Z(\xi_i) = \frac{\xi_i}{1 - \exp(-\xi_i)}$$

is the Sommerfeld factor, which accounts for the exciton effect in the band-to-band absorption;

$$\xi_i = 2\pi\left(\frac{R_i}{\hbar\omega - E_g}\right)^{1/2};$$

R_i is the ionization energy of the heavy-hole and light-hole excitons; and A_i are constants that determine the probabilities of direct band-to-band transitions from heavy-hole and light-hole bands (see formula (79) in [5]). The numerical values of the coefficients A_1 and A_2 can be determined from the experimental values of the absorption coefficient $\alpha_{exp} = 1.5 \times 10^4$ cm^{-1} at $\hbar\omega = 1.6$ eV [3], taking into account that the ratio of A_1 and A_2 equals the ratio of the corresponding reduced densities of states:

$$\frac{A_1}{A_2} = \frac{(m_e^{-1} + m_{h1}^{-1})^{3/2}}{(m_e^{-1} + m_{hh}^{-1})^{3/2}}.$$

For the values of effective masses $m_e = 0.063m_0$, $m_{h1} = 0.076m_0$, and $m_{hh} = 0.45m_0$, we obtain $A_1 = 3.77 \times 10^4$ eV$^{1/2}$/cm and $A_2 = 1.89 \times 10^4$ eV$^{1/2}$/cm.

It should be noted that, for the same photon energy $\hbar\omega$, energies ε_1 and ε_2 are different for transitions involving heavy and light holes ($i = 1, 2$), which means that the same optical pulse probes different states in the conduction band. Below, similarly to [1], we disregard the contribution from the light-hole band to the probe-pulse absorption coefficient.

In the absence of excitation, the concentrations of electrons and holes are low, and their Coulomb interaction is not screened in the entire range of measurements of the linear absorption coefficient. In the presence of excitation, the concentration of electron–hole pairs is as high as 5×10^{18} cm^{-3}, and the situation is different. The screening length r_s, i.e., the length scale at which a considerable exciton screening takes place, is determined by the inequality $r_s < \frac{e^2}{\kappa(\hbar\omega - E_g^*)}$ [4], where κ is the dielectric constant and $E_g^* = 1.37$ eV is the band gap of the sample under excitation. Estimations show that the effect of the exciton screening has to be taken into account for photon energies below 1.41 eV, which approximately corresponds to the boundary between the spectral regions of the "protrusion" and the "hole."

Then, using (3) and (6), we can obtain the following expressions for the absorption coefficient in the regions of the protrusion and the hole:

$$\alpha(\omega) = \alpha_{FD}(\omega) + \alpha_+,$$
$$\alpha_+ = -A_1\frac{\sqrt{\hbar\omega - E_g^*}}{\hbar\omega} Z(\xi_1^*) f_+, \quad (7)$$

$$\alpha(\omega) = \alpha_{FD}(\omega) + \alpha_-,$$
$$\alpha_- = -A_1\frac{\sqrt{\hbar\omega - E_g^* - \Delta}}{\hbar\omega - \Delta} f_-. \quad (8)$$

Here, $\alpha_{FD}(\omega)$ is the absorption coefficient for the case of Fermi distribution of electrons and holes (curve *4*), and α_+ and α_- represent the deviations of the absorption coefficient from $\alpha_{FD}(\omega)$ in the regions of the protrusion and the hole, respectively.

It now follows from (4), (7), and (8) that

$$\alpha_+(\hbar\omega) = A_1\frac{\sqrt{\hbar\omega - E_g^*}}{\hbar\omega} Z(\xi^*)\frac{N}{D}, \quad (9)$$

$$N = [f_0(\varepsilon) + N_q](\hbar\omega - \Delta)\alpha_-(A_1\sqrt{\hbar\omega - E_g^* - \Delta})^{-1} - \delta N_q[f_0(\varepsilon - \hbar\omega_O) - f_0(\varepsilon)],$$

$$D = [\beta\tau_0(\varepsilon)]^{-1} + (\hbar\omega - \Delta)\alpha_-(A_1\sqrt{\hbar\omega - E_g - \Delta})^{-1} + N_q + 1 - f_0(\varepsilon - \hbar\omega_O),$$

where

$$\xi^* = 2\pi\left(\frac{R}{\hbar\omega - E_g^*}\right)^{1/2}.$$

The spectrum in the region of the hole α_-, determined experimentally in [1], was used to calculate the absorption spectra in the region of the protrusion, according to formulas (7)–(9); the results are shown in the figure. We assumed that the sample under excitation is characterized by $E_g^* = 1.37$ eV, $T_c = 0.052$ eV, and $\mu_e = 0.145$ eV [1]. The spectra of the protrusion were calculated for different values of the parameter $(\beta\tau_0(\varepsilon))^{-1}$ and different optical-phonon temperatures T_q. The best agreement between the calculated dependence and the experimental curve is attained for $(\beta\tau_0(\varepsilon))^{-1} \approx 1$ and $T_q = 0.04$ eV. The deviation of T_q from the lattice temperature T_a (equal to the room temperature) is evidence of heating of the optical phonons that are

involved in the processes leading to the formation of the protrusion. This heating may be a consequence of the "phonon bottleneck" effect [6, 7]. To estimate $(\beta\tau_0(\varepsilon))^{-1}$, we can use the value $\beta^{-1} = \tau_{po} = 0.14$ ps (see Table P5 in [2]) and the formulas for $\tau_0(\varepsilon)$ obtained in [2]. For $\varepsilon = 0.05$ eV, an estimation yields $\tau_0(\varepsilon) \approx 0.13$ ps. Thus, we obtain $(\beta\tau_0(\varepsilon))^{-1} \approx 1.1$, which is in satisfactory agreement with the above result. Since the calculation was based on a simplified model and the value used for $\tau_0(\varepsilon)$ was obtained by a rough estimate, such a good agreement between the calculated and the measured values may be somewhat accidental.

Thus, in this study, we calculated the amplification and absorption spectra of a probe pulse in GaAs samples excited by a high-power picosecond light pulse. The calculation results are in satisfactory agreement with the experimental data reported in [1].

ACKNOWLEDGMENTS

We are grateful to V.I. Perel' for valuable comments.

This study was supported in part by the Russian Foundation for Basic Research, project no. 01-02-16694.

REFERENCES

1. N. N. Ageeva, I. L. Bronevoĭ, A. N. Krivonosov, *et al.*, Fiz. Tekh. Poluprovodn. (St. Petersburg) **36**, 144 (2002) [Semiconductors **36**, 136 (2002)].
2. V. F. Gantmakher and Y. B. Levinson, *Carrier Scattering in Metals and Semiconductors* (Nauka, Moscow, 1984; North-Holland, Amsterdam, 1987).
3. J. S. Blackmore, J. Appl. Phys. **53** (10), R123 (1982).
4. A. A. Rogachev, in *Proceedings of the IVth Winter School on the Physics of Semiconductors* (Fiz. Tekh. Inst., Leningrad, 1972).
5. E. J. Johnson, in *Semiconductors and Semimetals*, Vol. 3: *Optical Properties of III–V Compounds*, Ed. by R. Willardson and A. Beer (Academic, New York, 1967; Mir, Moscow, 1970).
6. W. Potz and P. Cocevar, Phys. Rev. B **28**, 7040 (1983).
7. S. E. Kumekov and V. I. Perel', Zh. Éksp. Teor. Fiz. **94** (1), 366 (1988) [Sov. Phys. JETP **67**, 193 (1988)].

Translated by M. Skorikov

Semiconductors, Vol. 38, No. 6, 2004, pp. 652–656. Translated from Fizika i Tekhnika Poluprovodnikov, Vol. 38, No. 6, 2004, pp. 678–683.

ELECTRONIC AND OPTICAL PROPERTIES OF SEMICONDUCTORS

Photosensitive Polyimides Containing Substituted Diphenylmethane Fragments in the Backbone

E. L. Aleksandrova, G. I. Nosova, N. A. Solovskaya, K. A. Romashkova, V. A. Luk'yashina, E. V. Konozobko, and V. V. Kudryavtsev

Institute of Macromolecular Compounds, Russian Academy of Sciences, Bol'shoi proezd 31, St. Petersburg, 119004 Russia

Submitted October 21, 2003; accepted for publication November 5, 2003

Abstract—Soluble aromatic polyimides were synthesized. Their monomer units contain alkyl and/or aryl substituents of diphenylmethane in both diamine and dianhydride components of polymers. It was shown that the photosensitive properties of the polyimides studied are far superior to those based on other known polycyclic diamines. The intrinsic photosensitivity of the polyimides under study is ~10^5 cm^2/J in the visible spectral range. These polymers have high photosensitivity and high polarizability of molecules, which makes them promising candidates for recording media. © *2004 MAIK "Nauka/Interperiodica".*

1. INTRODUCTION

Polyimides (PIs) have high optical transparency and thermal stability, as well as good insulating, adhesion, and film-forming properties. Polyimides with functional photosensitive fragments can be used to develop optical materials on their basis. PIs with a developed π system seem to be promising in terms of their photoconductive properties. As is well known [1], PIs have high polarizability (~10^{24} cm^{-3}, which is similar to that of anthracene molecules) and a high refractive index (n = 1.72–1.84) [1], which makes it possible to develop photorefractive materials on the basis of PIs.

The photoelectric properties of PI films are related to the excitation of the electron systems of PIs. Periodic monomer units of PIs contain acceptor diimide and donor (as a rule, in the diamine component) fragments. Their interaction results in the formation of both intra- and intermolecular complexes with charge transfer (CCTs). The efficiency of separation of electron–hole pairs generated by photon absorption and subsequent transport of generated free carriers in an electric field depend not only on the chemical structure of the PI monomer unit, but also on the packing of macromolecules in a film [2].

For polymers of this type, the highest photosensitivity was detected for PIs containing dibenzofuran, carbazole, and triphenylamine (TPA) fragments in the diamine component [2, 3]. Recently, high photosensitivity was detected in PIs containing *N*-substituted benzimidazole (BI) fragments in diamine [4]. These polymers both had a developed (i.e., branched) electron system and contained nitrogen heteroatoms in the donor component of the monomer unit [2, 5].

This study deals with the photosensitive properties of PIs with a branched π-electron system, but, in contrast to [3, 4], the polymers under investigation do not contain donor nitrogen atoms. It is well known that, in a neutral state, such fragments have a lower donor ability compared with their nitrogen-containing analogs. The donor ability is estimated by ionization potentials I_D, which are 0.5–1.0 eV higher than those of nitrogen-containing aromatic analogs [6]. However, the energies I_D of such fragments in the ionized state significantly decrease [6]. Hence, one can expect them to be efficiently involved in the formation of CCT, which to a large extent controls the photosensitive properties of PIs.

2. EXPERIMENTAL

The objects under study were PIs containing a monomer unit with the general formula

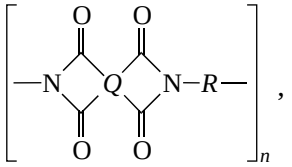

where *Q* is the dianhydride component of the PI monomer unit,

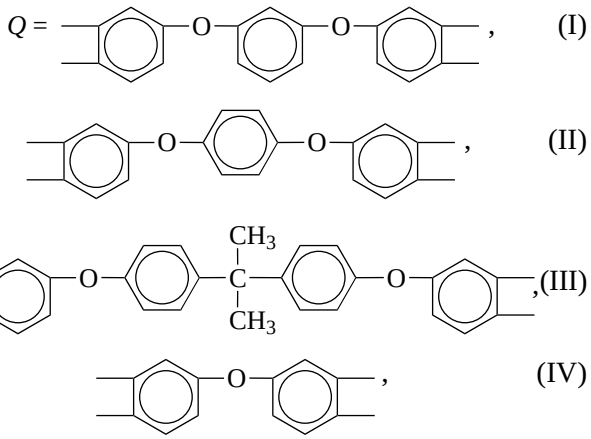

1063-7826/04/3806-0652$26.00 © 2004 MAIK "Nauka/Interperiodica"

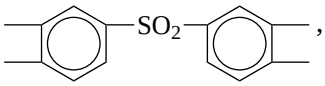
(V)

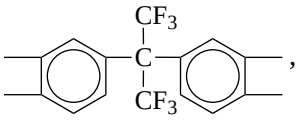
(VI)

and R is the diamine component of the monomer unit,

$R =$ 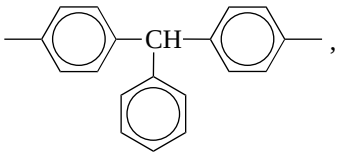
(1)

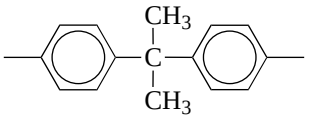
(2)

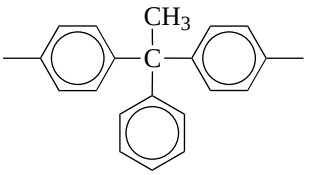
(3)

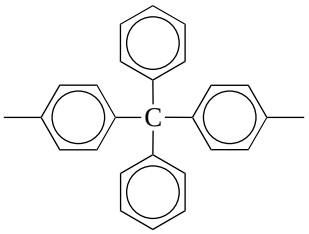
(4)

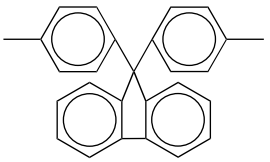
(5)

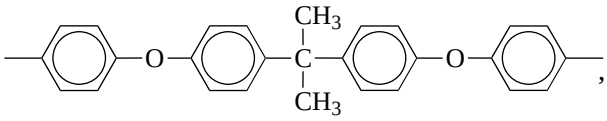
(6)

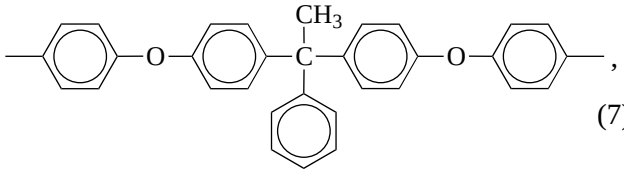
(7)

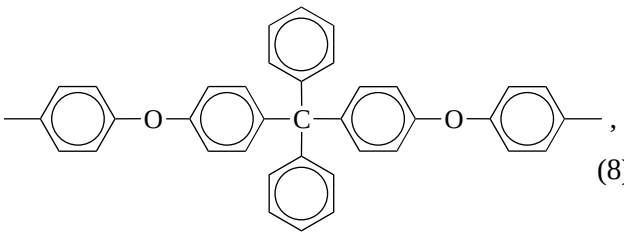
(8)

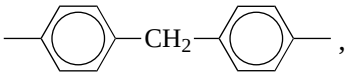
(9)

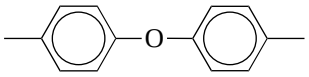
(10)

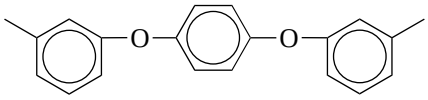
(11)


(12)

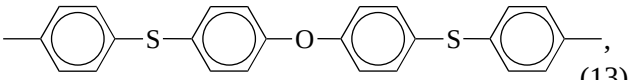
(13)

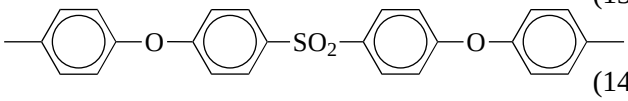
(14)

According to the known acceptor properties (electron affinity E_A) [1], dianhydrides form the series

I(1.13), II(1.19), III(1.14), IV(1.30), V(1.55), VI(1.6),

where Roman numerals are indices of formulas (I)–(VI) and Arabic numerals are the values of E_A (eV).

However, the values of E_A for the diimidyl fragments considered in this study are unknown. Hereafter, we assume that the ionization potentials E_A of diimidyl fragments are proportional to those of dianhydrides. It is known that the PI complexing properties improve as E_A of the initial (in synthesis) dianhydride increases and as the diamine ionization potential I_D decreases [3–5]. However, there are no values of I_D in the literature for most of the diamines mentioned above; only the data for the corresponding aromatic hydrocarbons are available [6].

Taking into account the fact that PIs absorb ultraviolet (UV) light ($\lambda < 400$ nm), they were sensitized with both dyes and acceptor-type compounds. As acceptor compounds, 2,4,5,7-tetranitrofluorenone (TNF) and tetracyanoethylene (TCE) were used. Malachite green, rhodamine 6G, and dicyclohexyl perylene diimide were used as dyes.

A one-stage method was used to produce the PIs. An equivalent amount of initial dianhydride was added to an initial diamine solution in *N*-methylpyrrolidone (MP). A viscous polymer solution (with content C = 25 wt %) was mixed for 8 h at room temperature. Then the solution was diluted to 5–8 %, and an imidizing mixture was introduced. This mixture consisted of acetic anhydride and pyridine (2 : 1 in volume), with a fivefold excess relative to the PI monomer mole unit. After 10-h mixing, the polymer solution was heated at 60°C for 2 h. The solution was then precipitated into methanol and dried in vacuum at 60°C.

The films were precipitated from a 2% PI solution in chloroform or MP onto glass substrates with a conducting indium–tin–oxide (ITO) layer. The dye and acceptor concentrations were 1% and (1–5)% of the polymer

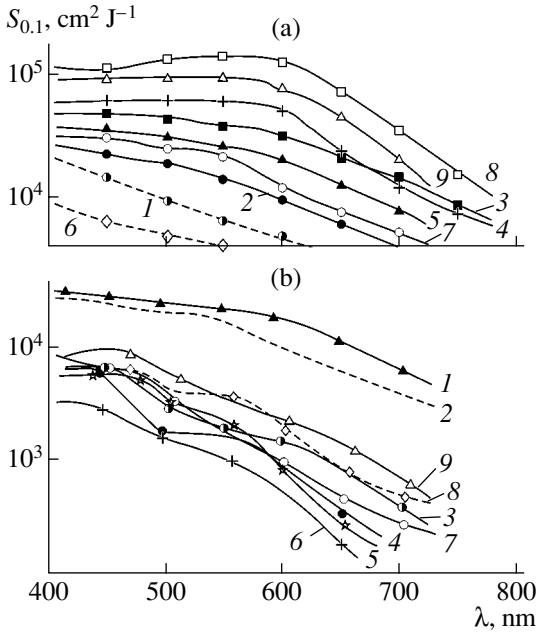

Fig. 1. Spectra of the energy photosensitivity of polyimides with varied (a) donor and (b) acceptor fragments (*Q*)–(*R*): (a) (*1*) (I)–(1), (*2*) (I)–(3), (*3*) (I)–(2), (*4*) (I)–(5), (*5*) (I)–(4), (*6*) (I)–(13), (*7*) (I)–(7), (*8*) (I)–(6), and (*9*) (I)–(8); (b) (*1*) (I)–(6), (*2*) (I)–(7), (*3*) (IV)–(6), (*4*) (II)–(6), (*5*) (I)–(10), (*6*) (III)–(6), (*7*) (V)–(6), (*8*) (VI)–(6), and (*9*) (VI)–(7).

weight. The films were dried at 60°C and then at 80–100°C in vacuum to a constant weight. The thickness of the PI layers was 1–2 μm. Absorption spectra were measured on a Specord-400 spectrophotometer in the range 400–800 nm. The photosensitivity $S_{0.1}$ and the quantum yield of carrier photogeneration were measured using the technique in [6] at $T = 300$ K in the electrophotographic mode in the equi-energy spectrum. The average photon flux density was 10^{14} cm^{-2} s^{-1} in the spectral range 400–700 nm, and the electric field E was $(0.2–1)E_0$, where E_0 is the ultimate field strength for this material, controlled by its permittivity ε.

The photosensitivity $S_{0.1}$ was determined using the criterion of a 10% decrease in the layer surface potential (V) from the initial value ($\Delta V/V = 0.1$) as a quantity inverse to the exposure required to attain the above change in the surface potential. The total photosensitivity $S_{0.1}$ was determined by exposing the layers to light from a 300-W KGM-300 halogen lamp, using the same criterion ($\Delta V/V = 0.1$).

The electron absorption $\alpha(\lambda)$ and photosensitivity $S_{0.1}(\lambda)$ spectra were used to determine the optical E_G^{opt} and adiabatic E_G^{ph} band gaps, according to [7].

The quantum yield η of the bound pair formation and the thermalization lengths r_T were determined using the technique in [8] (based on the Onsager model) by the slope of the dependences of the quantum yields η of carrier photogeneration on the applied electric field. The error of absolute measurements of the quantum yield was 30%, the error of relative measurements at a constant light intensity was 10%, and the error in determining r_T was 10%.

The values of η experimentally determined for PIs with unknown energies I_D and E_A of the donor and acceptor fragments (respectively) of the monomer unit, as well as the determined dependence $\eta(E_A - I_D + c)$ (c is a constant), were used to determine the energies E_A and I_D of corresponding fragments using the technique in [5, 8]. The slope

$$k = \frac{\Delta\eta(E_A - I_D)}{\Delta(E_A - I_D)}$$

of these dependences was used to determine (using the technique in [9]) the distance r_0 of the initial electron transport in the *D*–*A* complex formed by the donor and acceptor fragments of a photosensitive PI molecule.

3. RESULTS AND DISCUSSION

The absorption spectra $\alpha(\lambda)$ of a PI with a constant radical *Q* showed an absorption-edge shift to the long-wavelength region for polymers with a more branched π system in the radical *R*. The absorption-edge (the energies E_A and I_D) shift is caused by the substitution of the diphenylmethane fragment in the CH_2 bridge group with either the C_6H_5 or the CH_3 group (see table). In the case of long radicals *R* (additional introduction of phenoxy groups *R* = (6)–(8) into *R*), the long-wavelength shift is 0.3–0.4 eV. A similar effect was observed as the acceptor properties of initial dianhydrides were enhanced at constant *R* = (6). An analysis of the maxima in the absorption spectra of complexes of a strong TCE acceptor with the PIs under study and comparison of these spectra with the spectra $\alpha(\lambda)$ of PI complexes containing TPA and BI (for which ID are known) allows estimation of I_D of the donor fragments of the PIs studied here. The energies I_D are in the range 7.4–8.6 eV.

The photosensitivity spectra $S_{0.1}(\lambda)$ of the PIs under study are shown in Fig. 1. In the case of a varied donor fragment (Fig. 1a), we can see that the spectra are panchromatic in the range λ = 400–700 nm for all the PIs studied. Introducing phenoxy groups into the radical *R* causes an increase in the photosensitivity and further shifts the spectrum to longer waves (λ > 700 nm).

As follows from the data of the table and Fig. 1, the photosensitivity of synthesized PIs increases in the following sequence of diphenylmethane derivatives included in radical *R*: CH_2, $>CH(C_6H_5)$, $>C(C_6H_5)(CH_3)$, $>C(C_6H_5)_2$, $>C(C_6H_5)_2$. In this series, the energy photosensitivity increases from ~10^4 to 6×10^4 cm^2/J, the total photosensitivity increases from 2×10^{-3} to 6×10^{-3} (lx s)$^{-1}$, the quantum yield η increases from 0.03 to 0.1, and the thermalization length increases from 2.0 to 2.5 nm. The smallest values of the charge photogeneration parameters were obtained for the PIs based on 4.4'-bis(4-aminophenylthio)diphenyloxide (*R* = (13)) containing no branched structures, taken as a reference PI: $S_{0.1} \approx 3 \times 10^3$ cm^2/J, η = 0.012, and r_T = 1.8 nm. Enhancing the acceptor properties of

Widths of the optical (E_G^{opt}) and adiabatic (E_G^{ph}) band gaps, total photosensitivity $S'_{0.1}$, quantum yields of carrier photogeneration η and bound pair formation η_0, and thermalization lengths r_T of polyimides with varied dianhydride (*Q*) and diamine (*R*) components

Polyimides		E_G^{opt}, eV	E_G^{ph}, eV	$S'_{0.1}$, (lx s)$^{-1}$	η	r_T, nm	η_0
Q	*R*						
(I)	(1)	3.94	2.18	2.0×10^{-2}	0.028	2.0	0.059
(I)	(2)	3.92	1.65	4.3×10^{-2}	0.06	2.2	0.13
(I)	(3)	3.64	1.85	3.6×10^{-2}	0.047	2.1	0.096
(I)	(4)	3.81	1.58	4.5×10^{-2}	0.065	2.3	0.140
(I)	(5)	3.89	1.61	4.0×10^{-2}	0.072	2.5	0.160
(I)	(6)	3.52	1.50	5.1×10^{-2}	0.080	2.4	0.170
(I)	(7)	3.53	1.53	4.8×10^{-2}	0.072	2.4	0.150
(I)	(8)	3.50	1.45	5.5×10^{-2}	0.095		0.200
(I)	(10)	3.20	>2.25	3.6×10^{-3}	0.015	2.1	~0.020
(I)	(11)			2.3×10^{-3}	0.026	2.4	0.070
(I)	(13)	3.59	2.69	7.2×10^{-3}	0.012	1.8	0.023
(II)	(6)	3.17	>2.60	5.3×10^{-4}	<0.010		~0.020
(III)	(2)	3.44		1.3×10^{-3}	~0.010	~2.0	~0.020
(III)	(4)	3.35		1.8×10^{-3}	~0.010	~2.0	~0.020
(III)	(5)	3.26		3.1×10^{-4}	~0.005		
(III)	(6)	3.39		1.5×10^{-3}	~0.01	~2.0	~0.020
(III)	(9)	3.40		$<1.0 \times 10^{-4}$	<0.001		
(III)	(10)	3.54		3.2×10^{-4}	~0.006		
(III)	(11)	3.18		2.8×10^{-4}	~0.004		
(III)	(12)	3.41		1.2×10^{-4}	~0.002		
(IV)	(6)	3.30	>2.10	8.2×10^{-3}	0.025	2.2	~0.030
(IV)	(10)	3.60	2.95	2.0×10^{-4}			
(V)	(6)	3.24	>2.30	8.5×10^{-3}	0.028	~2.2	~0.060
(VI)	(3)	3.21	>2.25	1.0×10^{-2}	0.030	~2.2	0.060
(VI)	(7)	3.20	>2.20	1.2×10^{-2}	0.032	~2.2	~0.070

initial dianhydrides in the PI series (see Fig. 1b) also causes an increase in the photosensitivity $S_{0.1}$.

It is known that the PI dianhydride component is to a large extent responsible for the stacking of polymer chains. In this context, the dependence of the PI photosensitivity on the acceptor properties of an initial dianhydride in the series of selected initial diamines is less pronounced. For example, the PI based on 4.4'-bis(4-aminophenoxy)diphenylpropane (*R* = (6)) has the highest photosensitivity in combination with bis(3.4-dicarboxyphenoxy)resorcin dianhydride (*Q* = (I)) with the weakest acceptor properties.

However, the weak dependence of the PI photosensitivity on the acceptor properties of dianhydride is observed in some cases (Fig. 1b). For example, in the case of PIs based on diamine with *R* = (6), the photosensitivity increases in the dianhydride series: III(<0.01), II(~0.01), IV(0.025), V(0.030), and VI(0.035), which is shown by the values of η in parenthesis, which determine the photosensitivity $S \propto \eta\alpha$ (at the constant absorption coefficient α in this series).

The introduction of an acceptor-type sensitizer (-TNF-) into the polymeric layers causes a slight (by up to a factor of 2.5) increase in the photosensitivity due to the increase in absorption in the layer, which is probably associated with the PI complexing with TNF with almost unchanged parameters of charge photogeneration (compare curves *1* and *2* in Fig. 2). Introducing another acceptor (i.e., TCE) also increases $S_{0.1}$ by up to a factor of to 3 (Fig. 2, curve *2*). Introducing various dyes into PI layers (Fig. 2, curves *3*–*5*) results in a shift of the absorption maximum of the composition to the absorption region of the dye and, consequently, insignificantly (by a factor of 2–3) increases the total sensitivity of the composition. Thus, the introduction of dyes into PIs does not change the quantum yield η_0 of the bound pair formation but, however, causes an increase

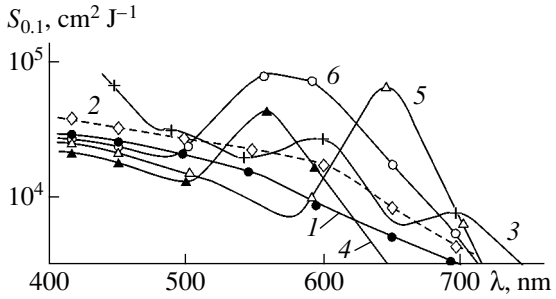

Fig. 2. Spectra of the energy photosensitivity of polyimide films (I)–(6) containing acceptor-type sensitizers (1–5 wt %) or dyes (1 wt % of the PI weight): (*1*) without additives, (*2*) TNF, (*3*) TCE, (*4*) rhodamine 6G, (*5*) malachite green, and (*6*) dicyclohexyl perylene diimide.

in η by a factor of 1.5–1.8 due to the increase in r_T up to 3.0–3.5 nm.

The features determined above allow us to clarify the mechanism of carrier photogeneration in PIs based on diamines, i.e., diphenylmethane derivatives.

The carrier photogeneration mechanism in these PIs, which contain a quaternary carbon atom, presumably involves the formation of ion–radical pairs during photon absorption, as was found in [2]. The introduction of phenoxy groups into the PI amino component increases the mobility of polymer chains and decreases the softening temperature. It is possible that the demonstrated increase in η for PIs with similar values of r_T indicates the influence of the conformational mobility of PI chains not only on the carrier photogeneration efficiency, but also on the carrier mobility.

After absorption of a photon by a D–A complex formed by donor and acceptor fragments of neighboring polymer chains (with distance $r_0 \approx 0.4$–0.5 nm of initial separation in pairs [10]), which form a nonthermalized ion–radical pair, the photoexcitation energy is thermalized and the pair charges are separated by the radius r_T = 2.0–2.5 nm (see table) with the efficiency $\eta_0 \le 0.2$. As a result of the Onsager field-assisted thermal dissociation of formed bound pairs of charges, some of the carriers ($\eta < 0.1$) become free, which provides the photoconductivity of the PI layer. This mechanism of photogeneration is confirmed by the following factors. First, the values of radii r_T are comparable to the sizes of the PI monomer unit. Second, the radius r_T increases by a factor of 1.5 (while η_0 remains unchanged) due to the introduction of a dye. This increase in r_T suggests that the exciplex [10] formed by a dye molecule that has absorbed a photon and a PI monomer unit is involved in the photogeneration process, as well as the ion–radical pairs containing a quaternary carbon atom (a similar process was detected in the case of PIs containing a nitrogen atom in the radical *R* [5]). Third, the dependence of η on the energy parameters (I_D and E_A) of the PI structural units is characteristic of the proposed photogeneration mechanism [10].

It should be noted that the electrophotographic effect in the $S_{0.1}$ measurements weakened in some cases when the film was charged at one of poles of the corona discharge. This effect can be caused by the polarization of the film [11] due to the high polarizability of PI molecules. To suppress this phenomenon and obtain correct results, copolymers were prepared in which some of the diamine (*R* = (6)) was substituted by 2,6-diaminopyridine or 2,4-bis(4-aminophenyl)-6-phenylpyrimidine (*Q* = (I)).

As a result, it turned out that covalent introduction of 10% pyrimidine or 30% pyridine monomer units into polymer chains almost completely suppresses the polarization in these PI layers with an insignificant decrease in the photosensitivity.

4. CONCLUSIONS

In this study, we revealed for the first time the high intrinsic (obtained without doping with dyes or electron-acceptor compounds) photosensitivity (10^5 cm^2/J in the visible spectral range) of soluble PIs whose polymer chains (namely, the diamine component) contain a quaternary carbon atom with various types of substitution. When a substituted quaternary hydrocarbon atom is introduced into the diamine component of the PI monomer unit, a more pronounced effect is observed in comparison with the dianhydride component.

REFERENCES

1. *Polyimides: a Class of Heat-Resistant Polymers*, Ed. by M. I. Bessonov (Nauka, Leningrad, 1983), p. 177.
2. B. V. Kotov, B. M. Rumyantsev, and V. I. Berendyaev, Vysokomol. Soedin., Ser. A **39**, 720 (1997); Dokl. Akad. Nauk **367**, 81 (1999).
3. N. A. Vasilenko, G. A. Rybalko, and B. V. Kotov, in *Abstracts of IV All-Russia Conference on Nonsilver and Unconventional Photographic Processes* (Élektrofotografiya, Vil'nyus, 1980), p. 59.
4. E. L. Aleksandrova, G. I. Nosova, K. A. Romashkova, *et al.*, Opt. Zh. **69** (10), 10 (2002) [J. Opt. Technol. **69**, 706 (2002)].
5. I. A. Akimov, Yu. A. Cherkasov, and M. I. Cherkashin, *Sensitized Photoelectric Effect* (Nauka, Moscow, 1980).
6. E. L. Aleksandrova and Yu. A. Cherkasov, Opt. Spektrosk. **64**, 1047 (1988) [Opt. Spectrosc. **64**, 624 (1988)].
7. É. A. Silin'sh, M. V. Kurik, and V. Chapek, *Electron Processes in Organic Molecular Crystals* (Zinatne, Riga, 1988), pp. 99, 189.
8. E. L. Aleksandrova and Yu. A. Cherkasov, Opt. Spektrosk. **84**, 455 (1998) [Opt. Spectrosc. **84**, 396 (1998)].
9. E. L. Aleksandrova and Yu. A. Cherkasov, Opt. Zh. **67** (3), 43 (2000) [J. Opt. Technol. **67**, 241 (2000)].
10. L. V. Gurevich, G. V. Karachevtsev, V. N. Kondrat'ev, Yu. A. Lebedev, V. A. Medvedev, V. K. Potapov, and Yu. S. Khodeev, *Chemical-Bond-Breaking Energies*, Ed. by V. N. Kondrat'ev (Nauka, Moscow, 1974).
11. E. L. Aleksandrova, Opt. Zh. **68** (7), 71 (2001) [J. Opt. Technol. **68**, 508 (2001)].

Translated by A. Kazantsev

Semiconductors, Vol. 38, No. 6, 2004, pp. 657–662. Translated from Fizika i Tekhnika Poluprovodnikov, Vol. 38, No. 6, 2004, pp. 684–689.

ELECTRONIC AND OPTICAL PROPERTIES OF SEMICONDUCTORS

Analysis of Polarization Modulation Spectra of Photopleochroism Induced by Uniaxial Compression in Ge Crystals

I. E. Matyash and B. K. Serdega*

Institute of Semiconductor Physics, National Academy of Sciences of Ukraine, Kiev, 03028 Ukraine

**e-mail: serdega@isp.kiev.ua*

Submitted October 13, 2003; accepted for publication November 27, 2003

Abstract—Photoconductivity of Ge crystals in which an anisotropy of conduction was induced by uniaxial compressive strain was studied using polarization modulation of light. The spectral characteristics measured by this method are energy-dependent differences of photoconductivities excited by linearly polarized light with polarizations periodically varying in space with respect to the crystal optical axis. A phenomenological analysis of the photopleochroism spectral characteristic showed that the expression for the photoconductivity includes three cofactors. It was shown that an additional measurement of the photoconductivity derivative or mathematical processing of the photoconductivity spectra makes it possible to expand the photoconductivity in cofactors. The use of one of these techniques allowed us to determine the absorption anisotropy and its spectral characteristic. © *2004 MAIK "Nauka/Interperiodica".*

1. As follows from the results of previous studies, the method of polarization modulation (PM) of light, applied to measure such polarization effects as photoelasticity [1] and linear dichroism [2], makes it possible not only to improve the detectability of the method for anisotropy of dielectric properties, but also to extend its informativeness. Using a PM study of the linear dichroism induced in Si crystals by uniaxial compression as an example, it was shown that differential transmission spectra have a fine structure. This suggests that not only optical but also acoustic phonons are involved in interband transitions with light absorption. Analysis of these characteristics revealed that the corresponding mathematical description includes several cofactors. It was shown that these characteristics can be expanded in cofactors only using an additional measurement or mathematical processing. One of these cofactors is dichroism, i.e., the absorption anisotropy, which can be a subject for studying the response of a material to an external factor.

Extending the field of application of PM spectroscopy to such photoelectric phenomena as photoconductivity, barrier photovoltage, and other photovoltaic effects seems to be expedient not only for collecting statistical data on the nature of anisotropy. Transferring the PM method from optical effects, where it showed high efficiency, to experimental studies of photoelectric phenomena is not trivial because of the different nature of these phenomena. In turn, this circumstance will inevitably manifest itself in the fact that an analysis of photopleochroism measurements using the PM technique will have certain features that should be determined in order to reliably interpret such data. Taking into account that the dichroism spectral characteristic includes a component related to the absorption [2], one can expect that specific features of the band energy spectrum will manifest themselves in the characteristics of photopleochroism (which, like dichroism, is caused by anisotropy of dielectric properties).

This assumption is based on a large body of experimental data on pleochroism in naturally anisotropic crystals both in the optical phenomenon—light absorption [3]—and in the photoelectric effects, for example, photoconductivity [4] and barrier photovoltage [5]. The spectral characteristics measured in these and many other studies are rather complex, which accounts for the features in the energy band dispersion.

Another argument in favor of the expediency of studying pleochroism in photoconductivity is as follows. As is well known, dichroism characteristics are obtained by measuring the transmittance of light that passes through a sample of finite thickness. The translucency condition under which dichroism manifests itself limits the spectral range that can be studied. Therefore, if it is necessary to advance to higher energies, progressively thinner samples should be used, taking into account the enhanced absorption. However, as was mentioned in [6], the diffusion length of excess charge carriers in the case of photoconduction is equivalent to the sample thickness in dichroism studies. For this reason, in the case of a material with a short diffusion length, analysis of pleochroism will make it possible to overcome the difficulties associated with uniaxial compression of thin samples.

2. In our opinion, the most appropriate (for a number of reasons) material to observe the photopleochro-

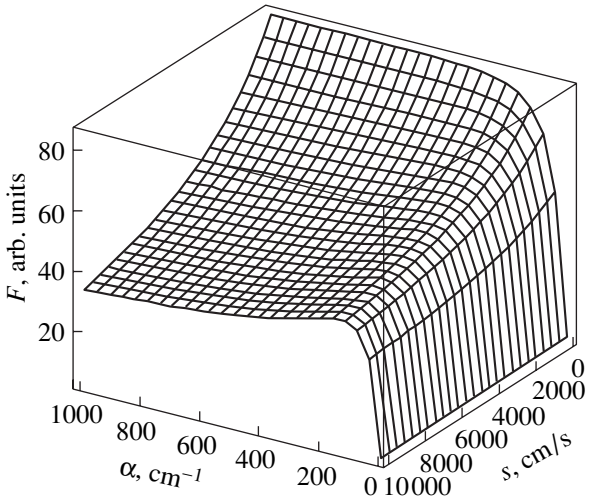

Fig. 1. Set of dependences of the photoconductivity F on the surface recombination velocity s and absorption coefficient α, calculated for a Ge sample using formula (1) at $L = 1$ mm, $d = 2$ mm, and $D = 50$ cm^2/s.

ism phenomena is crystalline germanium, in which the conductivity anisotropy is caused by uniaxial strain. First of all, the long lifetimes of light-generated carriers characteristic of lightly doped crystals make it possible to obtain sufficiently high signals from this material using conventional light sources. By no means the least important factor is the possibility of obtaining ohmic and mechanically strong contacts to Ge crystals by a simple laboratory technique. Furthermore, the possibility of attaining a surface recombination velocity in a wide range from 0 to 10^4 cm/s in the absence of surface barriers is a decisive argument in favor of this material.

The samples to be analyzed were cut from a lightly doped n-Ge ingot ($\rho = 5\ \Omega$ cm at 300 K). The samples had thickness $d = 1$ mm and an exposed surface of 4×10 mm^2. Since the effect under study, as well as linear dichroism, is described in tensor form, one has to take into account the crystallographic orientation of samples. However, in our case the orientation dependence of photopleochroism is not fundamental, especially since (as shown by the example of linear dichroism) it is not decisive. Therefore, we used samples of only one orientation at which the exposed surface coincided with the (100) plane, and the compressing force was aligned with the [100] direction.

The samples were prepared using a conventional procedure including mechanical and chemical polishing. We only note that, in polarization studies, the processing of the exposed surface should strictly satisfy the following condition. With periodic variation of the light polarization, the intensity of the light passing through front face of the sample can be modulated by the Fresnel conditions. Therefore, the exposed surface should be planar and perpendicular to the direction of exposure. In this case, provided that the optical system units are well aligned, there is no need to use a compensating plate, which is generally employed in such cases [7].

The samples were uniaxially strained in a system that maintains a uniform stress over the sample cross section. A semiconductor strain gauge was used to convert the compressing force into an electric signal.

Photopleochroism was measured using the PM technique described in detail in [2]. We only note that this technique is based on a photoelastic light modulator [8] representing a dynamic quarter-wave phase plate. In the case of alternating uniaxial strain of the plate, circularly polarized light incident on it becomes linearly polarized at the output. The direction of the electric vector of the wave periodically (with a frequency of 50 kHz) varies from parallel to perpendicular with respect to the sample optical axis (strain direction). The signal ΔF, proportional to the photoconductivity difference $F_\perp - F_\parallel$, was measured under exposure to light with orthogonal polarizations, depending on the quantum energy, strain, and surface recombination velocity. The photoconductivity spectra used in the further analysis were measured using the conventional technique. The measurements were carried out at room temperature and with a light intensity corresponding to the linear portion in the dependence of the photoconductivity on the excitation level. This circumstance made it possible to normalize the results of measurements to a constant intensity in the spectral range we used.

3. We should note that, in the case of isotropic conductivity, the dependence of the photoconductivity on the light absorption coefficient α for the samples under study is adequately described by the equation [9]

$$F(\alpha) = \frac{e\mu_n}{d} I_0 \tau \frac{\alpha}{1-(\alpha L)^2} \times \left\{ \frac{1-\exp(-\alpha d)}{\alpha L} - \frac{L(1+\alpha L_s)}{L+L_s}[1-\exp(-d/L)] \right\}, \quad (1)$$

where I_0 is the intensity of incident light, μ_n is the electron mobility, τ is the carrier recombination time, L is the diffusion length, $L^2 = D\tau$, D is the bipolar diffusivity (in the case under consideration, at $n \gg p$, it is equal to the hole diffusivity), $L_s = D/s$ is the recombination length, and s is the surface recombination velocity. The set of characteristics calculated using Eq. (1) is shown in Fig. 1 in relation to the parameters α and s, which determine the evolution of the dependences. The value of L for this specific case was determined by measuring the photomagnetic effect.

We can see that the experimental characteristics of the photoconductivity shown in Fig. 2a satisfactorily agree with those calculated using Eq. (1) and shown in Fig. 1. The agreement could be more satisfactory if the experimental curves were constructed as functions of the absorption coefficient, which is possible when the dependence of the absorption coefficient on quantum energy typical of Ge crystals is used. However, it is sufficient that the experimental values of photoconductivity in Fig. 2a fit in the range of parameter variation in

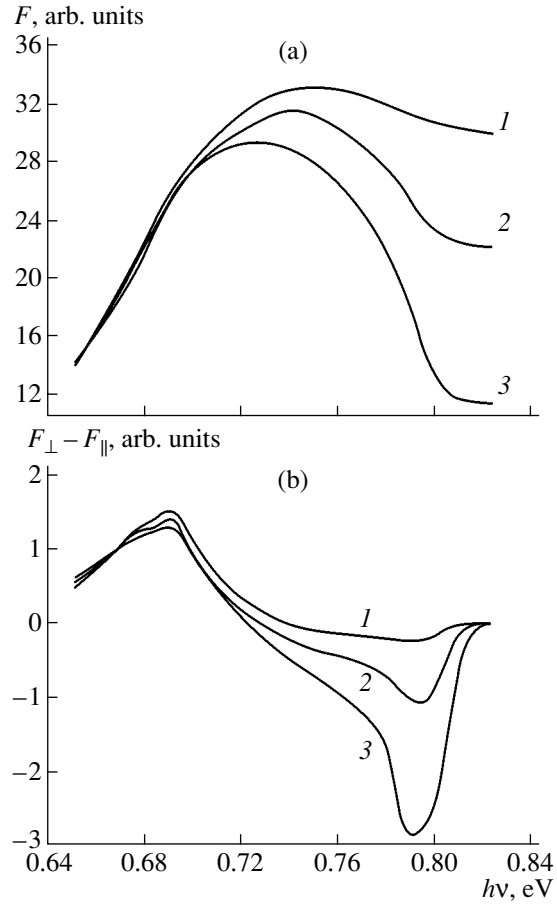

Fig. 2. Experimental spectral characteristics of the (a) photoconductivity F and (b) photopleochroism ΔF of a Ge sample strained by a stress of 3 kbar at surface recombination velocity s = (*1*) 10^2, (*2*) 10^3, and (*3*) 10^4 cm/s.

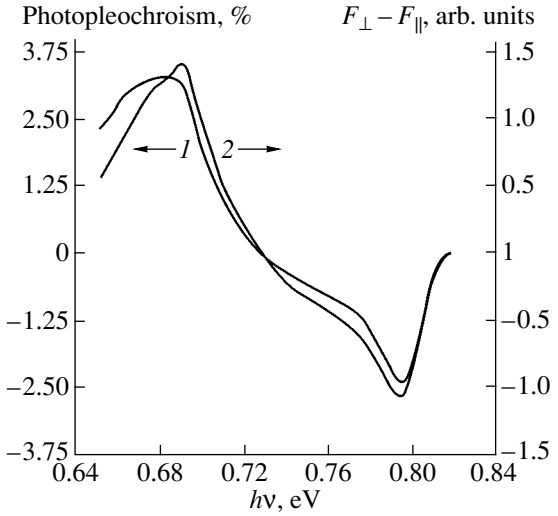

Fig. 3. Spectral dependences of the (*1*) photopleochroism and (*2*) polarization difference of photoconductivities at s = 10^3 cm/s and a stress of 3 kbar.

Fig. 1. As will be shown below, uniformity in the representation of measurement results is necessary for their analysis.

In the case of uniaxial strain of a sample with cubic symmetry (e.g., a germanium crystal), the complex refractive index becomes anisotropic due to the splitting of the energy levels of the conduction band and/or the valence band. Hence, the absorption coefficient takes two values, $\alpha_\perp$ and $\alpha_\parallel$, corresponding to two orientations of the electric vector of the wave with respect to the axes of the optical indicatrix describing the dielectric properties of the sample. When substituting these values separately into Eq. (1), we obtain two dependences that differ in the quantity measured using the PM method. In fact, this quantity is the spectral characteristic of photopleochroism.

We note that, according to the conventional terminology, the pleochroism is considered as the quantity given by

$$k = \frac{F_\perp - F_\parallel}{F_\perp + F_\parallel}, \qquad (2)$$

where $F_\perp$ and $F_\parallel$ are the photoconductivities measured at perpendicular and parallel orientations of the electric field of the wave with respect to the optical axis. The convenience of expression (2) lies solely in the fact that it illustratively characterizes the relative anisotropy, since the numerator of this expression contains both the physical meaning of anisotropy and its magnitude. An analysis of this numerator, which is the polarization difference of photoconductivities, yields (as will be shown below) data on the nature of the anisotropy and its properties. Therefore, in no way claiming to correct the terminology but simply for brevity, in this paper we take photopleochroism to mean the numerator in expression (2) in this study, especially because, as follows from the curves in Fig. 3, expression (2) does not contain a new meaning, at least in the case under consideration.

Figure 2b shows the experimental dependences $\Delta F = F_\perp - F_\parallel$ in the range of edge absorption of germanium for three cases differing in the surface recombination velocity s. We can see that the surface recombination velocity has a considerable effect on the portions of the pleochroism characteristics associated with the photoconductivity decrease in Fig. 2a in the range of a high absorption coefficient.

Comparison of the dependences shown in Figs. 2a and 2b allows one to conclude that the result obtained using the PM method is almost the same as in the case of measuring the photoconductivity derivative by the differential spectroscopy method, referred to as λ modulation [10]. To make sure of this, one of the curves in Fig. 2a was graphically differentiated. The result is shown in Fig. 4 in comparison with the photopleochroism characteristic of the same sample.

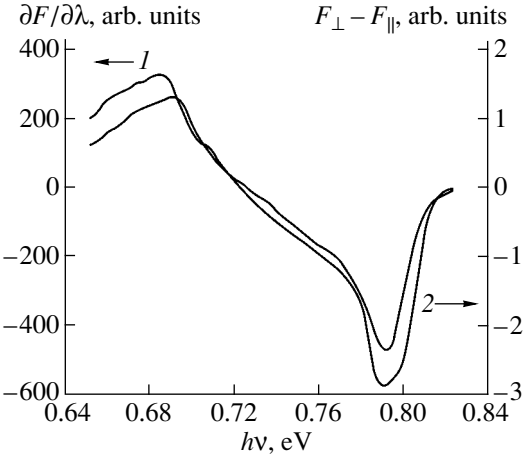

Fig. 4. Spectral dependences of the photoconductivity derivative (curve *1*) obtained by differentiation of curve *3* in Fig. 2a and the photopleochroism ΔF (curve *2*) for the same Ge sample at $s = 10^4$ cm/s.

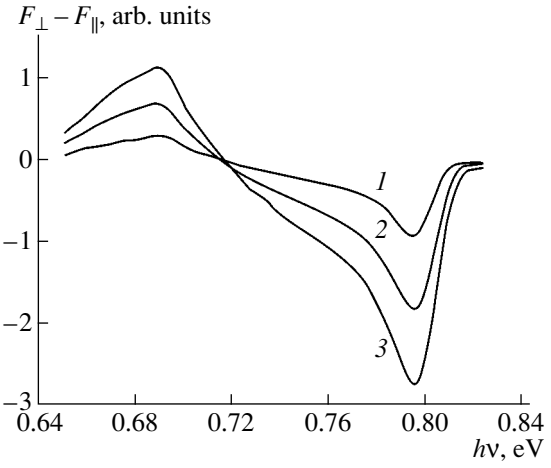

Fig. 5. Spectral characteristics of the photopleochroism ΔF of a Ge sample deformed by stresses of (*1*) 1, (*2*) 2, and (*3*) 3 kbar at $s = 10^4$ cm/s.

The results of the PM measurements (Fig. 2) can be solely attributed to the deformation-induced anisotropy of the dielectric properties of the sample under study. This statement is illustrated by the photopleochroism characteristics (Fig. 5) measured at different deforming forces and a fixed surface recombination velocity. It can be seen from Fig. 5 that both positive and negative amplitude values of photopleochroism linearly depend on the straining force at least within the strain range under study.

We applied the procedure reported in [11] to analysis of the results of the PM measurements. We recall that the quantity to be measured is the photoconductivity difference $\Delta F = F(\alpha_\perp) - F(\alpha_\parallel)$. Since $\Delta\alpha = \alpha_\perp - \alpha_\parallel$, we obtain $\Delta F = F(\Delta\alpha + \alpha_\parallel) - F(\alpha_\parallel)$.

Using the definition of a derivative, under the condition $\Delta\alpha \ll \alpha_\perp, \alpha_\parallel$, we can write this expression as

$$\Delta F = \frac{\partial F}{\partial \alpha}\Delta\alpha. \qquad (3)$$

It follows from (3) that PM, in contrast to λ modulation, yields the photoconductivity derivative with respect to the absorption coefficient. However, the physical nature of the features of the photopleochroism spectra is in the dependence of the light absorption coefficient on the photon energy $\alpha(h\nu)$. The derivative of complex function (3), expanded in partial derivatives, shows that

$$\Delta F = \frac{\partial F}{\partial (h\nu)}\frac{\partial (h\nu)}{\partial \alpha}\Delta\alpha. \qquad (4)$$

If one of the cofactors is zero, expression (4) yields $\Delta F = 0$. This explains the fact that the point of intersection with the line $\Delta F = 0$ in Fig. 2b shifts simultaneously with the peaks in Fig. 2a (at which $\partial F/\partial(h\nu) = 0$).

Equation (4) makes it possible to explain the cause of almost the complete absence of differences between the photopleochroism characteristics and the derivative of photoconductivity (Fig. 4). This fact becomes clear if we assume that the product $[\partial(h\nu)/\partial\alpha]\Delta\alpha$ is independent of the photon energy, i.e., is a constant in this spectral range. In this case, it becomes possible to determine the function $\Delta\alpha(h\nu)$ from the condition

$$[\partial(h\nu)/\partial\alpha]\Delta\alpha \simeq 1.$$

Thus, the anisotropy $\Delta\alpha$ is proportional to the derivative of absorption coefficient with respect to the energy, $\partial\alpha/\partial(h\nu)$. To determine the function $\Delta\alpha$, we use the graphic dependence of the germanium absorption coefficient [12]. The result of the graphical differentiation of this dependence is shown in Fig. 6, curve *1*.

It is pertinent to note that precisely such a model, following from the calculation in [13], was used to explain the experimental data in [6]. Its essence is in shifting the spectral dependence of the absorption coefficient for perpendicular (with respect to the strain direction) polarization by the value of band splitting in the strained sample.

The validity of the above assumption can be verified by two independent methods. In one case, relation (3) is used to calculate the function $\Delta\alpha(h\nu)$ by graphical differentiation of the photoconductivity spectrum $F(h\nu)$ with respect to the function $\alpha(h\nu)$ used above, $\Delta\alpha = \Delta F/(\partial F/\partial\alpha)$. The result of this procedure is shown in Fig. 6 (curve *2*). An even more independent method is based on the dichroism effect, where the transformation of the expression relating the transmittance T and absorption coefficient results in

$$\Delta\alpha = \frac{1}{d}\ln\left(1 + \frac{\Delta T}{T}\right).$$

This relation, along with the dependences $\Delta T(h\nu)$ and $T(h\nu)$ additionally measured by the technique described above, yields one more function, $\Delta\alpha$ (Fig. 6, curve *3*). Its spectral range is limited by the finite thickness of the sample; however, the agreement of all three characteristics is more than satisfactory. The slight disagreement is within the errors of graphic differentiation and measurements.

4. In conclusion, first, we note that the values of photopleochroism determined (attaining no more than 10%) could be obtained using only the differential technique. The reliability of the curves in Fig. 2b is confirmed by the fact that the maximum values of photopleochroism exceed the noise of the measuring system by two orders of magnitude.

As expected, the photopleochroism spectral characteristics, obtained by the PM method, reflect the features of the band energy spectrum. This is confirmed by the fact that the positions (on the energy scale) of the minima of the photopleochroism curves in Figs. 2b and 5 are not related to the deforming force or the surface recombination velocity. Indeed, at energy $h\nu = 0.798$ eV, Ge crystals exhibit a singularity in the form of the point M_0 of the Brillouin zone [14], i.e., in the region of direct transitions at the point Γ between the energy levels Γ'_{25} and Γ'_2.

This conclusion is confirmed independently by analysis of the photopleochroism spectral characteristic in crystalline InSb (Fig. 3 in [6]). The polarization difference of photoconductivities calculated from these data is a similar alternating dependence. As in the case under consideration, the position of the minimum corresponds to an energy that closely coincides with the band gap at the indicated temperature in InSb (which is a direct-gap semiconductor).

We emphasize that the negative portions of the photopleochroism characteristics are totally controlled by the linear dichroism demonstrated in [2] by the example of strained silicon samples. Indeed, the point where the dependence $\alpha_0(h\nu)$ changes sign, which stabilizes when the surface recombination velocity tends to infinity, is characteristic. This point, expressed in terms of the absorption coefficient, correlates with the diffusive displacement of carriers and satisfactorily agrees with the condition $1/\alpha_0 \simeq L$. As for the zero amplitude values of the photopleochroism characteristics at an energy close to 0.8 eV, the absorption coefficients for both polarizations (as in the case of linear dichroism) become so large that their difference remains within L. This means that, in this case, the pleochroism in photoconduction is dichroism at a diffusion length. However, as we have shown previously, the spectral characteristic of the linear dichroism is controlled exclusively by the specific features of the crystal energy bands. At the same time, the photopleochroism spectra also depend on the recombination parameters of a material and the properties of the sample surface.

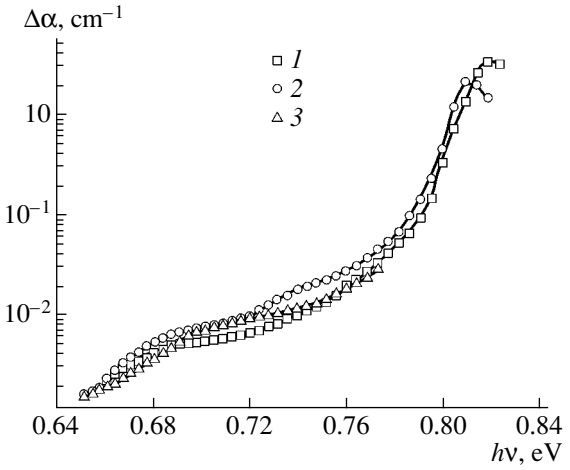

Fig. 6. Spectral characteristics of $\Delta\alpha$ (one of the cofactors in the expression for photopleochroism (4)) obtained by (*1*) differentiation of the typical spectral characteristic of the absorption coefficient, $\Delta\alpha = \partial\alpha/\partial(h\nu)$; (*2*) calculation based on the photoconductivity and photopleochroism measurements, $\Delta\alpha = \Delta F/(\partial F/\partial\alpha)$; and (*3*) calculation based on the linear-dichroism measurement, $\Delta\alpha = (1/d)\ln(1 + \Delta T/T)$.

One might expect that the state of the excited-light polarization (the effect of optical alignment of momenta [15]) affects the kinetic parameters, e.g., the mobility, and, hence, the photoconductivity. However, taking into account that the relaxation times of momenta are short at $T = 300$ K and that the crystallographic orientation is unfavorable for this effect, it seems unlikely that it will be observed experimentally.

We note that the phenomenon under study can be used for diagnostics of internal stresses in crystals. It was shown that a minimum stress of about 10 kg/cm^2 is reliably measurable using conventional measuring instruments. One should keep in mind that this stress corresponds to such a value of pleochroism, which is observed in a sample with the highest surface recombination velocity.

REFERENCES

1. I. I. Boiko, Ye. F. Venger, Ye. V. Nikitenko, and B. K. Serdega, Semicond. Phys., Quantum Electron. Opt. **2**, 352 (1999).
2. E. F. Venger, I. E. Matyash, and B. K. Serdega, Opt. Spektrosk. **94**, 38 (2003) [Opt. Spectrosc. **94**, 33 (2003)].
3. A. A. Lebedev, K. Ovezov, V. D. Prochukhan, *et al.*, Pis'ma Zh. Tekh. Fiz. **2**, 385 (1976) [Sov. Tech. Phys. Lett. **2**, 149 (1976)].
4. G. A. Medvedkin, Fiz. Tekh. Poluprovodn. (St. Petersburg) **34**, 533 (2000) [Semiconductors **34**, 521 (2000)].

5. G. K. Averkieva, A. Mamedov, V. D. Prochukhan, and Yu. V. Rud', Fiz. Tekh. Poluprovodn. (Leningrad) **12**, 1732 (1978) [Sov. Phys. Semicond. **12**, 1025 (1978)].
6. F. T. Vas'ko, S. G. Gasan-zade, M. V. Strikha, and G. A. Shepel'skiĭ, Fiz. Tekh. Poluprovodn. (St. Petersburg) **29**, 708 (1995) [Semiconductors **29**, 368 (1995)].
7. B. B. Krichevtsov, Pis'ma Zh. Éksp. Teor. Fiz. **74** (3), 177 (2001) [JETP Lett. **74**, 159 (2001)].
8. S. N. Jasperson and S. E. Sahnatterly, Rev. Sci. Instrum. **40**, 761 (1969).
9. T. S. Moss, Rep. Prog. Phys. **28**, 15 (1985).
10. M. Cardona, *Modulation Spectroscopy* (Academic, New York, 1969; Mir, Moscow, 1972).
11. E. F. Venger, I. E. Matyash, and B. K. Serdega, Fiz. Tekh. Poluprovodn. (St. Petersburg) **37**, 1188 (2003) [Semiconductors **37**, 1160 (2003)].
12. W. C. Dash and F. Newman, Phys. Rev. **99**, 1151 (1955).
13. F. T. Vas'ko and M. V. Strikha, Fiz. Tekh. Poluprovodn. (Leningrad) **24**, 1227 (1990) [Sov. Phys. Semicond. **24**, 773 (1990)].
14. B. O. Serafin and R. B. Hess, Phys. Rev. Lett. **14**, 138 (1965).
15. M. I. Karamash, V. P. Mushinskiĭ, and G. M. Shmelev, Zh. Tekh. Fiz. **53**, 1198 (1983) [Sov. Phys. Tech. Phys. **28**, 730 (1983)].

Translated by A. Kazantsev

Semiconductors, Vol. 38, No. 6, 2004, pp. 663–665. Translated from Fizika i Tekhnika Poluprovodnikov, Vol. 38, No. 6, 2004, pp. 690–692.

SEMICONDUCTOR STRUCTURES, INTERFACES, AND SURFACES

Physical Mechanisms of Laser Correction and Stabilization of the Parameters of Al–*n*–*n*$^+$-Si–Al Schottky Barrier Structures

G. I. Vorobets*^, M. M. Vorobets*, V. N. Strebezhev*, E. V. Buzaneva, and A. G. Shkavro**^^**

**Fed'kovich Chernivtsy National University (Department of Physics), Chernivtsy, 58012 Ukraine*

^e-mail: rt-dpt@chnu.cv.ua

***Shevchenko National University (Department of Radio Physics), Kiev, 01017 Ukraine*

^^e-mail: shkavro@univ.kiev.ua

Submitted July 17, 2003; accepted for publication September 25, 2003

Abstract—Optical and scanning electron microscopy in combination with layer-by-layer chemical etching are used to study the physical processes of solid-state diffusion induced by pulsed laser radiation in packageless thin-film Al–*n*–*n*$^+$-Si–Al Schottky barrier structures formed on free silicon surface and in SiO_2 windows.

Recent results [1–4] suggest that an appropriate choice of the mode of pulsed laser irradiation allows the controllable correction of the electrical properties of metal–semiconductor contacts (MSC) in Al–*n*–*n*$^+$-Si–Al Schottky barrier (SB) structures, as well as the stabilization of their parameters [5].

In this study, we consider two groups of Al–*n*-Si SB structures fabricated by a conventional technique [4, 5] on (111)-oriented KÉF-1 (*n*-Si:P, $\rho = 1\ \Omega$ cm) silicon wafers. Prior to the deposition of Al, we used chemical etching in order to remove a SiO_2 layer from the entire active area in the first-group structures and to open windows in the SiO_2 layer in the structures of the second group.

The parameters of the Al–Si contact (the potential barrier height φ_b, the nonideality factor n, and the differential coefficient of the linearity of current–voltage (I–V) characteristic α on the semilog scale) depend on the technological parameters, including the modes of laser irradiation (see table). As the laser source, we used an yttrium–aluminum garnet laser in free-running mode with the radiation wavelength $\lambda = 1.06$ μm and the output intensity I_0 ranging from 10 to 20 MW/cm^2. The SB structures under study were irradiated by single pulses of millisecond duration.

A metallographic study of the morphology of Al films by means of layer-to-layer etching in HF : HCl : H_2O indicated the existence of a threshold radiation intensity $I_c \approx 95$–105 kW/cm^2. When $I_0 < I_c$, no appreciable changes in the morphology of the Al surface are observed. At $I_0 \approx 105$–115 kW/cm^2, a uniformly darkened region appears at the center of the irradiation spot; this fact is related to the thermal effect of the laser pulse [6] and the heating of the structure at the Al–Si interface up to the eutectic temperature. With a further increase in I_0 to 125–135 kW/cm^2, the diameter of the first dark zone enlarges two- to threefold, and a second, darker zone appears at its center, where the Al film melting point is attained. This result agrees with the theoretically simulated radial distribution of temperature $T(r, x, t)$ over the radiation spot on the sample surface ($x = 0$) (the possible phase transformation of the irradiated material is disregarded) [7]:

$$T(r, 0, t) = [(1 - R)I_0 d/K\pi^{1/2}] \times \arctan(4\kappa t/d^2)^{1/2} \exp(-r^2/d^2), \quad (1)$$

where R is the reflectivity of the irradiated surface, d is the Gaussian beam radius, K is the heat conductivity coefficient, and κ is the thermal diffusivity of Si.

After Al is removed by the chromium etchant CrO_3 : H_2O : HF, the triangular etch pits typical of (111) Si substrate defects are clearly outlined in the surface Si layers. The majority of the defects are stacking faults and outcropping lines of the pileups of dislocations. An increase in I_0 from 60 to 95 kW/cm^2 yields a defect-free surface Si layer in the first-group MSC structures and reduces the density of defects by 1.5–2 orders of magnitude in the second-group structures. The etch pits are

Table

I_0, kW/cm^2	Group-I SD Al–*n*–*n*$^+$-Si–Al			Group-II SD Al–*n*–*n*$^+$-Si–Al		
	φ_b, eV	α, V^{-1}	n	φ_b, eV	α, V^{-1}	n
0	0.73	36.3	1.08	0.70	33.9	1.17
85	0.76	36.8	1.06	0.75	36.1	1.08
96	0.78	39.0	1.01	0.76	36.8	1.06
106	0.80	38.6	1.05	0.75	35.4	1.11
117	0.75	33.4	1.18	0.75	36.2	1.11

1063-7826/04/3806-0663$26.00 © 2004 MAIK "Nauka/Interperiodica"

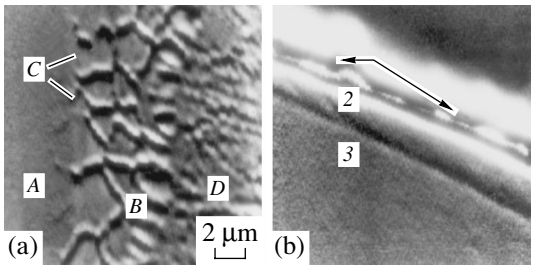

Fig. 1. The surface morphology of (a) silicon and (b) the cross section of an Al–n–n^+-Si–Al Schottky diode after the Al layer is etched off: (a) regions of the metal–semiconductor contact exposed to laser radiation with intensity I_0 = (*A*) 85–90, (*B*) 95–105, and (*D*) 105–115 kW/cm^2 (*C* marks the points where Al grains are connected); (b) the cross-section cleavage including (*1*) the residual aluminum film, (*2*) the transition p^+-Si layer, and (*3*) the n-Si substrate. A scanning electron microscope was used.

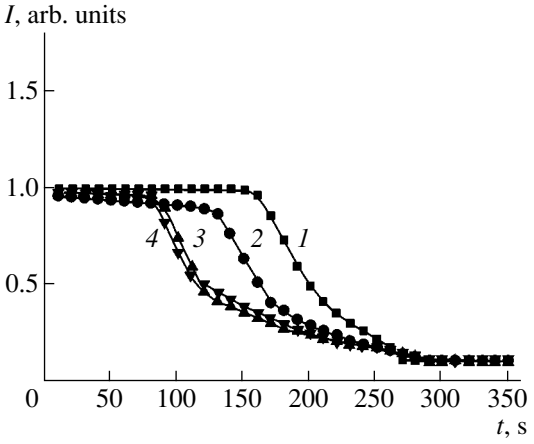

Fig. 2. Time dependences of the current of electrochemical etching of Al–n–n^+-Si–Al structures after exposure to laser radiation with intensities I_0 = (*1*) 0, (*2*) 85, (*3*) 95, and (*4*) 105 kW/cm^2.

larger in the vicinity of the Si–SiO_2 interface. Interaction between Al and Si occurs in the solid phase.

Figure 1a illustrates the results of Al–Si interphase interaction at the MSC interface in correspondence with the radial distribution of intensity over the beam cross section (*A*–*D*). In the region where $I_0 \approx$ 80–95 kW/cm^2 (Fig. 1, *A*), the Si surface is homogeneous and stacking faults are not observed. In the region irradiated with intensities $I_0 \approx$ 95–105 kW/cm^2 for the first-group MSC structures and 105–115 kW/cm^2 for the second-group structures, the diffusion of Si over the Al grain boundaries was stimulated (Fig. 1a, *B*). The prevailing diffusion directions are given by the points where Al grains are connected (Fig. 1a, *C*). At $I_0 \approx$ 105–110 kW/cm^2 for the first group of structures and 110–120 kW/cm^2 for the second group, the diffusion of silicon is activated over the entire Al grain area (Fig. 1a, *D*) with the subsequent deposition of the epitaxial p^+-Si film from supersaturated Si–Al solution.

The SEM images of the transverse cleavage of samples (Fig. 1b) indicate that there is a transition layer of Al–Si solid solution (*2*). This layer is formed in between the Al (*1*) and Si (*3*) materials as a result of the thermal treatment and the subsequent laser irradiation of structures. Depending on the irradiation mode, the transition-layer thickness varies in the range 0.6–1.2 μm, which is consistent with the measured time dependences of the electrochemical etch current (Fig. 2). The appearance of the transition layer can be attributed both to the formation of an epitaxial p^+-Si layer on the Si surface and to the dominant role of the diffusion of Al into Si. Solid-phase epitaxy of p^+-Si results in an approximately flat profile of Al dissolved in Si; accordingly, the value of the etch current should remain nearly constant in this case. The presence of steadily decreasing portions in the time dependences of current is evidence of the diffusive penetration of Al into Si under laser irradiation. These results can be interpreted in terms of the physical model of the diffusion processes stimulated by thermoelastic stress in the contact layers at the MSC interface.

It is predicted by calculation that the irradiation of Al–Si structures by laser pulses with duration $\tau \approx 10^{-3}$ s will result in the uniform heating of a 1-μm-thick Al layer (K_{Al} = 2.36 J/(s cm K), κ_{Al} = 1.03 cm^2/s). Within this time period, the thermal front propagates throughout the structure. The optimal mode of heating the Al–Si interface (up to the temperature $T \approx$ 550°C, which is not higher than the eutectic temperature of the Al–Si system $T_e \approx$ 577°C) was obtained at $I_0 \approx$ 95 kW/cm^2. Temperature gradients appearing in a 5-μm-thick near-contact Si layer are on the order of 1.6×10^4 K/cm, while the gradient near the irradiation-free silicon surface is on the order of 10^3 K/cm. Since the linear expansion coefficient α_T of Al is ten times that of Si ($\alpha_{T\mathrm{Al}} = 23.1 \times 10^{-6}$ K^{-1}, $\alpha_{T\mathrm{Si}} = 2.33 \times 10^{-6}$ K^{-1}), laser irradiation gives rise to elastic tension and elastic compression in the contact regions in Si and Al, respectively. Calculation [8] for $I_0 \approx$ 95–265 kW/cm^2 and without regard for phase transformations yields the maximal stress that appears at the MSC interface within the range $\sigma_{yy} = \sigma_{zz}$ = 6.7–18.7 MPa. The neutral plane ($\sigma_{yy} = \sigma_{zz} = 0$) lies at a distance of 35–40 μm from the contact. Both Al and Si crystal lattices are deformed at the MSC interface so that these deformations favor the diffusion of boundary Al to Si and the diffusion of Si from the crystal bulk to the contact region and also promote the relaxation of point defects, stacking faults, and the shift of dislocation lines in Si.

The estimations of the radial σ_r and tangential σ_θ stresses [9] at the Al–Si interface in a Si layer at 500°C yield $\sigma_r = \sigma_\theta \approx$ 15.6 MPa, which agrees well with the calculated values of σ_{yy} and σ_{zz} mentioned above.

It seems feasible that, due to the elastic stress relaxation, at $I_0 < I_c$, the presence of microplastic deformations in the space-charge region of SB stimulates the ordering of the atomic structure and reduces the density of centers whose deep levels provide for the generation–recombination current. As a result, the nonideality factor n of the Schottky barriers approaches unity and the potential barrier height φ_b increases by 0.03–0.05 eV. The pulsed laser irradiation of the contacts that were formed in SiO_2 windows induces an additional stress at the Al–SiO_2 boundary along the perimeter of the Al–n-Si contact; the effect of lowering the deep level concentration is weaker in this case. The irradiation at $I_0 \approx I_c$ activates Si-to-Al and Al-to-Si interdiffusion, which leads to the thickening of the transition p^+-Si layer at the interface, an increase in n to 1.08–1.12, and an increase in φ_b by 0.05–0.07 eV. The presence of a p^+-Si layer is confirmed by the greater value of φ_b determined from the C–V characteristic compared to that calculated for the above-barrier current from the I–V characteristic, by the results of SEM studies, and by the corresponding calculation of the transition layer parameters [4, 10].

Thus, we conclude that the optimal conditions for pulsed laser irradiation of Al–n-Si SB structures are those that provide for solid-phase interaction at the Al–Si interface; in optimal conditions, the potential barrier height is increased and the nonideality factor is close to unity. A possible mechanism of the laser correction of SB parameters is a decrease in the concentration of deep levels related to the structural defects in the Si surface layer due to the laser-enhanced relaxation of thermal stresses in MSC.

REFERENCES

1. V. I. Fistul' and A. M. Pavlov, Fiz. Tekh. Poluprovodn. (Leningrad) **17**, 854 (1983) [Sov. Phys. Semicond. **17**, 535 (1983)].
2. G. V. Maĭranovskiĭ, V. I. Fistul', and M. V. Fistul', Fiz. Tekh. Poluprovodn. (Leningrad) **19**, 2082 (1985) [Sov. Phys. Semicond. **19**, 1284 (1985)].
3. V. I. Fistul', A. M. Pavlov, A. P. Ageev, and A. Sh. Aronov, Fiz. Tekh. Poluprovodn. (Leningrad) **20**, 2140 (1986) [Sov. Phys. Semicond. **20**, 1339 (1986)].
4. E. V. Buzaneva, G. I. Vorobets, V. I. Strykha, *et al.*, in *Abstract Booklet of International School–Conference on Physical Problems in Material Science of Semiconductors* (Chernivtsi, Ukraine, 1995), p. 305.
5. G. I. Vorobets, O. I. Vorobets, and A. P. Fedorenko, in *Problems of Optics and High Technology Material Science: Scientific Works* (Kiev, 2002), p. 156.
6. V. N. Abakumov, Zh. I. Alferov, Yu. V. Koval'chuk, and E. L. Portnoĭ, Fiz. Tekh. Poluprovodn. (Leningrad) **17**, 2224 (1983) [Sov. Phys. Semicond. **17**, 1424 (1983)].
7. W. W. Duley, *Laser Processing and Analysis of Materials* (Plenum, New York, 1983; Mir, Moscow, 1986).
8. E. E. Kvasov and V. V. Makarov, Fiz. Tekh. Poluprovodn. (Leningrad) **18**, 747 (1984) [Sov. Phys. Semicond. **18**, 466 (1984)].
9. V. S. Sergeev, O. A. Kuznetsov, N. P. Zakharov, and V. A. Letyagin, *Tensions and Deformations in the Components of Microcircuits* (Radio i Svyaz', Moscow, 1987).
10. V. I. Strikha and E. V. Buzaneva, *Physical Foundations of the Reliability of Metal–Semiconductor Contacts in Integrated Electronics* (Radio i Svyaz', Moscow, 1987).

Translated by A. Sidorova

Semiconductors, Vol. 38, No. 6, 2004, pp. 666–671. Translated from Fizika i Tekhnika Poluprovodnikov, Vol. 38, No. 6, 2004, pp. 693–698.

SEMICONDUCTOR STRUCTURES, INTERFACES, AND SURFACES

Slow Relaxation of Conductance of Quasi-Two-Dimensional Highly Disordered MIS Structures

A. B. Davydov* and B. A. Aronzon

Institute of Molecular Physics, Russian Research Centre Kurchatov Institute, pl. Akademika Kurchatova 1, Moscow, 123182 Russia

**e-mail: davydov@imp.kiae.ru*

Submitted October 20, 2003; accepted for publication November 4, 2003

Abstract—Slow relaxation of 2D conductance of metal–nitride–oxide–semiconductor structures is investigated with various methods of disturbing the system from equilibrium. It is shown that slow relaxation appears only under a strong fluctuation potential, which is controllable in these systems. The main process determining conduction of the system is screening of the potential by channel electrons, both by free electrons and those localized in potential wells. The time dependence of conductance is logarithmic, which is typical of systems of the "electronic glass" type. © *2004 MAIK "Nauka/Interperiodica".*

A disordered system with a strong fluctuation potential, irrespective of its nature and scale, is a system with a phase space that contains a large number of local energy minima. Such a system is often far from thermodynamic equilibrium. Specifically, the authors of [1, 2] paid attention to many previous experiments for systems with hopping conduction and systems close to the metal–insulator transition on the insulator side of the transition. It is possible that these investigations were carried out in a mode when the system was in a certain "frozen" or "pseudoground" state rather than in thermodynamic equilibrium. By its nature, this pseudoground state is similar to a local energy minimum in glass systems. Transitions from this state can be very slow. It is evident that effects associated with the tendency of the system to attain a more energetically favorable state, i.e., its tendency towards equilibrium, can be expected in such systems. Recently, the observation of time dependences of conductance in such systems (electronic glasses) has attracted increasing attention. The research carried out by various (although not many) teams has shown that time dependences of conductance with characteristic times as long as several tens of hours can be observed for highly disordered systems (see, for example, [3]). The variation in conductance can attain several orders of magnitude in this case.

When the system is far from thermodynamic equilibrium, its behavior may be different from that characteristic of thermodynamic equilibrium. This indicates that studying the behavior of a system in a state far from thermodynamic equilibrium is of practical interest.

Among recent studies of glasslike behavior of electronic systems, specifically, slow relaxation of conductance in these systems, publications [3, 4] are noteworthy. In these publications, the results of studying the slow relaxation of conductance of the Anderson insulator using metal–insulator–semiconductor (MIS) structures based on In_2O_3 as an example were reported. Conductance of the samples increased severalfold (up to a factor of 10) after a sharp change in the gate over several hours (up to 10 h), depending on the degree of disorder.[1] Another example of glasslike behavior in semiconductor systems is two-dimensional (2D) Si mesoscopic (i.e., short but wide) structures near an expected metal–insulator transition on the insulator side [5]. Noise $1/f$ is enhanced as the system approaches the metal–insulator transition and the temperature decreases.

In this paper, we discuss time dependences of conductance for 2D semiconductor systems with a strong fluctuation potential with different methods of disturbing the system from equilibrium. The samples at our disposal differed from the structures investigated by other researchers both in the scale of the fluctuation potential in a 2D-conduction channel (large-scale in our case) and in the field effect. This effect exceeded the field effect for In_2O_3-based MIS structures by several orders of magnitude [3, 4]. Strong large-scale potential leads to substantial differences between the observed time dependences of conductance and those investigated by other teams of researchers [3–5].

We used metal–nitride–oxide–semiconductor (MNOS) structures based on Si with an inversion *n*-channel in lightly doped *p*-Si and with a composite gate insulator. A schematic diagram of the cross section of the structure is shown in the inset of Fig. 1. The SiO_2 and Si_3N_4 layers were 30 and 350 Å thick, respectively. The trap states capable of capturing and storing the charge exist at the interface between two insulators.

[1] It is noteworthy that the authors of [3, 4] suggest that the disturbance of thermodynamic equilibrium for a system with a small-scale fluctuation potential is always accompanied by an increase in conductance with its subsequent decrease with time.

This property is widely used in microelectronic memory cells [6]. The charge state of the traps can be varied by electron injection under the effect of a positive (rendering conduction in our case) potential applied to the structure gate. These traps, which are 30 Å from the conduction channel, are the sources of the fluctuation potential. The electron concentration at the traps can be varied within 10^{11}–10^{13} cm^{-2}. We will call structures with a strong fluctuation potential formed in a similar way "charged." The concentration of the sources of the fluctuation potential was evaluated from the shift of the conductance threshold. Figure 1 shows a typical dependence of conductance (G) of the charged structure on the gate potential (V_g). As one can see from Fig. 1, as V_g increases, conductance of the structure varies in a threshold manner on attaining a certain value $V_g = V_{gt}$, which corresponds to a sharp bend in the $G(V_g)$ curve. This threshold corresponds to the transition from the quasi-1D conduction along narrow channels of the percolation cluster to the 2D conduction, when the channel width starts to exceed the electron free path [7, 8]. The gate threshold voltage V_{gt} depends on the concentration of the sources of the fluctuation potential.

The samples were shaped like a "Hall cross" 20 μm wide and 150 μm long with potential probes spaced at 60 μm. The measurements were carried out in a weak longitudinal field of 3 mV/cm, which corresponded to a linear portion of the current–voltage (I–V) characteristic. Previously, we investigated short-channel (5 μm long, 50 μm wide) samples of similar structures with a channel length shorter than the correlation length of the percolation cluster [7, 8]. In contrast to the structures investigated in this study, a single saddle point of the fluctuation potential makes the main contribution to the conductance of a short-channel structure as a whole. This saddle point is located in the lowest-resistance path of the flow of the percolation cluster current, which encloses the drain and source of the structure. The conductance of this saddle point is quantized [9], and the conductance of the structure as a whole in a quasi-plateau portion in the $G(V_g)$ dependence is $G \approx 2e^2/h$. This research showed that the structure of the percolation cluster and the profile of the fluctuation potential, whose parameters were determined in [7, 8], play a critical role in the transport properties of Si-based MNOS structures.

The gate-voltage dependence of conductance of the structure $G(V_g)$ is hysteresis-like. This can be seen in Fig. 2, where the $G(V_g)$ curves are shown on a logarithmic scale for clarity. The $G(V_g)$ dependences shown in Fig. 2 are found for the forward and reverse variations, i.e., as the gate voltage increases and decreases. It was already noted that the conductance of the structure increased sharply as the gate voltage increased to $V_g = V_{gt}$. For the reverse variation, i.e., as V_g decreases, $G(V_g)$ behaves similarly. However, in this case, the threshold value of V_{gt} is noticeably smaller than the value observed as V_g increases. Note that the electron capture

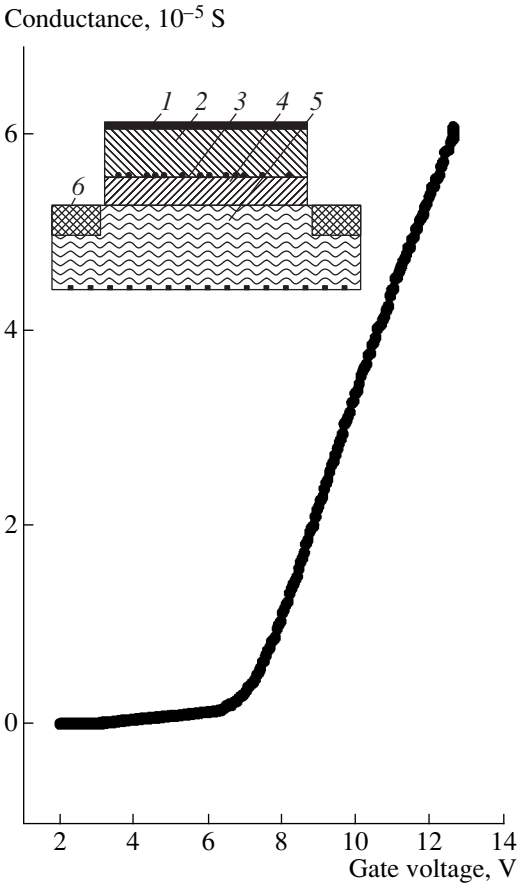

Fig. 1. Gate-potential dependence of conductance of the structure at 4.2 K. A schematic diagram of the cross section of the MNOS structure is shown in the inset: (*1*) metal gate; (*2*) nitride (350 Å); (*3*) nitride–oxide interface, at which the sources of the fluctuation potential (traps) are located; (*4*) oxide (30 Å); (*5*) two-dimensional conduction channel; and (*6*) *n*-contacts.

at the traps may cause an increase in V_{gt} as V_g decreases. The characteristic time of scanning over V_g is 10 min. A similar phenomenon is observed for the samples with a concentration of the sources of the fluctuation potential (i.e., the charge at the oxide–nitride interface) close to the highest possible concentration in these structures. This concentration is restricted by the breakdown voltages of the gate insulator, i.e., ~10^{13} cm^{-2}. If the experiment is repeated after a time under the same conditions, the run of curves is repeated. For a lower (by approximately a factor of 2) concentration of sources of the fluctuation potential, a similar dependence was not observed to within our experimental accuracy (see the inset in Fig. 2). The existence of slow relaxation of conductance with characteristic times longer or comparable with the time of scanning over V_g (~10 min) may be one possible explanation for the phenomenon observed. This assumption is confirmed by the data shown in Fig. 3. The variation in conductance when scanning was

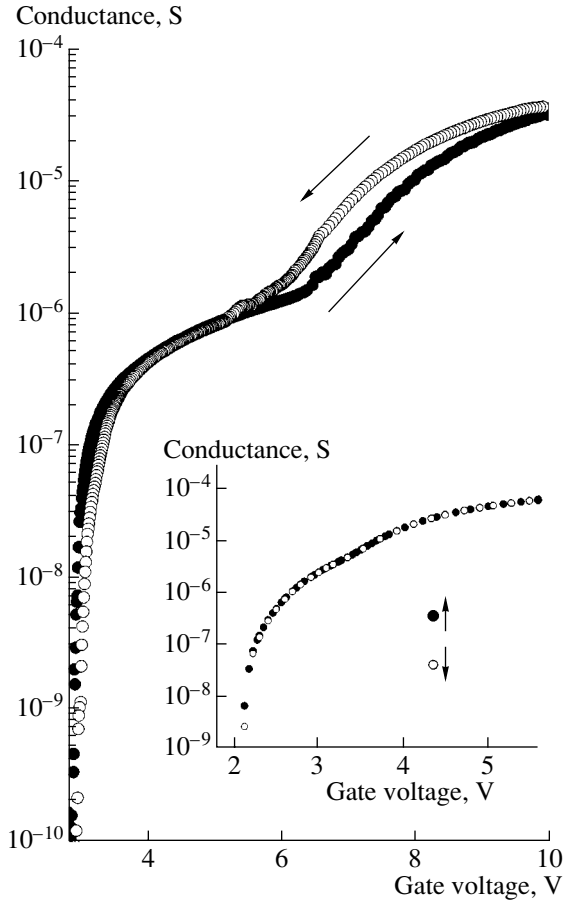

Fig. 2. Gate-potential dependence of conductance of the structure with increasing and decreasing gate voltage. The concentration of sources of the fluctuation potential ~10^{13} cm^{-2}, and the measurement temperature is 4.2 K. The same dependence for the concentration of the sources of the fluctuation potential (<5×10^{12} cm^{-2}) is shown in the inset. Arrows indicate the direction of variation in V_g.

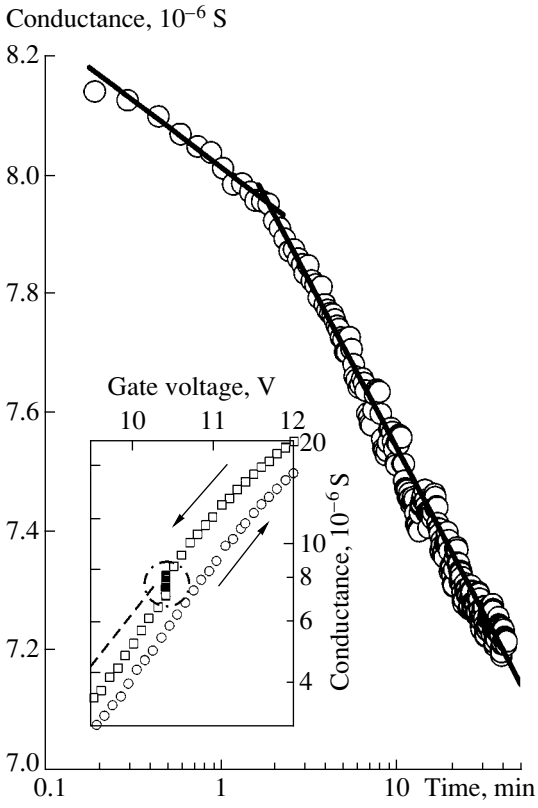

Fig. 3. Time dependence of conductance of the structure at V_g = 10.4 V close to V_{gt} for this structure. The concentration of sources of the fluctuation potential ~2×10^{13} cm^{-2}, and the measurement temperature is 4.2 K. The gate-potential dependence of conductance of the structure in the hysteresis region is shown in the inset. Arrows indicate the direction of variation in V_g. The encircled region corresponds to the time dependence of conductance for a fixed value of V_g after scanning was stopped.

stopped at a certain fixed value of V_g close to V_{gt} is shown in the inset to Fig. 3. In this case, conductance relaxes to a value that is intermediate between those measured on scanning over V_g as the gate voltage increases or decreases. One can see (Fig. 3) that the relaxation of conductance is logarithmic with the characteristic time > 10 min.

The above results (Figs. 2, 3) were obtained for $V_g \geq V_{gt}$. However, slow relaxation of conductance is also observed if the inverse inequality is satisfied. We measured the characteristic relaxation times of conductance for $V_g \approx$ (2–6) V, which is substantially lower than $V_{gt} \approx$ (7–9) V for maximal charging of the structures (see Fig. 4a). The experiment was carried out according to the following procedure. A preliminary charged sample was cooled under V_g = 0 to the liquid-helium temperature and was kept for a certain time (~2 h) under these conditions. Then a positive voltage jump V_g was applied to the sample, and the time dependence of conductance was studied for this value of V_g. Corresponding dependences are shown in Fig. 4a, where the measurement values of V_g are indicated. Prior to the measurement for each subsequent value of V_g, the structure was transferred to the state with a zero gate voltage and was kept in this state for 2 h. The characteristic time dependence of absolute conductance is shown in Fig. 4b. One can see that the $G(t)$ curve contains a portion that is linearized on a semilog scale. This means that the time dependence of conductance is logarithmic. The characteristic saturation time for this value of V_g is several minutes. Figure 4a shows that the characteristic time of variation in the conductance increases as V_g increases. In the situation under consideration ($V_g < V_{gt}$), this observation means that the transition from the percolation mode of conduction to 2D conduction is approached ($V_g \longrightarrow V_{gt}$). In addition, an increase in conductance with time is observed in this case rather than its decrease, as in study [3].

The response of the system to a rapid variation in temperature was also studied (see Fig. 5). The experi-

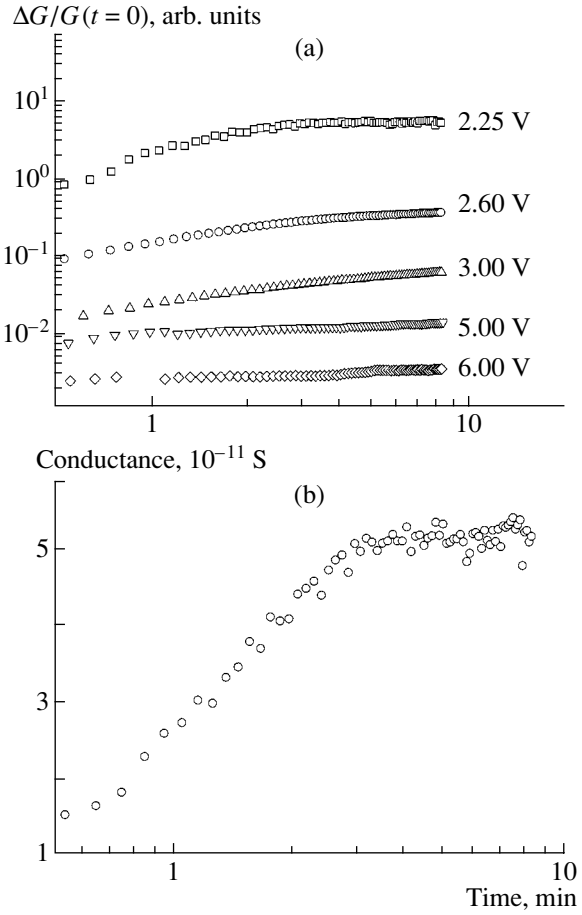

Fig. 4. (a) Time dependences of relative variation in conductance for various values of V_g and (b) time dependence of conductance for V_g = 2.25 V. The system was disturbed from equilibrium using a jumplike increase in V_g from V_g = 0 after keeping at V_g = 0 V for 2 h.

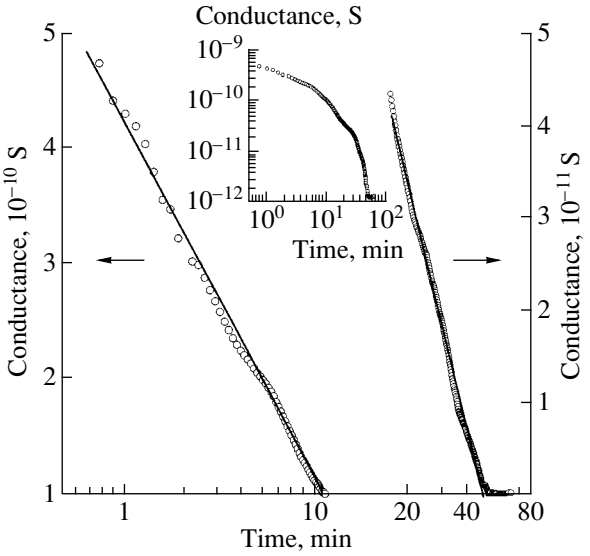

Fig. 5. Time dependences of conductance after rapid cooling of the sample from 300 to 4.2 K for ~5 min (V_g = 2 V). The variations started immediately after stabilizing the sample temperature. The total curve of relaxation of conductance is shown in the inset.

ments were carried out according to the following procedure. The sample was heated to room temperature and was then cooled to liquid-helium temperature rather rapidly. The time of cooling and stabilizing the temperature was less than 5 min. The measurement was started immediately after stabilization of the sample temperature. The corresponding time dependence is shown in Fig. 5. One can see that conductance varies by three orders of magnitude. Although the corresponding curve is not linearized as a whole in any coordinates, two portions separated by the instant $t \approx 20$ min can be distinguished. In these portions, the curve is linearized on a logarithmic time scale. The left-hand part of Fig. 5 corresponds to short times; the right-hand part, to long times. In ~1 h, saturation is observed.

The redistribution and variation in the trap charge at the nitride–oxide interface or the processes within the channel of the 2D conduction may be assumed to be the causes of the relaxation phenomena observed. The first of these assumptions, specifically, trap recharge with increasing V_g, is unlikely for the following reasons.

This process should cause a shift of the threshold of the ON state of the transistor to higher values of V_g, and the relaxation of conductance should be independent of the concentration of the sources of the fluctuation potential. However, these phenomena are not observed.[2]

In order to attain considerable charging of the structures (i.e., variation in the trap charge), the structures were kept for several hours under a voltage as high as 35 V at room temperature. At this temperature, the rate of electron capture is substantially higher, whereas the measurements were carried out at the liquid-helium temperature and at the highest values of V_g, which were lower by a factor of 3–4.

With sequential scanning over V_g, in some cases the $G(V_g)$ curves are reproduced completely even after keeping the samples at room temperature (with allowance made for the fact that the times the samples are kept at V_g = 0 V between sequential scanning are longer than the characteristic relaxation times in the system). In addition, for a low degree of charging (see the inset in Fig. 2), the $G(V_g)$ curves are completely repeated during the sequential scanning over V_g without any time lag between sequential scans over V_g. Taking into account that the shape of the $G(V_g)$ curve is determined by the parameters of the fluctuation potential, i.e., by the charge of the traps, the above indicates that this charge is invariable in time. This also indicates that the

[2] By virtue of the same cause, the ferroelectric properties of the gate insulator, e.g., silicon nitride, should not be considered as an explanation of the relaxation observed.

gate voltages we used in the measurements only slightly affect the magnitude of this charge.

Thus, we should assume that slow relaxation of conductance is associated with the behavior of electrons inside the 2D-conduction channel. However, our experiments show (Fig. 2, inset) that slow relaxation is not observed in measurements of uncharged or "weakly charged" structures, i.e., in the absence of the fluctuation potential. It was mentioned above that the parameters of the fluctuation potential of highly charged structures were determined in previous studies [7, 8]. According to [10], the energy scale of fluctuations $\Delta = (q^2/\chi)(\pi n_t)^{1/2}$, where χ is the averaged permittivity of the semiconductor and the gate insulator and n_t is the concentration of the built-in charge. For $n_t \approx 10^{13}$ cm^{-2}, which corresponds to the data shown in Fig. 2, $\Delta \approx$ 80 meV. This value exceeds the thermal energy kT even at room temperature. The characteristic spatial scale of the fluctuation potential is determined by the distance from the plane of the built-in charge (traps) to the 2D-conduction channel and by the length of screening of the fluctuation potential by electrons of the channel. The potential wells are 30–300 Å in size. We may conclude from the above that the potential in the structures is large-scale. Thus, the phenomena observed are associated with the existence of a large-scale fluctuation potential rather than with recharging of the traps or with electron localization at individual centers.

Structures with a small-scale potential (the phase of the Anderson insulator) were studied by Ben-Chorin *et al.* [3]. In this case, each shift of the system from equilibrium causes an increase in conductance [3, 4]. This circumstance, in particular, is associated with the fact that, in the case of electron–electron interaction in equilibrium, the density of states near the Fermi level is lower than in a nonequilibrium state due to the existence of the Coulomb gap [11]. Accordingly, an increase in conductance with time was observed irrespective of the method for disturbing the system from equilibrium [3, 4]. In contrast with such structures, the fluctuation potential in the structures of the type under consideration is large-scale. The parameters of the potential (the amplitude and the correlation radius) are largely determined by nonlinear electron screening or by the electron redistribution between the wells. In accordance with this fact, we believe that the electron screening of the fluctuation potential makes the main contribution to the existence and character of slow relaxation of conductance.

Let us consider the structure of the fluctuation potential for our case in more detail. The fluctuation potential is the alternation of the regions with a high local conductance (wells) and the regions with a low local conductance (hills). The wells separated by the so-called saddle regions form the percolation network. The wells that are separated from surrounding wells by a saddle region higher than a certain value practically do not contribute to conduction and are not within the path of the flow. However, the electron density of states for these regions is the same as for neighboring regions. Consequently, the electrons located in these regions do not contribute to conduction but contribute to screening of the fluctuation potential. At low temperatures, electron transitions between these regions and electron exchange between them and conduction regions, i.e., the percolation cluster current, proceeds via tunneling. Accordingly, the time of transition from these (into these) regions is determined by the tunneling probability and, consequently, by the potential parameters, in particular, by the height and width of the interwell barrier. These processes may be rather slow. However, the electrons that are located in these regions and not involved in conduction affect the conductance by screening the fluctuation potential. In other words, the concentration of electrons contributing to conduction rapidly responds to the variation in external conditions, particularly the temperature and gate voltage. In contrast with this, the electron concentration in isolated regions of the fluctuation potential varies slowly. The average electron energy in such a well can be both higher and lower than the electron energy in the percolation cluster. Here, we believe that the electron dynamics in the percolation cluster is much faster than the transitions from isolated wells. Consequently, the electron concentration in isolated regions will lag behind the concentration of electrons contributing to conduction. As a result, the electrons of isolated regions will either weaken or enhance screening of potential in the system, thus decreasing or increasing its conductance relative to an equilibrium value. The time dependence of relaxation of conductance to the equilibrium value will be controlled by electron tunneling from (into) isolated wells. By virtue of the wide energy distribution of the barrier heights, such a system should be glass-like with a logarithmic-type slow relaxation.

The difference between our system and the systems considered in [3] is that the sign of variation in the conductance as the system is disturbed from equilibrium can be any sign and depends on the method of disturbing. Thus, for example, the conductance increases as the system tends towards equilibrium, according to the results shown in Figs. 4a and 4b. At the initial instant, when we affect the system by increasing the value of V_g, the concentration of conduction electrons in the channel increases abruptly, whereas the electron concentration in isolated regions is still low. The electrons gradually occupy the isolated regions, thus increasing the degree of screening of the fluctuation potential and thereby reducing its amplitude, which causes an increase in conductance with time. An opposite situation is observed in the case shown in Fig. 5. At a high temperature, the electrons are distributed uniformly over the sample volume and, consequently, over the wells. After rapid cooling, electrons tend to occupy a narrower energy range compared to room temperature. In this case, electrons partially remain in isolated wells; they are in a nonequilibrium state with the energy

higher than the energy of conducting electrons in the system. A decrease in the concentration in wells leads to a decrease in the degree of screening, which causes an increase in the percolation level in the system and a decrease in the conductance with time.

Thus, we investigated slow relaxation of conductance of Si-based MNOS structures with the controlled large-scale fluctuation potential emerging as the system is disturbed from equilibrium due to rapid sample cooling or a jumplike variation in the potential at the structure gate. The time dependence of conductance is logarithmic, which is characteristic of glasslike systems. It is shown that, as distinct from the Anderson insulator, the nonequilibrium component of conductance in a system with a large-scale fluctuation potential can both decrease and increase as the system is disturbed from equilibrium. The relaxation of conductance observed is attributed to changes in the fluctuation potential as the screening effect of electrons varies due to slow relaxation of the electron concentration in isolated wells of the potential profile.

ACKNOWLEDGMENTS

We thank E.Z. Meĭlikhova and V.V. Ryl'kova for their interest in this study and for helpful discussions.

This study was supported by the Russian Foundation for Basic Research, project nos. 02-02-16974 and 03-02-06350, and the Ministry of Industry and Science of the Russian Federation (state contract no. 40.072.11.1176).

REFERENCES

1. S. D. Baranovskiĭ, B. L. Gelmont, B. I. Shklovskiĭ, and A. L. Efros, J. Phys. C **12**, 1023 (1979).
2. D. Menashe, O. Biham, B. D. Laikhtman, and A. L. Efros, Phys. Rev. B **64**, 115209 (2001).
3. M. Ben-Chorin, Z. Ovadyahu, and M. Pollak, Phys. Rev. B **48**, 15025 (1993).
4. A. Vaknin, Z. Ovadyahu, and M. Pollak, Phys. Rev. B **65**, 134208 (2002).
5. S. Bogdanovich and D. Popovic, Physica E (Amsterdam) **12**, 604 (2002).
6. S. M. Sze, *Physics of Semiconductor Devices*, 2nd ed. (Wiley, New York, 1981; Mir, Moscow, 1984).
7. B. A. Aronzon, D. A. Bakaushin, A. S. Vedeneev, *et al.*, Pis'ma Zh. Éksp. Teor. Fiz. **66**, 633 (1997) [JETP Lett. **66**, 668 (1997)].
8. B. A. Aronzon, D. A. Bakaushin, A. S. Vedeneev, *et al.*, Fiz. Tekh. Poluprovodn. (St. Petersburg) **35**, 448 (2001) [Semiconductors **35**, 436 (2001)].
9. M. Buttiker, Phys. Rev. B **41**, 7906 (1990).
10. V. A. Gergel' and R. A. Suris, Zh. Éksp. Teor. Fiz. **84**, 719 (1983) [Sov. Phys. JETP **57**, 415 (1983)].
11. B. I. Shklovskiĭ and A. L. Éfros, *Electronic Properties of Doped Semiconductors* (Nauka, Moscow, 1979; Springer, New York, 1984); I. P. Zvyagin, *Kinetic Phenomena in Disordered Semiconductors* (Mosk. Gos. Univ., Moscow, 1984).

Translated by N. Korovin

Semiconductors, Vol. 38, No. 6, 2004, pp. 672–674. Translated from Fizika i Tekhnika Poluprovodnikov, Vol. 38, No. 6, 2004, pp. 699–701.

SEMICONDUCTOR STRUCTURES, INTERFACES, AND SURFACES

Fabrication and Properties of an *n*-ZnO:Ga/*p*-GaN:Mg/α-Al_2O_3 Heterojunction

B. M. Ataev*^, Ya. I. Alivov, V. V. Mamedov*, S. Sh. Makhmudov*, and B. A. Magomedov***

**Institute of Physics, Dagestan Scientific Center, Russian Academy of Sciences, ul. 26 Bakinskikh Komissarov 94, Makhachkala, 367003 Russia*

^e-mail: crystal@dinet.ru

***Institute of Problems in Microelectronics Technology and Ultrapure Materials, Russian Academy of Sciences, Chernogolovka, Moscow oblast, 142432 Russia*

Submitted October 13, 2003; accepted for publication November 5, 2003

Abstract—The first results of growing ZnO/GaN/α-Al_2O_3 heteroepitaxial structures in a low-pressure flow-through reactor using chemical-vapor deposition and stimulation with a plasma of radio-frequency discharge are reported. Activation of reactants in the course of growth made it possible to significantly increase the effective pressure of atomic oxygen in the reactor, considerably reduce the temperature of epitaxy, improve the morphological and structural parameters of ZnO layers, and form a *n*-ZnO:Ga/*p*-GaN:Mg/α-Al_2O_3 heterojunction.

Zinc oxide (ZnO) and gallium nitride (GaN) are materials with a wurtzite structure; the lattice parameters (and other physical properties) of ZnO and GaN are similar to each other (see, for example [1]). At the same time, ZnO has a number of important advantages, such as the intense excitonic luminescence at high temperatures [2] caused by a high binding energy for excitons (~61 meV) and the resistance to high-energy radiation [3], which is a requirement for materials intended for use under extreme conditions.

One of the generally recognized methods for obtaining ZnO epitaxial layers is chemical vapor deposition (CVD) in various modifications. The common disadvantage of this method consists in the relatively high temperature in the substrate region (580–680°C), which stimulates unwanted reactions and, as a consequence, the appearance of an uncontrolled impurity in the composition of the epitaxial layer. It is well known that a deficit of oxygen in ZnO gives rise to intrinsic defects of the donor type (interstitial zinc atoms and oxygen vacancies). It is also known that the use of oxygen radicals (atoms) makes it possible to provide the highest attainable effective pressure of oxygen above the growing film (i.e., to increase this pressure by more than six orders of magnitude; see, for example, [4]) and shift the relation between elements in the direction of an excess of oxygen, thus reducing the concentration of intrinsic defects. Previously, this approach was used in practice only in the procedures of annealing of single crystals and epitaxial layers of oxides in order to attain a stoichiometric composition [5].

In this paper, we report for the first time on the development of a low-temperature variant of CVD, the deposition of a ZnO epitaxial layer stimulated by a radio-frequency (RF) plasma discharge, and the formation of an *n*-ZnO:Ga/*p*-GaN:Mg/α-Al_2O_3 heterojunction.

A flow-through low-pressure (FTLP) reactor described previously [6] was modified by using an RF discharge along the axis of the quartz reactor; the discharge encompassed both temperature zones (that of the source and that of the substrate; see Fig. 1). The characteristic operating pressure of H_2 in the reactor was no higher than 1 Torr, and the flux rate of reactants was 1–3 m s^{-1}. It is worth noting that activation of reactants in an RF-discharge plasma made it possible to significantly decrease the temperature of epitaxial growth in the ZnO/α-Al_2O_3 system (by at least 200°C). As a result, the lowest limit of the growth temperature for the epitaxial layer was $T \approx 420$°C (Fig. 1b, curve *2*) and the growth rate v was decreased by about a factor of 4 (Fig. 1b), which was important for controlled nucleation and growth of ZnO layers, especially in the initial stage of epitaxy. We managed to obtain very good morphological characteristics, structural parameters, and electrical characteristics by both decreasing the transition-layer thickness and reducing the content of uncontrollable impurities.

Investigation of the surface morphology of the $(11\bar{2}0)$ZnO/$(10\bar{1}2)Al_2O_3$ layers using a LEICA DM LP microscope with a magnification of 600 showed that epitaxial layers grown under conditions where the growth process was activated by the RF discharge featured a less developed surface (the sizes of the growth patterns differed by more than an order of magnitude). It is also noteworthy that there is a substantial decrease in the size and number of zinc clusters that delineate the

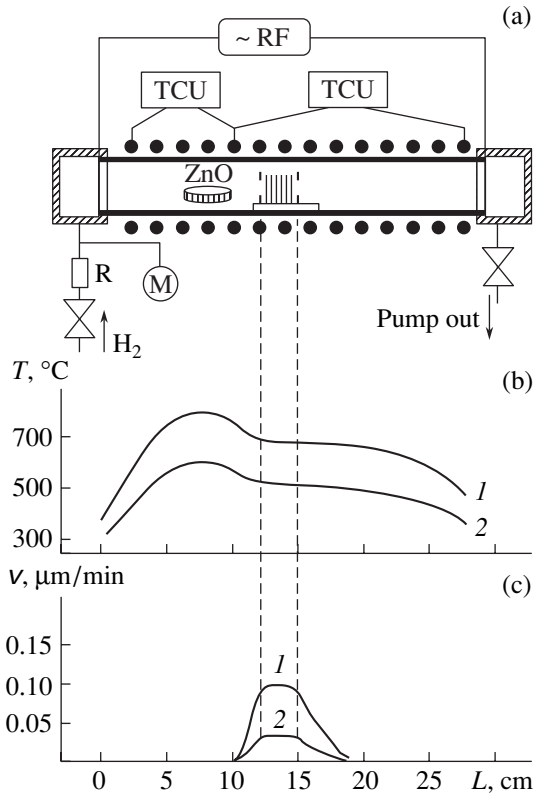

Fig. 1. Schematic representation of a modified CVD system in which an RF discharge is used: (a) a quartz reactor, (b) the distribution of temperature T over the reactor length L, and (c) the distribution of the growth rate v of layers in the deposition zone. Curve *1* is obtained for thermal growth, and curve *2* corresponds to the case of growth with an RF discharge. TCU is the temperature-control unit; M, the manometer; R, the regulator of the gas-flow rate; and RF, the RF oscillator.

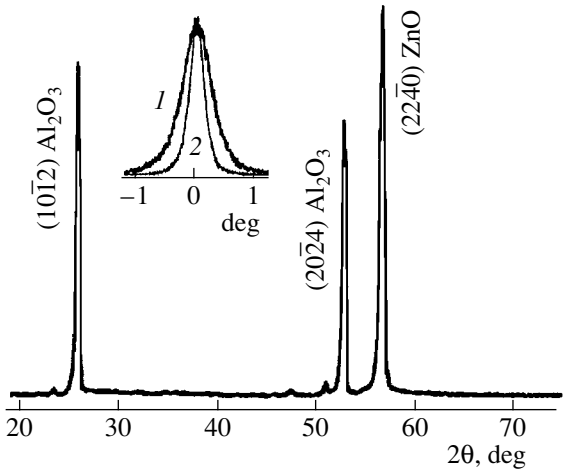

Fig. 2. Diffraction pattern of a $(11\bar{2}0)$ZnO/$(10\bar{1}2)Al_2O_3$ structure formed by growing the ZnO layer with growth activation using an RF discharge. The rocking curves about the $(22\bar{4}0)$ peak for a ZnO layer obtained (*1*) by thermal growth and (*2*) with activation using an RF discharge are shown in the inset.

growth patterns on the epitaxial-layer surface in the case of a typical thermal growth; as a result, a more smooth and specular surface is formed.

In Fig. 2 we show the results of the X-ray diffraction studies of ZnO layers; a DRON-2 diffractometer and CuK_α radiation were used. The diffraction pattern corresponds to a $(11\bar{2}0)$ZnO/$(10\bar{1}2)Al_2O_3$ epitaxial layer of a high structural quality. The inset shows the rocking curves about the $(22\bar{4}0)$ peak for a layer obtained by purely thermal deposition (curve *1*) and for a layer obtained with the growth process activated using an RF discharge (curve *2*). In the second case, one can see an almost twofold decrease in the peak width, which is no larger than 0.4° under optimal conditions. It is also established that the width of the peak related to ZnO can be less than 0.25° if the technology used for growing the thin (~15 nm) buffer ZnO layers is magnetron sputtering (including the autoepitaxy mechanism) and the method under consideration.

Although growth of ZnO epitaxial layers on thin GaN layers has been described in a number of publications, *n*-GaN buffer layers were invariably used taking into account that the lattice constants of ZnO and GaN are nearly the same. As far as we know, there have been no reports on the formation of an *n*-ZnO/*p*-GaN heterojunction. In our experiments, we used *p*-GaN:Mg layers as *p*-type substrates; these layers had a thickness of ~1 μm and were grown by molecular-beam epitaxy on α-Al_2O_3 (0001) substrates. For comparison, we grew *n*-ZnO/*n*-GaN structures under the same conditions in order to form an *n*–*n* heterojunction. After deposition, a part of the ZnO:Ga layer was etched off in a 10% HNO_3 solution and ohmic contacts of In and Au were formed on the ZnO:Ga and GaN:Mg surfaces, respectively. The concentration and mobility of holes in the GaN:Mg layers were measured by the four-point probe method and were found to be equal to 3×10^{17} cm^{-3} and 10 cm^2/(V s), respectively. The concentration and mobility of electrons in the ~2-μm-thick ZnO:Ga layers obtained in the FTLP reactor were found to be equal to 5×10^{18} cm^{-3} and 40 cm^2/(V s). In Fig. 3, we show the current–voltage (*I*–*V*) characteristic of an *n*-ZnO/*p*-GaN heterojunction. It can be seen that the heterojunction features a nonlinear *I*–*V* characteristic and is rectifying, whereas the *I*–*V* characteristic of an *n*-ZnO/*n*-GaN heterojunction is linear.

We studied the spectral distribution of the electroluminescence (EL) intensity observed in a structure with applied forward bias. The EL spectrum recorded at a forward current of 3 mA and at a temperature of 300 K (Fig. 4) consists of a broad emission band with a peak at 430 nm (2.88 eV) and full width at a half-maximum of 0.21 eV. As can be seen from Fig. 4, the peak at 430 nm located in the violet spectral region has a wing

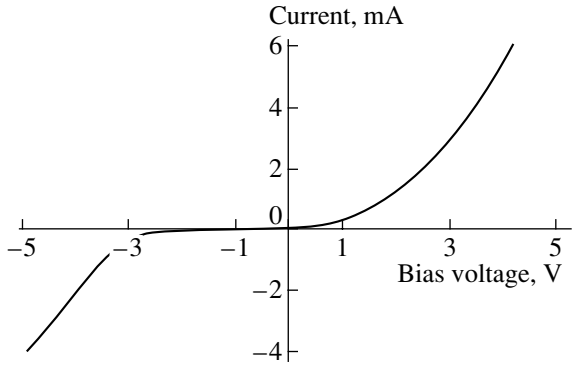

Fig. 3. Current–voltage characteristic of an *n*-ZnO:Ga/*p*-GaN:Mg heterostructure formed on α-Al_2O_3.

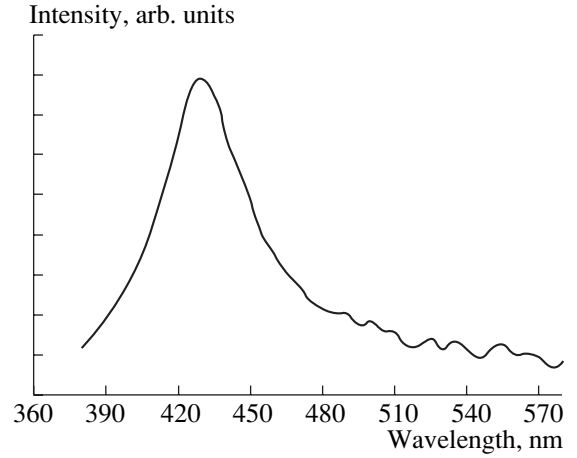

Fig. 4. Electroluminescence spectrum of an *n*-ZnO:Ga/*p*-GaN:Mg heterostructure formed on the α-Al_2O_3 substrate.

that extends to longer wavelengths. Our data are consistent with the results of previous studies that indicate that the band at 430 nm appears when charge carriers are injected into the *p*-type region of GaN:Mg from the *n*-type region [7, 8]. A comparison of the spectra of EL with those of cathodoluminescence of the ZnO and GaN layers also shows that the heterojunction properties are mainly controlled by the injection of electrons from *n*-ZnO into *p*-GaN if the EL and cathodoluminescence spectra are obtained at approximately equal concentration of excess charge carriers. Thus, the injection properties of the *n*-ZnO/*p*-GaN heterostructure are governed mainly by the injection of electrons from *n*-ZnO into *p*-GaN, where the recombination occurs. The probability of realizing this mechanism increases if the donor concentration in ZnO:Ga exceeds the acceptor concentration in GaN:Mg (in the case under consideration, the donor concentration is higher than the acceptor concentration by nearly an order of magnitude). The absence of short-wavelength excitonic emission in the EL spectra may also be related to the effect of self-absorption at 300 K.

It is especially noteworthy that another feature of modified CVD using an FTLP reactor and activation of growth by an RF discharge is the possibility of attaining doping and impurity-activation levels (including acceptor-type impurities) that are unattainable with the usual versions of CVD. Our preliminary experiments on the activation of the processes of formation and doping in an atmosphere of H_2 and N_2 with simultaneous doping with both donor and acceptor impurities (ZnO:Ga in an atmosphere of $H_2 : N_2 = 2 : 1$) showed that it is in principle possible to obtain *p*-ZnO epitaxial layers with a resistivity of $\sim 10^4\ \Omega$ cm. Apparently, *p*-ZnO epitaxial layers with a higher conductivity are also obtainable, and this is our next task.

Thus, we showed that it is possible to obtain high-quality ZnO layers by chemical vapor deposition in a flow-through low-pressure reactor using an RF-discharge plasma. The activation of reactants during growth made it possible to significantly increase the effective pressure of atomic oxygen above the growing layer, considerably reduce (by $\geq 200^\circ$C) the temperature of epitaxy, and improve the morphological surface characteristics and the structure of ZnO epitaxial layers. Using the aforementioned method, we formed *n*-ZnO:Ga/*p*-GaN:Mg/α-Al_2O_3 heteroepitaxial structures and studied the main electrical and emissive characteristics of these structures.

This study was supported by the Russian Foundation for Basic Research, project nos. 01-02-16200 and 02-02-17627.

REFERENCES

1. B. M. Ataev, I. K. Kamilov, V. V. Lundin, *et al.*, Pis'ma Zh. Tekh. Fiz. **27** (2), 30 (2001) [Tech. Phys. Lett. **27**, 55 (2001)].
2. A. Kh. Abduev, A. D. Adukov, and B. M. Ataev, Opt. Spektrosk. **50**, 1137 (1981) [Opt. Spectrosc. **50**, 626 (1981)].
3. D. C. Look, D. C. Reynolds, and J. W. Hemsky, Appl. Phys. Lett. **75**, 811 (1999).
4. A. N. Georgobiani, A. N. Gruzintsev, V. T. Volkov, and M. O. Vorob'ev, Fiz. Tekh. Poluprovodn. (St. Petersburg) **36**, 284 (2002) [Semiconductors **36**, 265 (2002)].
5. A. N. Georgobiani and M. V. Kotlyarevskiĭ, Neorg. Mater. **33**, 185 (1997).
6. A. Kh. Abduev, B. M. Ataev, and A. M. Bagamadova, Neorg. Mater. **23**, 1928 (1987).
7. S. Nakamura, S. Mukai, and M. Senon, Jpn. J. Appl. Phys., Part 2 **30**, L1998 (1991).
8. J. Molnar, R. Singh, and T. D. Moustakas, Appl. Phys. Lett. **66**, 268 (1995).

Translated by A. Spitsyn

Semiconductors, Vol. 38, No. 6, 2004, pp. 675–677. Translated from Fizika i Tekhnika Poluprovodnikov, Vol. 38, No. 6, 2004, pp. 702–704.

SEMICONDUCTOR STRUCTURES, INTERFACES, AND SURFACES

High-Frequency Barrier Capacitance of Metal–Semiconductor Contacts and Abrupt *p–n* Junctions

V. I. Murygin

Moscow State Institute of Electronic Engineering (Technical University), Zelenograd, Moscow oblast, 124498 Russia
e-mail: gpd@gf.miee.ru

Submitted November 4, 2003; accepted for publication November 10, 2003

Abstract—High-frequency capacitance of a Schottky barrier and an abrupt *p–n* junction are calculated taking into account the free charge carrier concentration in the space-charge region of a semiconductor with shallow and deep impurity levels. The expressions obtained are compared with the published results of the calculations of the high-frequency capacitance of a *p–n* junction and with experimental data. *© 2004 MAIK "Nauka/Interperiodica".*

1. INTRODUCTION

Until now, the high-frequency capacitance of a *p–n* junction has been calculated taking into account free electrons in the space-charge region for the case in which the band gap of an *n*-type semiconductor contains one shallow and one deep donor levels [1]. High-frequency capacitance of a fused diode based on a semiconductor with both shallow and deep donor and acceptor levels has been derived in [2, 3] disregarding free charge carriers in the space-charge region (SCR).

2. CALCULATIONS OF HIGH-FREQUENCY CAPACITANCE

We calculate the high-frequency barrier capacitance of a metal–semiconductor contact and that of an abrupt *p–n* junction for a semiconductor with various impurity levels by using the relation

$$C = \frac{dQ}{d\varphi}, \tag{1}$$

where Q is the space charge in the barrier and φ is the potential.

First we consider the case where there is only one shallow donor level in an *n*-type semiconductor of the metal–semiconductor contact or of the abrupt p^+–*n* junction. Let the blocking voltage applied to the diode structure be

$$V = V_0 + V'e^{-i\omega t}, \tag{2}$$

where V_0 is a constant bias and $V'e^{-i\omega t}$ is a small alternating voltage of frequency ω. In this case, the high-frequency capacitance can be calculated for frequencies satisfying the condition $\omega\tau_M \gg 1$, where τ_M is the Maxwell relaxation time. If the x axis is directed normally to the metal–semiconductor interface or to the plane of the *p–n* junction, then for a small ac voltage dV', the maximum increase in space charge at the limiting frequency is given by

$$dQ = e(n_0 - n)Sdx, \tag{3}$$

where e is the elementary charge; n and n_0 are the nonequilibrium and equilibrium free electron concentrations, respectively; and S is the area of the metal–semiconductor contact or of the *p–n* junction.

It is known that

$$n = n_0 \exp\left(-\frac{e\varphi}{kT}\right), \tag{4}$$

where k is the Boltzmann constant and T is temperature.

At the limiting frequency, the difference between n and n_0 is small, i.e., $e\varphi/kT \ll 1$. As a result, we have

$$n = n_0\left(1 - \frac{e\varphi}{kT}\right). \tag{5}$$

Substituting (5) into (3), we obtain

$$dQ = n_0\frac{e^2\varphi}{kT}Sdx. \tag{6}$$

The quantity $d\varphi$ is determined from the Poisson equation

$$\frac{d^2\varphi}{dx^2} = \frac{e(n - n_0)}{\varepsilon_0\varepsilon}, \tag{7}$$

where ε_0 is the permittivity of free space and ε is the relative permittivity of the material. Using (5), we can write the Poisson equation in the form

$$\frac{d^2\varphi}{dx^2} = -\frac{n_0}{\varepsilon_0\varepsilon}\frac{e^2\varphi}{kT}. \tag{8}$$

Equation (8) can be transformed as follows:

$$d\varphi\frac{d^2\varphi}{dx^2} = \frac{1}{2}d\left(\frac{d\varphi}{dx}\right)^2 = -\frac{n_0e^2}{\varepsilon_0\varepsilon kT}\varphi d\varphi. \quad (9)$$

We measure the potential from its value at the interface between the SCR and the base and assume that the potential increases in the negative direction of the x axis; therefore, after integrating Eq. (9), we obtain

$$\left(\frac{d\varphi}{dx}\right)^2 = -\frac{n_0e^2}{\varepsilon_0\varepsilon kT}\varphi^2\Big|_{\varphi}^{0} = \frac{n_0e^2}{\varepsilon_0\varepsilon kT}\varphi^2. \quad (10)$$

It follows that

$$d\varphi = \sqrt{\frac{n_0e^2}{\varepsilon_0\varepsilon kT}}\varphi dx. \quad (11)$$

Finally, using (1), (6), and (11), we obtain

$$C = S\sqrt{\frac{\varepsilon_0\varepsilon e^2n_0}{kT}}. \quad (12)$$

It interesting to note that the Debye screening length for a dc electric field is

$$L_D = \sqrt{\frac{\varepsilon_0\varepsilon kT}{e^2n_0}} \quad (13)$$

and the high-frequency capacitance in the case considered is given by the expression

$$C = \frac{\varepsilon_0\varepsilon S}{L_D}. \quad (14)$$

Below, we consider structures with a deep impurity level in the band gap of an n-type semiconductor. In this case the relaxation time is determined by the time required to reach the steady-state filling of this level.

If, in addition to a shallow donor level with concentration N_d, there is a deep donor level with concentration N, then the space-charge density is $\rho = e(N_d + N^+ - n) = e(n_0 - n)$ and the high-frequency capacitance is

$$C = S\sqrt{\frac{\varepsilon_0\varepsilon e^2(N_d + N^+)}{kT}}. \quad (15)$$

Now let the band gap of the semiconductor in the diode structures under consideration contain a deep acceptor level with concentration N in the upper half of the band gap, in addition to a shallow donor level with concentration N_d. We disregard electron transitions between the acceptor level and the valence band. Then the kinetics of the variation of charge on the acceptor level in the SCR obeys the equation

$$\frac{\partial N^-}{\partial t} = \gamma_n n N^0 - \alpha_n N^-. \quad (16)$$

Here, γ_n is the recombination coefficient for electron transitions to the acceptor level; α_n is the probability of electron generation from the acceptor level; and N^0 and N^- are the nonequilibrium concentrations of neutral impurity atoms and ions, respectively. According to the principle of detailed balance, we have

$$\alpha_n = \gamma_n n_0\frac{N_a^0}{N_a^-}, \quad (17)$$

where N_a^0 and N_a^- are the equilibrium concentrations of neutral impurity atoms and ions. Then, for a steady state, we can use Eq. (16) and formula (17) to obtain

$$nN^0 - N^-n_0\frac{N_a^0}{N_a^-} = 0. \quad (18)$$

Since $N = N^0 + N^-$, we have from Eq. (18)

$$N^- = \frac{NnN_a^-}{nN_a^- + n_0N_a^0}. \quad (19)$$

The space-charge density is

$$\rho = e(-n + N_d + N^-) = eN'. \quad (20)$$

Since $N_d = N_a^- + n_0$ and $N = N_a^0 + N_a^-$, we obtain from (19) and (20)

$$\begin{aligned} N' &= n_0 - n + \frac{(n_0 - n)N_a^-N_a^0}{nN_a^- + n_0N_a^0} \\ &\approx (n_0 - n)\left(1 + \frac{N_a^-N_a^0}{n_0N_a^- + n_0N_a^0}\right). \end{aligned} \quad (21)$$

It should be noted that expression (21) is valid for any relations between the concentrations of donors and acceptors. However, for $N_d < N$ we have to replace N_a^0 by the difference $N_d - N_a^- = n_0$, since the electrons can be excited to the conduction band from the level of ionized acceptors, whose concentration N_a^- cannot exceed N_d; i.e., $N_a^0 = n_0$. For $N_d > N$, the concentration n_0 becomes higher than the concentration N_a^0.

Now let us use expression (5) again; as a result, we obtain

$$N' = \frac{e\varphi}{kT}\left(n_0 + \frac{N_a^-N_a^0}{N_a^- + N_a^0}\right). \quad (22)$$

In this case the increase in charge is given by

$$dQ = eN'Sdx = \frac{e^2\varphi}{kT}\left(n_0 + \frac{N_a^- N_a^0}{N_a^- + N_a^0}\right)Sdx = \frac{e^2\varphi}{kT}n'Sdx. \quad (23)$$

By analogy with the above calculations, we use the Poisson equation to obtain

$$d\varphi = \sqrt{\frac{n'e^2}{\varepsilon_0\varepsilon kT}}\varphi dx. \quad (24)$$

Then the expression for the capacitance assumes the form

$$C = S\sqrt{\frac{\varepsilon_0\varepsilon e^2 n'}{kT}}, \quad (25)$$

$$n' = n_0 + \frac{N_a^- N_a^0}{N_a^- + N_a^0}. \quad (26)$$

Finally, we consider the case where a deep donor level with concentration N and an acceptor level with concentration N_a are present in the lower half of the band gap of the n-type semiconductor in the metal–semiconductor contact or in the abrupt p^+–n junction. We write the kinetics equation for the donor level in the form

$$\frac{\partial N^+}{\partial t} = -\gamma_n n N^+ + \alpha_n N^0. \quad (27)$$

Here, γ_n is the recombination coefficient for electron transitions to the donor level, and α_n is the probability of electron generation from the donor level. After calculations similar to those described above, we obtain expression (25), where n' is replaced by

$$n'' = n_0 + \frac{N_d^0 N_d^+}{N_d^0 + N_d^+}. \quad (28)$$

Again, we have

$$C = \frac{\varepsilon_0\varepsilon S}{L_D}, \quad (29)$$

where L_D is the Debye screening length,

$$L_D = \sqrt{\frac{\varepsilon_0\varepsilon kT}{e^2 n''}}. \quad (30)$$

Similarly, for a metal–semiconductor contact or an abrupt n^+–p junction where there is a deep acceptor level and a donor level in the p-type semiconductor, we obtain formulas (29) and (30) with n'' replaced by

$$n''' = p_0 + \frac{N_a^- N_a^0}{N_a^- + N_a^0}. \quad (31)$$

For compensated semiconductors with deep impurity levels, we derived expressions (28), (30), and (31) for the Debye screening lengths in [3, 4]. Formulas (26) and (31) differ only in their first terms. Therefore, it is obvious that expression (26) can also define the Debye length for an n-type semiconductor with an acceptor level lying in the upper half of the band gap.

3. CONCLUSION

Thus, for all the cases considered, the high-frequency barrier capacitance of a metal–semiconductor contact, an abrupt p^+–n junction, or an abrupt n^+–p junction does not depend on the magnitude of the applied reverse voltage, and the width of the space-charge region is equal to the Debye screening length.

The high-frequency capacitance obtained in [1] did not depend on the magnitude of the reverse voltage for $N_d > N^+$ either, and the corresponding expression was rather complicated. However, for $N_d < N^+$, the expression for the capacitance became

$$C = S\sqrt{\frac{\varepsilon_0\varepsilon e^2 N^+}{4kT}}; \quad (32)$$

i.e., it practically coincided with formula (15); only its magnitude was smaller by a factor of 2. This formula was obtained under more severe restrictions compared to (15); specifically, it is valid for $e\varphi/4kT \ll 1$.

In [5] the impedance of silicon-doped gallium arsenide p–n junctions was studied. The p-type region contained two acceptor levels with ionization energies of 0.03 and 0.1 eV. At high frequencies, a strong temperature dependence of the capacitance was observed (in the temperature range 77–293 K, the capacitance increased by an order of magnitude), and at 77 K the magnitude of the capacitance was bias-independent in the range of applied voltages under consideration (from 0 to 8 V). These experimental data completely agree with the results of our calculations.

REFERENCES

1. V. I. Perel' and A. L. Éfros, Fiz. Tekh. Poluprovodn. (Leningrad) **1**, 1693 (1967) [Sov. Phys. Semicond. **1**, 1403 (1967)].
2. L. S. Berman, Fiz. Tekh. Poluprovodn. (Leningrad) **3**, 1878 (1969) [Sov. Phys. Semicond. **3**, 1590 (1970)].
3. L. S. Berman, Fiz. Tekh. Poluprovodn. (Leningrad) **4**, 1511 (1970) [Sov. Phys. Semicond. **4**, 1295 (1970)].
4. V. K. Grigor'ev, O. I. Kazantsev, V. I. Murygin, *et al.*, Fiz. Tekh. Poluprovodn. (Leningrad) **3**, 1861 (1969) [Sov. Phys. Semicond. **3**, 1576 (1970)].
5. V. I. Murygin and V. B. Gundyrev, Izv. Vyssh. Uchebn. Zaved., Élektron., No. 3 (2000).

Translated by I. Zvyagin

Semiconductors, Vol. 38, No. 6, 2004, pp. 678–682. Translated from Fizika i Tekhnika Poluprovodnikov, Vol. 38, No. 6, 2004, pp. 705–709.

SEMICONDUCTOR STRUCTURES, INTERFACES, AND SURFACES

Growth of AlGaN Epitaxial Layers and AlGaN/GaN Superlattices by Metal-Organic Chemical Vapor Deposition

W. V. Lundin*, A. V. Sakharov, A. F. Tsatsul'nikov, E. E. Zavarin, A. I. Besyul'kin, A. V. Fomin, and D. S. Sizov

Ioffe Physicotechnical Institute, Russian Academy of Sciences, Politekhnicheskaya ul. 26, St. Petersburg, 194021 Russia
**e-mail: lundin.vpegroup@mail.ioffe.ru*

Submitted November 27, 2003; accepted for publication December 3, 2003

Abstract—Special features of metal-organic chemical vapor deposition of AlGaN epitaxial layers and AlGaN/GaN superlattices either in an Epiquip VP-50 RP research and development reactor (for a single wafer 2 in. in diameter) or in an AIX2000HT production-scale reactor (for up to six wafers 2 in. in diameter) are studied. It is found that the dependence of the aluminum content in the solid phase on the trimethylaluminum (TMA) flux in a reactor levels off; this effect hinders the growth of the layers with a high aluminum content in both types of reactors and is more pronounced in the larger reactor (AIX2000HT). Presumably, this effect is a consequence of spurious reactions in the vapor phase and depends on the partial pressure of TMA in the reactor. The aluminum content in the layers can be increased not only by reducing the total pressure in the reactor but also by increasing the total gas flow through the reactor and reducing the trimethylgallium flux. The approaches described above were used to grow layers with a mole fraction of AlN as large as 20% in the AIX2000HT production-scale reactor at a pressure of 400 mbar (this fraction was as large as 40% at 200 mbar). AlGaN layers with the entire range of composition were grown in the Epiquip VP-50 RP reactor. *© 2004 MAIK "Nauka/Interperiodica".*

1. INTRODUCTION

AlGaN and AlGaN/GaN heterostructures have been actively studied in recent years in relation to the possibility of fabricating various electronic and optoelectronic devices based on these heterostructures. The built-in piezoelectric and pyroelectric fields, the low efficiency of doping, and the complex process of stress relaxation in these structures at present hinder the complete realization of the entire potential of the material system under consideration and require additional studies. At the same time, the development of modes of epitaxial growth of individual layers and heterostructures based on AlGaN is of primary importance in this development.

Although the growth of AlGaN layers with a low aluminum content is a well-developed procedure, an increase in the aluminum content (especially, when the layers are grown in large-sized reactors) involves serious difficulties.

2. EXPERIMENTAL

We studied the special features of epitaxial growth of AlGaN layers and AlGaN/GaN superlattices by metal-organic chemical vapor deposition (MOCVD). Initially, we used an Epiquip VP-50 RP reactor modernized for the growth of III–N compounds; in the second stage of our studies, we used an AIX2000HT production-scale reactor in some of the experiments. The layers and superlattices were grown on sapphire substrates with (0001) orientation. Ammonia (NH_3), trimethylgallium (TMG), and trimethylaluminum (TMA) were used as the sources; hydrogen was used as the carrier gas. We employed the conventional procedure for GaN epitaxy on sapphire using a low-temperature nucleation layer.

A horizontal quartz reactor with inductive heating of a graphite substrate holder for a single wafer with a diameter of 2 in. is used in the Epiquip VP-50 RP system. Epitaxial AlGaN layers were grown in conditions that were optimal for the growth of GaN in this reactor; i.e., the temperature was 1050–1070°C and the pressure was 200 mbar. Because the substrates were not rotated, we could not attain an acceptable uniformity of the layers at higher pressures. In a number of experiments, a decrease in the pressure in the reactor did not lead to a variation in the aluminum content in the layers.

A planetary reactor for six substrates with a diameter of 2 in. in the AIX2000HT system features gas flows directed horizontally from the center to the perimeter and is very similar to the horizontal Epiquip reactor. However, individual rotation of the substrates, separate introduction of the Group III and V elements, and the possibility of controllably reducing the temperature of the reactor's quartz ceiling [1] makes it possible to carry out epitaxial processes in a wide range of pressures and gas flows without significant deterioration in the uniformity of the structure. In turn, the possibility of varying the pressure and gas flows in the reactor facilitates appreciably the optimization of the conditions of epitaxial growth.

1063-7826/04/3806-0678$26.00 © 2004 MAIK "Nauka/Interperiodica"

Epitaxial AlGaN layers were grown at temperatures of 1050–1180°C in the AIX2000HT reactor. It is noteworthy that the growth temperature is measured in the Epiquip and AIXX2000HT reactors by fundamentally different methods; therefore, a direct comparison of these temperatures is incorrect since the measured temperature is not equal to the substrate temperature. In order to ensure that the substrate temperatures are identical, the nominal temperature in the AIX2000HT reactor should be higher than that in the Epiquip reactor. For example, the optimal growth temperature of undoped GaN, which makes it possible to grow epitaxial layers with nearly identical properties, is equal to 1050–1070°C for an Epiquip VP-50 RP reactor and to 1150–1180°C for an AIX2000HT reactor.

The composition of AlGaN epitaxial layers was determined from an analysis of photoluminescence spectra (for layers with an AlN content lower than 15%) and Raman spectra [2], as well as from the results of X-ray diffractometry.

3. GROWTH OF ALGAN EPITAXIAL LAYERS IN AN EPIQUIP RESEARCH AND DEVELOPMENT REACTOR

In Fig. 1, we show the dependence of Al content in AlGaN epitaxial layers (X_s is the mole fraction of AlN) on the ratio between the molar fluxes X_v = TMA/(TMA + TMG) at the entry to the reactor. The saturation of aluminum incorporation into the epitaxial layers occurred at a relatively low level of Al content at a growth rate of 2–2.5 μm/h (the optimal growth rate of GaN in this reactor) [3]. This effect was especially pronounced for thin AlGaN layers grown on thick buffer GaN layers. If the growth rate is lowered (by reducing the TMG flux), the efficiency of aluminum incorporation increases significantly.

Thus, it is necessary to reduce the growth rate in order to grow AlGaN layers with a high AlN content. At the same time, it is difficult to grow AlGaN/GaN heterostructures (in particular, superlattices) at a constant low growth rate because a low growth rate of GaN layers leads to the formation of a nonplanar surface. Epitaxial growth of AlGaN/GaN superlattices, in which case the AlGaN layers are grown at a much lower rate than the GaN layers, was carried out using two sources of trimethylgallium (TMG-1 and TMG-2). The flux from the TMG-1 source was continuously introduced into the reactor, whereas the fluxes from the TMG-1 and TMA sources were introduced out of phase [4]. Using this approach, we managed to grow AlGaN/GaN superlattices with an Al content in the barriers from 20 to 50%.

The results of additional experiments showed that, if AlN or AlGaN epitaxial layers are grown with an Al content higher than 50–60%, it is necessary to decrease the ammonia flux and increase the flow of the main carrier gas in addition to reducing the growth rate. Thus, in the case of growing AlN/GaN heterostructures, it is necessary to vary rapidly large gas flows through the reactor, which gives rise to difficulties in ensuring the balance of pressures in the system.

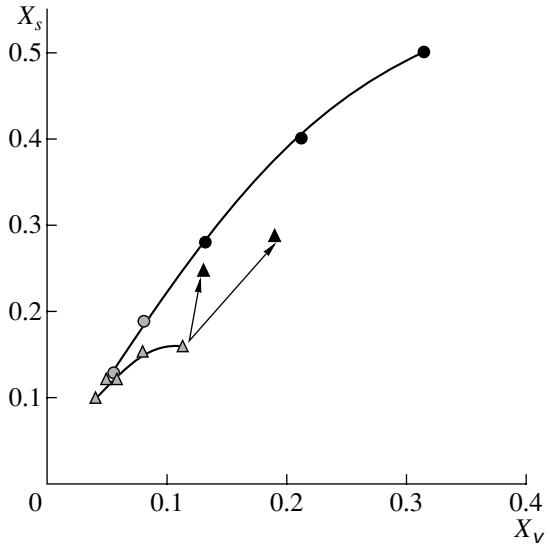

Fig. 1. Dependences of the Al content in an AlGaN epitaxial layer (X_s is the mole fraction of AlN) on the ratio between the molar fluxes X_v = TMA/(TMA + TMG) in the reactor (data for an Epiquip system). Open circles and triangles represent data obtained at a high growth rate of AlGaN, and closed circles and triangles represent data obtained at a low growth rate of AlGaN. Triangles correspond to thin AlGaN layers on buffer GaN layers; circles correspond to thick AlGaN layers and superlattices. Arrows indicate a change in the composition of the AlGaN layer as a result of a decrease in the TMG flux (the other fluxes in the reactor remained unchanged).

In spite of these problems, we used the above approach and considerations on the basis of the Epiquip system to grow multilayer AlN/GaN heterostructures and AlGaN epitaxial layers in the entire range of compositions [5]; these layers and heterostructures were then used to fabricate a number of semiconductor devices [6, 7].

4. GROWTH OF ALGAN EPITAXIAL LAYERS IN AN AIX2000HT PRODUCTION-SCALE REACTOR

We studied specific features of epitaxial growth of AlGaN in an AIX2000HT system in the context of the development of epitaxial technologies for semiconductor devices (primarily, for light-emitting diodes). We used the approaches developed for an Epiquip research and development reactor to realize the additional potential of an AIX2000HT reactor designed specifically for the growth of complex device heterostructures based on III–N compounds. The basic similarity of the reactors in the Epiquip and AIX2000HT systems gave us reason to believe that we would tackle the task set successfully.

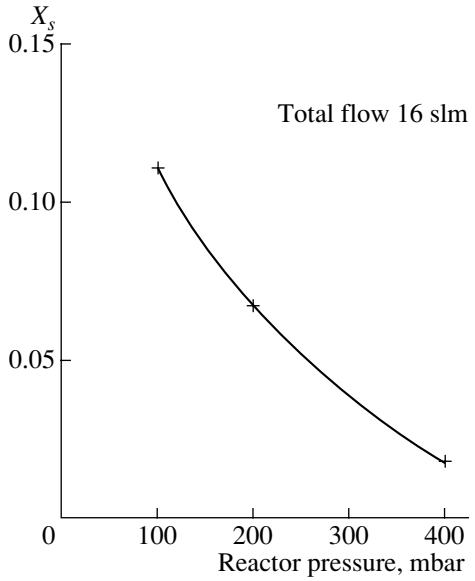

Fig. 2. Dependence of the Al content in the AlGaN epitaxial layer (X_s) on the pressure in the reactor with a total gas flow through the reactor equal to 16 slm (data for an AIX2000HT system).

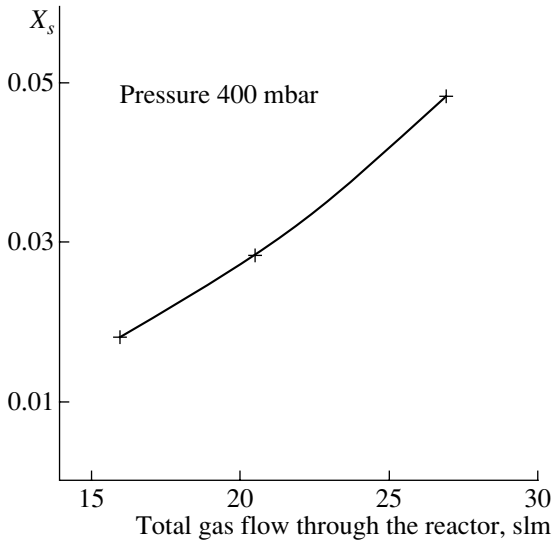

Fig. 3. Dependence of the Al content in the AlGaN epitaxial layer (X_s) on the total gas flow through the reactor at a pressure in the reactor equal to 400 mbar (data for an AIX2000HT system).

However, experiments showed that an increased size of the reactor gives rise to additional problems.

In Fig. 2, we show the dependence of Al content in AlGaN epitaxial layers on the pressure in an AIX2000HT reactor. The conditions in the reactor were nearly optimal for the growth of *p*-GaN: the temperature was 1050°C, the total gas flow through the reactor was equal to 16 standard liters per minute (slm), and the growth rate was 0.5–0.6 μm/h. The observed dramatic decrease in the aluminum content in epitaxial layers with increasing pressure in the reactor was predicted by the manufacturer of the system; this effect is well known and is related to spurious reactions between NH_3 and TMA in a reactor that is larger than an Epiquip.

Thus, a decrease in the pressure in the reactor can be considered as the simplest method for obtaining the AlGaN layers. However, the pressure in a reactor is one of the key parameters and controls both the special features of epitaxial growth and the properties of the layers grown. Moreover, a rapid change in pressure in an AIX2000HT reactor is impossible due to a number of specific features in the design. As a result, complex InGaN/GaN/AlGaN heterostructures with a thickness of the layers amounting to tens of nanometers or less have to be grown under a constant pressure; in a number of cases, a relatively high pressure in the reactor (300–400 mbar) is required to grow GaN. Consequently, the development of AlGaN growth modes at higher pressures can lead to a substantial increase in the degree of freedom in the optimization of the technology and design for complex heterostructures.

As the total gas flow through the reactor increases from 16 to 27 slm, the aluminum content in the AlGaN layers grown under a pressure of 400 mbar increases by approximately a factor of 3 (Fig. 3). However, the AlN content attained under these conditions in the layers (~5%) is still too low for the majority of device-oriented applications. It is even more important that, although an increase in the TMA flux at a pressure of 100 mbar in the reactor leads to an almost linear increase in the Al content in AlGaN, such an increase is not observed at a pressure of 400 mbar (Fig. 4).

All in all, the above results make it possible to advance the following hypothesis: the concentration of active aluminum-containing compounds involved in epitaxial growth cannot be increased beyond a certain critical level that is governed by the conditions in the reactor. Since the Al content in AlGaN solid solution cannot be increased by increasing the TMA flux, an obvious solution to the problem (as in the case of an Epiquip reactor) is to reduce the TMG flux. The effect of the TMG flux on the composition of AlGaN solid solutions is illustrated in Fig. 5. The Al content in AlGaN epitaxial layers is inversely proportional to the TMG flux in a wide range of fluxes. A decrease in the TMG flux at a pressure of 400 mbar in the reactor made it possible to grow AlGaN layers with an AlN content as high as 20%, which was adequate for the majority of device-related applications. This approach made it possible to increase the content of AlN in AlGaN to 40% at a pressure of 200 mbar.

Thus, as the reactor size increases, the epitaxial growth of AlGaN layers becomes much more complicated. However, the use of the approach described above made it possible to grow solid-solution layers with the required composition at pressures that were

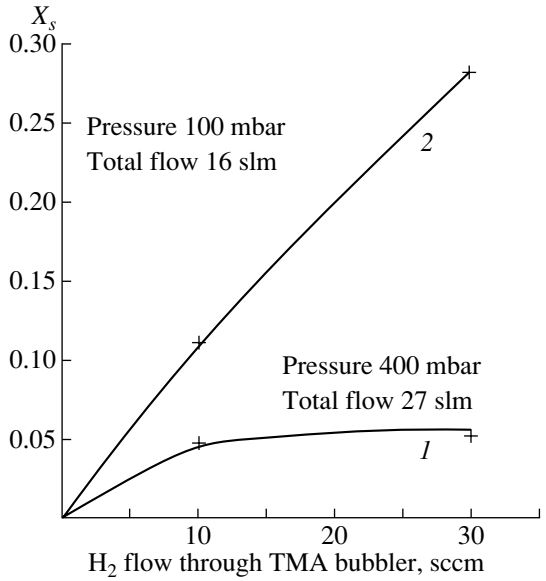

Fig. 4. Dependences of the Al content in an AlGaN epitaxial layer (X_s) on the TMA flow for two different growth conditions: (*1*) a pressure of 400 mbar and a total gas flow through the reactor equal to 27 slm; (*2*) a pressure of 100 mbar and a total gas flow through the reactor equal to 16 slm (data for an AIX2000HT system).

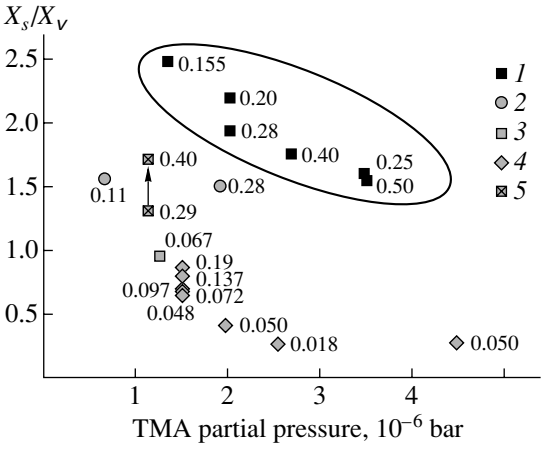

Fig. 6. Dependence of the efficiency of Al incorporation (the ratio between the Al mole fraction X_s in an AlGaN epitaxial layer and the ratio of the molar fluxes X_v = TMA/(TMA + TMG)) on the partial pressure of TMA in the reactor. Numbers by the symbols indicate the Al content X_s in the epitaxial layer: (*1*) data for an Epiquip system at a pressure of 200 mbar; (*2–5*) data for an AIX2000HT system at pressures of (*2*) 100, (*3*) 200, (*4*) 400, and (*5*) 200 mbar at two different temperatures in the reactor (X_s = 0.40 at 1180°C and X_s = 0.29 at 1050°C).

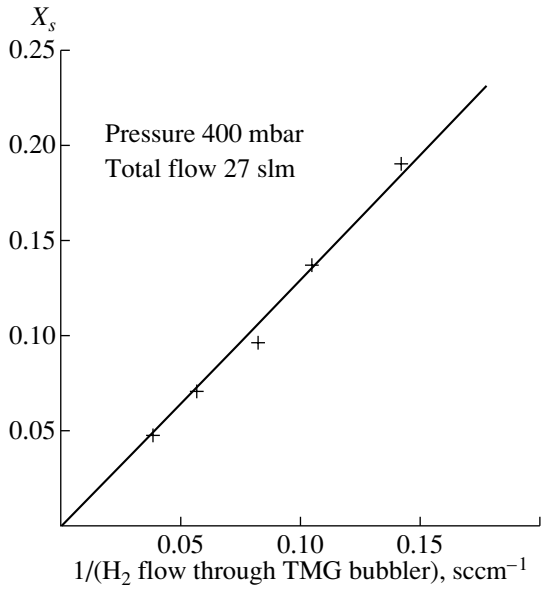

Fig. 5. Dependence of the Al content in the AlGaN epitaxial layer (X_s) on the TMG flux at a pressure of 400 mbar and at a total gas flow through the reactor equal to 27 slm (data for an AIX2000HT system).

higher than the pressures in the research and development reactor. Thus, the pressure in the reactor is found to be the single free parameter in the development of growth modes for complex heterostructures involving AlGaN layers in an AIX2000HT reactor. This parameter makes it possible to additionally optimize the properties of the structures under consideration. As in a research and development reactor, the AlGaN/GaN heterostructures are grown using a single TMA source and two TMG sources.

5. SPECIFIC FEATURES OF ALGAN EPITAXY THAT ARE COMMON TO BOTH THE EPIQUIP VP-50 RP AND AIX2000HT SYSTEMS

Despite the fact that there is a considerable difference between the conditions of AlGaN epitaxial growth in the Epiquip and AIX2000HT systems, the basic similarity of these two reactors makes it possible to consider the processes that govern the composition of the growing solid solution as almost the same. It is reasonable to assume that the observed effects (in particular, the leveling-off of the dependence of the Al content in the epitaxial AlGaN layer on the TMA flux) are related to spurious reactions involving TMA.

In Fig. 6, we show the data obtained as a result of a large number of experiments on the growth of AlGaN layers with a wide range of compositions in both types of reactors. The partial pressure of TMA in the reactor disregarding the exhaustion caused by the chemical reactions (i.e., at the reactor entrance) is plotted on the horizontal axis. The quantity X_s/X_v, defined as the ratio between the AlN mole fraction in the grown AlGaN X_s and the ratio of the molar fluxes X_v = TMA/(TMA + TMG) at the entry to the reactor, is plotted on the vertical axis. This representation makes it possible to qualitatively evaluate the effect of chemical reactions involv-

Characteristic features of AlGaN growth in relation to the partial pressure of trimethylaluminum (TMA)

Technological conditions	A high partial pressure of TMA	A low partial pressure of TMA
If the pressure in the reactor is decreased	The Al content increases	The Al content is not changed
If the temperature in the reactor is decreased	The Al content increases	The Al content decreases
The distribution of the Al content (without rotation of the substrate)	Increases in the direction toward the entry to the reactor	Decreases in the direction toward the entry to the reactor

ing TMA on the result of epitaxial processes in different reactors under widely differing conditions.

An analysis of the results shown in Fig. 6 makes it possible to draw a number of conclusions. The effect of spurious reactions is reduced, first, if the reactor size decreases and, second, if the pressure in the reactor is lowered. However, in addition to the effect of the above parameters, the partial pressure of TMA at the entry to the reactor is important. If this pressure is no higher than $(1–2) \times 10^{-6}$ bar at the entry to the reactor (and, consequently, in any other region of the reactor), the spurious reactions involving TMA do not significantly affect the growth of AlGaN. A drastic decrease in the ratio X_s/X_V as the TMA partial pressure increases indicates that the order of spurious reactions with respect to TMA is high.

Generally, one can recognize two different conditions of AlGaN growth: growth at a high and a low partial pressure of TMA. In the first case, the AlGaN composition is mainly controlled by chemical reactions involving TMA and depends nonlinearly on the TMA flux. In the second case, these reactions are unimportant and the composition of the growing solid-solution layer depends linearly on the TMA flux. Furthermore, the composition is controlled by reevaporation of gallium from the growing layer and by spurious reactions that reduce the content of active gallium compounds in the vapor phase. The characteristic features of the two deposition modes under consideration are listed in the table.

6. CONCLUSION

In this paper, we report the results of studying the special features of growing epitaxial AlGaN layers in an Epiquip VP-50 RP horizontal research and development reactor and in an AIX2000HT production-scale planetary reactor. It is established that the partial pressure of trimethylaluminum at the entry to the reactor is one of the parameters that govern the composition of the growing solid solution. It is shown that an appreciable increase in the Al content in the AlGaN epitaxial layer can be attained by reducing the epitaxial-growth rate.

ACKNOWLEDGMENTS

This study was supported by the “NATO for Peace” program (grant no. SfP-972614) and the Russian Foundation for Basic Research (project nos. 01-02-18011, 03-02-16657, and 01-02-17646).

REFERENCES

1. E. Woelk, G. Strauch, D. Schnitz, and H. Jurgensen, in *Proceedings of 1st International Symposium on Blue Laser and Light Emitting Diodes* (Chiba, Japan, 1996), p. 514.
2. V. Yu. Davydov, A. A. Klochikhin, I. N. Goncharuk, *et al.*, in *Proceedings of International Workshop on Nitride Semiconductors* (IPAP Conf. Ser., 2000), Vol. 1, p. 665.
3. W. V. Lundin, A. V. Sakharov, A. F. Tsatsulnikov, *et al.*, Phys. Status Solidi A **188**, 885 (2001).
4. W. V. Lundin, A. S. Usikov, I. L. Krestnikov, *et al.*, in *Booklet of the 8th EW-MOVPE* (Prague, 1999), p. 49.
5. V. V. Lundin, E. E. Zavarin, A. I. Besyul’kin, *et al.*, in *Abstracts of 2nd All-Russian Conference on Gallium, Indium, and Aluminum Nitrides: Structures and Devices* (St. Petersburg, 2003), p. 93.
6. A. V. Sakharov, W. V. Lundin, A. S. Usikov, *et al.*, MRS Internet J. Nitride Semicond. Res. **3**, 28 (1998).
7. O. E. Tereshchenko, G. É. Shaĭbler, A. S. Yaroshevich, *et al.*, in *Abstracts of VI Russian Conference on the Physics of Semiconductors* (St. Petersburg, 2003), p. 462.

Translated by A. Spitsyn

Semiconductors, Vol. 38, No. 6, 2004, pp. 683–688. Translated from Fizika i Tekhnika Poluprovodnikov, Vol. 38, No. 6, 2004, pp. 710–715.

SEMICONDUCTOR STRUCTURES, INTERFACES, AND SURFACES

Structural Defects at the Semiconductor–Ferroelectric Interface

L. S. Berman and I. E. Titkov

Ioffe Physicotechnical Institute, Russian Academy of Sciences, Politekhnicheskaya ul. 26, St. Petersburg, 194021 Russia

Submitted November 28, 2003; accepted for publication December 3, 2003

Abstract—Structural defects at the interface between $Pb_{0.95}La_{0.05}Ti_{0.8}Zr_{0.2}O_3$ and $La_{1.85}Sr_{0.15}CuO_4$ were studied using the method of isothermal current relaxation. Two cases were considered: (a) the width of the defect-containing layer is much smaller than the width of the space-charge region and (b) the width of the defect-containing layer is greater than the width of the space-charge region. It is shown that, for the samples studied, the width of the defect-containing layer exceeds 50–100 Å, and the density of states for deep-level centers in the energy interval E_v + (0.55–0.65) eV is about 3×10^{20} cm^{-3} eV^{-1}; this value corresponds to a surface state density of about 2×10^{14} cm^{-2} eV^{-1}. It is shown that the density of states for deep-level centers increases from the interface into the depth of the semiconductor. © *2004 MAIK "Nauka/Interperiodica".*

1. INTRODUCTION

In recent years, electronic memory devices based on ferroelectric–semiconductor structures have developed rapidly [1–4]. The quality of these devices substantially depends on the parameters of the ferroelectric–semiconductor interface [4–8]. We studied structural defects at the interface between a *p*-$Pb_{0.95}La_{0.05}Ti_{0.8}Zr_{0.2}O_3$ (PZT) ferroelectric and a *p*-$La_{1.85}Sr_{0.15}CuO_4$ (LSCO) semiconductor.

2. THEORY

We studied a structure consisting of a perovskite PZT ferroelectric (FE) and an LSCO semiconductor. A Schottky barrier (Au) was deposited on the FE. The contact to the semiconductor was ohmic. The formation of a passive (blocking) layer was possible in PZT under the gold layer, and the width of the passive layer d_p was much smaller than that of the PZT layer w_f [9, 10]. If we disregard the voltage drop across the passive layer, we have

$$V + V_{bi} = \psi_s + V_f, \tag{1}$$

where V is the applied voltage, V_{bi} is the built-in voltage between the contact to the FE and the semiconductor, ψ_s is the surface potential of the semiconductor, and V_f is the voltage drop across the FE. At the interface, the following relation is valid:

$$-(Q_{sc} + Q_{ss}) = \varepsilon_0 E_f + P(E_f), \tag{2}$$

where $\varepsilon_0 = 8.85 \times 10^{-12}$ F/m is the permittivity of the free space, E_f is the electric field in the FE, $P(E_f)$ is the polarization of the FE in the field E_f, Q_{sc} is the charge in the space-charge region of the semiconductor, and Q_{ss} is the charge in the surface states.

We consider a general expression for operation over a nonsaturated hysteresis loop (Fig. 1). To this end, we approximate the function $P(E_f)$ using the following expressions:

$$P(E_f) = P_s \tanh\left(\frac{E_f - E_c}{2d}\right) + P_r(1 - a) \tag{3}$$

for the ascending branch, and

$$P(E_f) = -P_s \tanh\left(\frac{-E_f - E_c}{2d}\right) + P_r(1 - a) \tag{4}$$

for the descending branch.

Here, P_s is the saturation polarization, P_r is the residual polarization, E_c is the coercive field, and $0 < a \le 1$. In this approximation, the derivative $\frac{d}{dE_f} P(E_f)$ does not depend on the amplitude of the ac field. For $a = 1$, expressions (3) and (4) transform into the formulas for

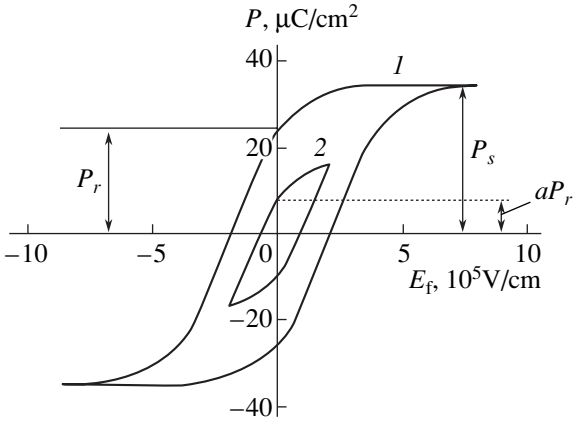

Fig. 1. Hysteresis loops: (*1*) saturated, (*2*) nonsaturated; the parameters of the calculation are P_s = 35 μC/cm^2, P_r = 25 μC/cm^2, $E_c = E_{max} = 2 \times 10^5$ V/cm, and a = 0.34.

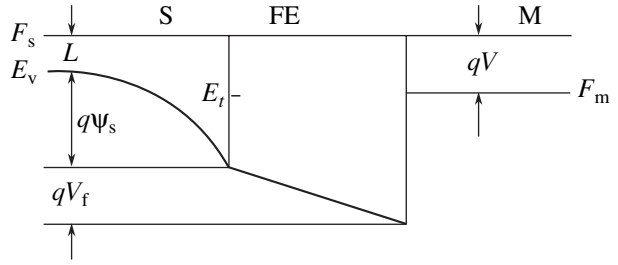

Fig. 2. Energy diagram of the M–PZT–LCO structure; M stands for metal; ψ_s is the surface potential of the semiconductor; V_f is the voltage drop across the ferroelectric; F_s and F_m are the Fermi levels in the semiconductor and the metal, respectively; V is the applied voltage; and q is the elementary charge.

the saturated hysteresis loop [11]. The maximum electric field E_{max} and the parameter a are related by

$$2P_r(1-a) = -P_s\tanh\left(\frac{E_{max}-E_c}{2d}\right) - P_s\tanh\left(\frac{-E_{max}-E_c}{2d}\right). \quad (5)$$

This equation can be used to determine a. The quantity d can be found from the expression

$$d = E_c\left[\ln\left(\frac{1+\frac{P_r}{P_s}}{1-\frac{P_r}{P_s}}\right)\right]^{-1}. \quad (6)$$

We study the defects that appear after the formation of the blocking layer. In this case, the inequality $\varepsilon_0 E_f \ll P$ is usually satisfied. Introducing the average field E_f, we obtain

$$V_f = E_f w_f, \quad (7)$$

where w_f is the width of the FE. Specifically, we assume that the defects are acceptors.

The following calculations are performed as applied to the method of measuring the current relaxation, i.e., the time dependence of the current after switching the voltage.

For a strong electric field, the change in polarization is fast ($t \le 1$ μs). However, a situation may occur in which a significant part of the polarization changes rapidly, while the remaining part (and the corresponding polarization current) changes slowly for the following reasons:

(i) the presence of the blocking layer between the PZT and the metal [9, 10];

(ii) the polycrystalline structure of the FE [12].

After the voltage V is switched from 0 in the ascending branch of the hysteresis loop to $V > 0$, the change in polarization is much greater than after the same switching in the descending branch. Therefore, the amplitude of the delayed polarization current can be much greater. In our experiments, the delayed polarization current is superimposed on the relaxation current. To diminish this effect, we switched the voltage from 0 on the descending branch to $V > 0$. In this situation, the curve $P(E_f)$ lies inside the hysteresis loop but close to its descending branch [13]. Therefore, expression (4) was used. Using (2) and (4), we obtain

$$E_f = -\left\{E_c + 2d\,\mathrm{arctanh}\left[\frac{(Q_{sc}+Q_{ss})-P_r(1-a)}{P_s}\right]\right\}. \quad (8)$$

Performing some transformations in the above expressions, we obtain

$$V + V_{bi} = \psi_s - \left\{E_c + d\ln\left[\frac{P_s+(Q_{sc}+Q_{ss})-P_r(1-a)}{P_s-(Q_{sc}+Q_{ss})+P_r(1-a)}\right]\right\}w_f, \quad (9)$$

where V is the applied voltage.

To estimate the width and other parameters of the defect-containing layer at the interface, we consider two limiting cases.

(I) The FE and the semiconductor are doped with shallow impurities only, and all defects are located at the interface in a thin transition layer of width $\Delta \ll h$, where h is the width of the space-charge region (SCR) in the semiconductor. In this case, the defects can be considered as surface states.

(II) The defect layer occupies the entire SCR in the semiconductor ($\Delta \ge h$). In this case, defects should be considered as deep-level centers in the semiconductor.

Let us discuss these two cases in turn.

2.1. Defects Producing Surface States ($\Delta \ll h$)

We choose the initial voltage V_0 at which the steady-state occupation of surface states is established in time t on the order of τ_m, where τ_m is the time constant of the measuring equipment. The steady-state occupation of surface states corresponds to the following initial values of the parameters: ψ_{s0}, E_{f0}, P_0, Q_{sc0}, and Q_{ss0}. At $t = 0$, we switch the voltage from V_0 to $V > V_0$. After switching, thermal emission of electrons from the valence band to the surface states with energy E_t occurs at the interface if energies E_t lie in the interval

$$F_s > F_t > L + \psi_{s0};$$

in other words, holes are thermally emitted from these surface states to the valence band. Here, F_s is the Fermi level in the semiconductor in the region of electrical neutrality, $L = F_s - E_v$ in the region of electrical neutrality, and E_v is the top of the valence band in this region (see Fig. 2). The emission gives rise to a current that consists of two components.

(i) The current through the surface states:

$$j_{ss} = \frac{d}{dt}Q_{ss} \quad \left(\frac{d}{dt}Q_{ss} < 0\right). \tag{10}$$

Filling the surface states with electrons results in the screening of the SCR and in a decrease in the surface potential ψ_s.

(ii) The current through the SCR:

$$j_{sc} = \frac{d}{dt}Q_{sc} \quad \left(\frac{d}{dt}Q_{sc} > 0\right). \tag{11}$$

With decreasing ψ_s, electrons leave the SCR. The currents j_{ss} and j_{sc} have opposite directions, and the total current density j is equal to their difference,

$$j = j_{ss} - j_{sc}. \tag{12}$$

Differentiating (9) with respect to time and performing some transformations, we obtain

$$\frac{d}{dt}\psi_s - B\left(\frac{d}{d\psi_s}Q_{sc}\frac{d}{dt}\psi_s + \frac{d}{dt}Q_{ss}\right) = 0, \tag{13}$$

where

$$B = \frac{2w_f dP_s}{P_s^2 - [(Q_{sc} + Q_{ss}) - P_r(1-a)]^2}. \tag{14}$$

The function $Q_{sc}(\psi_s)$ is known [14]; i.e.,

$$Q_{sc} = -H/\sqrt{\psi_s}, \quad \frac{d}{d\psi_s}Q_{sc} = -\frac{0.5H}{\sqrt{\psi_s}}, \tag{15}$$

where

$$H = \sqrt{2\varepsilon_0\varepsilon_s qN_a}$$

and N_a is the concentration of shallow acceptors in the semiconductor.

At any t, the derivative $\frac{d}{dE}Q_{ss}$ has a sharp peak at the energy E_t defined by the expression

$$E_t = kT\ln(\nu t), \tag{16}$$

where k is the Boltzmann constant, T is temperature, $\nu = \sigma_p v_{pT} N_v$, σ_p is the cross section of hole capture by the deep centers with energy E_t, v_{pT} is the thermal velocity of holes, and N_v is the effective density of states in the valence band. The energy E_t is measured from the valence band edge at the interface.

Expressions (10) and (16) can be used to approximate the dependence $j_{ss}(t)$ by the expression [13]

$$j_{ss}(t) = -qN_{ss}(E_t)\frac{kT}{t}, \tag{17}$$

where $N_{ss}(E_t)$ is the density of surface states at the energy E_t defined by (16).

We may also assume approximately that at time t the surface states with energies below the level E_t are filled with electrons and those with higher energies are empty. Then the charge $Q_{ss}(t)$ can be calculated from the expression

$$Q_{ss} = -q\int_0^{E_t} N_{ss}(E)dE. \tag{18}$$

Using (10)–(17) and performing some transformations, we obtain

$$\frac{d}{dt}\psi_s = -\frac{B}{1 + \dfrac{0.5B}{\sqrt{\psi_s}}}qN_{ss}\frac{kT}{t}, \tag{19}$$

$$j_{sc} = \frac{0.5BH}{\sqrt{\psi_s} + 0.5BH}qN_{ss}\frac{kT}{t}, \tag{20}$$

and j_{ss} is defined by (17). As a result, we have

$$j = j_{ss} - j_{sc} = -qN_{ss}\frac{kT}{t}\left(1 - \frac{0.5BH}{\sqrt{\psi_s} + 0.5BH}\right). \tag{21}$$

The current ratio j_{sc}/j_{ss} is given by

$$R = \frac{j_{sc}}{j_{ss}} = -\frac{0.5BH}{\sqrt{\psi_s} + 0.5BH}. \tag{22}$$

For $R \ll 1$, expression (22) transforms into formula (25) from [15] for an MIS structure with a linear dielectric.

Analysis of the experimental time dependence of the relaxation current $I(t)$ needed for processing experimental results is complicated by the fact that the quantities Q_{ss}, Q_{sc}, and ψ_s in (21) are not known. However, our estimation of the ratio j_{ss}/j_{sc} using formulas (17) and (20) has shown that in actual M–PZT–LSCO structures, the current j_{ss} is several times greater than the current j_{sc}. Thus we can set $j \approx j_{ss}$ and, in the first approximation, determine the energy spectrum of surface states from expressions (16) and (17) using the experimental dependence $I(t)$,

$$N'_{ss} = \frac{It}{qkTA}, \tag{23}$$

where A is the surface area. The dependence $Q_{ss}(t)$ is given by (18).

For $t < 0$, we express Q_{sc0} and Q_{ss0} in terms of ψ_{s0}; the quantity $\psi_s 0$ is determined from the transcendental equation (9), where we set $\psi_s = \psi_{s0}$. Next we determine the quantities E_{f0} and P_0.

At $t = 0$ (after switching from V_0 to $V_1 > V_0$) we have the initial values $\psi_s = \psi_s^{in}$ and $Q_{sc} = Q_{sc}^{in}$, as well as $Q_{ss}^{in} = Q_{ss0}$ (initial occupation of the surface states is unchanged). The quantity ψ_s^{in} can be determined from Eq. (9), where we set $V = V_1$ and ψ_s^{in}. Then we determine the quantities E_f^{in} and P^{in}.

The time dependences $\psi_s(t)$ and $Q_{sc}(t)$ are determined by the recursion method: we calculate the subsequent values of these functions in terms of their previous values. Next, using the dependence $Q_{sc}(t)$, we find $j_{sc}(t)$ from (20) and obtain the energy spectrum of surface states more accurately,

$$N_{ss} = \frac{N'_{ss}}{1 - \left|\frac{j_{sc}}{j_{ss}}\right|}. \quad (24)$$

The above results are valid if the inequality

$$L + q\psi_s > E_t \quad (25)$$

is satisfied. If the equality

$$L + q\psi_s = E_t \quad (26)$$

becomes valid at some time t_{cr} in the course of current relaxation, then a steady-state occupation of surface states is established and current relaxation stops. Equality (26) can hold for a high density of surface states, and a smaller time t_{cr} corresponds to a greater amplitude of the relaxation current (i.e., to a higher density of surface states). At low densities of surface states, equality (26) is not valid.

The density of surface states in a given energy interval does not depend on *V*. Therefore, the relaxation current in the corresponding time interval does not depend on the value of *V* (see expressions (16), (23), and (24)).

2.2. Defects Corresponding to Deep-Level Centers in the Space-Charge Region ($\Delta \geq h$)

We assume that $Q_{ss} = 0$ and disregard the edge effects in the SCR. Let the deep-level centers be acceptors and let the shallow impurity concentration N_a and the density of states for deep-level centers N_t be position-independent. Then integrating the Poisson equation, we obtain

$$2\varepsilon_0\varepsilon_s\psi_s(t) = qN_i(t)h^2(t), \quad (27)$$

where N_i is the sum of the concentrations of shallow acceptors and ionized deep-level centers in the SCR. The quantity N_i is defined by the expression

$$N_i(t) = N_a + \int_0^{E_t} N_t(E)dE, \quad (28)$$

and E_t is given by (16).

The charge Q_{sc} in the SCR is defined by

$$Q_{sc} = -qN_ih. \quad (29)$$

We analyze transient processes using the same method as in Subsection 2.1. We choose the initial voltage V_0 at which the steady-state occupation of deep-level centers in the SCR is established in time t_0 on the order of τ_m. At $t = 0$, we switch the voltage from V_0 to $V > V_0$. On switching at $t = 0$, the initial occupation of deep-level centers does not change, and therefore the width of the SCR increases abruptly. Then electrons are thermally emitted from the valence band to the deep-level centers. This process increases the space-charge density in the SCR and decreases the surface potential ψ_s and the width of the SCR *h*. This is accompanied by the current j_{sc} defined by expression (11). The quantity *h* is given by

$$h = \sqrt{\frac{2\varepsilon_0\varepsilon_s\psi_s}{qN_i}}. \quad (30)$$

We use (29) and (30) to obtain

$$Q_{sc} = -\sqrt{2\varepsilon_0\varepsilon_sqN_i\psi_s}. \quad (31)$$

Now we use (8), (9), (13), and (14) and set $Q_{ss} = 0$. Differentiating (9) with respect to time, we find

$$\frac{d}{dt}\psi_s = \frac{D}{P_s^2 - [Q_{sc} - P_r(1-a)]^2}\frac{d}{dt}Q_{sc}, \quad (32)$$

where $D = 2dw_fP_s$. Differentiating (31) with respect to time, we obtain

$$\frac{d}{dt}Q_{sc} = \frac{\varepsilon_0\varepsilon_s}{Q_{sc}}\left(\psi_s\frac{d}{dt}N_i + N_i\frac{d}{dt}\psi_s\right). \quad (33)$$

Performing an analysis similar to that in Subsection 2.1, we approximate the function $\frac{d}{dE}N_i$ by the expression

$$\frac{d}{dt}N_i = N_t(E_t)\frac{kT}{t}. \quad (34)$$

After some transformations, we derive

$$\frac{I}{A}\left\{\frac{\varepsilon_0\varepsilon_sN_iD}{Q_{sc}[P_s^2 - [Q_{sc} - P_r(1-a)]^2]} - 1\right\} = \frac{\varepsilon_0\varepsilon_s}{Q_{sc}}N_t\frac{kT}{t}\psi_s, \quad (35)$$

where $I = jA$ is the measured relaxation current and *A* is the sample area.

The subsequent analysis is also similar to that in Subsection 2.1. Time dependences $Q_{sc}(t)$, $\psi_s(t)$, $N_i(t)$, $N_t(t)$, and $h(t)$ are determined by the recursion method. The width of the SCR increases with voltage *V*. Therefore, for the energy interval considered, a greater relaxation current corresponds to a greater *V* in the corresponding time interval.

3. EXPERIMENT

3.1. Samples

Our structures were fabricated on the $NdGaO_3$ (110) substrates using laser sputtering [16]. A layer of $La_{1.85}Sr_{0.15}CuO_4$ (LSCO) of width 500 Å was formed at a substrate temperature of 630°C, then a layer of

$Pb_{0.95}La_{0.05}Ti_{0.8}Zr_{0.2}O_3$ (PZT) ferroelectric of width 1500 Å was deposited at a temperature of 500°C. The contacts to layers LSCO and PZT had an area of 200 × 200 μm² and were deposited by thermal evaporation of gold.

3.2. Measurement Procedure

The hysteresis loop was measured by the Sawyer–Tower method [17] at a frequency of 112 Hz. Measurements by the method of isothermal current relaxation were performed at $T \approx 300$ K. For this purpose, a step of positive voltage (with respect to the semiconductor contact) from the F-4810/1 device was applied to the FE contact. A 1-MΩ resistor was connected in series with the sample to protect the latter from overloading by the current pulse when the polarization changed. In this case, the rate of the polarization change was limited by the rate of relaxation of the voltage drop across the sample, i.e., by the time of sample-capacitance charging through the resistor. Current relaxation was measured using an SHCH-300 device.

4. EXPERIMENTAL RESULTS AND DISCUSSION

For a saturated hysteresis loop, we found the following values of the parameters:

$$P_s = 35\ \mu C/cm^2, \quad P_r = 25\ \mu C/cm^2, \text{ and}$$

$$E_c = 2 \times 10^5\ V/cm.$$

For the semiconductor, we had $N_a = 10^{19}$ cm^{-3}.

Voltage switching from $-V$ to $+V$ was performed in the following order: from $-V$ to 0 (we call this the position –0), then from –0 to V and from V to 0 (we call this the position +0), and finally from +0 to V and from V to $-V$. After each switching, a 5-min pause was made. Current relaxation was measured after switching from –0 to V and from +0 to V.

Figure 3 shows a typical experimental time dependence of the relaxation current after the voltage was switched from –0 to 1 V, from –0 to 2 V, from +0 to 1 V, and from +0 to 2 V.

Estimation of the pulse of capacitive current through the 1-MΩ resistor of, and through, the sample capacitance and a comparison of the capacitive and relaxation currents for our samples shows that, for $t > 0.1$ s, the capacitive current becomes much smaller than the relaxation current, and the voltage drop across the sample almost attains a steady-state value. Therefore, when processing the experimental data, we used the current values for $t > 0.1$ s.

Comparison of relaxation currents showed that, after switching from –0 to $V > 0$, the amplitude of the current was much greater than after switching from +0 to the same V. This circumstance may be caused by a slowing down of the polarization current relaxation (see above). For this reason, we determined the energy spectrum of surface states or deep-level centers by current relaxation after switching from +0 to $V > 0$.

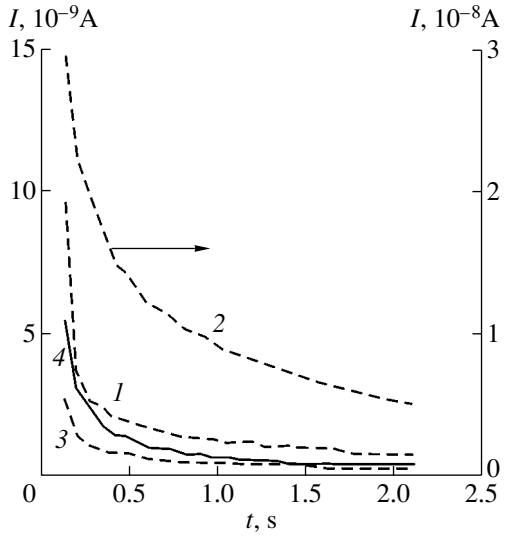

Fig. 3. Experimental time dependences of the currents after the voltage was switched (*1*) from –0 to 1 V, (*2*) from –0 to 2 V, (*3*) from +0 to 1 V, and (*4*) from +0 to 2 V. For curves *1*, *3*, and *4* the current scale is given on the left-hand axis and for curve *2*, on the right-hand axis.

After switching the voltage from +0 to 2 V, the current was much greater than after switching from +0 to 1 V; accordingly, if we use expressions (17), (23), and (24) to determine $N_{ss}(E_t)$, the values of $N_{ss}(E_t)$ would be greater. This result is apparently incorrect (see conclusions at the end of Subsection 2.1). Therefore, we cannot assume that the width of the defect-containing layer is much smaller than the width of the SCR, and we must consider defects as deep-level centers distributed over the entire SCR (see conclusions at the end of Subsection 2.2).

Figure 4 shows the calculated time dependences of the energy E_t, the barrier height $L + q\psi_s$, and the width of the SCR h after switching the voltage from +0 to 1 V. The features of these dependences were discussed in Subsection 2.2.

The densities of states for deep-level centers N_t are plotted in Fig. 5 as functions of E_t after the voltage was switched from +0 to 1 V and from +0 to 2 V. It follows from comparing these functions that the density of states for deep-level centers increases from the FE–semiconductor interface into the depth of the semiconductor. We note that the value $N_t = 4 \times 10^{20}$ cm^{-3} eV^{-1} for a space-charge region of width 50 Å corresponds to the density of surface states of 2×10^{14} cm^{-2} eV^{-1}; i.e., it is of the same order of magnitude as for Ge–Si heterojunctions [18].

Determination of the parameters of deep-level centers in the defect-containing layer is a problem for further study.

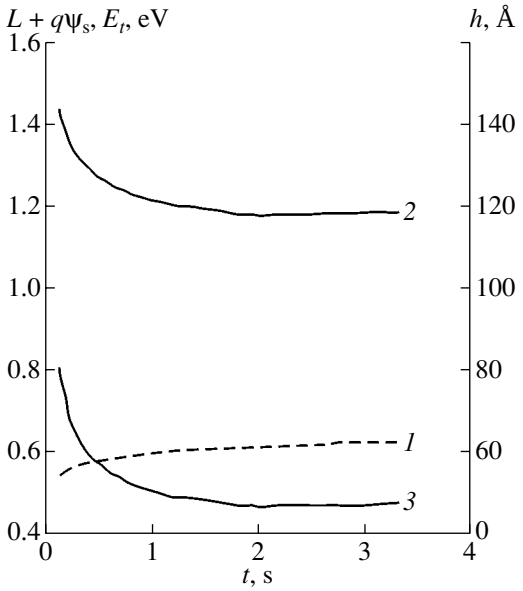

Fig. 4. Time dependence after switching voltage from +0 to 1 V for (*1*) the energy E_t, (*2*) the potential barrier height $L + q\psi_s$, and (*3*) the width of the space-charge region h (for $\nu = 10^{10}$ s^{-1}).

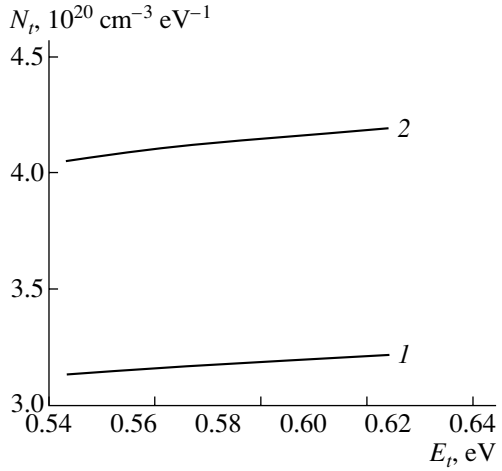

Fig. 5. Energy spectrum of the density of states for deep-level centers. The voltage was switched (*1*) from +0 to 1 V and (*2*) from +0 to 2 V (for $\nu = 10^{10}$ s^{-1}).

5. CONCLUSION

Structural defects are formed at the interface between a ferroelectric (PZT) and a semiconductor (LSCO). To study these defects, we used the method of isothermal current relaxation with the voltage switched from zero to different positive voltages. We developed a method for determining the density of surface states in the case where the width of the defect-containing layer is much smaller than the width of the space-charge region, and a method for determining the density of states for deep-level centers in the case where the width of the defect-containing layer is greater than the width of the space-charge region. We show that the width of the defect layer is greater than 50–100 Å, and, in the energy interval $E_v + (0.55 – 0.65)$ eV, the density of states for deep-level centers is on the order of 3×10^{20} cm^{-3} eV^{-1}; this value corresponds to a density of surface states of about 2×10^{14} cm^{-2} eV^{-1}. We showed that the density of states for deep-level centers increases from the interface into the depth of the semiconductor.

ACKNOWLEDGMENTS

We thank I.V. Grekhov for formulating the problem and discussing the results, D.V. Mashovets for performing the measurements, I.A. Liniichuk for fabricating the samples, and I.A. Liniichuk and L.A. Delimova for their helpful participation in discussions.

This study was supported by the Russian Foundation for Basic Research, project no. 00-15-96770.

REFERENCES

1. Y. Watanabe, Jpn. J. Appl. Phys., Part 1 **35**, 1564 (1995).
2. Y. Watanabe, Phys. Rev. B **59**, 11257 (1999).
3. M. W. Prins, S. E. Zimmers, J. F. Cilessen, and J. B. Giesbers, Appl. Phys. Lett. **70**, 458 (1997).
4. I. A. Veselovskiĭ, I. V. Grekhov, L. A. Delimova, and I. A. Liniĭchuk, Pis'ma Zh. Tekh. Fiz. **27** (1), 39 (2001) [Tech. Phys. Lett. **27**, 17 (2001)].
5. Y. Watanabe, Y. Matsumoto, and M. Tanamura, Jpn. J. Appl. Phys., Part 1 **34**, 5254 (1995).
6. W. Wu, K. H. Wong, C. L. Mak, *et al.*, J. Appl. Phys. **88**, 2068 (2000).
7. H. Sugiyama, T. Nakaiso, Y. Adachi, *et al.*, Jpn. J. Appl. Phys., Part 1 **39**, 2131 (2000).
8. T. Mihara and Y. Watanabe, Integr. Ferroelectr. **1**, 269 (1992).
9. J. M. Benedetto, R. A. Moore, and F. B. McLean, J. Appl. Phys. **75**, 460 (1994).
10. P. K. Larsen, G. J. M. Dormans, D. J. Taylor, and P. J. van Veldhoven, J. Appl. Phys. **76**, 2405 (1994).
11. S. L. Miller, R. D. Nasby, J. R. Schwank, *et al.*, J. Appl. Phys. **68**, 6463 (1990).
12. Y. S. Yang, S. J. Lee, S. H. Kim, *et al.*, J. Appl. Phys. **84**, 5005 (1998).
13. S. L. Miller, J. R. Schwank, R. D. Nasby, and M. S. Rodgers, J. Appl. Phys. **70**, 2849 (1991).
14. S. M. Sze, *Physics of Semiconductor Devices*, 2nd ed. (Wiley, New York, 1981; Mir, Moscow, 1984), Vol. 1.
15. J. G. Simmons and L. S. Wei, Solid-State Electron. **17**, 117 (1974).
16. I. Grekhov, L. Delimova, I. Liniichuk, *et al.*, Integr. Ferroelectr. **43**, 175 (2002).
17. C. B. Sawyer and C. H. Tower, Phys. Rev. **35**, 269 (1930).
18. A. G. Milnes and D. L. Feucht, *Heterojunctions and Metal–Semiconductor Junctions* (Academic, New York, 1972; Mir, Moscow, 1975).

Translated by I. Zvyagin

Semiconductors, Vol. 38, No. 6, 2004, pp. 689–695. Translated from Fizika i Tekhnika Poluprovodnikov, Vol. 38, No. 6, 2004, pp. 716–722.

LOW-DIMENSIONAL SYSTEMS

Electron–Electron Scattering in Stepped Quantum Wells

V. L. Zerova*^, L. E. Vorob'ev*, and G. G. Zegrya**

**St. Petersburg State Polytechnical University, St. Petersburg, 195251 Russia*

^e-mail: VZerova@rphf.spbstu.ru

***Ioffe Physicotechnical Institute, Russian Academy of Sciences, St. Petersburg, 194021 Russia*

Submitted October 29, 2003; accepted for publication November 3, 2003

Abstract—A method for calculating the probability of intersubband electron–electron scattering in quantum wells of complex shape is suggested. Numerical data for stepped InGaAs/AlGaAs quantum wells are obtained. The principal mechanisms of electron–electron scattering that exert the strongest effect on the intersubband inversion of population in laser structures are determined. © *2004 MAIK "Nauka/Interperiodica".*

1. INTRODUCTION

The operation of lasers and detectors for the mid-IR range, based on semiconductor quantum wells (QW), is based on intersubband transitions of charge carriers, and the probability of this process is defined by the parameters of the QWs. QWs of complex shape are promising for optoelectronic devices because they facilitate the design of structures with the necessary relaxation times. The period of a structure containing a QW of complex configuration comprises several layers of semiconductors with different band gaps. Setting the sequence and composition of these layers, one can control the rates of radiative and nonradiative recombination. The possibility of obtaining an intersubband population inversion in QW lasers is mainly defined by the relative rates of different nonradiative intersubband transitions. Among these processes, electron-electron (*e–e*) scattering can dominate when there is a high density of nonequilibrium electrons [1, 2].

In this study, we suggest a method for calculating the probability of intersubband *e–e* scattering in QWs of complex shape with finite depth. The electron wave functions are constructed in terms of Kane's model [3]. The method is applied in the calculations of scattering probability in stepped InGaAs/AlGaAs QWs. The types of *e–e* processes that exert the strongest effect on the intersubband population inversion in the structures under study are established, and the probabilities of the main intersubband *e–e* processes are calculated. It is shown that the destruction of the population inversion as a result of the *e–e* interaction can be prevented by optimizing the parameters of complex QWs in these heterostructures.

2. SUBJECT OF INQUIRY

The rate of intersubband *e–e* processes in a QW of complex configuration is calculated using the heterostructure proposed in [4] (Fig. 1) as an example. The special configuration of QW provides a long lifetime of electrons on the third level (*e*3) with respect to the intersubband scattering with the emission of optical phonons. The lifetime on the second level (*e*2) is small because of the large overlap between the electron wave functions of levels *e*2 and *e*1. The probability of capture of injected electrons to level *e*3 is much larger than the

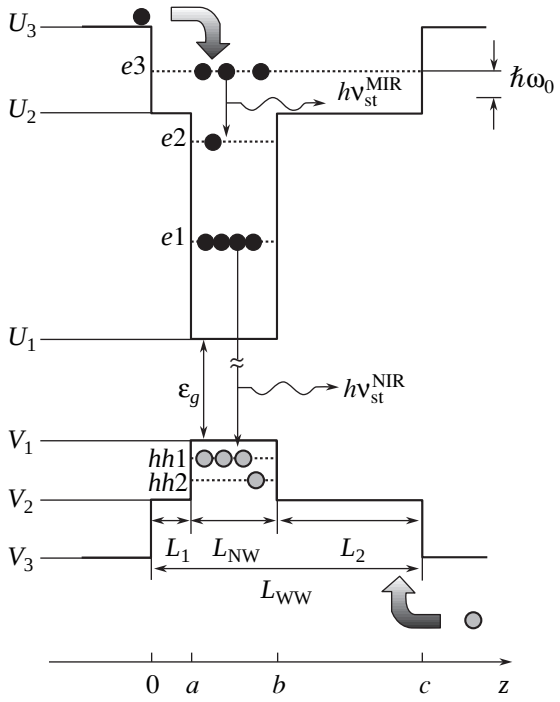

Fig. 1. QW with complex configuration. Scheme of stepped potentials $U_c(z)$ and $V_v(z)$ of c and v bands and energy levels of electrons (*e*1, *e*2, *e*3) and heavy holes (*hh*1, *hh*2). $h\nu_{st}^{MIR}$ is the energy of intersubband stimulated emission of the mid-IR range; $h\nu_{st}^{NIR}$, the energy of band-to-band near-IR stimulated emission; and $\hbar\omega_0$, the polar optical phonon energy.

1063-7826/04/3806-0689$26.00 © 2004 MAIK "Nauka/Interperiodica"

probability of capture to level $e2$. Therefore, population inversion appears between levels $e3$ and $e2$. As current increases, the electron density on level $e1$ ceases to increase if there arises a stimulated intersubband emission. Nevertheless, the threshold electron density on the lower level, which is necessary for the onset of intersubband emission, can be rather high. As a consequence, the probability of intersubband e–e scattering can become comparable with the probability of intersubband electron–phonon scattering, which will reduce the factor of intraband population inversion between levels $e3$ and $e2$.

We studied the effect of intersubband e–e scattering on the intraband population inversion. Although we only consider one specific heterostructure, the principle used in the calculation of the rate of e–e scattering is of general nature, and it can be applied for other types of QW heterostructures.

3. WAVE FUNCTIONS IN KANE'S MODEL

As shown earlier for the case of Auger processes in the bulk, multiband approximation must be used in the calculation of the wave functions of carriers [5]. In this situation, the effective Hamiltonian must take into account the admixture of $|\mathbf{p}\rangle$-states of holes to electron $|s\rangle$-states. This specific feature of the energy spectrum and the wave functions of electrons in QWs is well described by Kane's model [3]. In this model, basis wave functions of the bottom of the conduction band are chosen as Bloch's functions of $|s\rangle$ and $|\mathbf{p}\rangle$ type, with angular momentum 0 and 1, respectively (the direction of z axis is perpendicular to the QW plane). The electron wave function is a superposition of basis states:

$$\psi_c(\mathbf{r}) = u(\mathbf{r})|s\rangle + \mathbf{v}(\mathbf{r})|\mathbf{p}\rangle, \tag{1}$$

where $u(\mathbf{r})$ and $\mathbf{v}(\mathbf{r}) \equiv (v_x(\mathbf{r}), v_y(\mathbf{r}), v_z(\mathbf{r}))$ are smooth envelopes of Bloch's functions. In the vicinity of point Γ, the system of equations for envelopes in the spherical approximation takes the form

$$\begin{cases} \left[\varepsilon - \dfrac{\varepsilon_g}{2} - U_c(z)\right]u(\mathbf{r}) - \gamma\hat{\boldsymbol{\kappa}}\mathbf{v}(\mathbf{r}) = 0, \\ \left[\varepsilon + \dfrac{\varepsilon_g}{2} + V_v(z)\right]\mathbf{v}(\mathbf{r}) - \gamma\hat{\boldsymbol{\kappa}}u(\mathbf{r}) = 0. \end{cases} \tag{2}$$

Here, ε is the energy reckoned from the middle of the band gap $\varepsilon_g/2$ of a narrow-gap semiconductor (see Fig. 1); $\hat{\boldsymbol{\kappa}} = -i\hat{\nabla}$; $U_c(z)$ and $V_v(z)$, the heights of heterobarriers for electrons and holes, respectively; and γ, the Kane's matrix element. We use the approximation $\gamma = \text{const}$, which is valid for heterostructures based on III–V semiconductors. System (2) corresponds to the system of equations used in [6]. However, in contrast to [6], system (2) does not include terms describing the spin–orbit interaction. Furthermore, (2) does not contain the term describing the heavy-hole states, because taking these states into account in the calculation of electron wave functions would lead to excessive accuracy in terms of the method of wave function envelopes [7].

For a type-I heterostructure with a QW of complex configuration, the potentials of the c and v bands have a stepped form (Fig. 1):

$$U_c(z) = \begin{cases} U_1 & \text{for } a < z < b, \\ U_2 & \text{for } 0 < z < a, \quad b < z < c, \\ U_3 & \text{for } z < 0, \quad z > c, \end{cases} \tag{3}$$

$$V_v(z) = \begin{cases} V_1 & \text{for } a < z < b, \\ V_2 & \text{for } 0 < z < a, \quad b < z < c, \\ V_3 & \text{for } z < 0, \quad z > c. \end{cases} \tag{4}$$

Electron wave functions determined from system (2) must satisfy the following boundary conditions. Components u and v_z must be continuous across each heterointerface ($z = 0, a, b, c$) [7]:

$$u^{>} = u^{<}, \quad v_z^{>} = v_z^{<}, \tag{5}$$

where the superscripts $<$ and $>$ of components u and v_z indicate the values of these components on the left and right of the heterointerface, respectively. The components of the electron wave function v_x and v_y, which are parallel to the heterointerface, have discontinuities.

In a QW of complex configuration, the region of electron localization can span one or several layers of a heterostructure, depending on the electron energy. For example, when the energy of an electron localized in the region $a < z < b$ near the bottom of a QW increases to $\varepsilon > U_2$, the boundaries of the QW change abruptly. The regions $0 < z < a$ and $b < z < c$ are the barrier regions for an electron with energy

$$U_1 + \frac{\varepsilon_g}{2} < \varepsilon < U_2 + \frac{\varepsilon_g}{2},$$

and they are the QW region for

$$U_2 + \frac{\varepsilon_g}{2} < \varepsilon < U_3 + \frac{\varepsilon_g}{2}.$$

Therefore, Kane's equations and their solutions can be determined by different values of potentials and effective masses in different spatial regions and at different energies.

We seek the solution to the system of equations (2) in the general form of a linear combination of exponentials with different amplitudes:

$$\begin{aligned} u &= [A_1\exp(i\kappa_i z) + A_2\exp(-i\kappa_i z)]\exp(i\mathbf{q}\boldsymbol{\rho}), \\ v_z &= -i\lambda_i[A_1 i\kappa_i\exp(i\kappa_i z)] \\ &\quad - A_2 i\kappa_i\exp(-i\kappa_i z)]\exp(i\mathbf{q}\boldsymbol{\rho}), \end{aligned} \tag{6}$$

where the parameters

$$\lambda_i = \frac{\gamma}{\varepsilon + \frac{\varepsilon_g}{2} + V_i}$$

and components

$$\kappa_i = \sqrt{\frac{2m_i}{\hbar^2}\left(\varepsilon - \frac{\varepsilon_g}{2} - U_i\right)}$$

are defined by the potentials V_i and U_i and effective masses m_i in the i region, and A_1 and A_2 are unknown coefficients. The κ_i components of the wave vector $\boldsymbol{\kappa} = (\mathbf{q}, \kappa)$ are initially assumed to be complex, but they will automatically be real in the QW regions and imaginary in the barriers.

The electron wave functions in i regions have the form

$$\psi_{ci}(\mathbf{r}) = \exp(i\mathbf{q}\boldsymbol{\rho}) \begin{bmatrix} A_1\exp(i\kappa_i z) + A_2\exp(-i\kappa_i z) \\ \lambda_i q_x[A_1\exp(i\kappa_i z) + A_2\exp(-i\kappa_i z)] \\ \lambda_i q_y[A_1\exp(i\kappa_i z) + A_2\exp(-i\kappa_i z)] \\ \lambda_i \kappa_i[A_1\exp(i\kappa_i z) - A_2\exp(-i\kappa_i z)] \end{bmatrix}. \quad (7)$$

The unknown coefficients A_j can be found from the system of equations obtained by substituting (6) into boundary conditions (5) at each heterointerface. Since λ_i and κ_i depend on energy ε, the determined coefficients A_j are functions of energy ε. Substituting the found $A_j(\varepsilon)$ dependences into the system and equating its determinant to zero, we obtain a transcendental equation in energy. The dependence $\kappa_i(\varepsilon)$ determined from this equation is used in the determination of the energy spectrum of electrons.

Using the system of equations (2) and taking into account the coordinate dependence of $u(\mathbf{r})$ and $\mathbf{v}(\mathbf{r})$ components, we find that the spectrum of electron energies in the plane of a quantum-confined layer $\varepsilon_c(\mathbf{q})$ can be found from the equation

$$\left(\varepsilon_c + \frac{\varepsilon_g}{2} + V_v(z)\right)\left(\varepsilon_c - \frac{\varepsilon_g}{2} - U_c(z)\right) = \gamma^2(\mathbf{q}^2 + \kappa^2(\varepsilon_c)). \quad (8)$$

The above method for determining the wave functions and energy spectrum of electrons in QWs of complex shape is based on the application of Kane's model to each quantum-confined layer. This method is more versatile and, at the same time, easier as applied to QWs of complex shape than similar calculations for rectangular QWs discussed in the literature.

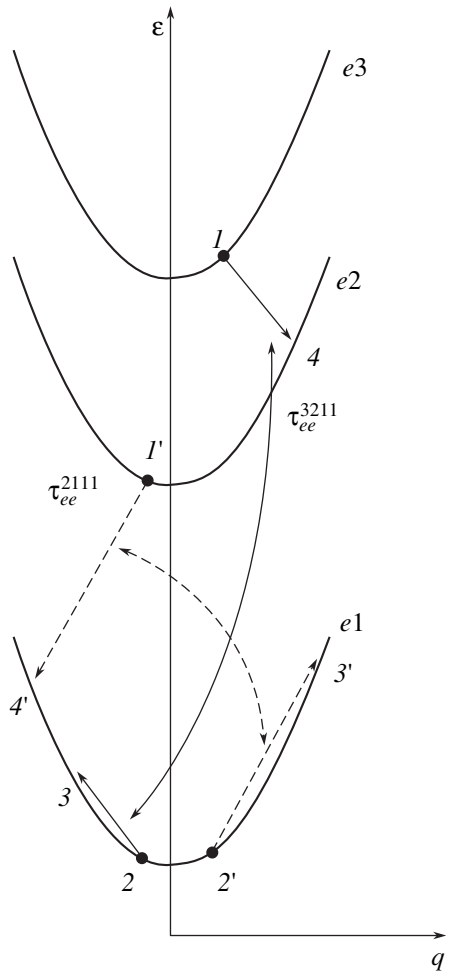

Fig. 2. Principal *e–e* processes in a stepped QW that affect the intersubband population inversion. Numbers i = 1, 2, 3, and 4 indicate the initial and final electron states for transition 3211; i' = 1', 2', 3', and 4' indicate the same for transition 2111.

4. RATE OF INTERSUBBAND ELECTRON–ELECTRON SCATTERING

Now we discuss *e–e* processes in a heterostructure with stepped QWs. Electron–electron collisions can either reduce or raise the intersubband population inversion of electrons in a QW. The inversion is reduced by *e–e* process in which an electron passes from subband *e*3 to *e*2 (Fig. 2). This transition has the highest probability when an electron in subband *e*3 interacts with an electron in the lowest subband *e*1, because the density of electrons at the lowest level is the highest. In this case, the energy of the electron in the lowest subband increases within the same subband, because the energy spacing between the first and second subbands is large. We denote this process by index 3211 (using the numbers of the initial and final states of two electrons). Similar processes for the transition $e2 \longrightarrow e1$ (2111) deplete level *e*2 and, consequently, enhance the

inversion. Other processes of the intersubband *e–e* scattering are less important [2].

The matrix element of the Coulomb *e–e* interaction can be used disregarding the screening, because the screening only slightly affects the probability of scattering in GaAs QWs with the given parameters at the temperatures $T = 80$–300 K [8]:

$$M_{ee} = \frac{4\pi e^2}{2\pi\varepsilon_0}\int_{q_z}\frac{I^{14}(q_z)I^{23}(q_z)}{(\mathbf{q}_3-\mathbf{q}_2)^2+q_z^2}\delta_{q_1-q_4,\,q_3-q_2}dq_z. \quad (9)$$

Here, $\mathbf{q}_i$ is the electron wave vector in the state i ($i = 1, 2, 3, 4$) in the QW plane (see Fig. 2); q_z, the magnitude of the wave vector transferred in the interaction in the direction z, which is normal to the heterointerface; e, the elementary charge; and ε_0, the static dielectric constant of the semiconductor. The integrals $I^{14}(q_z)$ and $I^{23}(q_z)$ are defined by the overlap of envelopes of the electron wave functions $\psi_{qi}(z)$ in the z direction in the states with wave vectors q_i:

$$I^{14}(q_z) = \int\psi^*_{q1}(z)\psi_{q4}(z)e^{iq_zz}dz,$$
$$I^{23}(q_z) = \int\psi^*_{q2}(z)\psi_{q3}(z)e^{-iq_zz}dz. \quad (10)$$

The Kronecker symbol in (9) expresses the law of conservation of the longitudinal component of the wave vector:

$$\mathbf{q}_4 + \mathbf{q}_3 = \mathbf{q}_2 + \mathbf{q}_1. \quad (11)$$

In first-order perturbation theory in *e–e* interaction, the rate of Auger processes is given by

$$G_{ee} = \frac{2\pi}{\hbar}\sum_{\mathbf{q}_1,\,\mathbf{q}_2,\,\mathbf{q}_3,\,\mathbf{q}_4}|M_{ee}|^2 f(\mathbf{q}_1)f(\mathbf{q}_2)[1-f(\mathbf{q}_3)] \times[1-f(\mathbf{q}_4)]\delta(\varepsilon_{q1}+\varepsilon_{q2}-\varepsilon_{q3}-\varepsilon_{q4}), \quad (12)$$

where $f(\mathbf{q}_i)$ is the distribution function of electrons with the wave vector $\mathbf{q}_i$ over energy; ε_{q1} and ε_{q2}, the energies of the initial states; and ε_{q3} and ε_{q4}, the energies of the final states. The summation is done over all the initial and final states of electrons. The dispersion law near the bottom of subbands is assumed to be parabolic.

In the stationary mode of laser operation, injected carriers are distributed over the subbands in accordance with the times of intersubband relaxation. At a high injection level, the distribution function of electrons can be assumed to be quasi-equilibrium within each subband if the intersubband relaxation times are significantly longer than those of intrasubband relaxation [9]. The intrasubband relaxation of the electron energy occurs via the emission of optical and acoustic phonons, as well as via fast ($\sim 10^{-12}$ s) *e–e* scattering involving optical phonons [10–12]. Therefore, we can assume that, in a time less than the intersubband relaxation time, electrons within each subband reach a quasi-equilibrium state with an average energy of about k_BT (k_B is the Boltzmann constant; T, the lattice temperature).

If the density of injected carriers is sufficiently high ($n_s > 10^{11}$ cm^{-2}), we may assume that there is a Boltzmann distribution of electrons in each subband and that the electrons have the same temperature as the lattice [10]:

$$f(q_1) = \frac{n_i}{N_c}\exp\left(-\frac{\hbar^2q_1^2}{2m_1k_BT}\right),$$
$$f(q_2) = \frac{n_1}{N_c}\exp\left(-\frac{\hbar^2q_2^2}{2m_1k_BT}\right). \quad (13)$$

Here, n_1 and n_i (i =2 and 3 for 2111 and 3211 transitions, respectively) are the electron densities in subbands, where the electron states are described by wave vectors $\mathbf{q}_1$ and $\mathbf{q}_2$, respectively, and $N_c = m_1k_BT/\pi\hbar^2$, the reduced 2D density of states.

As can be seen from (9), the probability of Coulomb interaction of two electrons is the higher, the smaller the magnitude of the wave vector transferred in the interaction. However, in *e–e* processes of 3211 and 2111 types, a transition with a transfer of a small wave vector can occur only with the transfer of high energy, on the order of the intersubband distance ($\Delta \gg k_BT$). In this case, the energy conservation law is obeyed only for electrons with the initial energy $\varepsilon_{q2} \approx \Delta$, and the number of such electrons is small.

Thus, the Auger processes discussed above are the most probable at some intermediate energies and magnitudes of wave vectors transferred in the interaction:

$$k_BT \ll \varepsilon_{q3}-\varepsilon_{q2} \le \Delta, \quad (14)$$

$$q_T \ll |\mathbf{q}_3-\mathbf{q}_2| \le \sqrt{2m_1\Delta/\hbar^2}. \quad (15)$$

Here, $q_T = \sqrt{2m_1k_BT/\hbar^2}$ is the magnitude of the thermal wave vector, and Δ is the energy spacing between the subbands among which electrons are redistributed in a specific Auger process. For transition 3211, $\Delta \equiv \Delta_{32}$; for 2111, $\Delta \equiv \Delta_{21}$. Since the average magnitudes of the wave vectors of initial states of electrons q_1 and q_2 are about q_T, the inequality

$$|\mathbf{q}_4|, |\mathbf{q}_3| \gg |\mathbf{q}_1|, |\mathbf{q}_2| \quad (16)$$

holds true.

The final states of electrons, which are described by wave vectors $\mathbf{q}_4$ and $\mathbf{q}_3$, are, with high probability, free, and the corresponding filling factors, $[1 - f(\mathbf{q}_3)]$ and $[1 - f(\mathbf{q}_4)]$ in (12), are close to unity. Furthermore, we shall use the approximation

$$q_4^2 \approx q_3^2, \quad (17)$$

which follows from the conservation law (11) if inequality (16) is taken into account.

To perform the summation over initial and final states in (12), we pass from the electron energies to magnitudes of the corresponding wave vectors. First, we sum over $\mathbf{q}_4$ using the Kronecker δ function. We

replace the remaining summations, over $\mathbf{q}_1$, $\mathbf{q}_2$, and $\mathbf{q}_3$, by integrations. Owing to approximation (17), the integrand contains no dependences on angles φ_{12}, φ_{13}, and φ_{23} between vectors $\mathbf{q}_1$, $\mathbf{q}_2$, and $\mathbf{q}_3$, so each integral over φ_{12}, φ_{13}, and φ_{23} equals 2π.

We then integrate over q_1 with the use of the δ function. Since the distribution function $f(\mathbf{q}_1)$ has the form of Boltzmann's distribution, we can pass from integration over q_1 to integration over q_1^2. Taking into account (17), we can separate out q_1^2 under the δ symbol into an individual summand:

$$\delta(\varepsilon_{q1} + \varepsilon_{q2} - \varepsilon_{q3} - \varepsilon_{q4}) = \frac{2m_1}{\hbar^2}\delta(q_1^2 - \alpha(q_2, q_3)), \quad (18)$$

$$\alpha(q_2, q_3) = 2q_3^2 - q_2^2 - \frac{2m_1\Delta}{\hbar^2}.$$

Now, using the inequality $q_3^2 \gg q_2^2$ in Eq. (9) [see (16)], substituting (9), (10), and (18) into (12), and integrating over q_1^2, we obtain for the rate of the Auger process

$$G_{ee} = \frac{1}{2\hbar(2\pi)^2}\left(\frac{2e^2}{\varepsilon_0}\right)^2\frac{2m_1}{\hbar^2}\int_{q_{2\min}}^{q_{2\max}} q_2 dq_2 \int_{q_{3\min}}^{q_{3\max}} q_3 dq_3 \times \left|\int_{q_z}\frac{I_z^{14}(q_z)I_z^{23}(q_z)}{q_3^2 + q_z^2}dq_z\right|^2 f(\alpha(q_2, q_3))f(q_2). \quad (19)$$

We now find the limits of integration over q_3 and q_2. As follows from the form of the argument of the δ function in (18), the sign and value of function $\alpha(q_2, q_3)$ must coincide with q_1^2. Since $q_1^2 \geq 0$, it should be $\alpha(q_2, q_3) \geq 0$. Using this inequality and the condition $q_3 > q_2$ (see Fig. 2), we can find the lower limit of integration over q_3. Evidently, it is a function of q_2:

$$q_{3\min}(q_2) = \sqrt{\frac{q_2^2}{2} + \frac{m_1\Delta}{\hbar^2}}. \quad (20)$$

The upper limit of integration over q_3 corresponds to the maximum wave vector that can be transmitted in the transition of an electron from state 1 to state 4. Its value must be determined by the energy spacing between these subbands, and it must be reckoned from the initial wave vector q_2:

$$q_{3\max}(q_2) = q_2 + \sqrt{\frac{2m_1\Delta}{\hbar^2}}. \quad (21)$$

Since q_2 is the magnitude of the wave vector of an electron with the initial state in the ground subband, the integration over q_2 will be performed within the limits from $q_{2\min} = 0$ to $q_{2\max} = 2q_T$. As can be seen from (20) and (21), the limiting values of q_3 are indeed much larger than q_2 at $\Delta \gg k_B T$; thus, the approximation (16) used in our model is satisfactory.

We perform integrations over q_2 and q_3 in (19) and over q_z and z numerically. It is noteworthy that in the case of an infinitely deep rectangular QW, when the wave function is localized in a single quantum-confined layer, it is convenient to calculate the integral over q_z in analytic form using the residue theorem.

From the known rates G_{ee}^{3211} and G_{ee}^{2111} of 3211 and 2111 processes, respectively, we can determine the inverse relaxation times for these processes:

$$\frac{1}{\tau_{ee}^{3211}} = \frac{G_{ee}^{3211}}{n_3}; \quad \frac{1}{\tau_{ee}^{2111}} = \frac{G_{ee}^{2111}}{n_2}. \quad (22)$$

It follows from (22) that the dependence of inverse relaxation times on n_1, which is the threshold density for the onset of band-to-band emission, is linear.

Since large wave vectors are transferred in the Auger processes under study [see (15)], the probability of *e*–*e* scattering can be insignificant [see (9)], and it will have no effect on the intersubband population inversion. The temperature dependence of the rate of the Auger transition is weak and is defined by the temperature dependence of the distribution function and that of the limiting values of the wave vectors $\mathbf{q}_2$ and $\mathbf{q}_3$.

5. RESULTS AND DISCUSSION

We have calculated times τ_{ee}^{3211} and τ_{ee}^{2111} for a stepped QW with the parameters listed below [4] (see Fig. 1):

$z < 0$, the region of the $Al_{0.28}Ga_{0.72}As$ barrier;

$0 < z < a$, the $Al_{0.26}Ga_{0.74}As$ layer with width $L_1 = 3.8$ nm;

$a < z < b$, the $In_{0.24}Ga_{0.76}As$ strained layer, $L_{NW} = 6.8$ nm;

$b < z < c$, the $Al_{0.26}Ga_{0.74}As$ layer, $L_2 = 11.4$ nm;

and $z > c$, the region of the $Al_{0.28}Ga_{0.72}As$ barrier.

The energies of the levels are reckoned from the bottom of the QW; they are $\varepsilon_{01} = 60$ meV, $\varepsilon_{02} = 229$ meV, and $\varepsilon_{03} = 345$ meV.

Figure 3 shows times τ_{ee}^{3211} and τ_{ee}^{2111} calculated for the temperature range 80–300 K for the density $n_1 \approx 5 \times 10^{11}$ cm^{-2}. This density is close to the threshold for the onset of band-to-band emission. It can be seen that time τ_{ee}^{3211} is quite large compared with τ_{ee}^{2111} (at $T = 80$ K, $\tau_{ee}^{3211} \approx 47$ ps, $\tau_{ee}^{2111} \approx 8$ ps.) This considerable difference is due to the stepped form of the QW; it is related to the small overlap between the wave functions of states *e*3 and *e*2 and the large overlap between the wave functions of states *e*2 and *e*1. As temperature

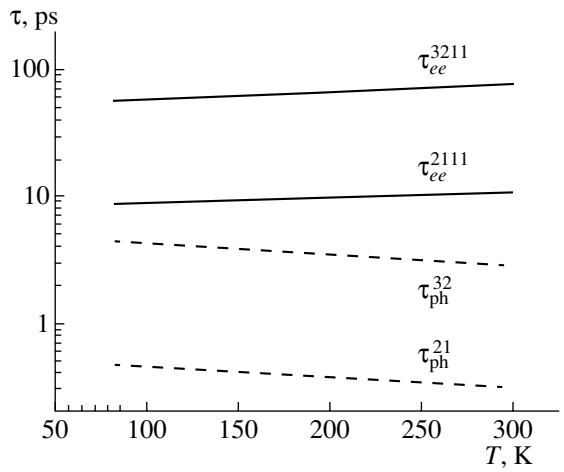

Fig. 3. Temperature dependence of the times of the main intersubband relaxation processes in a stepped QW with density $n_1 \approx 5 \times 10^{11}$ cm^{-2}; the solid and dashed lines indicate *e*–*e* and electron–phonon scattering, respectively.

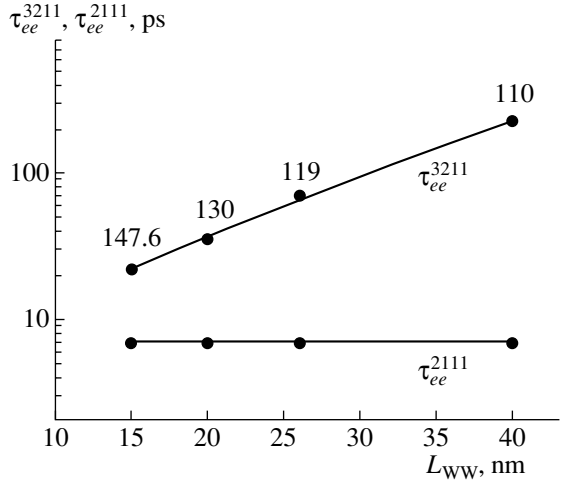

Fig. 4. Times τ_{ee}^{3211} and τ_{ee}^{2111} as functions of the width of a wide part of a QW, L_{WW}; $T = 300$ K. The dots indicate calculated data; the lines, approximation for intermediate values of L_{WW}; numbers by the dots indicate energies Δ_{32} (meV) for the given L_{WW}.

increases, the relationship between times, $\tau_{ee}^{3211} > \tau_{ee}^{2111}$, is retained.

The same figure shows the characteristic times τ_{ph}^{ij} of the basic processes of the electron scattering on polar optical phonons, whose relative values determine the possibility of obtaining intersubband population inversion in a QW. As can be seen, τ_{ee}^{3211} and τ_{ee}^{2111} at density $n_1 \approx 5 \times 10^{11}$ cm^{-2} are much larger than characteristic times τ_{ph}^{32} and τ_{ph}^{21} related to the emission of optical phonons. This means that the population inversion, determined earlier in [4], is only slightly affected by intraband Auger processes at density $n_1 \approx 5 \times 10^{11}$ cm^{-2}.

The values of τ_{ee}^{3211} and τ_{ee}^{2111} obtained agree with the times of intersubband Auger processes calculated by other authors. Specifically, estimations presented in [2] yield approximate values $\tau_{ee}^{32} \approx 50$ ps and $\tau_{ee}^{21} \approx 3$ ps for electron density $n_1 \approx 5 \times 10^{11}$ cm^{-2}.

It is noteworthy that characteristic times τ_{ee}^{3211} and τ_{ee}^{2111} depend on the shape of the QW, which defines the energy spacing between the levels and the degree of overlap between the wave functions of different subbands. We calculated these times for several QWs that differed in the width L_{WW} of the wide portion of a complex well. L_{WW} was increased by increasing L_2 (see Fig. 1). As L_{WW} increases, the energy of level *e*3 decreases, whereas the positions of levels *e*2 and *e*1 remain virtually unchanged. As a result, the energy spacing Δ_{32} decreases, and Δ_{21} remains nearly unchanged. Figure 4 shows the dependences of τ_{ee}^{3211} and τ_{ee}^{2111} on L_{WW} and Δ_{32}. In contrast to a rectangular QW, the increase in L_{WW} (and, consequently, the decrease in Δ_{32}) reduces the probability of a 3211 process. The explanation is that the probability of the Auger process is affected more strongly by the overlap of wave functions (which decreases in this situation) than by the transition energy. The characteristic time τ_{ee}^{2111} remains virtually unchanged as L_{WW} increases, therefore the ratio $\tau_{ee}^{3211}/\tau_{ee}^{2111}$ increases, which means that the population inversion is improved. The times of intersubband scattering on optical phonons behave in a similar way [4].

However, decreasing the overlap of wave functions leads to a decrease not only in the time of nonradiative processes, but also in the gain. Moreover, at $L_{WW} >$ 30 nm, additional levels appear in a QW, and injected electrons are trapped by these levels, so that the population inversion n_3–n_2 sharply decreases. Therefore, the width $L_{WW} = 22$ nm is optimal to obtain population inversion in this structure [4].

The population inversion n_3–n_2 at a given injection current J can be estimated by solving the system of rate equations describing the electron densities on the levels in a QW. In our calculation, we used a system of equations including the rates of electron–phonon and *e*–*e* interactions, as well as the rates of stimulated band-to-band emission and electron capture on QW levels. It was found that the population inversion n_3–n_2 depends on n_1.

The density n_1 depends on the parameters of the QW, waveguide, and cavity. It corresponds to the threshold current for band-to-band stimulated emission J_{th}, and

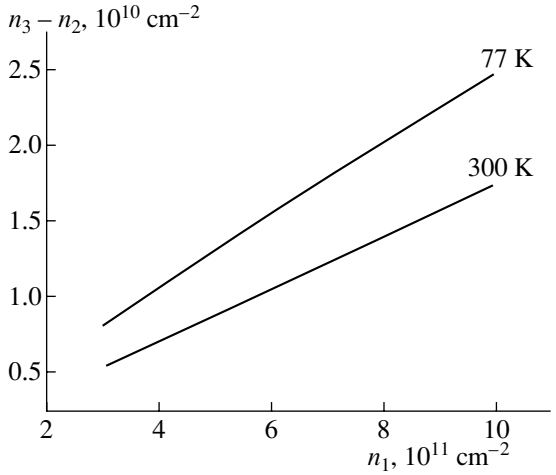

Fig. 5. Population inversion n_3–n_2 vs. density n_1; the data were calculated by solving a system of rate equations for two temperatures at currents near the threshold for band-to-band stimulated emission.

when $J \approx J_{th}$ it can be found from the system of kinetic equations for the steady state [4]

$$n_1 \approx \eta J_{th} \tau_{sp}^{v1}, \quad (23)$$

where the factor η defines the loss of electron–hole pairs in different regions of the heterostructure and τ_{sp}^{v1} is the characteristic time of spontaneous band-to-band emission.

Figure 5 shows results of calculating the population inversion at currents J_{th} corresponding to the density n_1 (23), which depends on the parameters of a structure. The small increase in the calculated values of n_3–n_2 with n_1 is caused by the enhanced effect of *e–e* processes on the inversion, whereas the probabilities of electron–phonon scattering processes are independent of n_1. As temperature increases, the population inversion decreases, because the absorption of optical phonons becomes stronger; however, this decrease is small.

6. CONCLUSION

The effect of intersubband *e–e* scattering on intersubband population inversion in QWs of complex shape was studied. It is shown that *e–e* scattering in stepped QWs exerts only a weak effect on intersubband scattering with electron density $n_1 \approx 5 \times 10^{11}$ cm^{-2}, and the population inversion is not affected. The suggested model for the calculation of *e–e* processes in a multilayer heterostructure is based on the wave functions in Kane's model, and it can be used to calculate *e–e* scattering in QWs of an arbitrary shape.

The studied temperature dependence of probabilities of *e–e* processes that have the strongest effect on the population inversion give reason to believe that lasers of this type of laser with duly optimized parameters will operate at high (over 77 K) temperatures.

REFERENCES

1. W. T. Tsang, in *Semiconductors and Semimetals*, Vol. 22: *Light-Wave Communications Technology*, Ed. by W. T. Tsang (Academic, New York, 1985).
2. P. Kinsler, P. Harrison, and R. W. Kelsall, Phys. Rev. B **58**, 4771 (1998).
3. E. O. Kane, J. Phys. Chem. Solids **1**, 249 (1957).
4. A. Kastalsky, L. E. Vorobjev, D. A. Firsov, *et al.*, IEEE J. Quantum Electron. **37**, 1356 (2001).
5. B. L. Gel'mont, Zh. Éksp. Teor. Fiz. **75**, 536 (1978) [Sov. Phys. JETP **48**, 268 (1978)].
6. G. G. Zegrya and A. S. Polkovnikov, Zh. Éksp. Teor. Fiz. **113**, 1491 (1998) [JETP **86**, 815 (1998)].
7. G. G. Zegrya and V. A. Kharchenko, Zh. Éksp. Teor. Fiz. **101**, 327 (1992) [Sov. Phys. JETP **74**, 173 (1992)].
8. V. V. Mitin, V. A. Kochelap, and M. A. Stroscio, *Quantum Heterostructures* (Cambridge Univ. Press, Cambridge, 1999), p. 242.
9. S.-C. Lee and I. Calbraith, Phys. Rev. B **55**, R16025 (1997).
10. L. E. Vorob'ev, S. N. Danilov, E. L. Ivchenko, M. E. Levinshteĭn, D. A. Firsov, and V. A. Shalygin, *Kinetic and Optical Phenomena in Strong Electric Fields in Semiconductors and Nanostructures* (Nauka, St. Petersburg, 2000).
11. C. H. Yang, J. M. Carlson-Swindle, S. A. Lyon, and J. M. Worlock, Phys. Rev. Lett. **55**, 2359 (1985).
12. B. L. Gel'mont, R. I. Lyagushchenko, and I. N. Yassievich, Fiz. Tverd. Tela (Leningrad) **14**, 533 (1972) [Sov. Phys. Solid State **14**, 445 (1972)].

Translated by D. Mashovets

Semiconductors, Vol. 38, No. 6, 2004, pp. 696–701. Translated from Fizika i Tekhnika Poluprovodnikov, Vol. 38, No. 6, 2004, pp. 723–728.

LOW-DIMENSIONAL SYSTEMS

Spectroscopy of Exciton States of InAs Quantum Molecules

V. G. Talalaev[1, 2, 3]*, J. W. Tomm[2], N. D. Zakharov[3], P. Werner[3], B. V. Novikov[1], G. É. Cirlin[3, 4, 5], Yu. B. Samsonenko[4, 5], A. A. Tonkikh[3, 4, 5], V. A. Egorov[4, 5], N. K. Polyakov[4, 5], and V. M. Ustinov[4]

[1]*Institute of Physics (Peterhof Branch), St. Petersburg State University, ul. Pervogo Maya 100, Peterhof, 198504 Russia*

[2]*Max Born Institut für Nichtlineare Optik und Kurzzeitspektroskopie, 12489 Berlin, Germany*

[3]*Max Planck Institut für Mikrostrukturphysik, 06120 Halle (Saale), Germany*

[4]*Ioffe Physicotechnical Institute, Russian Academy of Sciences, Politekhnicheskaya ul. 26, St. Petersburg, 194021 Russia*

[5]*Institute for Analytical Instrumentation, Russian Academy of Sciences, Rizhskiĭ pr. 26, St. Petersburg, 198103 Russia*

**e-mail: talalaev@mpi-halle.mpg.de*

Submitted October 27, 2003; accepted for publication November 4, 2003

Abstract—Tunnel-coupled pairs of InAs quantum dots (quantum molecules) were formed by molecular beam epitaxy in a GaAs matrix. Optical and structural properties of the obtained quantum molecules were studied. Four molecular exciton states forming a photoluminescence spectrum were revealed. The photoluminescence decay times indicate the possibility of interlevel radiative recombination from the second excited state, which is of particular importance for designing mid-infrared devices. *© 2004 MAIK "Nauka/Interperiodica".*

1. INTRODUCTION

Recently, interest in low-dimensional semiconductor structures has been growing steadily. The smallest structures of this type are quantum dots (QDs) [1]. QDs are characterized by a discrete set of levels, which corresponds to the electronic spectrum of a single atom. New semiconductor devices are being designed on the basis of QDs: vertically emitting and cascade lasers [2, 3], as well as photodetectors and emitters operating in the mid- and far-infrared (IR) ranges [4, 5]. One of the most interesting effects observed when several QD layers grows is their vertical correlation, which was established earlier for various heteroepitaxial systems [6, 7]. In this case, in-plane ordering of nanoislands also occurs [8, 9]. On the basis of these effects, the formation of so-called quantum molecules (QMs) is being actively developed [10]. A QM is a pair of tunnel-coupled QDs that similar in size and, accordingly, have a similar electronic structure. The formation of a QM leads to the splitting of an energy level of an individual QD into symmetric and antisymmetric states, depending on the superposition of the wave functions of the electron and hole in the QM. In this case, the value of splitting is dependent on the distance between the QDs and can be controlled during the growth of the structure. These objects are not only of fundamental interest, but can also be used in device applications, in particular, in alternative transceivers operating in the megahertz and gigahertz regions [11, 12], as well as in switching devices, such as quantum computers [13]. At the same time, the formation of a system of symmetric QMs from two tunnel-coupled QD layers remains a nontrivial technological problem, because this process must satisfy at least two conditions: (i) the QDs forming a molecule should be identical and (ii) the spacer between them has to provide for the necessary value of splitting. In addition, the question of the possibility of radiative transitions between neighboring split states, which is fundamentally important for the practical application of QMs, has not been solved experimentally.

In this paper, we report the results of studying the specific features of molecular-beam epitaxy (MBE) of symmetric QMs in the InAs/GaAs system. The structural features were analyzed by transmission electron microscopy (TEM). The methods of steady-state photoluminescence (PL) and time-resolved PL were used to study the energy spectrum and mechanisms of carrier relaxation in QMs.

2. EXPERIMENTAL

Growth experiments were performed in an ÉP1203 MBE system with semi-insulating GaAs(100) substrates. The process was optimized by fitting the growth parameters that affect the formation of QMs. According to the requirements for the QM symmetry and the distance between QDs, the influence of the amount of deposited InAs and the thickness of the GaAs spacer were studied. The effective thickness of deposited InAs was two and four monolayers (MLs), and the thickness of the GaAs spacer was 5 and 10 nm. We report here the results for two combinations of these parameters. Samples of type *A* contained two InAs MLs in each of the two QD layers and a spacer 10 nm thick. Samples of type *B* contained four MLs in the lower QD layer, two MLs in the upper QD layer, and a spacer 5 nm thick. During the deposition of InAs, the substrate temperature was maintained at 510°C and the growth rate of InAs layers amounted to 0.06 ML/s. After the deposition of each QD layer, the growth was interrupted—the

sample was kept at the same temperature in arsenic flux for 60 s. The QD array was then coated by a layer of GaAs at a rate of 0.7 ML/s, after which the substrate temperature was increased to 610°C and the sample was kept at this temperature for 60 s (high-temperature annealing). In order to prevent the transport of excess carriers to the surface and into the substrate, the active region was limited from both sides by short-period superlattices $Al_{0.25}Ga_{0.75}As/GaAs$ (10 pairs, 2.5 nm/2.5 nm) and placed at the center of a 50-nm thick GaAs layer. The state of the surface was monitored using reflection high-energy electron diffraction (RHEED) patterns [14]. The appearance of bulk reflections after the deposition of 1.7 MLs of the first (lower) InAs layer indicated the formation of three-dimensional (3D) nanoislands. When the second (upper) InAs layer was deposited, bulk reflections arose at smaller effective thicknesses of InAs. The growth interruption and high-temperature annealing were deliberately used to make the InAs QDs in an array more uniform in size and to reduce the height/base ratio, i.e., to obtain disk-shaped islands.

The structure of the samples was studied by diffraction microscopy and high-resolution electron microscopy on JEM 4010 (accelerating voltage 400 kV) and Philips CM20 (accelerating voltage 200 kV) microscopes, respectively. Quantitative analysis of the QM composition was performed using the TEM images recorded with atomic resolution.

Steady-state PL was excited by the radiation of a cw Ar laser with a wavelength of 488 nm (2.54 eV). In measurements of the dependence of the PL intensity on the excitation radiation intensity, the laser beam was focused on a sample and the power density was varied from 0.2 to 300 W/cm^2 using neutral filters. The PL signal was detected by a cooled Ge photodetector (Edinburgh Instruments) at the output of a 50-cm monochromator. To study the time-resolved PL spectra, we used excitation by 100-fs pulses of a Tsunami Ti:sapphire laser with a wavelength of 790 nm (1.57 eV) and a pulse repetition frequency of 82 MHz. The PL signal was dispersed by a 25-cm monochromator matched with a Hamamatsu-C1587 streak camera and recorded by a CCD camera. The instrumental resolution of the system was 15 ps. In all the cases, the samples were placed in cryostats, which made it possible to vary and stabilize the temperature in the range 5–300 K.

3. RESULTS AND DISCUSSION

The problem of obtaining QDs tunnel-coupled along the growth direction with a very small difference in geometric parameters lies in the fact that the size of QDs in the upper layer depends on the spacer thickness and the size of QDs in the lower layer. Figure 1 shows the cross sectional TEM image of an *A*-type sample containing two InAs MLs in each QD layer. It can be seen that, given the same thickness of the deposited InAs layer, the sizes of islands in the upper and lower

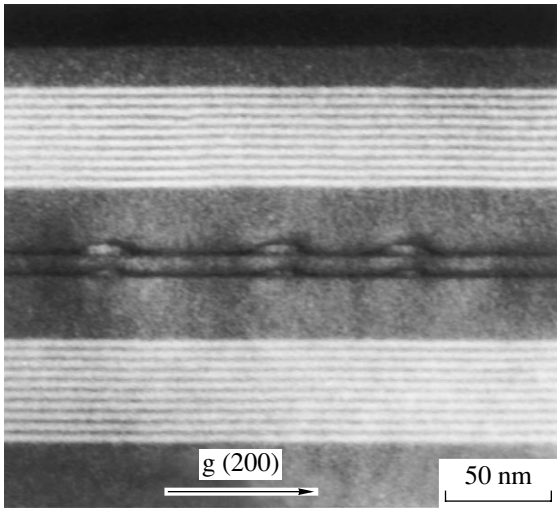

Fig. 1. Dark-field TEM image of an *A*-type structure.

layers differ significantly: the parameter h (height) $\times$ B (base) for the upper QD$|1\rangle$ and lower QD$|0\rangle$ is equal to 7×28 and 4×22 nm^2, respectively. The vertical correlation between QDs is due to the elastic-stress fields formed by the QDs of the lower layer. The increase in the QD size and the decrease in the effective critical thickness corresponding to the transition from two-dimensional (2D) to 3D growth, which was observed by RHEED, is explained by the effect of the accumulation of elastic energy in the upper layer [9]. A decrease in the thickness of the GaAs spacer between the QD layers leads to an even larger difference in the sizes of the islands, all other factors being equal. Thus, the main growth parameters that are responsible for the formation of QMs and need to be optimized are the effective thicknesses of InAs layers, the ratio of these thicknesses, and the spacer size. The optimization of these parameters made it possible to obtain a structure with characteristics meeting the necessary conditions for formation of QMs (*B*-type sample). The TEM image of such a structure is shown in Fig. 2a. The high-resolution electron microscopy image of a separate QM is shown in Fig. 2b. Figure 2c shows the In-depth profile along the growth direction. In contrast to the *A*-type samples, both the composition and the sizes of islands forming a molecule in the *B*-type structure are very similar. Thus, $h \times B \approx 4 \times 18$ nm^2 for both islands in a molecule. The general decrease in the QD size and symmetrization of the QM were obtained as a result of the combined action of two factors: high-temperature annealing and the small thickness of the GaAs spacer. It was shown in [11] that high-temperature annealing removes the residual In layer from the surface, thus simplifying the control of the effective thickness of the subsequent layer. At the same time, high-temperature annealing of an array of InAs islands covered by a thin (5 nm or thinner) GaAs layer improves the uniformity of QD sizes due to the evaporation of high islands. Tak-

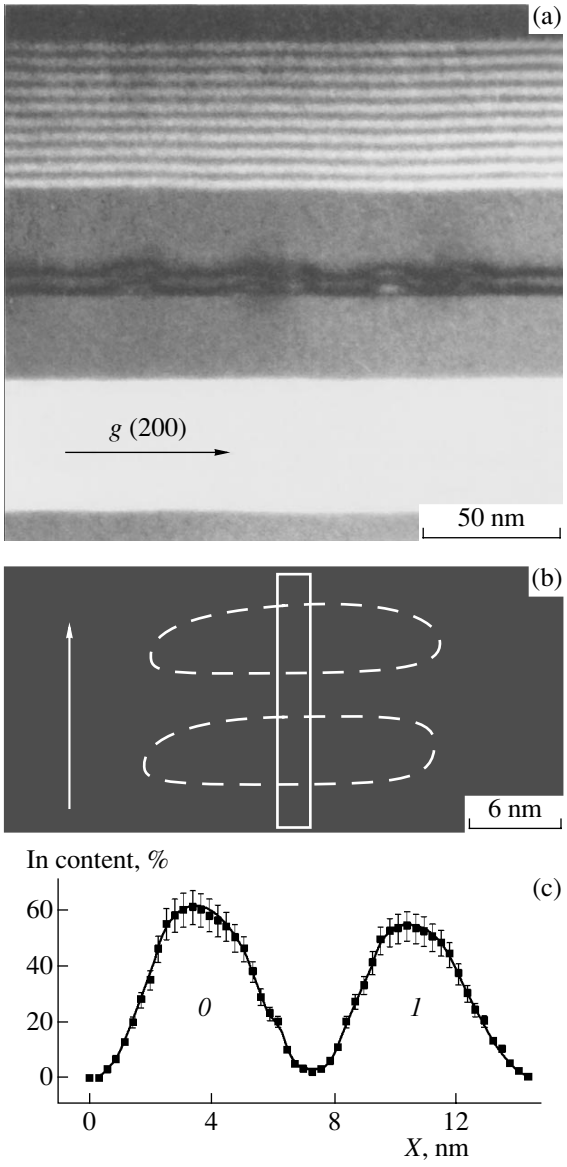

Fig. 2. Results of structural analysis of a *B*-type structure: (a) dark-field TEM image; (b) high-resolution TEM image obtained after Fourier filtration (one transmitted and four reflected beams sensitive to indium content were used to form the image); and (c) indium depth profile along the growth direction *X* for a coupled QD pair (the In content was measured in the region marked by a rectangle in (b)). *0* and *1* stand for QD|0⟩ and QD|1⟩, respectively. The arrow in (b) shows the growth direction.

ing these factors into account in optimization of the QM structures, we obtained the following parameters: the effective thicknesses of the lower and upper InAs layers are four and two MLs, respectively, and the spacer size is 5 nm. According to the TEM data, the spacer size strictly corresponded to the distance between the wetting layers: 10 and 5 nm for *A*- and *B*-type structures, respectively (Figs. 1, 2). The vertical gap between neighboring QDs was 7 and 3 nm (*A* and *B* types, respectively).

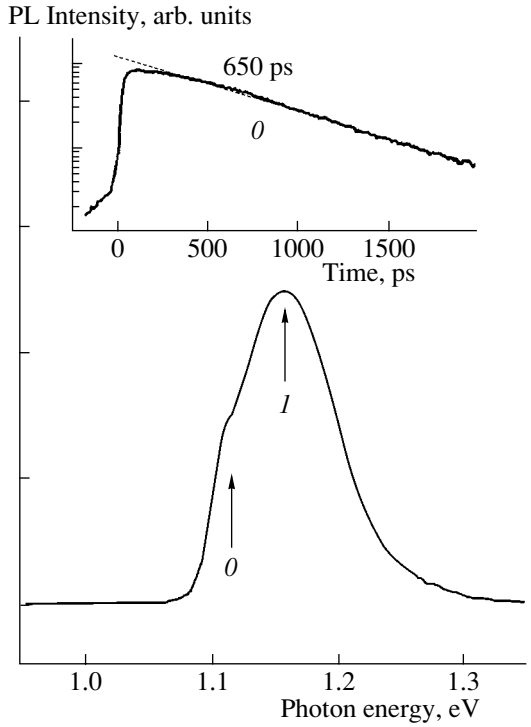

Fig. 3. PL spectrum of an *A*-type structure at a temperature of 10 K and excitation density of 2 W/cm^2; excitation by an Ar^+ laser; *0* and *1* stand for QD|0⟩ and QD|1⟩, respectively.

To study the energy-band structure and interactions between exciton levels in QMs, we measured the PL and time-resolved PL spectra. The PL spectrum of an *A*-type sample is shown in Fig. 3. As can be seen, this spectrum has an asymmetric shape, which is independent of both the excitation intensity and the measurement temperature. Decomposition into Gaussian profiles shows that the spectrum consists of two bands peaked at 1.115 and 1.165 eV. Such a spectrum is not characteristic of transitions involving excited states but is typical of two groups of QDs uncoupled with each other. In our case it is obvious that these QDs are the QD|0⟩ and QD|1⟩ of the lower and upper layers, respectively, whose sizes, according to the TEM data, differ significantly (Fig. 1). The absence of PL-active excited states in the spectrum of *A*-type QDs is confirmed by the high-resolution PL data, which show only one PL-decay time for the band measured: ~650 ps (see inset in Fig. 3). In addition, no signal was observed in the high-energy part of the time-resolved PL spectrum of the *A*-type structure.

The *B*-type structure has a radically different low-temperature PL spectrum (Fig. 4). At low excitation levels, two PL bands could be easily resolved: s_+ (1.21 eV) and p_+ (1.25 eV). When the excitation density exceeded 50 W/cm^2, the p_+ band became dominant in the PL spectrum and a new band d_+ (1.30 eV) arose in the high-energy region. At an excitation density of 300 W/cm^2, the band d_+ became dominant and another short-wave-

length band arose: d_x (1.32 eV). Before coming to the steady state, the dependence of the integrated PL intensity on the excitation density ($J = P^\nu$) was described well by the factor $\nu = 1$ for the selected PL bands. The found evolution of the PL spectrum of the *B*-type structure is typical of a unified system of energy levels with a low rate of nonradiative carrier recombination. The temperature dependence of the PL of the *B*-type structure cannot be described quantitatively by a simple Arrhenius plot and is not reported here. Radical changes occur above 120 K, when all the bands due to the transitions involving excited states (p_+ and d_+) disappear in the PL spectrum.

The TEM and PL data, as well as the calculations performed in the adiabatic effective-mass approximation [15], indicate the possibility of existence of a QM in the *B*-type structure. The state of an individual single QD is characterized by an isospin and angular momentum. When two identical QDs approach each other, the following processes occur: coherent tunneling, overlapping of the electron wave functions, and isospin mixing. The distribution of the wave functions of an electron *e* and a hole *h* between two identical QDs (QD|0⟩ and QD|1⟩) gives rise to the following four isospin configurations:

$$b_1 = (|0\rangle_e + |1\rangle_e)(|0\rangle_h + |1\rangle_h)/2,$$

$$b_2 = (|0\rangle_e - |1\rangle_e)(|0\rangle_h - |1\rangle_h)/2,$$

$$a_1 = (|0\rangle_e + |1\rangle_e)(|0\rangle_h - |1\rangle_h)/2,$$

$$a_2 = (|0\rangle_e - |1\rangle_e)(|0\rangle_h + |1\rangle_h)/2.$$

The b_1 and b_2 states are symmetric (coupled) and optically active, while the a_1 and a_2 states are antisymmetric (uncoupled) and "dark" in PL. The presence of QD states with different angular momenta $m = 0, \pm 1$ in this basis leads to the mixing of *s* and *p* states in the QM. However, the separation into the *a* and *b* states is retained even when Coulomb interaction is taken into account. Because of this, each exciton level (*s* and *p*) in a QM is split into two states: symmetric $|+\rangle$ and antisymmetric $|-\rangle$; the *d* state can be split into a larger number of levels [16, 17]. The symmetric *s* and *p* states remain optically active and can contribute to PL. Obviously, these states manifest themselves in the PL spectrum of the *B*-type structure in the form of s_+ and p_+ bands (Fig. 4). Successive occupation of states with increasing excitation intensity leads to the manifestation of higher-lying states (d_+ and d_x) in the PL spectrum of the QM. In the dependence of the PL spectrum on the excitation density (Fig. 4), the short-wavelength shift of the positions of the p_+ and d_+ bands is also quite reasonable. This shift is due to the nonuniformity of the QD sizes and occupation of shallower QMs by excitons. We attribute the insignificant red shift of the s_+ band to the formation of biexcitons due to the exciton–exciton interaction at high pump density. Radiative recombination of a biexciton in an InAs QM with an

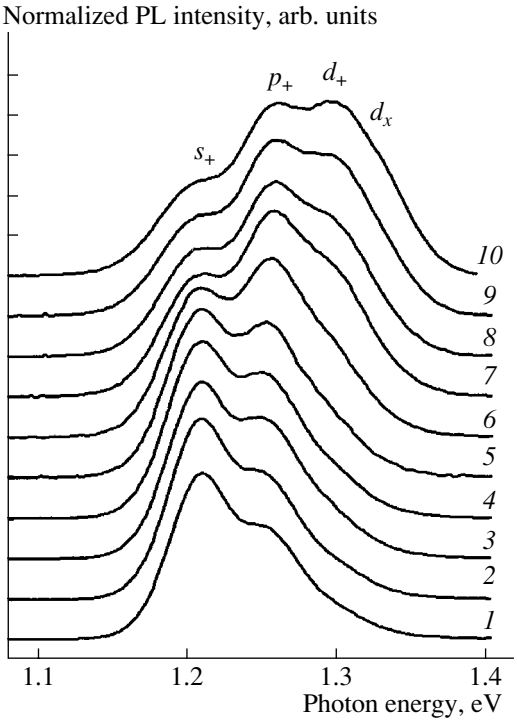

Fig. 4. Steady-state PL spectra of a *B*-type structure with a QM at a temperature of 10 K and excitation density P = (*1*) 0.2, (*2*) 2, (*3*) 10, (*4*) 13, (*5*) 25, (*6*) 50, (*7*) 100, (*8*) 130, (*9*) 200, and (*10*) 300 W/cm^2.

energy 5 meV below the symmetric *s* state was also observed [17]. Decomposing the PL spectra into Lorentzian profiles, we obtained the following values of splitting in the portions of the dependence $J = P^\nu$ with $\nu = 1$: 40 meV between the s_+ and p_+ states, 50 meV between the p_+ and d_+ states, and 20 meV between the d_+ and d_x states. The ratio of the values of the energy gaps obtained by us is in good agreement with the results of calculations [15–17]. The value of the s_+–p_+ gap (40 meV) corresponds to the experimental data [18] for a spacer ~4.5 nm thick. A gap 23 ± 7 meV wide between the active states was observed for a spacer 5 nm thick in [17]. The insignificant discrepancy between these data is obviously due to the difference in the shapes and sizes of the QDs forming a QM. However, the relatively large values of splitting and gaps between the levels (up to 50 meV) do not ensure the conservation of the PL spectrum of a QM at room temperature ($kT \simeq 25$ meV). According to the calculations [15–17], intersection of the symmetric $p|+\rangle$ and antisymmetric $s|-\rangle$ levels occurs when the spacer thickness does not exceed 4.5 nm. It should be noted that, although the antisymmetric dark states do not manifest themselves in the steady-state PL spectra, they may be involved in thermally activated interlevel transitions and the processes of excitation relaxation. In this context, it was very interesting to measure the PL decay time in QMs. Figure 5 shows the time-resolved PL

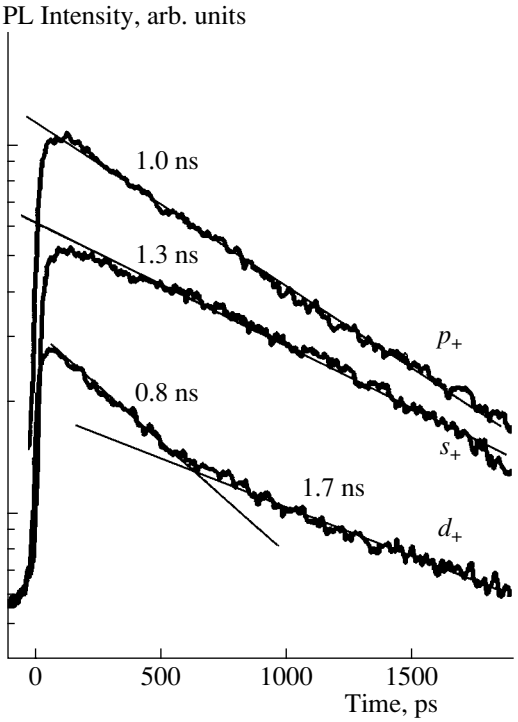

Fig. 5. Time-resolved PL for *B*-type structures. The PL decay times are measured in the central parts of the s_+, p_+, and d_+ bands. The measurement temperature is 10 K and the average excitation density is 5 W/cm^2.

spectrum of a *B*-type structure. The following results are important to note.

(1) The exciton emission times in InAs QMs are no less than 1 ns, specifically, 1.3, 1, and 1.7 ns for the s_+, p_+, and d_+ states.

(2) For the second excited state d_+, the radiative lifetime of excitons exceeds that for the lower exciton states s_+ and p_+.

(3) For the first excited state p_+, the relaxation PL decay is absent, in contrast to the second excited state d_+, for which the relaxation decay time is 0.8 ns.

The time-resolved PL data are in favor of the mechanism of inverse population of the second excited state d_+ with respect to the lower s_+ and p_+ states. In this case, the emission is in the wavelength range 13–25 μm. Taking into account the factor $\nu = 1$ (low rate of nonradiative recombination and low concentration of defects in the *B*-type structure), we can suggest that the primary PL decay time in the d_+ band is the time of radiative transition to lower exciton levels (0.8 ns). The absence of relaxation from the first excited state p_+ to the ground exciton state s_+ can be caused by the proximity of the $p|+\rangle$ level to the point of intersection with the antisymmetric dark state $s|-\rangle$, due to which the radiative transition $p_+ \longrightarrow s_+$ becomes forbidden, while there is practically no intermediate level for successive relaxation.

QMs were not observed in the *A*-type structure for various reasons. As calculations [15–17] show, a 10-nm GaAs barrier is too thick to allow for tunnel coupling between QDs. The value of splitting expected in this case (5 meV) is much smaller than the inhomogeneous broadening of the PL bands (~50 meV) due to the dispersion of QM sizes. QM may also be absent in the upper layer of the *A*-type structure because of the inconsistency in the sizes of the QDs. Since QDs are larger in the *A*-type structure, a spectrally resolved structure of PL bands involving excited states cannot be formed (Fig. 3) and, instead of rotation of isospins and splitting of exciton levels, carrier transport occurs in asymmetric QD pairs.

Thus, we determined the process parameters necessary to obtain InAs/GaAs structures with QMs. Using intermediate high-temperature annealing, we obtained symmetric QMs with a 5-nm spacer. Four radiative transitions in the PL spectrum, related to the symmetric exciton QM states (one ground and three excited), were investigated. The values of the decay times of the QM PL indicate the probability of interlevel radiative recombination from the second excited state and the absence of any relaxation between the first excited and ground exciton states of the QM.

ACKNOWLEDGMENTS

We are grateful to L.E. Vorob'ev and D.A. Firsov for their discussion of the results.

This study was supported in part by INTAS; the scientific programs of the Ministry of Industry, Science, and Technology of the Russian Federation; and the Russian Foundation for Basic Research.

G.É. Cirlin acknowledges the support of the Alexander von Humboldt Foundation. V.M. Ustinov acknowledges the support of the Foundation for the Promotion of Leading Scientific Schools.

REFERENCES

1. D. Bimberg, M. Grundmann, and N. N. Ledentsov, *Quantum Dot Heterostructures* (Wiley, Chichester, 1998).
2. N. A. Maleev, A. R. Kovsh, A. E. Zhukov, *et al.*, Fiz. Tekh. Poluprovodn. (St. Petersburg) **37**, 1265 (2003) [Semiconductors **37**, 1234 (2003)].
3. V. M. Apalkov and T. Chakraborty, Appl. Phys. Lett. **78**, 1820 (2001).
4. S. Sauvage, P. Boucaud, T. Brunhes, *et al.*, Appl. Phys. Lett. **78**, 2327 (2001).
5. S. Sauvage, P. Boucaud, T. Brunhes, *et al.*, Phys. Rev. B **60**, 15589 (1999).
6. B. V. Volovik, D. S. Sizov, A. F. Tsatsul'nikov, *et al.*, Fiz. Tekh. Poluprovodn. (St. Petersburg) **34**, 1368 (2000) [Semiconductors **34**, 1316 (2000)].
7. K. Eberl, O. G. Schmidt, R. Duschl, *et al.*, Thin Solid Films **369**, 33 (2000).
8. J. Tersoff, C. Teichert, and M. G. Lagally, Phys. Rev. Lett. **76**, 1675 (1996).

9. G. É. Cirlin, V. N. Petrov, S. A. Masalov, and A. O. Golubok, Fiz. Tekh. Poluprovodn. (St. Petersburg) **33**, 733 (1999) [Semiconductors **33**, 677 (1999)].
10. N. N. Ledentsov, V. M. Ustinov, V. A. Shchukin, *et al.*, Fiz. Tekh. Poluprovodn. (St. Petersburg) **32**, 385 (1998) [Semiconductors **32**, 343 (1998)].
11. Z. R. Vasilewski, S. Fafard, and J. P. McCaffrey, J. Cryst. Growth **201–202**, 1131 (1999).
12. P. Boucaud, J. B. Williams, K. S. Gill, *et al.*, Appl. Phys. Lett. **77**, 4356 (2000).
13. W. Sheng and J.-P. Leburton, Appl. Phys. Lett. **81**, 4449 (2002).
14. V. N. Petrov, V. N. Demidov, N. P. Korneeva, *et al.*, Zh. Tekh. Fiz. **70**, 97 (2000) [Tech. Phys. **45**, 618 (2000)].
15. W. Sheng and J.-P. Leburton, Appl. Phys. Lett. **81**, 4449 (2002); Phys. Status Solidi B **237**, 394 (2003).
16. K. Hinzer, M. Bayer, J. P. McCaffrey, *et al.*, Phys. Status Solidi B **224**, 385 (2001).
17. M. Korkusinski, P. Hawrylak, M. Bayer, *et al.*, Physica E (Amsterdam) **13**, 610 (2002).
18. M. Bayer, P. Hawrylak, K. Hinzer, *et al.*, Science **291**, 451 (2001).

Translated by Yu. Sin'kov

Semiconductors, Vol. 38, No. 6, 2004, pp. 702–711. Translated from Fizika i Tekhnika Poluprovodnikov, Vol. 38, No. 6, 2004, pp. 729–738.

LOW-DIMENSIONAL SYSTEMS

Role of Si-Doped $Al_{0.3}Ga_{0.7}As$ Layers in the High-Frequency Conductivity of GaAs/$Al_{0.3}Ga_{0.7}As$ Heterostructures under Conditions of the Quantum Hall Effect

I. L. Drichko[1]*, A. M. D'yakonov[1], I. Yu. Smirnov[1], Yu. M. Gal'perin[1, 2], V. V. Preobrazhenskiĭ[4], and A. I. Toropov[4]

[1]*Ioffe Physicotechnical Institute, Russian Academy of Sciences, Politekhnicheskaya ul. 26, St. Petersburg, 194021 Russia*
**e-mail: Irina.L.Drichko@mail.ioffe.ru*
[2]*Department of Physics, University of Oslo, PO Box 1048 Blindern, 0316 Oslo, Norway*
[3]*Argonne National Labaratory, 9700 S. Cass av., Argonne, IL 60439, USA*
[4]*Institute of Semiconductor Physics, Siberian Division, Russian Academy of Sciences, pr. Akademika Lavrent'eva 13, Novosibirsk, 630090 Russia*

Submitted November 17, 2003; accepted for publication November 17, 2003

Abstract—The complex high-frequency conductivity of GaAs/$Al_{0.3}Ga_{0.7}As$ heterostructures that are δ-doped and modulation-doped with silicon was investigated by acoustic methods under conditions of the integer quantum Hall effect. Both the real (σ_1) and imaginary (σ_2) parts of the complex conductivity $\sigma(\omega, H) = \sigma_i - i\sigma_2$ were determined from the dependences of the absorption and velocity of surface acoustic waves on magnetic field. It is shown that, in the heterostructures with electron density $n_s = (1.3–7) \times 10^{11}$ cm^{-2} and mobility $\mu = (1–2) \times 10^5$ cm^2/(V s), the high-frequency conductivity near the centers of the Hall plateau is due to electron hopping between localized states. It is established that, with filling numbers 2 and 4, the conductivity of the $Al_{0.3}Ga_{0.7}As$:Si layer efficiently shunts the high-frequency hopping conductivity of the two-dimensional interface layer. A method of separating the contributions of the interface and $Al_{0.3}Ga_{0.7}As$:Si layers to the hopping conductivity $\sigma(\omega, H)$ is developed. The localization length of electrons in the interface layer is determined on the basis of the nearest neighbor hopping model. It is shown that, near the centers of the Hall plateau, both $\sigma(\omega, H)$ and n_s depend on the cooling rate of a GaAs/$Al_{0.3}Ga_{0.7}As$ sample. As a result, the sample "remembers" the cooling conditions. Infrared light and static strain also change both $\sigma(\omega, H)$ and n_s. We attribute this behavior to the presence of two-electron defects (so-called DX^- centers) in the $Al_{0.3}Ga_{0.7}As$:Si layer. © *2004 MAIK "Nauka/Interperiodica".*

1. INTRODUCTION

Studies of the dc magnetoresistance components ρ_{xx}^{dc} and ρ_{xy}^{dc} and the conductivity σ_{xx}^{dc} calculated from the values of these components for heterostructures with the quantum Hall effect showed that, in the magnetic fields corresponding to Hall plateaus with small even filling numbers ν, the values of ρ_{xx}^{dc} and σ_{xx}^{dc} are exponentially small [1]. It is agreed that this circumstance is due to the localization of charge carriers at a random potential formed by charged impurities separated from the two-dimensional (2D) interface layer by an undoped layer (spacer). When conductivity is due to hops of electrons between localized states, dc conductivity can be observed only when an electron passes through the entire sample along the cluster of impurity atoms. At the same time, ac conductivity can be observed only when electrons hop within so-called compact pairs [2]. Therefore, the ac conductivity exceeds the dc conductivity: $|\sigma_{xx}^{as}(\omega)| > \sigma_{xx}^{dc}$.

If the absorption of a surface acoustic wave (SAW) with frequency ω is measured simultaneously with the change in its velocity ΔV (both the absorption and the change in velocity are related to the interaction of this wave with electrons in the heterostructure), one can determine the complex high-frequency conductivity $\sigma_{xx}^{ac}(\omega) = \sigma_1(\omega) - i\sigma_2(\omega)$ at frequency ω. In this case, both the imaginary and real parts can be determined separately. It was shown by Éfros [3] that, for a structure with 2D hopping conductivity, $\sigma_2(\omega) \gg \sigma_1(\omega)$ and $\sigma_1(\omega) \propto \omega\xi^3$ (ξ is the localization length of electrons). If the hops between the electronic states localized in the 2D layer mainly contribute to $\sigma_{xx}^{as}(\omega)$, the measured value of the complex conductivity can be used to determine the localization length in the 2D interface layer near the centers of the Hall plateau. This was the initial aim of our study.

The results of high-frequency measurements carried out on a large number of GaAs/$Al_{0.3}Ga_{0.7}As$ hetero-

structures δ-doped and modulation-doped with silicon [4] made it possible to conclude the following.

(1) In the magnetic fields corresponding to the centers of the Hall plateau, the value of σ_{xx}^{ac} at $T = 1.5$–4.2 K, as expected, turned out to be finite.

(2) In this case, it was observed that $\sigma_2(\omega) \gg \sigma_1(\omega)$. According to [3], this fact indicates the hopping nature of the high-frequency conductivity.

(3) At the same time, the localization length of electrons ξ, calculated from the experimental value of the high-frequency conductivity, turned out to be too large: about 10^{-5} cm. Such a large value of ξ is beyond the range of applicability of the two-site model [2], on which the calculations are based [4]. In addition, we did not observe in [4] dependences of σ_1 and σ_2 and, accordingly, ξ on magnetic field near $\nu = 2$. The results of the experiments carried out in [4] were inconsistent with the data of [5], where ξ was determined from dc measurements under conditions of hopping conductivity. The experiments performed in [5] demonstrated a very heavy dependence of the localization length ξ on magnetic field in the vicinity of $\nu = 2$.

On the basis of all these facts, we concluded that the observed high-frequency hopping conductivity is, apparently, due to the carrier transport not only over the interface layer but also over parallel layers. It is likely that the $Al_{0.3}Ga_{0.7}As$:Si layer, which supplies charge carriers to the interface channel, serves as a shunt in the multilayer heterostructures under study.

It is well known (see, for example, [6]) that silicon forms defects called DX^- centers in the alloy $Al_{0.3}Ga_{0.7}As$:Si. These centers are generally believed to be responsible for the effects observed in this compound: persistent photoconductivity [7], the difference in the energies of thermal and optical activation, and the increase in the carrier mobility in the 2D interface layer, which arises due to the effects of correlation in the position of charged impurities [8].

In order to determine the role of $Al_{0.3}Ga_{0.7}As$:Si layers in the high-frequency conductivity of the multilayer $Al_{0.3}Ga_{0.7}As$:Si heterostructure with small filling numbers, it was reasonable to measure the acoustoelectric effects arising due to various external factors. We investigated the influence of the following factors: infrared (IR) light, strain, and the cooling of samples to $T = 4.2$ K under different conditions, since it is precisely these factors that affect the electron configuration of DX^- centers and, accordingly, the conductivity of the system under study. It should be noted that the extensive data in the literature on DX^- centers in $Al_{0.3}Ga_{0.7}As$:Si films and $GaAs/Al_{0.3}Ga_{0.7}As$:Si heterostructures refer mainly to the effect of these centers on static conductivity due to the presence of delocalized electrons. In this paper, we report the results of studying the influence of external factors and, accordingly, the state of DX^- centers on the high-frequency conductivity in a magnetic field due to the presence of localized charge carriers, i.e., on the high-frequency hopping conductivity. Analysis of the experimental data is performed for magnetic fields corresponding to small even filling numbers. In essence, we generalize here the results of our previous research [4, 9–11].

2. EXPERIMENTAL

2.1. Measuring Technique

The experimental technique was described in detail in [12]. We only note here that the heterostructure under study was pressed by a spring against the surface of an insulator substrate made of lithium niobate ($LiNbO_3$), over which a piezoactive SAW propagated (Fig. 1a). The electric field accompanying the strain wave and changing with time with the SAW frequency penetrates the 2D layer. Interacting with electrons, the wave induces electric currents and, therefore, gives rise to Joule losses. As a result, the amplitude of the wave decreases and its velocity changes. It is important that, under these experimental conditions, the piezoelectric crystal and sample are not mechanically coupled and a SAW is only used to introduce an ac electric field into the sample using no electric contacts.

In this study, we measured the absorption coefficient Γ and the relative variation in the velocity $\Delta V/V$ of SAWs with frequency $f = \omega/2\pi = (30$–$150)$ MHz in magnetic fields up to 7 T, at $T = 4.2$ and 1.5 K, in $GaAs/Al_{0.3}Ga_{0.7}As$:Si heterostructures grown by molecular-beam epitaxy (MBE) and doped in different ways. The heterostructures δ-doped with Si had electron density in the 2D layer $n_s \approx (1.4$–$4) \times 10^{11}$ cm^{-2} and mobility $\mu \approx 1.5 \times 10^5$ cm^2/(V s), whereas the heterostructures modulation-doped with Si had $n_s \approx (2.4$–$7) \times 10^{11}$ cm^{-2} and $\mu \approx (0.4$–$1.2) \times 10^5$ cm^2/(V s). The values of n_s and μ were determined from acoustic measurements [13]. The structure of the samples is shown in Figs. 1b and 1c. As can be seen, the heterostructures are multilayer systems in which the interface channel is located at distance d from the sample edge.

The penetration depth of the electric field of an SAW in the dielectric part of the structure is about q^{-1}, where $q = \omega/V$ is the wave vector of the SAW. For an adequate interpretation of the experimental results, it is important that, in the frequency range under study, this depth is much larger than the distance between the interface layer and the doped AlGaAs region. Therefore, the high-frequency conductivity $\sigma_{xx}^{ac}(\omega)$ measured by us is the effective conductivity of the interface and doped layers connected in parallel. In determining the high-frequency conductivity from the experimental data on the absorption and velocity of SAWs, a system consisting of the interface and doped layers is simulated by one layer with effective complex conductivity $\sigma_{xx}(\omega)$. In this case, the permittivities of the GaAs and AlGaAs layers are assumed to be the same: $\varepsilon_s = 12$, and the effective permittivity of $LiNbO_3$ ε_1 is assumed to be

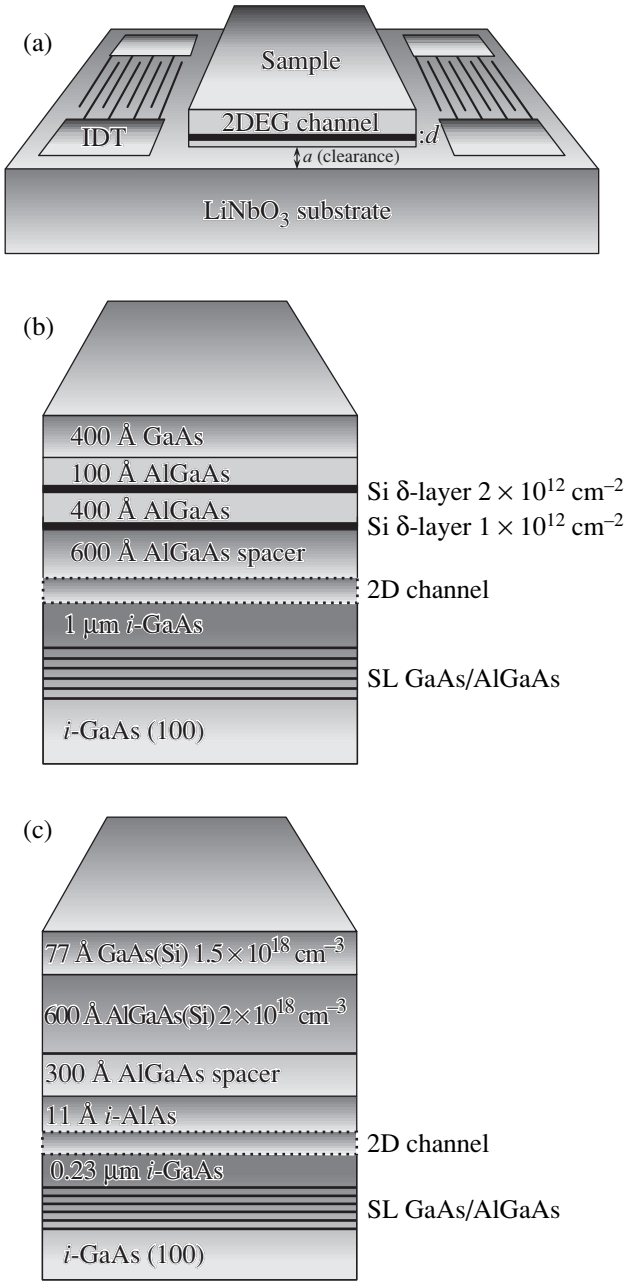

Fig. 1. (a) Schematic of the acoustic experiment, (b) the structure of a sample δ-doped with Si ($n_s = 1.5 \times 10^{11}$ cm^{-2}), and (c) the structure of a sample modulation-doped with Si ($n_s = 2.4 \times 10^{11}$ cm^{-2}).

equal to 50. The vacuum gap between the heterostructure and the $LiNbO_3$ plate a is determined by the surface roughness of the sample and insulator plate. It is difficult to control the value of a in experiment; hence, it is considered as a fitting parameter. This parameter can be determined in the range of magnetic fields where electrons are delocalized and the high-frequency conductivity can be considered frequency-independent. For differently mounted samples, these values are in the range $(1–5) \times 10^{-5}$ cm.

The absorption coefficient Γ and the relative variation in the SAW velocity $\Delta V/V$ are related to the complex conductivity as follows [4]:

$$\Gamma = 8.68\frac{K^2}{2}qA\frac{4\pi\sigma_1 t(q)/\varepsilon_s V}{[1+4\pi\sigma_2 t(q)/\varepsilon_s V]^2 + [4\pi\sigma_1 t(q)/\varepsilon_s V]^2},$$
$$A = 8b(q)(\varepsilon_1+\varepsilon_0)\varepsilon_0^2\varepsilon_s\exp[-2q(a+d)], \quad (1)$$
$$\frac{\Delta V}{V} = \frac{K^2}{2}A\frac{[1+4\pi\sigma_2 t(q)/\varepsilon_s V]}{[1+4\pi\sigma_2 t(q)/\varepsilon_s V]^2 + [4\pi\sigma_1 t(q)/\varepsilon_s V]^2},$$
$$b(q) = [b_1(q)[b_2(q)-b_3(q)]]^{-1},$$
$$t(q) = [b_2(q)-b_3(q)]/[2b_1(q)],$$
$$b_1(q) = (\varepsilon_1+\varepsilon_0)(\varepsilon_s+\varepsilon_0) - (\varepsilon_1-\varepsilon_0)(\varepsilon_s-\varepsilon_0)\exp(-2qa),$$
$$b_2(q) = (\varepsilon_1+\varepsilon_0)(\varepsilon_s+\varepsilon_0) + (\varepsilon_1+\varepsilon_0)(\varepsilon_s-\varepsilon_0)\exp(-2qd),$$
$$b_3(q) = (\varepsilon_1-\varepsilon_0)(\varepsilon_s-\varepsilon_0)\exp(-2qa) + (\varepsilon_1-\varepsilon_0)(\varepsilon_s+\varepsilon_0)\exp[-2q(a+d)],$$

where the absorption coefficient Γ is expressed in dB/cm; K^2 is the electromechanical coupling constant of $LiNbO_3$; q and V are the wave vector and velocity of the SAW, respectively; ε_1, ε_0, and ε_s are the permittivities of lithium niobate, vacuum, and gallium arsenide, respectively; a is the distance between the insulator and heterostructure under consideration; d is the depth at which the 2D layer is located [4]; and $\sigma_{xx}^{ac} = \sigma_1 - i\sigma_2$. These formulas make it possible to determine σ_1 and σ_2 from the measured values of Γ and $\Delta V/V$.

2.2. Dependence on the Cooling Conditions

One of the specific features of the acoustic technique used here is that one has to work in vacuum or rarefied gas, since SAWs are strongly absorbed by a liquid when the latter is used. In order to cool a sample (mounted on a cold finger) to 4.2 K, an exchange gas (rarefied He^4 at a pressure of ~0.1 Torr) was let into the preliminary pumped chamber containing a sample. The chamber was placed in liquid He^4, which could be pumped. In addition, before pouring the liquid helium, the superconducting solenoid was, as a rule, preliminarily cooled by liquid nitrogen.

If the exchange gas was let into the chamber with a sample at room temperature and the Dewar flask containing the chamber was slowly (for 1.5–2 h) cooled by a flow of cold He^4 gas, the filling of the Dewar flask with liquid helium began at sample temperature T_0 no higher than 7–8 K. We call this cooling procedure slow.

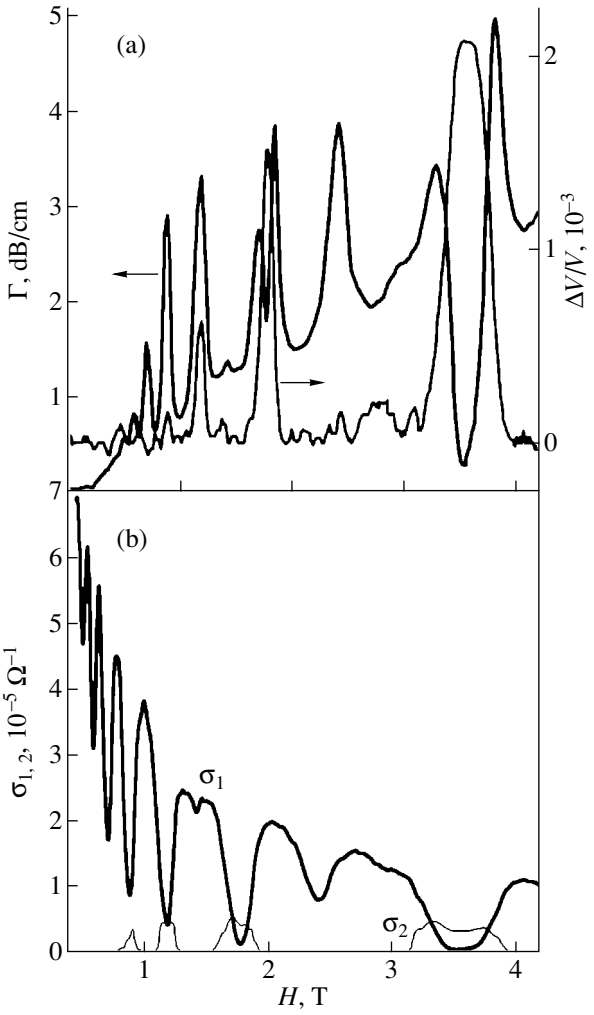

Fig. 2. Dependences of (a) Γ and $\Delta V/V$ and (b) σ_1 and σ_2 on magnetic field H for a slowly cooled sample with $n_s \approx 1.5 \times 10^{11}$ cm^{-2} at $f = 30$ MHz and $T = 1.5$ K.

To change the cooling procedure, the chamber with a sample was pumped and the Dewar flask with the chamber inside was filled with liquid helium. In this case, the sample temperature T_0 was higher than liquid helium temperature and depended on the residual pressure. After liquid helium was poured into the Dewar flask, an exchange gas was let into the chamber; as a result, the sample was cooled from T_0 to $T = 4.2$ K in 5–10 min. The highest temperature from which the fast cooling was performed was $T_0 \approx 77$ K. Samples were always cooled to $T = 1.5$ K by pumping liquid helium from the Dewar flask to a pressure of 5–6 Torr for 40–60 min.

Figure 2a shows the experimental dependences of Γ and $\Delta V/V$ (slow cooling) on magnetic field H at $T = 1.5$ K. These data were used to calculate the dependences $\sigma_1(H)$ and $\sigma_2(H)$ shown in Fig. 2b for a GaAs/AlGaAs sample δ-doped with silicon. It should be noted that, in magnetic fields corresponding to small integer even filling numbers (electrons are localized), $\sigma_2 \gg \sigma_1$ and, in magnetic fields corresponding to half-integer filling numbers (electrons are delocalized), $\sigma_2 = 0$.

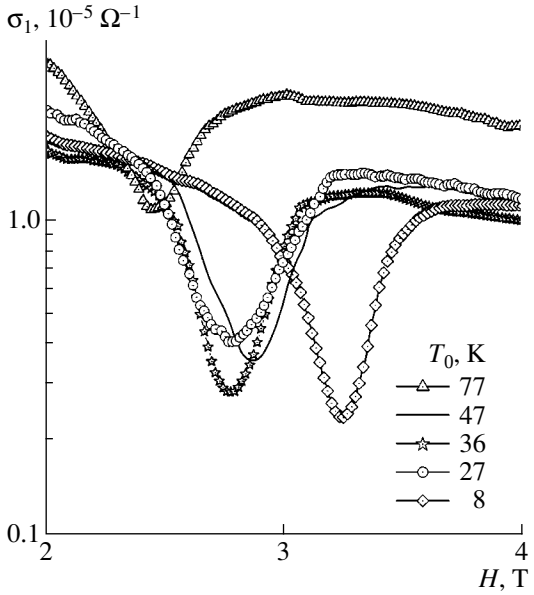

Fig. 3. Dependences of σ_1 on magnetic field H near $\nu = 2$ for different values of quenching temperature T_0 for a sample with $n_s \approx 1.5 \times 10^{11}$ cm^{-2} at $f = 30$ MHz and $T = 4.2$ K.

Figure 3 shows the dependences of σ_1 on magnetic field H in the range 2–4 T (near $\nu = 2$) for different values of T_0. It can be seen from Fig. 3 that, depending on T_0, not only the value of σ_1 at its minimum changes but also the impurity concentration in the 2D interface layer (equal to the electron density n_s), since the minima of conductivity are obtained in different magnetic fields. Similar results were obtained for σ_1 in magnetic fields corresponding to filling number $\nu = 4$. Figure 4 shows the dependences of (a) σ_1 and σ_2 and (b) n_s on T_0 at $\nu = 2$ for $T = 4.2$ K. It can be seen from Figs. 3 and 4 that the conductivities σ_1 and σ_2 increase and the concentration n_s decreases with increasing T_0. At low T_0, the ratio of conductivities σ_1/σ_2 is about 1.5; at $T_0 \approx 30$ K, $\sigma_1 \approx \sigma_2$; and at higher T_0 $\sigma_1 > \sigma_2$. Thus, in this case, the mechanism of high-frequency conductivity is not purely hopping even at low T_0, since, according to [4], the characteristic values of the ratio σ_2/σ_1 range from 3 to 4 under conditions of high-frequency hopping conductivity. The decrease in this ratio with increasing T_0 indicates that the contribution of delocalized electrons to conductivity increases. The same behavior of σ_1 and σ_2 was observed in the samples that were modulation-doped with silicon. When a sample was cooled from maximum temperature $T_0 = 77$ K, the electron density in the interface layer was the lowest ($n_s = 1.2 \times 10^{11}$ cm^{-2}), while the conductivity σ_1 was the highest. The values of these parameters remained the same for 28 h.

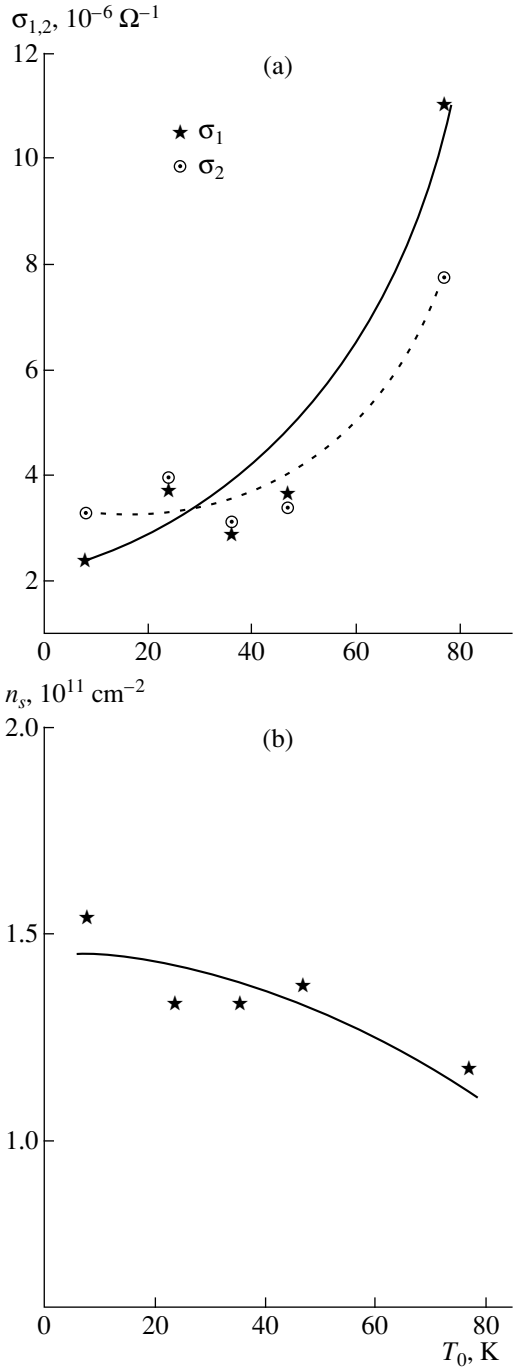

Fig. 4. Dependences of (a) σ_1 and σ_2 and (b) n_s on T_0 at $\nu = 2$ for a sample with $n_s \approx 1.5 \times 10^{11}$ cm^{-2} at $f = 30$ MHz and $T = 4.2$ K.

2.3. Effect of Illumination

We measured acoustoelectric effects in identical GaAs/$Al_{0.3}Ga_{0.7}$As:Si heterostructures exposed to IR light of different wavelengths. Proportioned illumination of samples was performed by micro-light-emitting diodes (LEDs) operating in the wavelength range λ = 0.8–5 μm, installed in the chamber with a sample,

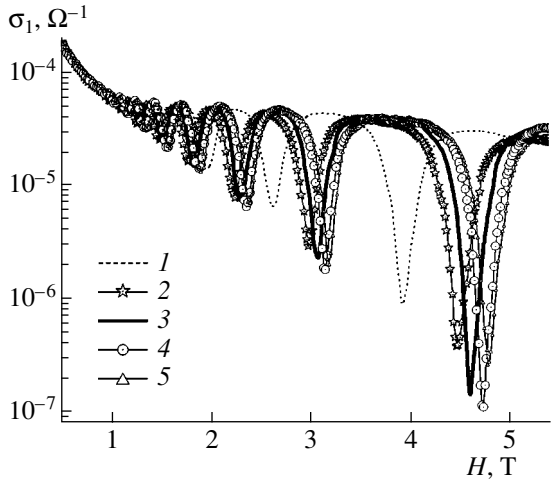

Fig. 5. Dependences of σ_1 on H for a sample with $n_s \approx 3.9 \times 10^{11}$ cm^{-2} (*1*) before illumination and (*2*–*5*) after successive proportioned IR illumination at $\lambda = 0.81$ μm; $T = 4.2$ K and $f = 30$ MHz.

which made it possible to increase the concentration of carriers in the 2D layer by small amounts. LEDs with wavelengths of 0.81, 1.44, 2.6, and 5.3 μm [14] were used for illumination. It turned out that when the energy of an IR photon decreases below a certain threshold value, frozen high-frequency hopping photoconductivity is not observed. This threshold is between 0.86 eV (λ = 1.44 μm) and 0.48 eV (λ = 2.6 μm). The dependences of σ_1 on H under successive illumination of a δ-doped sample with $n_s \approx 3.9 \times 10^{11}$ cm^{-2} with small doses of radiation from an LED with λ = 0.81 μm are shown in Fig. 5 ($T = 4.2$ K, $f = 30$ MHz). It can be seen from Fig. 5 that the values of σ_1 at its minimum decrease under successive short-term (shorter than 10 s) events of illumination and are obtained in different magnetic fields, which is indicative of a change in n_s.

Figure 6 shows the characteristic dependences of σ_1 and σ_2 on the electron density n_s obtained from the curves in Fig. 5. It can be seen from Fig. 6 that, under proportioned successive illumination of a sample, the increase in n_s is accompanied by a decrease in both σ_1 and σ_2, while their ratio $\sigma_2/\sigma_1 \approx$ 3–4 remains almost constant. Such values correspond to the conditions of high-frequency hopping conductivity [4]. However, such behavior is observed only at n_s below a certain limiting value above which the illumination hardly changes the value of n_s but significantly increases the conductivity.

2.4. Effect of Strain

The aforementioned measurements of acoustoelectric effects were performed under the following experimental conditions: a sample was freely lying on the surface of lithium niobate, only slightly pressed by a spring. In this experimental layout, the strain induced

by a sound wave is not introduced into the sample; only the electric field accompanying the strain wave penetrates the sample. However, in this experiment, one of the samples was glued to lithium niobate by a special adhesive capable of transferring strain into the sample. Figure 7 shows the dependences of the high-frequency conductivity σ_1 for (a) the sample slightly pressed by a spring against the lithium niobate substrate (slow cooling), (b) the same sample glued to the substrate (slow cooling), and (c) the sample glued to the substrate, after illumination. It can be seen from the curves in Fig. 7 that the electron density n_s in the glued sample decreases relative to the initial value by almost 30%, while the high-frequency conductivity of the heterostructure increases by almost two orders of magnitude. Thus, no contribution of hopping conductivity is observed. Short-term exposure to IR light (curve *3*) increased n_s almost to the initial value and returned the sample to the state with hopping conductivity; however, the value of $\sigma_1 = 3 \times 10^{-7}\ \Omega^{-1}$ at its minimum was in this case an order of magnitude larger than in the same sample freely lying on the substrate. All the above refers to the effects observed in a magnetic field corresponding to $\nu = 4$.

It is well known [15] that a hydrostatic pressure applied to $GaAs/Al_{0.3}Ga_{0.7}As$:Si heterostructures decreases the electron density n_s and increases the free-electron mobility. This effect is generally attributed to the enhanced filling of deep-level DX^- centers with increasing pressure (increase in the thermal activation energy) and, accordingly, the correlation in the position of charged impurities.

Since the changes in n_s in the sample glued to the lithium niobate substrate are the same as in the deformed sample [16], we can suggest that, upon cooling, a static strain arises in the glued sample, because the adhesive and the sample have different expansion coefficients. Regarding the dynamic strain, the very small power of the SAW introduced into the sample ($\sim 10^{-8}$ W) induces a strain of about 10^{-7}, which apparently does not affect the state of the sample. The absorption due to the strain interaction of an SAW with electrons should also be very low in the frequency range from 30 to 150 MHz in comparison with the piezoelectric interaction observed in this experiment. Thus, we believe that gluing $GaAs/Al_{0.3}Ga_{0.7}As$:Si heterostructure to a lithium niobate substrate exerts a static strain-like effect on the heterostructure.

3. RESULTS AND DISCUSSION

For definiteness, we will call "true" a value of n_s in the interface channel that is observed upon slow cooling of a sample in darkness, since apparently this value is closest to equilibrium. We will also focus on the vicinities of small even integer filling numbers (i.e., the regions where electrons are localized) and leave spin effects out of the discussion.

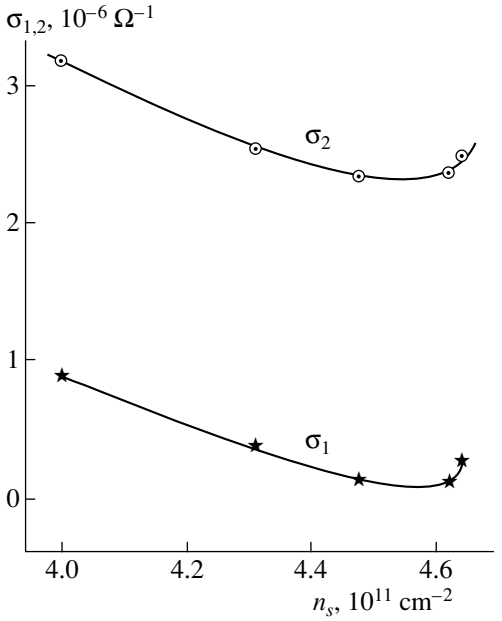

Fig. 6. Dependences of σ_1 and σ_2 on electron density n_s; $\lambda = 0.81$ μm, $T = 4.2$ K, $f = 30$ MHz, and $\nu = 4$.

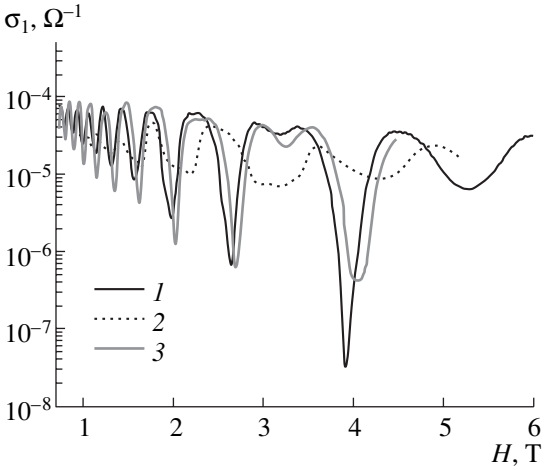

Fig. 7. Dependences of σ_1 on H for (*1*) a sample with $n_s \approx 3.9 \times 10^{11}$ cm^{-2} slightly pressed by a spring onto a lithium niobate substrate (slow cooling), (*2*) the same sample glued to a lithium niobate substrate (slow cooling), and (*3*) a sample glued to a lithium niobate substrate, after illumination; $T = 1.5$ K and $f = 30$ MHz.

The main experimental facts that relate to these regions and have to be explained are as follows.

(1) The high-frequency conductivity increases and n_s decreases with increasing quenching temperature T_0 (Fig. 4).

(2) Exposure of the samples to IR light leads to a decrease in σ_1 and σ_2 and an increase in n_s (Figs. 5, 6).

(3) A strain decreases n_s and increases σ_1 (Fig. 7).

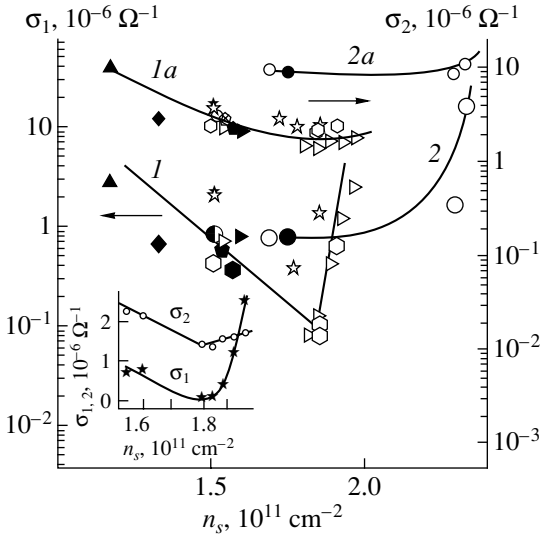

Fig. 8. Correlation between the components of high-frequency conductivity of the heterostructure, σ_1 (large symbols; curves *1*, *2*) and σ_2 (small symbols; curves *1a*, *2a*), and the electron density in the interface channel n_s. The values of σ_1 and σ_2 were obtained under different cooling conditions (close symbols) and successive illumination of a slowly cooled sample (open symbols); T = 1.5K, f = 30 MHz, and $\nu = 2$. The inset shows the dependences $\sigma_1(n_s)$ and $\sigma_2(n_s)$ after illumination of a slowly cooled sample.

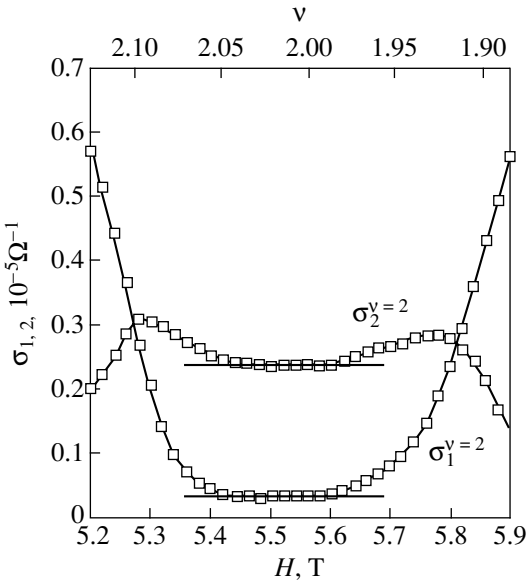

Fig. 9. Dependences of σ_1 and σ_2 on H near $\nu = 2$ for a sample with $n_s = 2.7 \times 10^{11}$ cm^{-2} at f = 30 MHz and T = 1.5 K (slow cooling).

(4) Dissimilar values of σ_1 and σ_2, obtained under different cooling conditions or due to the effect of different external factors on a sample, may correspond to the same value of n_s (Fig. 8).

(5) Under IR illumination, minima are observed in the dependences of σ_1 and σ_2 on n_s (Fig. 8).

(6) σ_1 and σ_2 are independent of H near even filling numbers (Fig. 9).

In order to explain the above experimental facts, we have to analyze the complex set of phenomena related to electronic transitions in the heterostructures under study. According to [17], doping with silicon introduces shallow donor levels with an activation energy of ~7 meV [17] (related to the Γ band) into the band gap of $Al_{0.3}Ga_{0.7}As$ alloys and gives rise to deep donor DX^- centers with an activation energy of ~80 meV [18] (related to the minimum of the L band) as a result of the reaction

$$2d_0 \longrightarrow d^+ + DX^-. \quad (2)$$

Here, d_0 is a neutral Si atom and d^+ is a Si ion. In a heavily doped material, where electrons form a degenerate gas (the case under consideration), DX^- centers can be formed as a result of the trapping of two electrons by an ion:

$$d^+ + 2e \longrightarrow DX^-. \quad (3)$$

In this case, if the Si atoms forming the shallow levels substitute the Ga atoms in the AlGaAs lattice, the formation of a DX^- center leads to the displacement of the Si atoms into interstitial sites and is accompanied by lattice strain.

Thus, the situation when donors in $Al_xGa_{1-x}As$ are partially occupied by electrons corresponds to the presence of positively charged d^+ ions and negatively charged DX^- centers. The occupation of donor impurity Si centers by electrons occurs so as to minimize the Coulomb interaction between these centers [16]. In this case, spatial correlations between impurity centers arise. Correlations in the position of impurity charges lead to a noticeable decrease in the amplitude of the random impurity potential [15]. Since it is precisely this random potential that is responsible for the localization of electrons in the interface layer, the correlations in the position of impurities should also affect the hopping conductivity in this layer.

When a sample is cooled, carriers are transferred from the conduction band of $Al_{0.3}Ga_{0.7}As$ to the Si impurity states and tunnel into the 2D interface layer.

We believe that, when fast cooling occurs, the electron distribution at the quenching temperature T_0 is frozen in a sample and does not change significantly as the temperature is further decreased to 4.2 K. Thus, in these cases, σ_1 and n_s at T = 4.2 K are in fact controlled by the corresponding values of σ_1 and n_s at $T = T_0$. Therefore, at the high quenching temperature T_0 = 77 K, both the electron density n_s and the population of impurity levels in the barrier $Al_{0.3}Ga_{0.7}As$ layer are low. Apparently, at this temperature, not all the electrons are frozen out of the conduction band. Therefore, conductivity occurs not only over the interface layer with large mobility, but also over the conduction band of $Al_{0.3}Ga_{0.7}As$. In this case, the localization effects manifest themselves only slightly and hopping conductivity is absent (Fig. 4). According to our experimental data for all the samples,

the electron density n_s and the random-potential amplitude increase with decreasing T_0. The role of localized states in the conductivity also increases. Accordingly, the conductivity via extended states decreases in this case. These processes manifest themselves in the aforementioned decrease in the high-frequency conductivity and the change in the ratio σ_1/σ_2 with decreasing T_0.

If we assume that, at $T = 4.2$ K, the conduction band of a slowly cooled $Al_{0.3}Ga_{0.7}As$:Si sample is completely depleted, the sum of the concentrations of electrons at impurity levels in the $Al_{0.3}Ga_{0.7}As$:Si layer and in the interface layer should be equal to the concentration of Si impurity in the $Al_{0.3}Ga_{0.7}As$ barrier layer. Therefore, the experimentally observed change in n_s due to the external effects occurs with changes in the occupation of donor levels and subsequent rearrangement of impurity ions (correlation effects), along with changes in the random potential amplitude.

Indeed, exposure of the samples to IR light leads to the depletion of the donor DX^- centers, which is confirmed by the existence of the IR energy threshold at which the frozen hopping high-frequency photoconductivity arises. In this case, n_s increases and σ_1 decreases. Such behavior is consistent with the above concepts of the corresponding decrease in the occupation of impurity levels, reduction in the correlation in the position of impurity ions [8, 15], increase in the random potential amplitude (Fig. 5), and increase in the role of localization effects.

The opposite effect is observed when a strain is applied to the sample under study. Indeed, in this case, the electron density n_s decreases and the high-frequency conductivity increases by more than two orders of magnitude relative to the equilibrium value (Fig. 7). This effect can be explained in the same way: the decrease in n_s corresponds to a larger degree of occupation of donors, greater influence of the correlation effects, and, accordingly, smaller random potential amplitude (Fig. 7, curve *2*). When the random potential is low, the localization of electrons in the 2D interface channel is almost absent; therefore, conductivity occurs via delocalized electrons and the hopping contribution is absent. The explanation of the effect of IR illumination on the glued sample is the same as the one above.

At 1.5 K, under conditions of the quantum Hall effect, all electrons are localized in both the interface and barrier layers and the hopping conductivity becomes the dominant mechanism. The radical change in the high-frequency conductivity caused by the external effects (in magnetic fields corresponding to the center of the Hall plateau) confirms the suggestion [4] that the hopping conductivity over the interface layer is shunted by the hopping conductivity over the $Al_{0.3}Ga_{0.7}As$:Si layer.

The question of the mechanism of the hopping high-frequency conductivity via localized states in the $Al_{0.3}Ga_{0.7}As$:Si barrier layer remains open. According to [19], high-frequency hopping conductivity can be implemented via hops of a pair of electrons as a whole. However, the probability of this process occurring seems to be low. One-electron hops via shallow donor levels may also play an important role. Since these levels cannot be completely filled with electrons due to the presence of the interface layer, there should always be at least one pair of ionized impurity atoms with one electron (two-site model), which can hop between these atoms.

Let us estimate the high-frequency hopping conductivity due to one-electron hops between shallow donor levels of the impurity band formed by Si in $Al_{0.3}Ga_{0.7}As$ using the model of relaxation absorption in the two-site approximation [2–4]. For this mechanism, the expression for σ_1 has the form

$$\sigma_1 = \frac{\pi^2}{2}\frac{g^2\xi^3\omega e^4}{\varepsilon_s}\left(L_T + \frac{L_\omega}{2}\right)^2. \quad (4)$$

Here, g is the one-electron density of states at the Fermi level; ξ is the localization length; e is the elementary charge; ε_s is the permittivity of GaAs; $L_T = \ln J_0/kT$ (J_0 is the typical value of the overlap integral, which is on the same order of magnitude as the Bohr energy); and $L_\omega = \ln(1/\omega\tau_0)$, where τ_0 is the time of refilling pairs during hops, which is controlled by the mechanism of interaction between electrons and phonons. In the case of piezoelectric interaction, $\tau_0 \approx 10^{-11}$ s. The radius of the state a_B can be estimated using the value of the activation energy for shallow levels $E \approx 7$ meV [17]: $a_B = \sqrt{\hbar/m^*E} \approx 9 \times 10^{-7}$ cm. Then, the width of the impurity band can be roughly estimated as $\Delta E \approx e^2/\varepsilon_s a_B \approx 14$ meV. According to this estimation, the impurity band is almost completely overlapped with the conduction band, which makes further estimations very rough. When the total Si concentration in the barrier layer $N = 10^{12}$ cm^{-2}, $n_s \approx 1.5 \times 10^{11}$ cm^{-2}. Under the assumption that, due to reaction (2), the concentration of Si impurity atoms responsible for shallow impurity centers is twofold lower than N, $N_{d^+} \approx 5 \times 10^{11}$ cm^{-2}. Bearing in mind the above values, we obtain the density of states in the impurity band: $g = N_{d^+}/\Delta E \approx 3.6 \times 10^{10}$ cm^{-2} meV^{-1}.

As a result, the calculation by formula (4) for $f = 30$ MHz yields $\sigma_1 = 9 \times 10^{-8}$ Ω^{-1}, which is in satisfactory agreement with experiment.

Obviously, high-frequency hopping conductivity should depend on the number of pairs at which one electron is localized. If all the impurity levels are occupied by electrons or completely depleted, the hopping conductivity should be zero. Thus, the high-frequency hopping conductivity attains its maximum at some intermediate filling of levels. Therefore, the reduction in the hopping conductivity under illumination of a sample or upon cooling at different rates can be easily explained by the change in the degree of filling of localized electronic states, i.e., the number of pairs involved in the high-frequency hopping conductivity.

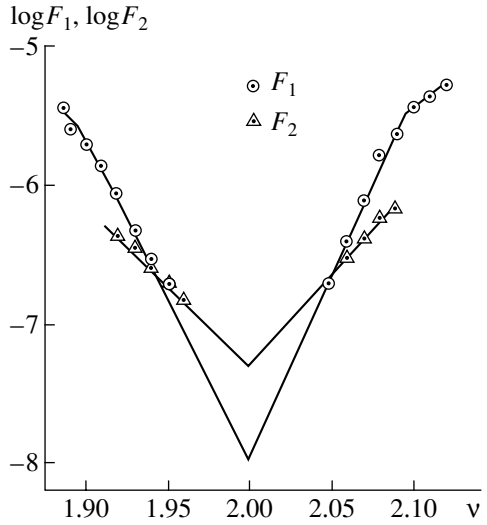

Fig. 10. Dependences of $\log F_1$ and $\log F_2$ on filling number ν near ν = 2 at f = 30 MHz and T = 1.5 K.

Figure 8 shows all the experimental curves obtained for the sample with $n_s \approx 1.5 \times 10^{11}$ cm^{-2} cooled under different conditions (close symbols) and exposed to IR light after slow cooling (open symbols), plotted in the coordinates $\sigma_{1,2}(n_s)$. It can be seen from Fig. 8 that the values of σ_1 (large symbols) and σ_2 (small symbols), although showing a large spread, seem to yield "universal" curves *1* and *1a*, respectively (the curves are plotted manually). The data for the sample cooled under different conditions (specifically, the sample was kept for a day at 77 K before the liquid helium was poured) are shown by curves *2* and *2a*. The spread of experimental points shows that the occupation of impurity levels and 2D interface channel by electrons occurs randomly, and, thus, the sample "remembers" its history. This result is consistent with the conclusions of [15, 16]. The changes in σ_1 and σ_2 in comparison with the changes in n_s upon illumination of the sample by small portions of IR radiation are shown in the inset to Fig. 8. It can be seen that the decrease in σ_1 and σ_2, with the ratio σ_2/σ_1 remaining constant (3–4), corresponds to the variations in n_s in the range $(1.5–1.8) \times 10^{11}$ cm^{-2}. This situation corresponds to the conditions of high-frequency hopping conductivity. With a further increase in n_s (up to more than 1.8×10^{11} cm^{-2}), σ_1 begins to increase much faster than σ_2 and the conditions for hopping conductivity become violated. We explain this fact by the depletion of the impurity DX^- centers and the development of conductivity via delocalized carriers.

Figure 9 shows the dependences of σ_1 and σ_2 on H in the vicinity of ν = 2 for the slowly cooled modulation-doped sample with $n_s = 2.7 \times 10^{11}$ cm^{-2}. It can be seen that both σ_1 and σ_2 are almost independent of H. If hopping conductivity occurs over the impurity band formed by shallow-level donor centers, then, according to the above calculations, the magnetic length $l_H > a_B$ up to fields of 6 T. Thus, the condition of a weak field is satisfied. That is why the dependence of the conductivity on magnetic field is weak and does not manifest itself in a narrow magnetic field range.

Summing up, we believe that the strong effect of external factors on the hopping high-frequency conductivity and the fact that this parameter is not dependent on magnetic field in the vicinity of small even filling numbers, along with the inconsistency of the theoretically predicted value of the localization length ξ [5, 20], indicate that, in the magnetic fields corresponding to these filling numbers, the high-frequency hopping conductivity is completely controlled by the $Al_{0.3}Ga_{0.7}As$:Si layer.

This circumstance makes it possible to determine the high-frequency hopping conductivity over the interface layer by extrapolation. Let us return to Fig. 9. If the conductivities $\sigma_1^{\nu=2} = 4 \times 10^{-7}\ \Omega^{-1}$ and $\sigma_2^{\nu=2} = 2.4 \times 10^{-6}\ \Omega^{-1}$ are completely controlled by the $Al_{0.3}Ga_{0.7}As$ layer, the contributions of the interface layer to σ_1 and σ_2 near ν = 2 are $F_{1,2} = \sigma_{1,2} - \sigma_{1,2}^{\nu=2}$. The dependences of $\log F_{1,2}$ on ν near ν = 1 are shown in Fig. 10. Both dependences can be extrapolated to ν = 2 using linear functions. Such an extrapolation yields $F_1^{\nu=2} = 10^{-8}\ \Omega^{-1}$ and $F_2^{\nu=2} = 5 \times 10^{-8}\ \Omega^{-1}$. It should be noted that these values of $F_{1,2}^{\nu=2}$ are almost two orders of magnitude smaller than the experimental values of $\sigma_{1,2}^{\nu=2}$. Using these values of $F_{1,2}^{\nu=2}$ to determine the localization length, we obtain $\xi = 2 \times 10^{-6}$ cm, which is twofold smaller than the spacer width and is similar to the value of magnetic length in this magnetic field. This estimation makes it possible to use the two-site model for analysis of the high-frequency hopping conductivity in a 2D interface channel under conditions of the integer quantum Hall effect.

4. CONCLUSION

In this paper, we report the results of studying $GaAs/Al_{0.3}Ga_{0.7}As$:Si heterostructures with a mobility of about 10^5 cm^2/(V s) at T = 4.2 K. A pronounced integer quantum Hall effect is observed in these heterostructures with direct current. In fact, this means that the dc conductivity is entirely determined by the 2D interface layer. The situation with high-frequency conductivity of these heterostructures at low temperatures is quite different. It is shown that external factors—IR light, strain, and different conditions of cooling—significantly affect both the high-frequency conductivity near the centers of the Hall plateau and the electron density n_s in these heterostructures. This fact, as well as the large value of high-frequency conductivity of the

samples at low temperatures after their slow cooling, is reason to conclude that high-frequency hopping conductivity occurs over the impurity band formed by shallow donor levels in the $Al_{0.3}Ga_{0.7}As$:Si layer. The contribution of this effect significantly exceeds the contribution of the hopping conductivity over the interface layer in the magnetic fields corresponding to small even integer filling numbers and, therefore, shunts the latter. The results obtained can be explained qualitatively in terms of the well-known concept of DX^- centers in $Al_{0.3}Ga_{0.7}As$:Si alloys.

A method is proposed that makes it possible to determine both the high-frequency hopping conductivity and the localization length ξ in a 2D interface layer from simultaneous measurements of the absorption and velocity of an SAW as functions of magnetic field.

It should be noted that a certain spread of the values of carrier density and mobility in these and similar heterostructures was also observed in dc measurements. The results obtained here suggest that this spread may be related to different conditions of cooling the sample.

ACKNOWLEDGMENTS

This study was supported by the Russian Foundation for Basic Research, project no. 01-02-17891; the Presidium of the Russian Academy of Sciences; the President of the Russian Federation, grant no. NSh-2200.2003.2; NATO-CLG.979355; and the US DOE Office of Science, grant no. W-31-109-ENG-38.

REFERENCES

1. *The Quantum Hall Effect*, Ed. by R. E. Prange and S. M. Girvin, 2nd ed. (Springer, New York, 1990; Mir, Moscow, 1989).
2. M. Pollak and T. Geballe, Phys. Rev. **122**, 1742 (1961).
3. A. L. Éfros, Zh. Éksp. Teor. Fiz. **89**, 1834 (1985) [Sov. Phys. JETP **62**, 1057 (1985)].
4. I. L. Drichko, A. M. Diakonov, I. Yu. Smirnov, *et al.*, Phys. Rev. B **62**, 7470 (2000).
5. M. Furlan, Phys. Rev. B **57**, 14818 (1998).
6. P. M. Mooney, J. Appl. Phys. **67**, R1 (1990).
7. D. V. Lang and R. A. Logan, Phys. Rev. Lett. **39**, 635 (1977).
8. E. Buks, H. Heiblum, and H. Shtrikman, Phys. Rev. B **49**, 14790 (1994).
9. I. L. Drichko, A. M. Diakonov, Yu. M. Galperin, *et al.*, in *Proceedings of 9th International Symposium on Nanostructures: Physics and Technology* (St. Petersburg, Russia, 2001), p. 582.
10. I. L. Drichko, A. M. Diakonov, V. V. Preobrazenskii, *et al.*, in *Proceedings of 10th International Symposium on Nanostructures: Physics and Technology* (St. Petersburg, Russia, 2002), p. 520.
11. I. L. Drichko, A. M. Diakonov, V. V. Preobrazenskii, *et al.*, Physica E (Amsterdam) **17**, 276 (2003).
12. I. L. Drichko, A. M. D'yakonov, A. M. Kreshchuk, *et al.*, Fiz. Tekh. Poluprovodn. (St. Petersburg) **31**, 451 (1997) [Semiconductors **31**, 384 (1997)].
13. I. L. Drichko and I. Yu. Smirnov, Fiz. Tekh. Poluprovodn. (St. Petersburg) **31**, 1092 (1997) [Semiconductors **31**, 933 (1997)].
14. N. V. Zotova, S. A. Karandashev, D. A. Matveev, *et al.*, Proc. SPIE **1587**, 334 (1991).
15. T. Suski, P. Wiśnevski, I. Gorczyca, *et al.*, Phys. Rev. B **50**, 2723 (1994).
16. W. Knap, W. Zduniak, L. H. Dmowski, *et al.*, Phys. Status Solidi **198**, 267 (1996).
17. D. J. Chadi and K. J. Chang, Phys. Rev. B **39**, 10063 (1989).
18. N. Chand, T. Henderson, J. Klem, *et al.*, Phys. Rev. B **30**, 4481 (1984).
19. M. Foygel, A. G. Petukhov, and A. S. Andreev, Phys. Rev. B **48**, 17018 (1993).
20. M. M. Fogler, A. Yu. Dobin, and B. I. Shklovskii, Phys. Rev. B **57**, 4614 (1998).

Translated by Yu. Sin'kov

Semiconductors, Vol. 38, No. 6, 2004, pp. 712–716. Translated from Fizika i Tekhnika Poluprovodnikov, Vol. 38, No. 6, 2004, pp. 739–744.

AMORPHOUS, VITREOUS, AND POROUS SEMICONDUCTORS

Formation of Thick Porous Silicon Layers with Insufficient Minority Carrier Concentration

D. N. Goryachev*, L. V. Belyakov, and O. M. Sreseli

Ioffe Physicotechnical Institute, Russian Academy of Sciences, St. Petersburg, 194021 Russia

**e-mail: Dmitri.Goryachev@mail.ioffe.ru*

Submitted December 3, 2003; accepted for publication December 4, 2003

Abstract—Specific features of the formation of thick porous silicon layers on *n*-type silicon substrates in the galvanostatic mode have been studied. An abrupt change in the electrolyzer voltage with time was observed in the course of anodization with exposure to a visible light without the IR component. This abrupt change is accompanied by the formation of a large-grained disrupted silicon layer. It was shown that these effects are due to an insufficient density of holes, which are necessary for etching silicon. As a result, the mechanism for the generation of minority carriers changes from light generation to that of the avalanche type. © *2004 MAIK "Nauka/Interperiodica".*

1. INTRODUCTION

Layers of porous silicon (*por*-Si) are most frequently fabricated by anodic etching (anodization) of silicon in aqueous or aqueous-alcoholic solutions of hydrofluoric acid (HF). This method was developed as far back as the middle of the 20th century [1]. When *por*-Si layers are fabricated on *n*-Si substrates, the silicon substrate is exposed to high-intensity illumination, most often, white light. The illumination increases the surface density of minority carriers, holes, whose absence hinders the electrochemical dissolution of silicon. It is known that *por*-Si layers are far from uniform across their thickness. A clearly pronounced boundary that separates *por*-Si into two regions that differ sharply in color and morphology can be seen in cross-sectional microscopic images. It has also been noted that these two layers have different luminescent properties. The upper layer is a conglomerate of quantum-confined silicon crystallites with a characteristic size on the order of several nanometers (nanocrystallites). This layer exhibits a strong photoluminescence (PL) in the visible spectral range. The lower layer is composed of a macrocrystalline (or mesoporous) *por*-Si with crystallites more than 10 nm in size. This layer exhibits PL in the IR spectral range [2, 3]. It was mentioned in [3] that the reason why a two-layer structure of *por*-Si is obtained is the strong absorption of light in the surface region of the *por*-Si as it forms.

The illumination of the substrate not only generates holes, which are necessary for etching, but also has a considerable effect on many physicochemical properties of the formation of *por*-Si, e.g., the intensity and spectral composition of PL, irrespective of the type of conduction in silicon. The reasons for, and the mechanisms of, such an effect of illumination on the growth of *por*-Si were considered in [4, 5].

In the present study, an attempt was made to correlate some specific features of how thick *por*-Si layers grow on *n*-Si substrates with the type of illumination of silicon during its anodization.

2. EXPERIMENTAL PROCEDURE

The study was performed with (100) *n*-Si substrates that were chemically and mechanically polished with a resistivity of 2–3 Ω cm.

The electric contacts on the samples were fabricated by chemical deposition of copper on the back (nonworking) side of the samples. A mixture of 48% HF with ethanol in a 1 : 1 ratio served as the electrolyte. The counter electrode was fabricated in the form of a coil of platinum wire. All the experiments were carried out at a constant anode current, i.e., in the galvanostatic mode, which was maintained automatically with a current stabilizer (potentiostat). In the course of electrolysis, the electrode potential of the anode or the electrolyzer voltage was measured and recorded. Preference was given to the second method, which is simpler.

Illuminators with halogen or tungsten lamps served as the sources of light. In most of the experiments, the IR light (with $\lambda > 0.65$ μm) was cut off with an SZS-23 glass filter. The maximum illumination level of the samples was about 0.1 W/cm^2. When necessary, the intensity of light was attenuated with neutral glass filters.

3. EXPERIMENTAL RESULTS

3.1. Electrolyzer Voltage and Outward Appearance of the Samples

In the open-circuit mode and with zero illumination, the voltage across the electrolytic cell, V_{el}, is determined by the electromotive force of the Si/electro-

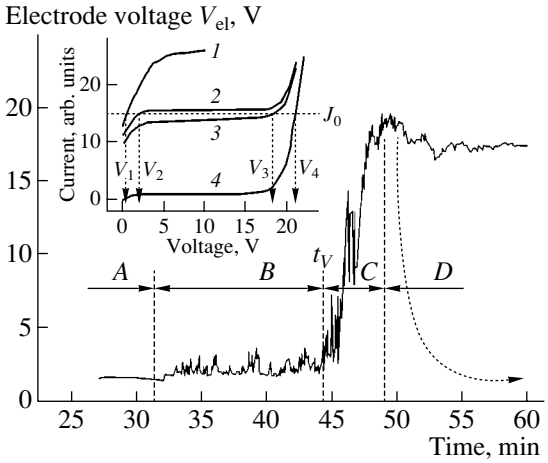

Fig. 1. Electrolyzer voltage vs. electrolysis duration; *n*-Si, current density 15 mA/cm^2, illumination level 0.92 of the maximum value, IR part of the spectrum cut off with an SZS-23 filter. Portion *A* of the curve in the figure is shown incompletely. Inset: reverse current–voltage characteristic of a photodiode (for explanation, see text).

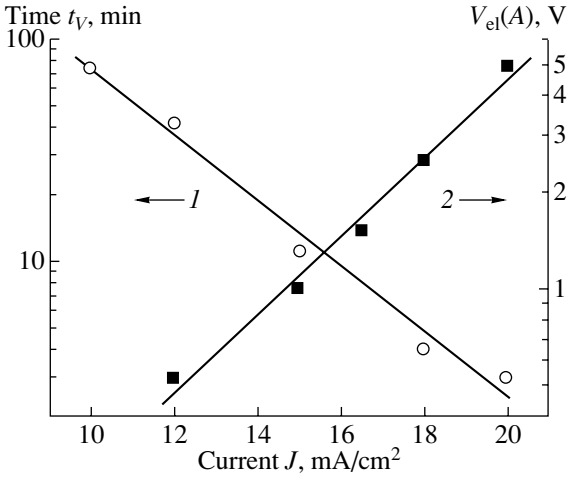

Fig. 2. (*1*) Time of occurrence of an abrupt change in voltage and (*2*) initial electrolyzer voltage corresponding to curve portion *A* in Fig. 1 vs. the current density; *n*-Si, illumination level 0.75 of the maximum value, IR part of the spectrum cut off.

lyte/Pt galvanic cell. When a sample is exposed to light, V_{el} changes by an amount equal to the steady-state photovoltage.

In the course of electrolysis when the sample is illuminated, the electrolyzer voltage is set automatically at a level from tenths of a volt to several volts (with Si positive) and remains virtually stable until a certain instant of time t_V at which the voltage increases fast to several tens of volts. A typical dependence of the electrolyzer voltage V_{el} on the duration of electrolysis is shown in Fig. 1.

It can be seen that, during the first 30 min, the electrolyzer voltage remains unchanged, at a level of about 2 V (portion *A* of the curve). Then chaotic voltage surges (spikes) appear (portion *B*), and, beginning at the instant of time t_V, a rapid (over 3–4 min) rise (abrupt change) in the voltage by more than 16 V occurs (portion *C*). At the same time the outward appearance of the sample changes. Its smooth, shining, and nearly black surface turns matte (velvety) and light yellow. Later, the voltage gradually stabilizes at about 17–18 V, and the oscillatory mode gives way to a slow and gradual change in the voltage, usually toward lower values (portion *D*). In this region, illumination has virtually no effect on V_{el}.

It is important to note that the dependence of the voltage on the electrolysis duration mentioned above is only observed in the case when the white light used for illumination contains no IR component with wavelengths longer than about 0.65 μm. Otherwise, the electrolyzer voltage remains equal to several volts and no abrupt change in the voltage is observed. Moreover, if additional IR illumination is switched on after this abrupt change (i.e., in region *D*), the voltage decreases to values characteristic of region *A* (dotted line in Fig. 1).

As the anode current density *J* is raised, the time t_V, after which the abrupt change in the voltage occurs, becomes shorter (Fig. 2, curve *1*) and the voltage corresponding to portion *A* increases [Fig. 2, curve *2*, $V_{el}(A)$]. These dependences are nearly exponential. At the same time, after the abrupt change in the voltage, V_{el} is virtually independent of the current density.

The intensity of sample illumination also strongly affects the course of the electrolysis. The time t_V, at which the steplike change occurs, becomes longer as the illumination level increases (Fig. 3, curve *1*). Despite the wide scatter of the experimental points, this dependence can also be interpreted as exponential. The

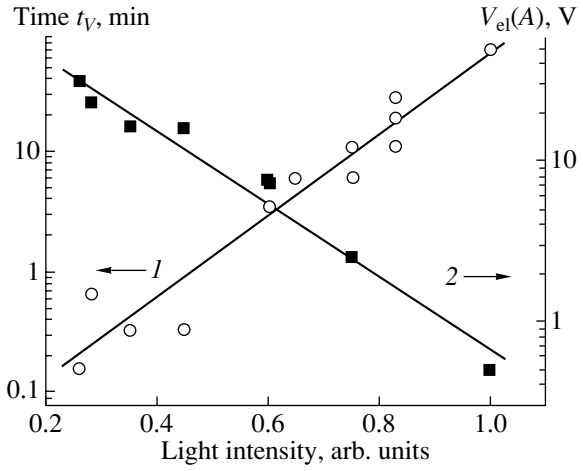

Fig. 3. (*1*) Time of occurrence of an abrupt change in the voltage and (*2*) initial electrolyzer voltage vs. the current density. *n*-Si, current density 15 mA/cm^2, IR part of the spectrum cut off.

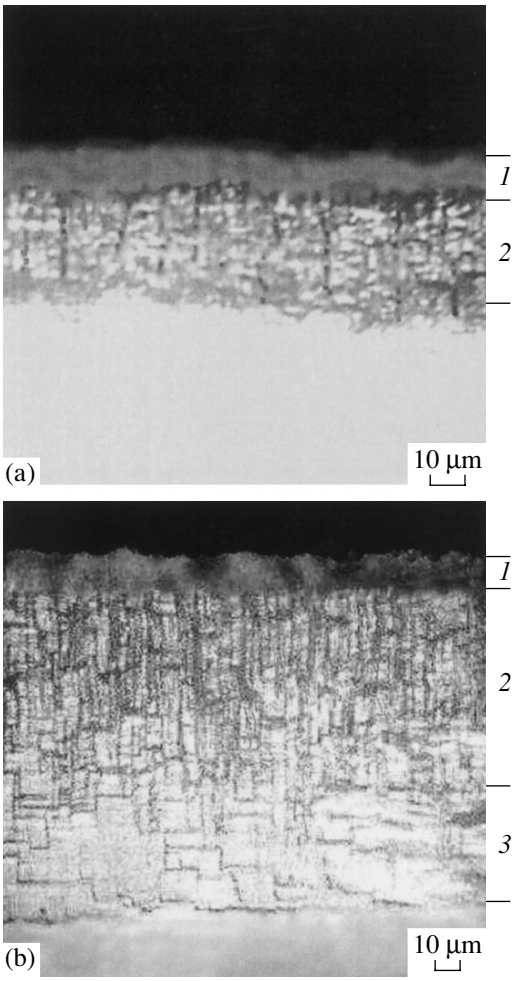

Fig. 4. Cross-sectional micrographs of the samples. (a) Stage of *por*-Si formation before the abrupt change in the potential ($t \approx 20$ min): (*1*) upper structureless porous layer and (*2*) second layer with columnar structure. (b) The result of a more prolonged electrolysis, $t = 90$ min: (*1*) and (*2*) the same layers, and (*3*) the third layer with a horizontal "block" structure.

value $V_{el}(A)$ decreases exponentially as the illumination level grows (Fig. 3, curve *2*).

3.2. Thickness and Morphology of por-Si Layers

Cross-sectional microscopic studies of the samples demonstrated that a two-layer structure of *por*-Si is formed in all the samples, irrespective of whether the spectral composition of the light used includes an IR component, and an abrupt change in voltage is observed in the course of electrolysis.

The upper layer of *por*-Si has a chaotic loose structure. Below lies the second layer, which is pierced by numerous vertical pores hundreds of nanometers in diameter (columnar structure) (see Fig. 4a). The lower boundary of this layer may not be clearly pronounced (Fig. 4b). With the total thickness of the samples studied ranging from 8 to 175 μm, the thickness of the upper layer varies within a comparatively narrow range, from 1–2 to 20 μm. There is a certain relationship between the quantity Q of electricity that passes and the thickness of *por*-Si layers. The thickness of the upper layer ceases to increase further after 50–80 C has passed and stabilizes at a level of 15–20 μm (Fig. 5, curve *1*), whereas that of the lower layer grows virtually linearly with Q (Fig. 5, curve *2*). It is noteworthy that, after the abrupt change in the voltage occurs, illumination no longer has a noticeable effect on the rate of formation of the *por*-Si layer and its thickness increases further at the same rate in the dark and under illumination.

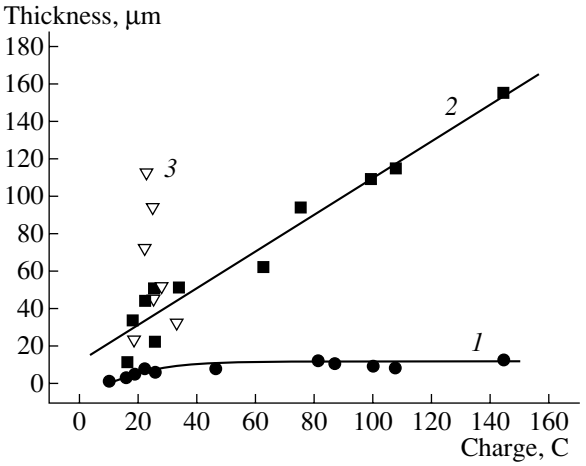

Fig. 5. Variation of the thickness of *por*-Si layers with the quantity of electricity that passed through the electrolyzer: (*1*) upper layer, (*2*) second layer, and (*3*) third layer.

In some cases, a third layer is formed under the second, columnar *por*-Si layer. This layer is a conglomerate of large (of micrometer size) grains and crystallites. These grains may be arranged both chaotically and in the form of inclined, or even horizontal, layers (Fig. 4b). According to original observations by the authors, this layer starts to be formed at approximately the same instant of time as when the abrupt change in the electrolyzer voltage is observed. However, if the electrolysis is continued, the third layer starts to gradually disappear 30–40 min after this abrupt change occurs. As a result, the third layer is observed in a relatively narrow range of the quantities of electricity that passes through the electrolyzer, which is illustrated by points *3* in Fig. 5.

4. DISCUSSION

Below, the experimental results described above are considered taking into account the fundamental aspects of *por*-Si formation and the nature of the absorption of light in the formation of a *por*-Si layer.

The exponential dependence of V_{el} on the current density (Fig. 2) indicates that a major contribution to this dependence is made by abrupt changes in the electrode potentials across the electrode/electrolyte inter-

faces and in the space-charge region (SCR) in silicon, rather than by the ohmic voltage drop in the electrolyte or in the bulk of a sample. However, the abrupt changes of the potentials across the phase boundaries cannot exceed tenths of a volt at the current densities used. Hence, it follows that the increase in the voltage to 15–20 V in region *C* is primarily due to the abrupt change in the potential in the SCR of the semiconductor.

The behavior of the voltage during the formation of the porous layer, namely, the voltage spikes in region *B* and the abrupt change in the voltage in region *C*, can be understood by taking into account the fact that the semiconductor/electrolyte interface is a rectifying contact whose properties are similar to those of a Schottky diode and by using the model of a reverse-biased photodiode.

Owing to the absorption of light in the growing *por*-Si layer, the illumination level in the SCR of the crystalline Si substrate gradually decreases as the thickness of *por*-Si increases, which results in the fact that the rate of carrier generation becomes lower. The inset in Fig. 1 shows schematically the reverse current–voltage characteristics of a photodiode at various illumination levels: at a high illumination level of the semiconductor/electrolyte interface (curve *1*); at a certain critical illumination level (*2*); at a somewhat lower illumination level, which is insufficient to provide the process with holes (*3*); and in the dark (curve *4*).

At the chosen current J_0 and a high illumination level of the substrate, the working point of the diode corresponds to a small voltage V_1 across the electrochemical cell. As the illumination level gradually decreases because of the absorption of light in the growing porous layer, the system reaches a state in which, ideally, the number of holes that are formed is exactly that necessary to stabilize the current at J_0 (curve *2* and potential V_2). After that, upon a further rather small decrease in the illumination level, a transition to curve *3* occurs, when the potentiostat raises the applied voltage in order to maintain the preset current J_0. In this case, as can be seen from the figure, the working point falls within the initial region of the avalanche breakdown, and the voltage increases to V_3. In the limiting case, in the dark, a voltage (V_4) that corresponds to the avalanche breakdown is established.

Region *A* in Fig. 1 corresponds to a high illumination level of the electrolyte/semiconductor interface (curve *1* in the inset), when the number of holes generated by light far exceeds that necessary for ensuring the preset current J_0. Region *B*, in which potential fluctuations are observed at the preset current J_0, corresponds to the critical etching mode (curve *2*). In this case, fluctuations in the level of illumination of the sample, which are attributed to, e.g., gas evolution at the silicon electrode or to convective flows in the electrolyte, become important. Region *C* corresponds to the mode with a clearly pronounced deficiency of holes generated by light, when a transition to the avalanche breakdown mode occurs. In this case, too, fluctuations in the illumination level manifest themselves in a return to a lower voltage upon an accidental increase in light intensity (part of the current is provided by photogeneration of carriers, and the rest, by avalanche generation). Region *D* corresponds to a very low illumination level, and in the limiting case, to total darkness at the electrolyte/semiconductor interface.

In principle, current J_0 can be maintained under conditions of insufficient illumination not only by means of an avalanche breakdown. The rise in the electric field strength at the electrolyte/semiconductor interface (not only in the SCR, but also in the Helmholtz layer) may lead to the tunneling of electrons from atoms or ions in solution into the conduction band of the silicon substrate. In this case, an electrochemical reaction that leads to the release of electrons should occur at the anode. The discharge of hydroxy ions of water by the reaction $2OH^- \longrightarrow O_2 + 2H^+ + 2e^-$ may serve as such a process. However, this part of the current will be expended on the formation of oxygen, rather than on the dissolution of silicon, which will decrease the rate of *por*-Si formation. Since, according to Fig. 5, the rate of formation of the main (second) *por*-Si layer is time-independent, the main mechanism of carrier generation at this stage is, admittedly, avalanche ionization. In this case, there is no need for further illumination of the sample, and the growth of *por*-Si can proceed in the dark.

It follows from the authors' observations that the formation of the third *por*-Si layer coincides in time with the onset of the oscillatory electrolysis mode. The thickness of this layer may exceed severalfold the *por*-Si thickness corresponding to the quantity of electricity that has passed and to the amount of silicon dissolved in the process. Moreover, there is no clearly pronounced dependence of the thickness of the third layer on the quantity of electricity passed (points *3* in Fig. 5). This gives reason to believe that the "third layer" is not porous silicon in the conventional understanding of this term, but rather a mechanically damaged part of the silicon substrate. Such a layer may appear as a result of local electric breakdowns at the bottom of pores under conditions in which the generation of carriers by light is insufficient to maintain the preset current density. This process continues until a fundamental change in the mechanism of carrier generation occurs: a transition to avalanche ionization, which provides further growth of *por*-Si. In this case, the second layer grows through dissolution of the previously disrupted layer of the substrate, which leads to a gradual elimination of the third layer.

It is, again, noteworthy that the above refers to the case when a sample is exposed to light that contains no IR component. Otherwise, the IR light passes freely through the *por*-Si layer and provides the necessary rate of carrier generation in the substrate and the formation of the second, mesoporous layer. There is no characteristic abrupt change in the voltage in this case.

It does not, however, follow from these conclusions that mesoporous silicon can be formed on *n*-type substrates without any illumination. As experiment shows, illumination should be present in the early stages of electrolysis. Otherwise, carriers are predominantly generated in places where the crystal structure of the surface layer of silicon is disrupted, rather than uniformly over the entire surface of the silicon. In these local places, the current density is so high that the silicon dissolves without any *por*-Si being formed. At the same time, illumination makes the distribution of the carrier density uniform over the surface. Moreover, it is the illumination that largely provides the growth of the nanoporous layer, which exhibits strong PL in the visible spectral range.

Thus, it may be stated that mainly mesoporous *por*-Si, which has no luminescent properties (second layer), is formed in the course of prolonged electrolytic etching of *n*-Si under illumination. The upper luminescent layer is formed only as a relatively thin film whose thickness does not exceed 10–20 μm. The third, lower sublayer of *por*-Si is far from always formed. Both the thicknesses of separate *por*-Si layers and their structural features are largely determined by the intensity and spectral composition of the illuminating light used in etching *n*-Si (silicon). Specifically, the morphology (formation) of the mesoporous layer depends on whether the illuminating light has an IR component. If it does, an ordinary mesoporous layer with a columnar or branching structure (depending on the crystallographic orientation of the substrate) grows. In the absence of an IR component, the generation of holes, which are necessary for etching, ceases to be caused by light, and this is accompanied by the formation of a disrupted (third) layer composed of micrometer-size silicon conglomerates.

As for the formation of the upper *por*-Si layer, which has no clearly pronounced crystal structure and exhibits strong luminescence, the discussion above and the reasoning in [4, 5] once more lead the authors of the present study to conclude that this layer is predominantly composed of atoms of secondary origin. They are formed via charge exchange between Si^{2+} ions as a result of the so-called disproportionation of ions, described in detail in [5]. The disproportionation of Si^{2+} ions occurs according to the scheme

$$Si^{2+} + Si^{2+} \longrightarrow Si + Si^{4+}$$

and leads to the formation of amorphous and nanocrystalline silicon. As demonstrated in [4], the disproportionation of Si^{2+} ions is markedly accelerated by strong illumination, and, therefore, it mostly occurs at the surface of *por*-Si, where the illumination level is the highest. At the same time, the concentration of Si^{2+} ions at the surface of *por*-Si may be rather high, since Si^{2+} ions formed at the lower boundary of *por*-Si can move to the surface of *por*-Si both through diffusion in the electrolyte and as a result of convective flows in the electrolyte in coarse pores. However, the thicker the *por*-Si layer, the more difficult the transport of Si^{2+} ions to the surface of *por*-Si, and, therefore, the upper layer gradually ceases to increase in thickness in the course of electrolysis, which can be clearly seen in Fig. 5 (curve *1*). The same scheme describes the formation of the upper, strongly luminescent layer of *por*-Si on *p*-type silicon under illumination [5].

5. CONCLUSION

While studying how the electrolysis parameters affect the growth of thick (>10 μm) films of *por*-Si on *n*-Si substrates, we discovered that the use of visible light without an IR component results in the fact that the electrolyzer potential changes abruptly in the course of anodization and a very thick disrupted silicon layer appears. This is due to a change of the mechanism by which the holes necessary for etching silicon are generated: the generation of minority carriers by light in the SCR of the silicon substrate is replaced by avalanche breakdown and the ionization of silicon atoms.

It was shown that the morphological structure of porous silicon strongly depends on the intensity and spectral composition of the light used in the electrolysis. Previous assumptions about the secondary nature of the silicon that constitutes the upper, nanoporous layer of *por*-Si were confirmed. The thickness of this layer is determined by the intensity of illumination and by the possibility of transporting Si^{2+} ions from the interior to the surface of *por*-Si.

Thus, in fabricating thick *por*-Si layers on *n*-Si, it is necessary to take into account changes in the distribution of light absorption in the structure that is formed and the different mechanisms of generation of minority carriers in the substrate.

ACKNOWLEDGMENTS

This study was supported in part by the “Physics of Solid-State Nanostructures” program of the Ministry of Industry, Science, and Technology of the Russian Federation and the “Low-Dimensional Quantum Structures” program of the Presidium of the Russian Academy of Sciences, as well as by a grant from the President of the Russian Federation for Support of Leading Scientific Schools (NS 2223.2003.02).

REFERENCES

1. A. Uhlir, Bell Syst. Tech. J. **35**, 333 (1956).
2. C. Levy-Clement, A. Logoubi, and M. Tomkiewicz, J. Electrochem. Soc. **141**, 958 (1994).
3. P. Steiner, F. Kozlowski, and W. Lang, IEEE Electron Device Lett. **14**, 317 (1993).
4. L. V. Belyakov, D. N. Goryachev, O. M. Sreseli, and I. D. Yaroshetskiĭ, Fiz. Tekh. Poluprovodn. (St. Petersburg) **27**, 1961 (1993) [Semiconductors **27**, 1078 (1993)].
5. D. N. Goryachev, L. V. Belyakov, and O. M. Sreseli, Fiz. Tekh. Poluprovodn. (St. Petersburg) **34**, 1130 (2000) [Semiconductors **34**, 1090 (2000)].

Translated by M. Tagirdzhanov

Semiconductors, Vol. 38, No. 6, 2004, pp. 717–723. Translated from Fizika i Tekhnika Poluprovodnikov, Vol. 38, No. 6, 2004, pp. 745–752.

PHYSICS OF SEMICONDUCTOR DEVICES

Transformation of a Short-Wavelength Emission Band of a Double-Charged Intrinsic Acceptor into a Long-Wavelength Band in GaSb-Based LEDs

E. A. Grebenshchikova, A. N. Imenkov, B. E. Zhurtanov, T. N. Danilova, M. A. Sipovskaya, N. V. Blasenko, and Yu. P. Yakovlev*

Ioffe Physicotechnical Institute, Russian Academy of Sciences, Politekhnicheskaya ul. 26, St. Petersburg, 194021 Russia
**e-mail: yak@iropt.ioffe.rssu.ru*

Submitted October 20, 2003; accepted for publication October 21, 2003

Abstract—GaSb-based crystals shaped like a stepped pyramid with smoothed steps are obtained. The crystals are intended for the fabrication of light-emitting diodes in which the short-wavelength emission band of a double-charged intrinsic acceptor is transformed into the long-wavelength band without loss in the amount of photons emitted. It is shown experimentally and theoretically that an increase in the ratio of the area of the light-emitting diode crystal to its volume increases the external quantum yield of photons. A yield of 5.1% for the intrinsic acceptor in GaSb is attained. © *2004 MAIK "Nauka/Interperiodica".*

1. INTRODUCTION

In our previous paper, we showed that electrochemical faceting of a crystal for fabrication of light-emitting diodes (LEDs) allows one to make one of the crystal faces in the shape of a truncated cone [1]. A crystal with such surface has an emissivity higher than that with a plane surface due to the convexity of the cone. This circumstance yielded an increase in the emissivity by a factor of 1.5 for the first incidence onto a surface. This surface is nonorthogonal with respect to other mutually orthogonal crystal faces, and the beams incident on this surface partially undergo a total internal reflection. Thus, these beams may fall onto other surfaces at an angle smaller than the angle of the total internal reflection and can be emitted by the crystal. These circumstances allow one to use multiple passage to increase the external quantum yield of emission. This especially concerns the impurity emission, which is weakly absorbed at band-to-band transitions. In addition, due to the absorption of the short-wavelength emission of a double-charged acceptor at band tails in GaSb [1], multiple passage along with reemission can be used to transform short-wavelength band into long-wavelength one.

The objectives of this study were the following. First, we aimed to obtain a developed convex pyramidal surface of an LED crystal via multistage electrochemical etching. Second, we planned to use such an LED chip to transform the short-wavelength band of a double-charged acceptor into the long-wavelength band without substantial loss in the total number of photons. This study continues our research on the development of LEDs for the mid-range infrared (IR) spectral region (1.6–2.4 μm) [1–7].

2. EXPERIMENTAL

The LED structures under investigation were formed by liquid-phase epitaxy on Te-doped *n*-GaSb(100) substrates 400 μm thick with an electron concentration as high as 8×10^{17} cm^{-3}. Initially, an active undoped layer with a composition similar to GaSb was grown from the usual solution–melt with the addition of 0.03% In. This addition decreased the band gap by a mere 1 meV. The layer grown has *p*-type conduction due to the partial accommodation of Ga atoms at Sb sites of the crystal lattice. The layer was 2 μm thick. A wider-gap confining Ge-doped *p*-$Ga_{0.66}Al_{0.34}SbAs$ layer 3.5 μm thick with a hole concentration as high as 10^{18} cm^{-3} was then grown. The *p*-GaSb contact layer 0.5 μm thick heavily doped with Ge had a hole concentration as high as 8×10^{18} cm^{-3} and was grown on the previous layer.

For experiments with electrochemical faceting of semiconductor crystals, one large wafer with epitaxial layers was cut into several parts. Using contact photolithography, LEDs with variously shaped crystals were fabricated from these parts (Fig. 1).

(i) Type I LED semiconductor crystals were ~380 μm thick (Fig. 1a). On the epitaxial layer, i.e., in the *p*-region, the contacts 100 μm in diameter were formed by sequential deposition of the layers of Cr, Au + Ge, and Au using a VUP-4 system. On the substrate, i.e., in the *n*-region, layers of Cr, Au + Te, and Au were also deposited. The contact layers were then fused for 1 min at 250°C. On the epitaxial layer, the pattern in the form of squares with a side of 480 μm and a step of 500 μm was formed to divide the structure into separate chips. At the next stage, mesas 300 μm in diameter and 10 μm in height were formed at the center of these squares. The earlier fused contacts 100 μm in

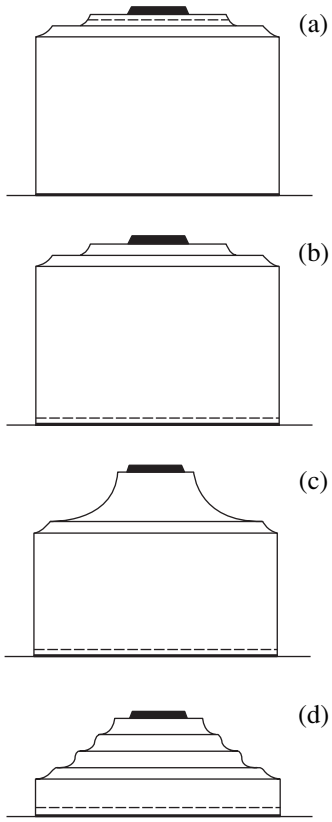

Fig. 1. Schematic structure of four types of LED crystals: (a) parallelepiped-shaped with the substrate soldered to the crystal holder, (b) parallelepiped-shaped with the epitaxial layer soldered to the crystal holder, (c) with a parallelepiped-shaped substrate, and (d) shaped like a stepped pyramid with smoothed steps.

diameter were at the center of these mesas. Then the semiconductor crystal was divided into separate small parallelepiped-shaped crystals (chips) by cleaving. Each small crystal (chip) was mounted with the substrate down on a TO-18 LED plane-stage crystal holder.

(ii) Type II LEDs (Fig. 1b) were fabricated so that the point contacts, mesas, and dividing channels were formed in the *n*-type region, i.e., on the substrate, whereas a continuous contact layer was formed on the epitaxial *p*-layer. Each of these chips was mounted with the epitaxial layer down on a TO-18 LED plane-stage crystal holder. The radiation was emitted mainly through the substrate.

Thus, type I and type II LED chips had the usual plane-rectangular geometry and differed only in emission direction. Type I chips emitted radiation mainly through the epitaxial layers, and type II chips emitted radiation through the substrate.

(iii) For comparison with standard-geometry LEDs (types I and II), LED chips with a developed surface (Fig. 1c) were fabricated from the same LED structure via multiple electrochemical faceting of the LED crystal. Chemical faceting was carried out using contact photolithography as follows. At the first stage, windows for nonrectifying contacts were photolithographically formed on a chemically cleaned *n*-type substrate. Contact layers were formed in these windows. The contacts to the *p*-region were formed over the entire surface of the epitaxial *p*-layer. To separate out the boundaries of individual chips, a pattern made up of squares with a side of 480 μm and a step of 500 μm was formed on the substrate of the LED crystal, and boundary channels were etched to a depth of 70 μm by electrochemical etching in a CrO_3-based etchant. The channels were 160 μm wide. At the next stage of photolithography, a pattern shaped made up of circles 300 μm in diameter was formed at the center of the open squares. By etching it similarly to the squares, a pattern 140 μm in height was formed. The pattern was pyramid-shaped at the base and shaped like a truncated cone at the top with an upper area 200 μm in diameter. After dividing the LED crystal into separate small crystals (chips) by cleaving, each chip was mounted with the epitaxial layer down on the TO-18 LED plane-stage crystal holder.

(iv) In order to reduce the emission optical path, one-quarter of the starting LED structure was thinned to 200 μm (Fig. 1d). Thinning was carried out from the substrate side by grinding with subsequent chemical etching. The LEDs were fabricated by multistage deep etching. The first stage of fabrication, specifically, the formation of windows for nonrectifying contacts 100 μm in diameter and the deposition of a gold-containing alloy on the substrate side, was carried out similarly to procedure (iii). At the second stage of photolithography, i.e., at the stage of pattern formation on the substrate side of the LED structure, the duration of etching of each separate pattern was shortened. As a result, the squares, circles, etc. obtained were less deep than in procedure (iii). We strived to round and smooth the sharp bulges that are inevitably formed during multistage etching (four photolithographic stages). To this end, at the fifth stage, when the upper area with a nonrectifying contact was 200 μm in diameter, a mesa 200 μm in diameter was formed photolithographically. All the features beyond the circle 200 μm in diameter were etched electrochemically for 20 s. As a result of this, a pattern 120 μm in height shaped like a stepped pyramid with smoothed steps was obtained (Fig. 2). Then the LED crystals were divided into separate chips by cleaving. Each chip was mounted with the epitaxial side down on the TO-18 LED plane-stage crystal holder.

The spectra and directivity diagrams of emission were measured for various pulse currents with an amplitude of 10–300 mA, frequency of 512 Hz, and off-duty factor of 2. The measurements were carried out at room temperature with the LED cooled by a household fan. The MDR-2 diffraction monochromator that was used to measure the spectra was calibrated in units of emission power divided by the wavelength range in micrometers. To calculate emission power, the spectra were measured in two directions, in particular, in the direction normal to the *p*–*n* junction plane or par-

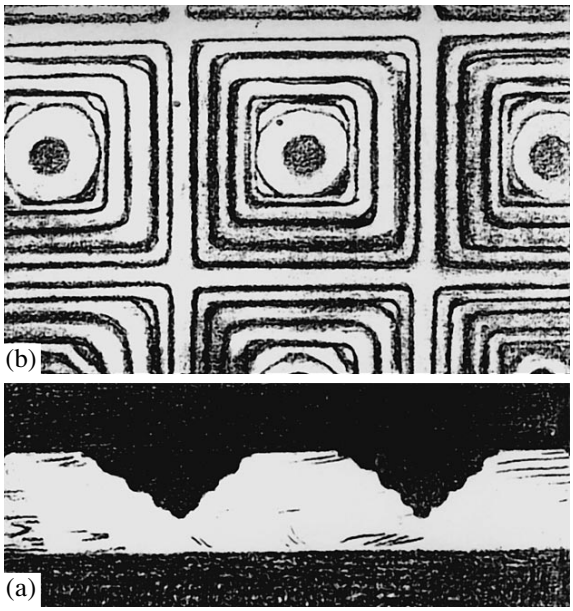

Fig. 2. Photomicrographs of a wafer with etched pyramid-shaped LED crystals having smoothed steps: (a) the substrate-side view and (b) the profile obtained by cleaving.

allel to it but normal to one of the crystal facets. In the parallel direction, power was taken as doubled for the calculation of total emission power, which corresponded exactly to the direction diagram of parallelepiped-shaped type I and II LEDs. This procedure of calculation was also retained for other LEDs, since they were based on a parallelepiped.

3. RESULTS

3.1. Emission Spectra

The design of type I LEDs included the arrangement of epitaxial layers at the outer facet of the parallelepiped; radiation is emitted through epitaxial layers. These circumstances allow one to observe virtually an undistorted spectrum of recombination radiation of the double-charged acceptor, as we showed previously [1]. Such a spectrum is observed in the direction normal to the *p–n* junction plane (Fig. 3, curve *1*) due to the short emission path in the crystal (~5 μm). In this direction, the spectrum comprises a doublet peaked at the wavelengths λ_s = 1.76 μm (photon energy $h\nu_s$ = 0.705 eV) and λ_1 = 1.9 μm (photon energy $h\nu_1$ = 0.65 eV) with band half-widths of 0.06 and 0.07 eV, respectively. In the direction lying in the *p–n* junction plane (Fig. 3, curve *2*), the long-wavelength band of the doublet is dominant in the emission spectrum. The short-wavelength band is almost indistinguishable. The intensity of the long-wavelength band is lower by a factor of 2 than that in the direction normal to the *p–n* junction plane.

Type II, III, and IV LEDs, in which the crystal is soldered to the crystal holder by the epitaxial side, emit

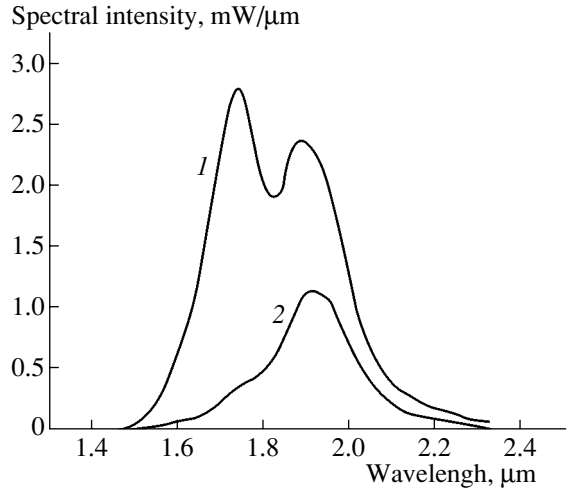

Fig. 3. Spectra of emission of type I LEDs in the direction (*1*) normal to the *p–n* junction plane and (*2*) parallel to the *p–n* junction plane.

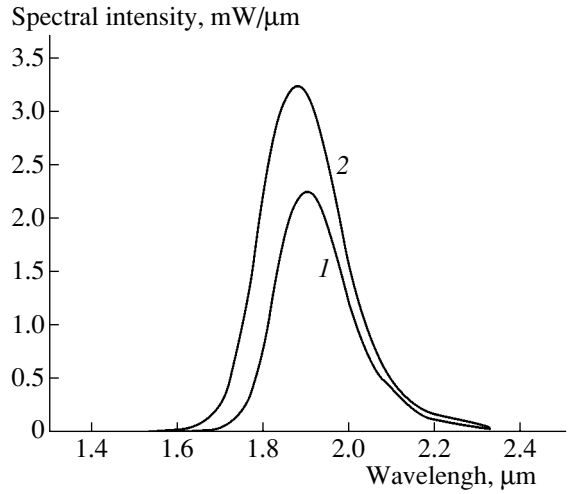

Fig. 4. Spectra of emission of type II LEDs in the direction (*1*) normal to the *p–n* junction plane and (*2*) parallel to the *p–n* junction plane.

virtually one band with parameters close to those of the long-wavelength band mentioned above (Figs. 4–6).

In the type II LEDs (Fig. 4), the emission intensity in the direction normal to the *p–n* junction plane is lower than that in the direction parallel to this plane. In the type III and IV LEDs (Figs. 5, 6), the emission intensities in these directions are approximately equal.

3.2. Directivity Diagrams

Each shape of the LED crystal is characterized by a specific radiation distribution in the far-field zone (Fig. 7). Type I LEDs emit most intensely in the direction normal to the *p–n* junction plane (Fig. 7, curve *1*). The emission intensity falls off gradually as the angle

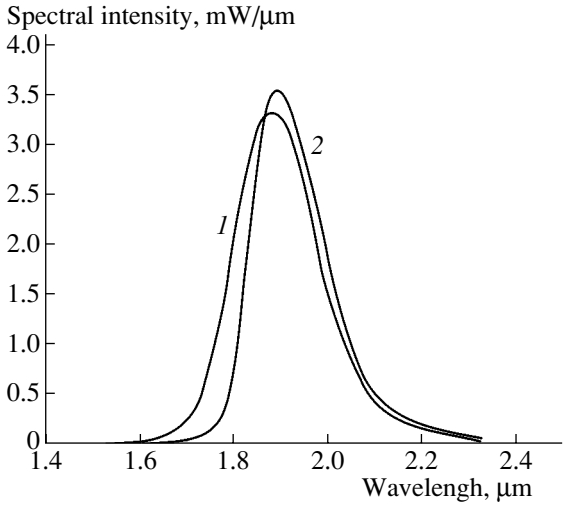

Fig. 5. Spectra of emission of type III LEDs in the direction (*1*) normal to the *p–n* junction plane and (*2*) parallel to the *p–n* junction plane.

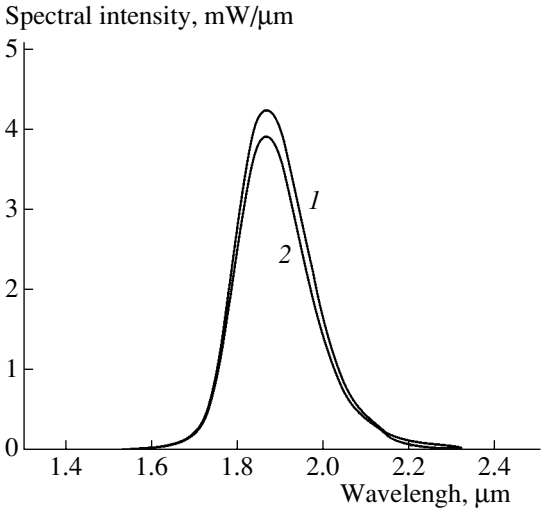

Fig. 6. Spectra of emission of type IV LEDs in the direction (*1*) normal to the *p–n* junction plane and (*2*) parallel to the *p–n* junction plane.

of deviation from this direction increases, and at deviation angle $\theta = 90°$, the intensity is 10–20% of that at $\theta = 0$. For a deviation angle larger than 90°, the emission intensity of all types of LEDs drops due to shading by the crystal holder.

The direction diagram for type II, III, and IV LEDs, in which the crystal is soldered to the holder by the epitaxial side, has a minimum at $\theta = 0$ (Fig. 7, curves *2–4*). This feature is most pronounced for type II LEDs (Fig. 7, curve *2*), which are parallelepiped-shaped with a square base of 500×500 μm^2 and a height of 380 μm. At angles of 75° and 90°, the emission intensity exceeds that at the zero angle by a factor of 2.2 and 1.5, respectively.

Type III LEDs, whose substrate part was subjected to deep etching, are characterized by lower angles (~60°), at which the emission intensity is the highest (Fig. 7, curve *3*). The peak intensity exceeds that at $\theta = 0$ only by a factor of 1.5. At an angle of 90°, the emission intensity is the same as at $\theta = 0$. The central minimum is less pronounced in the direction diagram for type IV LEDs (Fig. 7, curve *4*) with the crystal shaped like a stepped pyramid with a total height of 200 μm. These LEDs have a weak dependence of emission intensity on the observation angle up to an angle of deviation from the normal to the *p–n* junction plane of 90°.

3.3. Photon Quantum Yield

Emission power W depends on current I (Fig. 8) nonlinearly. For small currents up to 10 mA for type I LEDs and up to 75 mA for LEDs of other types, this dependence is superlinear, and for heavier currents, this dependence is sublinear.

For currents larger than 250 mA, the emission power of type I LEDs starts to decrease as the current increases. This circumstance is associated with the fact that the emission is concentrated under a nonrectifying contact with a corresponding increase in the rate of the Auger recombination, as was shown by Grebenshchikova *et al.* [1]. Among LEDs of various designs, these LEDs have the lowest power for currents larger than 70 mA.

The highest emission power is characteristic of type IV LEDs with crystals shaped like a stepped pyramid (Fig. 8, curve *4*). For a current of 300 mA, their emission power is as high as $W = 7$ mW. These LEDs also have the highest differential quantum yield of photons, which is no lower than $\eta_e = 5.1\%$ at a current of 75 mA (see table). For type III and IV LEDs, the quantum yield peak $\eta_e = 3.2$ and 4.1% is also attained at a current of

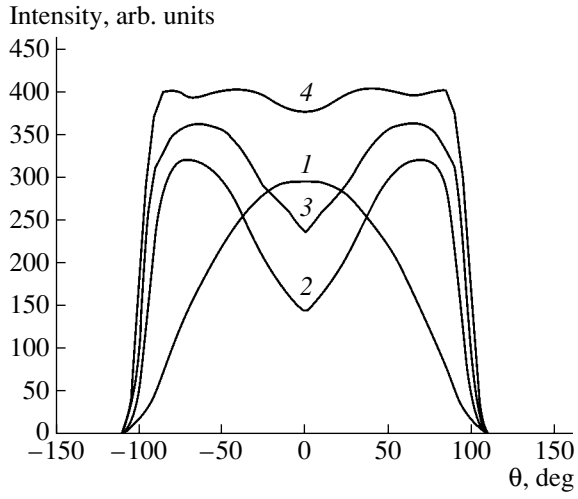

Fig. 7. Directivity diagram of emission of LEDs with variously shaped crystals: (*1*) type I, (*2*) type II, (*3*) type III, and (*4*) type IV.

75 mA. For type I LEDs, the highest differential quantum yield of photons is $\eta_e = 3.8\%$ at a current of 10 mA.

In addition, the table presents average photon energies $h\bar{\nu}$, wavelengths $\bar{\lambda}$, and half-widths $\Delta\lambda$ of the emission spectrum, which are necessary for the calculation of the external quantum yield of photons, as well as other quantities considered below.

4. DISCUSSION

4.1. Theoretical Grounds

The emission spectra, direction diagrams, and quantum efficiency of LEDs with various crystal shapes are different. This is an indication of the effect crystal shape has on electroluminescence processes and phenomena: the generation, propagation, and absorption of recombination radiation, reemission, etc.

To reveal the relationship between these phenomena, let us consider the generalized pattern of operation of an LED chip.

In the operation mode, photons are initially emitted into the crystal and only then are emitted outwards. Let us denote their total number in a crystal as Φ. The spectral distribution of photons in wavelengths λ will be expressed by the function $d\Phi/d\lambda$. Photons are generated due to the recombination of electron–hole pairs formed as a result of injection by the electrical current I and due to the band-to-band or quasi-band-to-band absorption of photons circulating in the crystal. This process can be described by the definite integral $\int_0^\infty \alpha c(d\Phi/d\lambda)d\lambda$, where α is the coefficient of photoactive absorption averaged over the crystal and c is the speed of light in the crystal. The number of photons decreases due to the photoactive absorption mentioned above and absorption loss, including absorption in metal contacts, which is denoted by α_d. An additional decrease is due to emission outwards, represented by the corresponding absorption coefficient α_e. We will express the spectral resolution of the primary recombination radiation by the function $d\eta/d\lambda$, where

$$\eta = \int_0^\infty (d\eta/d\lambda)d\lambda$$

is the internal quantum yield of emission.

We will assume that the emission in the crystal is isotropic. The resulting equation of balance of the spectral distribution of photons is written as

$$\frac{d(d\Phi/d\lambda)}{dt} = \frac{d\eta}{d\lambda}\left[\frac{I}{e} + \int_0^\infty c\alpha\frac{d\Phi}{d\lambda}d\lambda\right] - c(\alpha + \alpha_d + \alpha_e)\frac{d\Phi}{d\lambda} = 0, \quad (1)$$

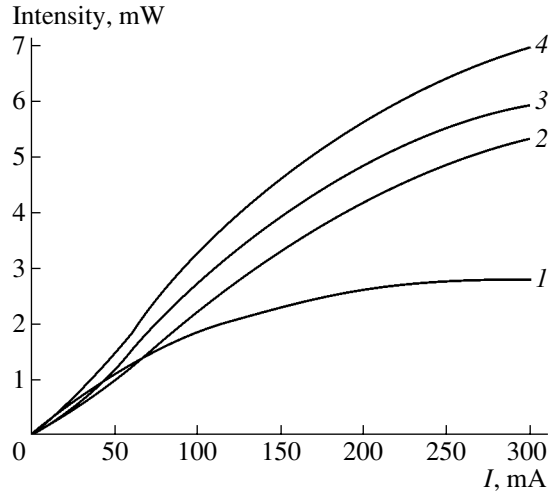

Fig. 8. Emission power vs. the current of LEDs with variously shaped crystals: (*1*) type I, (*2*) type II, (*3*) type III, and (*4*) type IV.

where e is the elementary charge. From Eq. (1), the spectrum of the radiant flux from the crystal can be determined:

$$\frac{dP_e}{d\lambda} = c\alpha_e\frac{d\Phi}{d\lambda} = \frac{d\eta}{d\lambda}\alpha_e\left[\frac{I}{e} + \int_0^\infty c\alpha\frac{d\Phi}{d\lambda}d\lambda\right](\alpha + \alpha_d + \alpha_e)^{-1}. \quad (2)$$

Important conclusions follow from Eq. (2). Specifically, the spectrum of emitting radiation is independent of reemission, which is represented here by a definite integral taken over λ. However, this spectrum depends on the spectrum of primary recombination radiation $\frac{d\eta}{d\lambda}$ and on the absorption spectrum $(\alpha + \alpha_d + \alpha_e)$. Quantities α_d and α_e are almost unchanged within the limits of wavelengths of the larger part of primary radiation. However, α increases strongly as the wavelength decreases and can reduce the emitted part of the short-wavelength radiation compared with its initial part. This takes place in the wavelength region $\lambda < \lambda_b$, for which $\alpha > \alpha_d + \alpha_e$, and allows us to calculate approxi-

Table

LED type	W, mW	η_e, %	$h\bar{\nu}$, eV	$\Delta\lambda$, μm	$\bar{\lambda}$, μm	S/V, cm^{-1}	α_e, cm^{-1}	η_e^{calc}, %
I	2.8	3.8	0.68	0.35	1.8	106	1.13	3.9
II	5.3	3.2	0.65	0.21	1.9	106	1.13	3.9
III	6.7	4.1	0.65	0.20	1.9	122	1.30	4.4
IV	7.0	5.1	0.65	0.20	1.9	167	1.79	5.7

mately the definite integral mentioned above. Multiplying Eq. (2) by α/α_e and integrating over λ, we derive

$$\int_0^\infty c\alpha\frac{d\Phi}{d\lambda}d\lambda = \frac{\eta_s}{1-\eta_s}\frac{I}{e}, \quad (3)$$

where η_s is the internal quantum yield of short-wavelength photons with $\lambda < \lambda_b$. Substituting integral (3) into Eq. (2), integrating over λ, and dividing the result by I/e, we derive the external quantum yield of photons

$$\eta_e = \frac{\eta_l}{(1-\eta_s)(1+\alpha_d/\alpha_e)}, \quad (4)$$

where η_l is the internal quantum yield of long-wavelength photons with $\lambda > \lambda_b$.

It follows from expression (4) that, in order to increase the external quantum yield of photons η_e, it is necessary not only to increase the internal quantum yield of long-wavelength (η_l) and short-wavelength (η_s) photons. It is also necessary to increase the effective absorption coefficient α_e that expresses the emission of photons from the crystal. For $\eta_s + \eta_l = 1$ and $\alpha_d/\alpha_e \ll 1$, η_e is close to unity, which points to the possible transformation of short-wavelength photons into long-wavelength photons without loss in their number. To determine α_e, let us take into account that the density of photons $d\Phi/dV$ close to various areas dS of the crystal surface can be different. Hence, the integral of $d\Phi/dV$ over the crystal volume V is equal to Φ. Taking into account that photons intersect the surface only at the angle of total internal reflection and undergo partial reflection into the crystal, let us find α_e if the refraction index of the crystal $n \gg 1$:

$$\alpha_e = \frac{1}{\Phi}\int_S \frac{d\Phi}{dV}\frac{dS}{n(n+1)^2}. \quad (5)$$

For a uniform photon distribution and optical homogeneity of the crystal, Eq. (5) is simplified:

$$\alpha_e = \frac{S}{Vn(n+1)^2}, \quad (6)$$

where S is the area of a free light-emitting surface of the crystal.

It follows from formula (6) that α_e can be increased by increasing the S/V ratio, for example, by thinning the crystal. Changing the crystal shape from cubic to semispherical increases α_e by a factor of 1.5. The curvature of a spherical surface is favorable for the uniformity of distribution and isotropy of emission in the crystal. In contrast, plane orthogonal facets of a cube are unfavorable since they reduce α_e. The mesa etched on one of the facets of the LEDs investigated is favorable for a certain restoration of isotropy of emission. Bulges or hollows over the whole surface of the crystal could do it more radically. They additionally increase the crystal surface thus additionally increasing α_e. Metal contacts cover a part of the surface and decrease α_e. In addition, they can absorb radiation, thereby strongly increasing α_d. Diffuse radiation reflection into the crystal from the metallized surface, which reorients photon fluxes, can play a positive role.

The photon density can be slightly different in different areas of the crystal surface. In this case, Eq. (5) can be used to estimate the equivalent absorption factor corresponding to the radiation emitted outward through each area by integrating Eq. (5) only within the limits of this area. The result obtained can be used to calculate the photon flux through separate areas of the crystal surface. Thus, despite the simplicity and conventionality of the theoretical consideration above, it allows us to answer the most important questions of the generation, reemission, and propagation of photons, as well as their emission by the crystal. Let us now analyze the experimental data on the basis of this theoretical consideration.

4.2. Analysis of Experimental Data

The emission intensities in the direction normal to the *p–n* junction plane for type I and type II LEDs are different. This difference can be explained by the difference in distances from the active regions to the outer surfaces parallel to the *p–n* junction plane. This circumstance manifests itself both in the spectra of emission power and in directivity diagrams (Figs. 3–8). A large crystal thickness (380 μm) leads to different photon densities close to the outer surfaces and different equivalent absorption factors that define the radiation emitted outwards according to Eq. (5). In type I LEDs, the epitaxial layers adjoin the outer surface, and the aforementioned coefficient is larger than for type II LEDs. Accordingly, a larger photon flux is emitted through the outer surface with a much larger fraction of short-wavelength photons. Photon densities at outer surfaces in these LEDs differ by a factor of approximately 2, since this is the difference between the fluxes emitted through the outer surfaces.

It follows from the approximate equality of the external quantum yield of emission for these LEDs that the contacts, which cover the entire *p*-type surface in type II LEDs and only a small area of the surface in type I LEDs, are virtually nonabsorbing. Moreover, the contacts can diffusely reflect photons, since the semiconductor–metal interface is not optically smooth because of lattice mismatch. Therefore, metal contacts are favorable for isotropy of the photon flux in the crystal.

The small average crystal thickness in type III and IV LEDs provides equality of radiation intensities in directions normal and parallel to the *p–n* junction plane. This equality is an indication of the uniformity of radiation flux in the crystals. Isotropy of fluxes in them is sustained by radiation reflection from the smoothed intersections of faces. Therefore, the conditions for the above theoretical consideration can be considered satisfied for type III and IV LEDs. To calculate the equiva-

lent absorption factor related to the radiation emitted by the crystal, we can use formula (6). Let us also apply this formula to type I and II LEDs. The table lists the equivalent absorption factors α_e related to the radiation emitted by the crystal and the theoretical external quantum yield of photons η_e^{calc}. These quantities are calculated from the ratios of the area of the light-emitting surface S to the crystal volume V corresponding to LEDs of various types. The typical internal quantum yield of photons η = 58% and the ratio of generated fluxes of short-wavelength and long-wavelength photons η_s/η_l = 2 [1], the coefficient of photoinactive absorption $\alpha_d = 8$ cm^{-1}, and the refractive index n = 3.9 [8] are used in calculations. The theoretical external quantum yield of photons η_e^{calc} is found to be close to the measured η_e for all types of LEDs. An insignificant excess of η_e^{calc} over η_e can be accounted for by the disregarded absorption in the heavily doped contact layer and other disregarded factors.

Despite the fact that type III and IV LEDs emit only a short-wavelength band, unlike type I LEDs, which also emit a stronger short-wavelength band, they have a higher external quantum yield of radiation. This fact points to the transformation of short-wavelength photons into long-wavelength photons with conservation of, and even an increase in, the total number of photons. The increase is accounted for by the effective reemission and by a decrease in the substrate thickness. Both theoretical and experimental values of the external quantum yield of photons increase as the ratio of the light-emitting surface area to the LED crystal volume increases.

5. CONCLUSION

The main result of this study is the fabrication of variously shaped LEDs, including those with a highly developed light-emitting surface, which shows the considerable potential of multistage electrochemical etching. LEDs shaped like a stepped pyramid with smoothed steps in which isotropic luminous flux is well sustained are

fabricated. Isotropy is favorable for reemission and a high external quantum yield of photons. In these LEDs, the two-band emission spectrum of a double-charged acceptor is transformed into a single-band spectrum without a loss in the total number of photons.

Theoretical formulas for the spectrum of emitting radiation and the external quantum yield of photons are derived. It is shown both theoretically and experimentally that the spectrum of emission is determined by the spectrum of primary recombination radiation and by the absorption spectrum of the crystal. The external quantum yield of photons is proportional to the ratio between the light-emitting area and the volume of the crystal.

ACKNOWLEDGMENTS

We thank S.S. Evdokimova and E.V. Kuznetsova for assembling the LEDs.

This study was partially supported by CRDF, grant no. RPO-1407-ST-03.

REFERENCES

1. E. A. Grebenshchikova, A. N. Imenkov, B. E. Zhurtanov, *et al.*, Fiz. Tekh. Poluprovodn. (St. Petersburg) **37**, 1465 (2003) [Semiconductors **37**, 1414 (2003)].
2. A. Andaspaeva, A. N. Baranov, A. A. Guseĭnov, *et al.*, Pis'ma Zh. Tekh. Fiz. **14**, 845 (1988) [Sov. Tech. Phys. Lett. **14**, 377 (1988)].
3. A. Andaspaeva, A. N. Baranov, E. A. Grebenshchikova, *et al.*, Fiz. Tekh. Poluprovodn. (Leningrad) **23**, 1373 (1989) [Sov. Phys. Semicond. **23**, 853 (1989)].
4. A. Andaspaeva, A. N. Baranov, A. A. Guseĭnov, *et al.*, Pis'ma Zh. Tekh. Fiz. **15** (18), 71 (1989) [Sov. Tech. Phys. Lett. **15**, 734 (1989)].
5. T. N. Danilova, B. E. Zhurtanov, A. P. Zakgeĭm, *et al.*, Fiz. Tekh. Poluprovodn. (St. Petersburg) **33**, 239 (1999) [Semiconductors **33**, 206 (1999)].
6. A. Andaspaeva, A. N. Baranov, A. A. Guseĭnov, *et al.*, Fiz. Tekh. Poluprovodn. (Leningrad) **24**, 1708 (1990) [Sov. Phys. Semicond. **24**, 1067 (1990)].
7. B. Zhurtanov, É. V. Ivanov, A. N. Imenkov, *et al.*, Pis'ma Zh. Tekh. Fiz. **27** (5), 1 (2001) [Tech. Phys. Lett. **27**, 173 (2001)].
8. O. Madelung, *Physics of III–V Compounds* (Wiley, New York, 1964; Mir, Moscow, 1967).

Translated by N. Korovin

Semiconductors, Vol. 38, No. 6, 2004, pp. 724–726. Translated from Fizika i Tekhnika Poluprovodnikov, Vol. 38, No. 6, 2004, pp. 753–756.

PHYSICS OF SEMICONDUCTOR DEVICES

Soft Breakdown as a Cause of Current Drop in an MOS Tunnel Structure

A. F. Shulekin*^, S. É. Tyaginov*, R. Khlil, A. El Hdiy**, and M. I. Vexler***

**Ioffe Physicotechnical Institute, Russian Academy of Sciences, St. Petersburg, 194021 Russia*

^e-mail: shulekin@pop.ioffe.rssi.ru

***LASSI/DTI, CNRS-UMR 6107, UFR Sciences BP 1039, F-51687, Reims cedex 2, France*

Submitted November 10, 2003; accepted for publication November 11, 2003

Abstract—The effect of electric stress on current–voltage characteristics of Al/SiO_2/p^+-Si MOS diodes with a tunnel-thin (2.5–3.0 nm) insulator was studied at constant current and constant voltage. Under constant-voltage stress, the current increase related to soft breakdown was followed in several cases by an abrupt drop in current. Typically, the drop occurs at a high bias, and it may be a specific manifestation of a soft breakdown. At strong nonuniformity of the SiO_2 thickness, the effect can be significant even if the breakdown is localized within a rather small area. © *2004 MAIK "Nauka/Interperiodica".*

1. INTRODUCTION

The process of miniaturization of MOSFETs requires that increasingly thin SiO_2 layers be used as gate insulators. In modern MOSFETs, the thickness of insulators is 3–4 nm, and substrates are doped to ~10^{18} cm^{-3} [1], but the investigation of transistors with a thinner insulator or a higher doping level has attracted considerable attention [2].

We studied a soft breakdown of MOS diodes with tunnel-thin SiO_2, fabricated on *p*-Si substrates doped to $N_A = 2 \times 10^{18}$–2×10^{19} cm^{-3}.

The damage of a thin oxide layer is often qualitatively regarded as a three-stage process: the increase in stress-induced current at a fixed voltage, soft breakdown, and, finally, hard breakdown [3]. Soft breakdown [4] is a local breakdown of an insulator without further enlarging of the broken-down area, unlike a hard (catastrophic) breakdown, when local damage may expand over the whole area of a device.

An abrupt rise in current seems to be a natural, and the only possible, result of a soft breakdown [3–6]. However, as shown in this study, an abrupt drop in current can and must be observed along with the possible rise in current, although this might seem strange at first glance.

2. MODEL OF CURRENT DROP AFTER A SOFT BREAKDOWN

For simplicity, we assume that the region of a soft breakdown is a portion of the MOS structure area in which the local current–voltage (*I–V*) characteristic is nearly ohmic, in contrast to undamaged portions, where this characteristic is tunnel-type (roughly, exponential [7], Fig. 1).

With a small bias *V*, the total current in the structure sharply increases after the soft breakdown, owing to the contribution of the defective area. However, the tunnel resistance sharply decreases as the bias increases and finally becomes smaller than any ohmic resistance, regardless of the parameters of tunneling. In other words, sooner or later, the tunneling exponential will cross the linear *I–V* dependence of the breakdown area ($V = V^*$, Fig. 1). This simple reasoning shows that at $V > V^*$, the current should fall, not rise, after the soft breakdown.

A natural suggestion [6] is that the conducting region formed under a soft breakdown (breakdown spot) is quite small. Thus, the possibility of experimental observation of the drop in current seems unlikely. Indeed, if the current density is uniform, even total exclusion of the breakdown area from the charge trans-

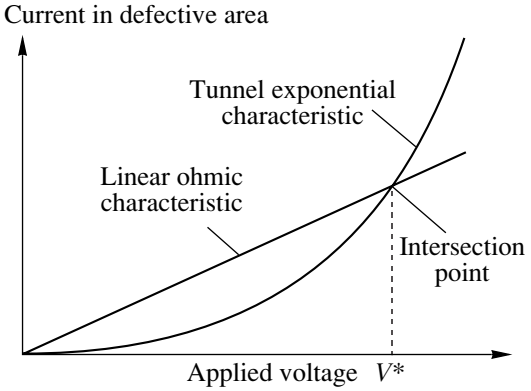

Fig. 1. Schematic *I–V* characteristics of the undamaged portion of a MOS structure (exponential) and of the region of soft breakdown (linear). At high voltage ($|V| > |V^*|$), the tunneling resistance exceeds the ohmic resistance.

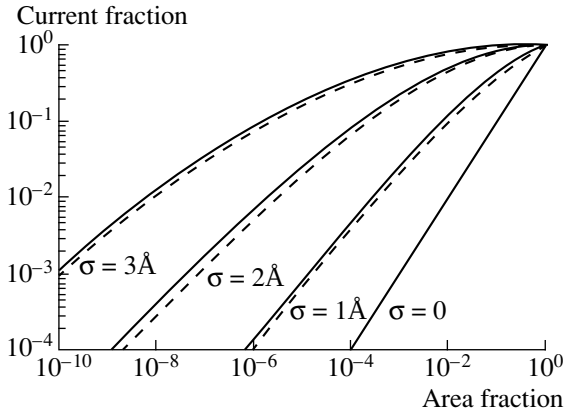

Fig. 2. Fraction of current flowing through the thinnest region of a device as a function of the relative area of this region, with different values of the standard deviation σ of oxide thickness. The nominal thickness of SiO_2 is 25 Å, the doping level in *p*-Si $N_A = 2 \times 10^{18}$ cm^{-3}. Temperature T = 300 K. Gate voltage V = –2 V (solid line) and –3V (dashes).

port will not lead to any measurable decrease in the current across the device. However, the distribution of the oxide thickness over the area is always nonuniform, and the breakdown occurs at the thinnest fragments, so the influence of defective regions on the total current increases drastically.

Figure 2 shows the fraction of the current that flows through the thinnest region of a structure as a function of relative area of this region for different values of the standard deviation σ of thickness from its nominal value. This dependence was obtained using a model similar to [8]. It can be seen that, when σ is as small as ~0.1 nm, 10^{-4} of the total current flows through a 10^{-6} fraction of the device area (note that in the best commercial samples σ ~ 0.15 nm [9]).

It appears that the presence (or intentional formation) of a considerable spatial variation of SiO_2 thickness enables a significant drop in current as a result of a soft breakdown, even if the damaged area is very small.

3. EXPERIMENTAL RESULTS AND DISCUSSION

In our experiments, we used MOS tunnel diodes fabricated on boron-doped (111) p^+-Si substrates. Thin SiO_2 oxide was grown in a dry [O_2 (20%) + N_2] mixture at a temperature of 700°C; the average thickness of the oxide was ~2.7 nm, and σ ≈ 0.3 nm. Circular Al contacts with area $S = 1.26 \times 10^{-3}$ cm^2 were deposited at 200°C.

The value of parameter σ is quite large, so the *I–V* characteristics of our samples agree well with those calculated theoretically for a slightly lower thickness of an insulator (2.2–2.3 nm) [10].

Samples were tested under constant current stress (CCS) and under constant voltage stress (CVS). In CCS mode, the current was kept at a level of 5×10^{-6} A, and

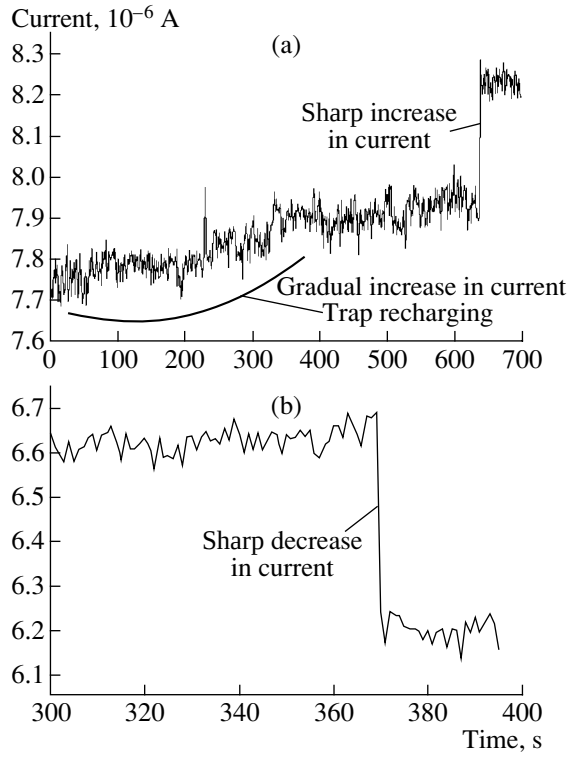

Fig. 3. Variations of current under constant bias: (a) smooth and sharp increase in current (V = –3.5 V); (b) stepwise drop in current V = –3 V).

in CVS mode, the voltage was fixed at 1.0–3.5 V. Variations of voltage and current were recorded simultaneously as functions of time. *I–V* characteristics were recorded after each series of tests. All measurements were done at temperature T = 300 K in the dark (to exclude the photovoltaic effect).

Typical examples of the evolution of current with time are shown in Fig. 3. Usually, smooth variations arise immediately as the bias is applied to the structure; they are related to the capture of carriers on the interface. An abrupt step in current can occur either to higher (Fig. 3a) or to lower (Fig. 3b) values. The novel effect revealed in this study is the drop in current. It can be clearly seen in Fig. 3b (>1–3%), and it was observed in the many devices under study. It is noteworthy that both up and down steps may be observed at the same voltage (or at similar voltages). The model suggested in Section 2 can be made to agree with this experimental observation if we assume that the value of V^* can vary between successive breakdown events in a sample or between samples.

Now we discuss the modification of the *I–V* characteristics as a whole (Fig. 4). An increase in current is observed at small voltages |*V*|, whereas at high voltages the current definitely decreases. Figure 5 gives additional information concerning this behavior: the dependence of $(I_{st} - I_0)/I_0 = \Delta I/I_0$ as a function of the applied bias is constructed for another sample (I_{st} was recorded

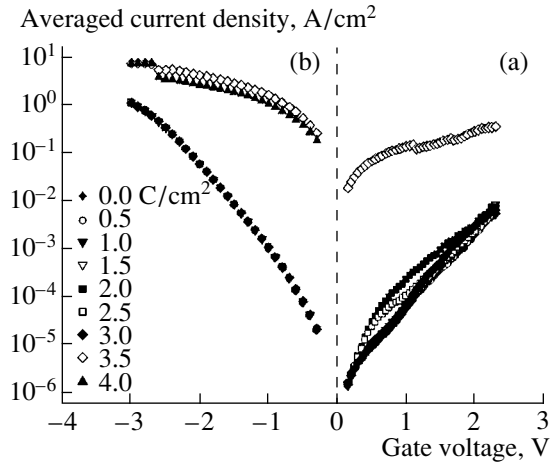

Fig. 4. *I–V* characteristics after a series of stresses with the injection of electrons from (a) the substrate and (b) the metal. The values of the charge that crossed the structure prior to recording the corresponding curve, averaged over area, are shown; (a) and (b) are different samples.

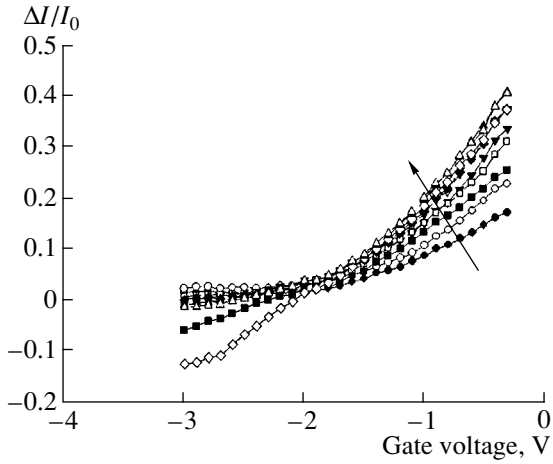

Fig. 5. The ratio $\Delta I/I_0 = (I_{st} - I_0)/I_0$ as a function of the bias across the structure in the most typical case: ΔI is positive at low voltage and negative at high $|V|$. The arrow indicates the evolution of characteristics during tests.

after applying the stress; I_0, before it). The results presented in Figs. 4 and 5 can be explained in terms of the suggested model. The resistance of the defective region at high voltage ($|V| > |V^*|$) becomes higher than the tunnel resistance (see Fig. 1), which results in the decrease in current. At small voltages, we have the opposite situation; thus, the current increases.

Certain devices only demonstrated the increase in current, but one should stress that it was significant only at small voltages and was almost imperceptible at high voltage. This behavior also supports the model of current drop discussed above. We believe that voltage V^* is not reached in these structures, although the reduction of the rise in current indicates that a value near this voltage is attained.

The data in Fig. 2 allow us to obtain the lower estimate of the characteristic size of the defective region, l_{def} (assuming that the current in the broken-down region is zero). In our samples with $\sigma \approx 0.3$ nm, 1% of current flows through 10^{-8} of the device area. Assuming a drop in current of 1%, we obtain the estimated minimum size $l_{def} \approx (10^{-8}S)^{1/2} \approx 40$ nm.

We have presented the first observation of the decrease in current in an MOS tunnel structure after a soft breakdown. Note that the significance of this effect may grow as FETs become increasingly miniaturized, because the relative fraction of a defective area increases when the device size decreases.

4. CONCLUSION

The behavior of $Al/SiO_2/p^+$-Si MOS tunnel diodes with 2.5 to 3.0-nm-thick SiO_2 was studied under electric stress in the constant-current and constant-voltage modes. A nontrivial stepwise decrease in current was observed, mainly in the high-voltage range; the effect is interpreted as a consequence of the soft breakdown. The drop in current should be even stronger in samples of small area and/or with a significant spatial scatter of the oxide thickness, which raises the relative contribution of the broken-down region to the formation of the total current.

ACKNOWLEDGMENTS

The study was supported by a grant from the President of the Russian Federation for Support of Leading Scientific Schools (grant no. NSh-758.2003.02) and by the program of the Ministry of Industry, Science, and Technology of the Russian Federation “Physics of Solid-State Nanostructures 2003.”

REFERENCES

1. *SEMATECH. The International Technology Roadmap for Semiconductors* (2001), http://public.itrs.net/home.htm.
2. B. Yuwono, T. Schloesser, A. Gschwandtner, *et al.*, Microelectron. Eng. **48**, 51 (1999).
3. R. Degraeve, in *Reliability of Ultra-Thin Oxide Gate Dielectrics: 9th European Symposium on Reliability of Electron Devices, Failure Physics and Analysis (Tutorial)* (IMEC, Leuven, 1998).
4. M. Depas, T. Nigam, and M. M. Heyns, IEEE Trans. Electron Devices **43**, 1499 (1996).
5. F. Crupi, R. Degraeve, G. Groeseneken, *et al.*, IEEE Trans. Electron Devices **45**, 2329 (1996).
6. E. Miranda, J. Suñé, R. Rodíguez, *et al.*, Jpn. J. Appl. Phys., Part 1 **38**, 80 (1999).
7. S. M. Sze, *Physics of Semiconductor Devices*, 2nd ed. (Wiley, New York, 1981; Mir, Moscow, 1984), Vol. 2, Chap. 9.
8. M. I. Vexler, A. F. Shulekin, Ch. Dieker, *et al.*, Solid-State Electron. **45**, 19 (2001).
9. H. S. Momose, S. Nakamura, T. Ohguro, *et al.*, IEEE Trans. Electron Devices **45**, 691 (1998).
10. J. P. Shiely, PhD Dissertation (Duke Univ., 1999).

Translated by D. Mashovets

Semiconductors, Vol. 38, No. 6, 2004, pp. 727–731. Translated from Fizika i Tekhnika Poluprovodnikov, Vol. 38, No. 6, 2004, pp. 757–762.

PHYSICS OF SEMICONDUCTOR DEVICES

Electroluminescent Studies of Emission Characteristics of InGaAsN/GaAs Injection Lasers in a Wide Temperature Range

L. Ya. Karachinsky[1]*, N. Yu. Gordeev[1], I. I. Novikov[1], M. V. Maximov[1], A. R. Kovsh[1, 2], J. S. Wang[2], R. S. Hsiao[2], J. Y. Chi[2], V. M. Ustinov[1], and N. N. Ledentsov[1, 3]

[1]*Ioffe Physicotechnical Institute, Russian Academy of Sciences, St. Petersburg, 194021 Russia*

**e-mail: Karach@switch.ioffe.ru*

[2]*Industrial Technology Research Institute, Hsinchu 310, Taiwan, ROC*

[3]*Institut für Festkörperphysik, Technische Universität Berlin, D-10623 Berlin, Germany*

Submitted November 19, 2003; accepted for publication November 27, 2003

Abstract—Light–current, spectral, and far-field characteristics of InGaAsN injection lasers on GaAs substrates were studied in a wide temperature range (77–300 K) at various driving current densities. The increase in indium content in InGaAsN solid solution results in a modification of the QW structure, which is manifested in the spontaneous formation of InGaAsN nanoclusters. These changes result in *N*-shaped temperature dependences of the threshold current density and slope efficiency. *© 2004 MAIK "Nauka/Interperiodica".*

1. INTRODUCTION

Semiconductor lasers with a 1.3-μm wavelength are widely used in optoelectronic telecommunication systems. In recent years, great attention has been paid to the problem of growing such lasers on GaAs substrates. First lasers based on an InGaAsN/GaAs system were suggested and fabricated by Kondow *et al.* [1], and since then they have been the main alternative to InGaAsP/InP lasers of the same wavelength range. In the time since Kondow's work (1995), many attempts have been made to fabricate lasers on GaAs substrates with an active region made up of InGaAsN quantum wells (QW) [2–7].

Currently, lasers on InP substrates are the most popular sources of 1.3-μm emission. Their characteristic temperature is not high (T_0 = 50–70 K) [8], which is related to the weak localization of electrons in the active region [9, 10]. For InGaAsN/GaAs lasers, the predicted value of T_0 is above 150 K; this is related to the strong electron confinement caused by the larger difference between the band gaps. The prospect of designing low-cost long-wavelength lasers with improved temperature characteristics makes InGaAsN QW lasers a very attractive object for investigations and further applications.

This study is concerned with the emission characteristics of InGaAsN/GaAs lasers in a wide temperature range.

2. EXPERIMENTAL

The laser structures that were studied were grown on Si-doped (100) GaAs substrates in a Riber Epineat MBE setup. The source of atomic nitrogen was a UNI Bulb (Applied EPI) plasma source. The operating mode of the source was carefully optimized to suppress the negative effect of bombardment of the surface by high-energy ions formed in the plasma source. The active region of the laser structures was a single QW, $In_{0.36}Ga_{0.64}As_{0.97}N_{0.03}$ (structure *1*) and $In_{0.38}Ga_{0.62}As_{0.974}N_{0.026}$ (structure *2*). The growth rate was 2.5 Å/s at a temperature of 440°C. The active region was embedded in a 0.35-μm-thick GaAs waveguide confined by *p*- and *n*-$Al_{0.33}Ga_{0.67}As$ emitter layers. The emitters were grown at 700°C. Structure *2* was annealed at 750°C for 15 min, structure *1* was not annealed. The lasing wavelength at room temperature was 1.28 and 1.24 μm for structures *1* and *2*, respectively.

Lasers with stripe contacts were produced from the heterostructures grown. The width of contact was 100 μm; the length of the cavity, 2000 μm. The samples were pumped in quasi-CW mode by current pulses of 1 μs duration with a repetition rate of 5 kHz. Spectral, light–power and far-field characteristics of the electroluminescence were studied in a wide temperature range (77–300 K). For this study, the samples were soldered onto the heat sink with the epitaxial layer facing down and placed into a cryostat.

3. EXPERIMENTAL RESULTS

The light–current characteristics of both structures were measured. The data obtained were used to reconstruct the temperature dependences of the threshold current density and slope efficiency, which are shown in Fig. 1. The heterostructure with a 3% nitrogen content (structure *1*) demonstrates an *N*-shaped temperature dependence of these characteristics, whereas for structure *2* (2.6% nitrogen) this specific feature is not

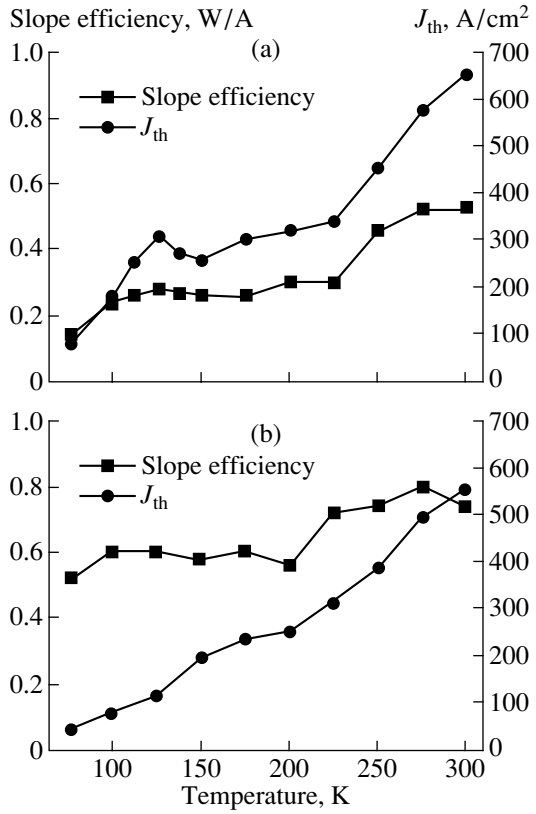

Fig. 1. Temperature dependences of the threshold current density J_{th} and slope efficiency for laser heterostructures (a) *1* and (b) *2*.

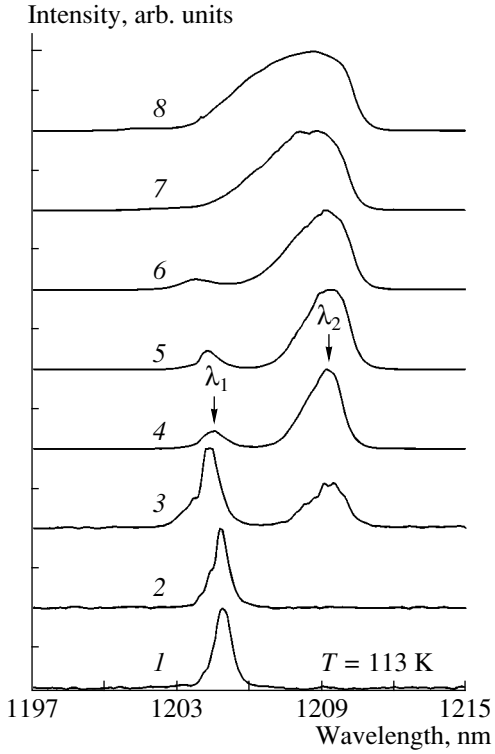

Fig. 2. Lasing spectra of heterostructure *1* at T = 113 K; density of driving current: (*1*) 190, (*2*) 205, (*3*) 255, (*4*) 380, (*5*) 510, (*6*) 765, (*7*) 1015, and (*8*) 1270 A/cm^2.

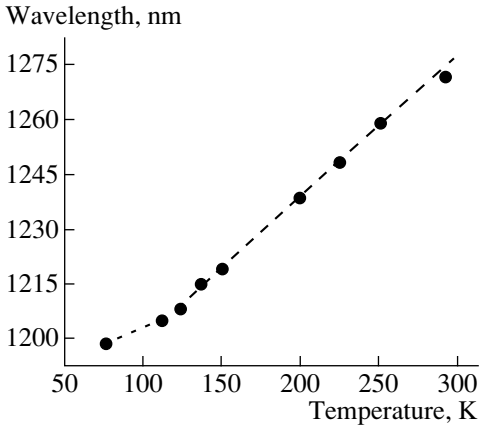

Fig. 3. Temperature dependence of the lasing wavelength of heterostructure *1*.

observed, and the characteristics change steadily as the temperature increases.

The emission spectra of structure *1* were recorded in the temperature range corresponding to that of the light–current measurements. In this study, special attention was given to those temperatures at which specific features in the temperature dependences of the threshold current density and slope efficiency were observed.

It appeared that, in the temperature range 110–130 K, lasing is first obtained in the short-wavelength spectral range, and then, as the driving current increases, a second peak appears at longer wavelengths, and lasing at two different wavelengths occurs simultaneously. As the driving current is further increased, the short-wavelength spectral peak virtually disappears. The evolution of this process at a temperature of 113 K is shown in Fig. 2. At all the other temperatures, lasing started at a definite wavelength and remained in the same spectral range as the driving current increased. Figure 3 shows the temperature dependence of the lasing wavelength. Two specific portions are seen in this dependence, in the temperature ranges 77–120 and 120–300 K.

In order to determine whether two spectral peaks, which are observed in the temperature range 110–130 K, correspond to the same transverse mode of emission or whether they refer to different modes, we studied the spectrally resolved far-field emission from structure *1*. The measurements were performed in planes normal and parallel to the *p–n* junction plane (Figs. 4a and 4b, respectively) at 113 K; the driving current density was 255 A/cm^2. The monochromator was tuned to different peaks of the emission spectrum (λ_1 and λ_2, Fig. 2). The procedure we used was suggested in [11]. These experiments have shown that both spectral peaks are identical in the distribution profile, and they correspond to the same transverse mode.

The spectra of spontaneous emission from structure *1* were studied at different temperatures at a driving cur-

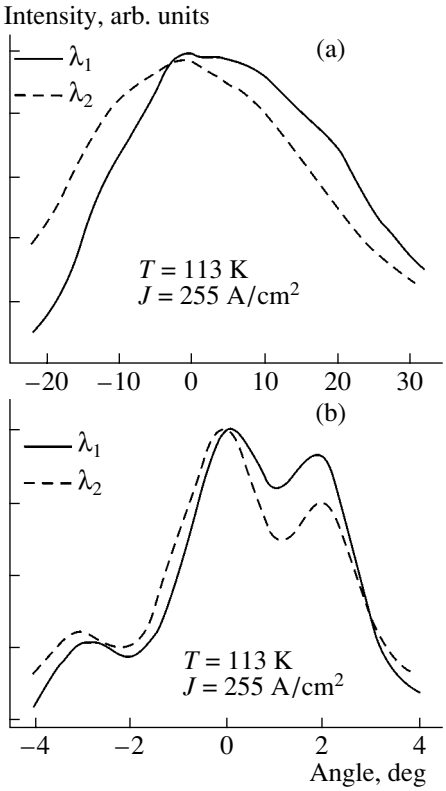

Fig. 4. Spectrally resolved far-field emission of heterostructure *1* in planes: (a) normal and (b) parallel to the plane of the *p*–*n* junction.

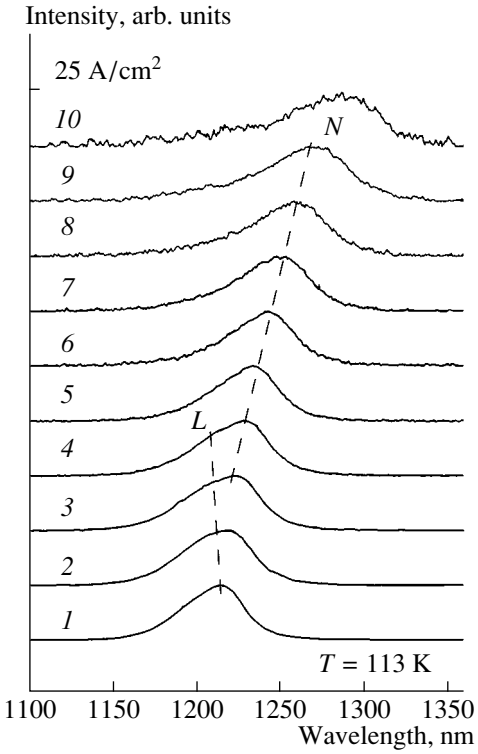

Fig. 5. Spectra of spontaneous emission from heterostructure *1* at different temperatures; the driving current density was 25 A/cm^2. *L* and *N* are peaks related to radiative recombination via localized states and standard band-to-band recombination in a QW, respectively. Temperature: (*1*) 77, (*2*) 113, (*3*) 125, (*4*) 138, (*5*) 150, (*6*) 175, (*7*) 200, (*8*) 225, (*9*) 250, and (*10*) 300 K.

rent density of 25 A/cm^2 (Fig. 5). This driving current density was chosen considering the condition that it must be considerably lower than the threshold current density at each temperature in the range under study. Figure 6 shows the temperature dependence of FWHM of the spontaneous emission spectrum. It can be readily seen that the dependence is *N*-shaped, similar to those for the threshold current density and the slope efficiency.

4. DISCUSSION

The characteristic temperature T_0 was estimated from the temperature dependence of the threshold current density for structure *2* (Fig. 1b). The value obtained was 80 K, which means that the characteristics of the laser are improved compared with lasers on InP substrates [8]. The dependences of the threshold current density and the slope efficiency, similar to those obtained for structure *1* (Fig. 1a), were observed earlier in the study of laser heterostructures based on InAs/GaAs quantum dots (QDs) [12]. Taking into account the transition from a nonequilibrium to equilibrium distribution of nonequilibrium carriers in the active region of a laser, which occurs as the temperature increases, made it possible to account for specific features of this kind in the behavior of the temperature characteristics of QD lasers [12, 13]. Earlier, it was stated that clusters can be formed in an InGaAsN solid solution with a high (>30%) In content to give quantum entities with 3D confinement [14]. Thus, we have every reason to believe that the *N*-shaped temperature dependences of the threshold current density and the slope efficiency in structure *1* are related to entities with properties similar to those of QDs, which are formed in the active region of this heterostructure.

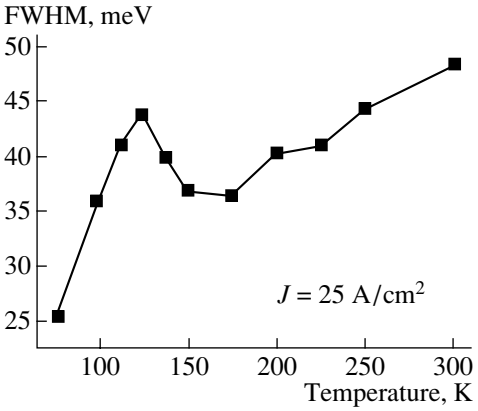

Fig. 6. Temperature dependence of FWHM of spontaneous emission from heterostructure *1*.

Spectral studies of structure *1* have shown that, in the temperature range 110–130 K and at a current density slightly exceeding the threshold current density, simultaneous lasing at two different wavelengths occurs (Fig. 2). In this case, lasing first arises in the short-wavelength region, and later a "switchover" to longer wavelength occurs. As discussed in the previous section, the spectrally resolved study of far-field emission of this heterostructure allowed us to reject the possibility that two spectral peaks belong to different transverse modes. Furthermore, the relatively small energy spacing (~4 meV) between the two spectral peaks, along with the fact that the short-wavelength peak arises first when the driving current is raised, suggests that these two peaks are not related to lasing via the ground and excited states of some entities with 3D spatial confinement of carriers. The point is that the characteristic distance between the ground and first excited state in QDs is over 50 meV [15, 16]. In this case, when the driving current density increases, the switchover to lasing via the high-energy state in QDs (the short-wavelength peak) occurs only after the lasing via the ground state (the long-wavelength peak) is saturated [17].

It is well known that there are localized states in QW heterostructures, and the recombination of carriers can proceed via these states [18–20]. In this case, the emission wavelength can be less than that in the case of ordinary recombination of electrons and holes in a QW [18–20]. The energy spacing between the two peaks corresponding to recombination via the localized and normal states in a QW is about 5 meV [18–20]. When the driving current density increases, the emission via these states must be rapidly saturated, and this was observed in our experiment. As can be seen in Fig. 2, the contribution of the short-wavelength component to the total intensity of emission is already very small when the driving current density becomes equal to twice the threshold density, and it tends to zero as the driving current increases further. Therefore, we may suggest that the coexistence of two peaks in the emission spectrum of heterostructure *1* under certain conditions is caused by the presence of a large number of localized states in this structure, which are responsible for the short-wavelength emission.

The *N*-shaped temperature dependence of FWHM of the photoluminescence line of an unannealed heterostructure with an InGaAsN QW was observed earlier in [20]. This specific feature disappears after the annealing. In [20], the *N*-shaped dependence was explained as follows: At low temperatures, the emission is mainly associated with localized states. Then, in a certain temperature range, radiative recombination proceeds simultaneously via localized and normal states in a QW; thus, the photoluminescence line is broadened. As temperature increases further, the contribution of localized states to emission virtually disappears, so the spectral line turns narrow again. We have observed similar behavior of the line of electroluminescence for structure *1* (Fig. 5). The sharp drop in intensity of the short-wavelength peak with increasing temperature can be explained as follows: as stated above, our data show that InGaAsN nanoclusters are formed in the active region of structure *1*. If their size is small enough, the additional quantum confinement of carriers in the QW plane raises the energy of the ground state (we suppose that the energy states in nanoclusters and QWs are separated by barriers). At low temperatures, the time of radiative recombination of carriers in nanoclusters is less than the time of their thermal excitation to the continuum. Thus, carriers captured in a nanocluster recombine within it, and lasing occurs via the nanocluster states. As temperature increases, carriers are excited from nanoclusters, a quasi-equilibrium distribution is established in the system, and lasing occurs via the QW states.

Annealing reduces the efficiency of carrier localization, because the localization is induced by inhomogeneities in the solid solution. Apparently, the *N*-shaped temperature dependence of FWHM of the spontaneous emission spectrum of heterostructure *1* (Fig. 6) is caused precisely because no annealing procedure was used in the postgrowth treatment of this structure. We believe that the physical reasons of this *N*-shaped dependence are similar to those discussed in [20]. Thus, the results obtained for the temperature dependence of FWHM in heterostructure *1* are additional confirmation of our suggestion that simultaneous lasing at two different wavelengths under certain conditions, which was observed in structure *1*, is caused by localized states in this structure. Besides, these data present indirect evidence of the existence of cluster units in the active region of heterostructure *1*, because it is precisely these units that can be a source of a large number of localized states. In the annealed structure *2*, clusters were destroyed, so the specific features related to localized states discussed above were not observed.

5. CONCLUSION

Light–current, spectral, and far-field characteristics of emission of InGaAsN/GaAs QW injection lasers were studied in a wide temperature range (77–300 K). A heterostructure with a 3% nitrogen content that was not subjected to annealing exhibits *N*-shaped temperature dependences of the threshold current density, slope efficiency, and FWHM of spontaneous emission. These specific features are attributed to the possible formation of InGaAsN nanoclusters. This interpretation agrees with the data of transmission electron microscopy [14]. The characteristic temperature T_0 = 80 K was obtained for an annealed heterostructure with a 2.6% nitrogen content. In this case, the slope efficiency was 0.74 W/A at room temperature. The results obtained expand our understanding of processes in lasers with an active region based on InGaAsN QWs, and they can be used in the design of advanced semiconductor light sources.

ACKNOWLEDGMENTS

The authors are grateful to N.V. Kryzhanovskaya for discussing results and to Yu.M. Shernyakov for assistance in the preparation of samples.

This study was supported by the Russian Foundation for Basic Research; the Program of the Ministry of Industry, Science, and Technology of the Russian Federation "Physics of Solid-State Nanostructures"; and the joint program of Ioffe PTI and ITRI "Research and Development of Advanced Light Sources for Application in the Next Generation of Optoelectronic Systems." L.Ya. Karachinsky and I.I. Novikov acknowledge the support of the Dynasty Foundation and the International Center for Fundamental Physics in Moscow; L.Ya. Karachinsky is also grateful to INTAS (grant YSF 2001/2-97).

REFERENCES

1. M. Kondow, K. Uomi, A. Niwa, *et al.*, Jpn. J. Appl. Phys., Part 1 **35**, 1273 (1996).
2. A. Yu. Egorov, D. Bernklau, D. Livshits, *et al.*, Electron. Lett. **35**, 1643 (1999).
3. C. W. Coldren, M. C. Larson, S. G. Spruytte, and J. S. Harris, Electron. Lett. **36**, 951 (2000).
4. M. Fischer, M. Reinhardt, and A. Forchel, Electron. Lett. **36**, 1208 (2000).
5. J. S. Harris, IEEE J. Sel. Top. Quantum Electron. **6**, 1145 (2000).
6. G. Steinle, H. Riechert, and A. Yu. Egorov, Electron. Lett. **37**, 93 (2001).
7. V. A. Odnoblyudov, A. Yu. Egorov, A. R. Kovsh, *et al.*, Pis'ma Zh. Tekh. Fiz. **29** (10), 77 (2003) [Tech. Phys. Lett. **29**, 433 (2003)].
8. H. Temkin, D. Coblentz, R. A. Logan, *et al.*, Appl. Phys. Lett. **62**, 2402 (1993).
9. M. Yano, H. Nishi, and M. Tukusagawa, J. Appl. Phys. **52**, 3172 (1981).
10. H. Ishikawa and I. Suemune, IEEE Photonics Technol. Lett. **6**, 344 (1994).
11. N. Yu. Gordeev, A. M. Georgievski, V. I. Kopchatov, *et al.*, in *Proceedings of International Symposium on Nanostructures: Physics and Technology* (St. Petersburg, Russia, 1997), p. 183.
12. I. I. Novikov, M. V. Maksimov, Yu. M. Shernyakov, *et al.*, Fiz. Tekh. Poluprovodn. (St. Petersburg) **37**, 1270 (2003) [Semiconductors **37**, 1239 (2003)].
13. L. V. Asryan and R. A. Suris, Semicond. Sci. Technol. **11**, 554 (1996).
14. B. M. Volovik, A. R. Kovsh, W. Passenberg, *et al.*, Semicond. Sci. Technol. **16**, 186 (2001).
15. N. Yu. Gordeev, S. V. Zaĭtsev, V. I. Kopchatov, *et al.*, Pis'ma Zh. Tekh. Fiz. **26** (6), 78 (2000) [Tech. Phys. Lett. **26**, 259 (2000)].
16. M. V. Maximov, N. N. Ledentsov, V. M. Ustinov, *et al.*, J. Electron. Mater. **29**, 476 (2000).
17. A. Markus, J. X. Chen, C. Paranthonen, *et al.*, Appl. Phys. Lett. **82**, 1818 (2003).
18. A. Polimeni, M. Capizzi, M. Geddo, *et al.*, Appl. Phys. Lett. **77**, 2870 (2000).
19. R. A. Mair, J. Y. Lin, H. X. Jiang, *et al.*, Appl. Phys. Lett. **76**, 188 (2000).
20. S. Shirakata, M. Kondow, and T. Kitatani, Appl. Phys. Lett. **80**, 2087 (2002).

Translated by D. Mashovets

Semiconductors, Vol. 38, No. 6, 2004, pp. 732–735. Translated from Fizika i Tekhnika Poluprovodnikov, Vol. 38, No. 6, 2004, pp. 763–766.

PHYSICS OF SEMICONDUCTOR DEVICES

High-Power 1.5 μm InAs–InGaAs Quantum Dot Lasers on GaAs Substrates

M. V. Maksimov*, Yu. M. Shernyakov, N. V. Kryzhanovskaya, A. G. Gladyshev, Yu. G. Musikhin, N. N. Ledentsov, A. E. Zhukov, A. P. Vasil'ev, A. R. Kovsh, S. S. Mikhrin, E. S. Semenova, N. A. Maleev, E. V. Nikitina, V. M. Ustinov, and Zh. I. Alferov

Ioffe Physicotechnical Institute, Russian Academy of Sciences, St. Petersburg, 194021 Russia

**e-mail: Maximov@beam.ioffe.ru*

Submitted November 26, 2003; accepted for publication November 27, 2003

Abstract—Light–current, spectral, and temperature characteristics of long-wavelength (1.46–1.5 μm) lasers grown on GaAs substrates, with an active area based on InAs–InGaAs quantum dots, are studied. To reach the required lasing wavelength, quantum dots were grown on top of a metamorphic InGaAs buffer layer with an In content of about 20%. The maximum output power in pulsed mode was 7 W at room temperature. The differential efficiency of the laser, which had a 1.5-mm-long cavity, was 50%. The temperature dependence of the threshold current is described by a characteristic temperature of 61 K in the temperature range 10–73°C. © *2004 MAIK "Nauka/Interperiodica".*

1. INTRODUCTION

Lasers of 1.55 μm range are principal components of fiber-optic telecommunication lines. GaInAsP or AlGaInAs heterostructures on InP substrates, which are usually used for this range, have an insufficient thermal stability of the lasing wavelength and threshold current. Because of the small difference between the refractive indices of GaInAs and AlInAs, no less than 50 pairs of layers are needed to reach a reflectivity of >0.99 in a distributed Bragg reflector, which is the level necessary for VCSEL. Thus, in this system of materials, the design of monolithic VCSELs based on a vertical microcavity seems highly problematic. Therefore, considerable effort has been made to devise structures on GaAs substrates in the 1.45–1.55 μm range. It is expected that the stronger localization of carriers in the active region of these structures will make it possible to improve the temperature stability of long-wavelength lasers. In VCSELs on GaAs substrates, it is possible to apply the routine techniques of GaAs–AlGaAs Bragg reflectors, oxidized GaAs–AlO mirrors, and oxidized apertures.

Several technological approaches have been suggested to attain 1.45–1.55 μm wavelengths in structures on GaAs substrates: vertically coupled quantum dots (QD) [1], the growing of QDs on low-temperature substrates [2], and the use of GaInAsN/GaAsN [3] or GaInNAsSb/GaNAsSb [4, 5] quantum wells (QW). In a laser with an active region based on GaInAsN/GaAsN QW, lasing at 1.49 μm with a threshold current density of 7 kA/cm^2 was obtained [3]. The slope efficiency and maximum output power in pulsed mode were, respectively, 0.14 W/A and 130 mW in a stripe 4 μm in width and 1200 μm in length, with two cleaved faces. Lasing at 1.463 μm was obtained in a laser with a GaInNAsSb active region, the differential efficiency was rather high (45%), and the threshold current density was comparatively low (2.8 kA/cm^2) [4]. The maximum output power was about 70 mW (the stripe width was 5 μm; the length, 1200 μm). Lasing at a long (compared to [4]) wavelength of 1.5 μm was obtained in a laser with similar GaInNAsSb active region in [5]. At the same time, the threshold current density (3.5 kA/cm^2) was somewhat higher, and the differential efficiency (12%), lower than those obtained in [4].

Self-organized QDs seem to be the most promising choice for use in an active layer of long-wavelength light-emitting devices on GaAs substrates. This concept made it possible to produce lasers for the ~1.3-μm range [6, 7] with a low threshold current density (100 A/cm^2 with ten layers of QDs), a high differential efficiency (88%), and high temperature stability (characteristic temperature T_0 = 150 K). Recently, we demonstrated lasing at a wavelength of 1.488 μm in structures with an active region based on multilayer arrays of self-organized QDs grown on GaAs substrates [8]. To reach this spectral range, structures were grown on a thick metamorphic $In_{0.2}Ga_{0.8}As$ buffer layer. In a stripe of length L = 1200 μm, the threshold current density was 1.5 kA/cm^2 at room temperature. The maximum quantum efficiency was 50% (L = 2000 μm) [7].

In this study, we investigate power, temperature, and spectral characteristics of lasers with an active region based on QDs deposited on an $In_{0.2}Ga_{0.8}As$ metamorphic buffer layer and show that the use of these structures makes it possible to obtain a record-breaking high output power in 1.5-μm lasers on GaAs substrates.

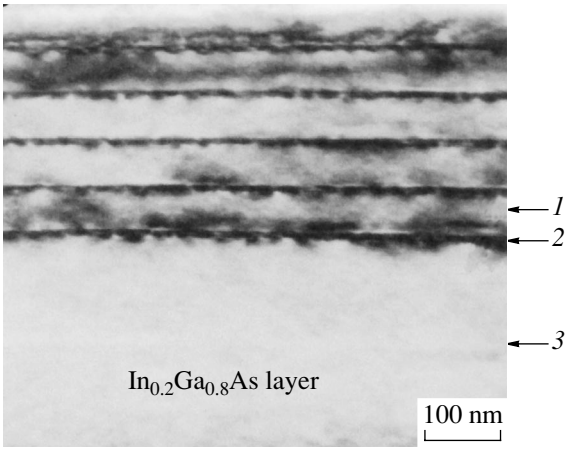

Fig. 1. Cross-sectional electron micrograph of InAs–InGaAs QDs grown on a metamorphic InGaAs buffer layer: (*1*) $In_{0.2}Ga_{0.8}As$ spacer, (*2*) QD layer, (*3*) $In_{0.2}Ga_{0.8}As$/AlGaAs superlattice.

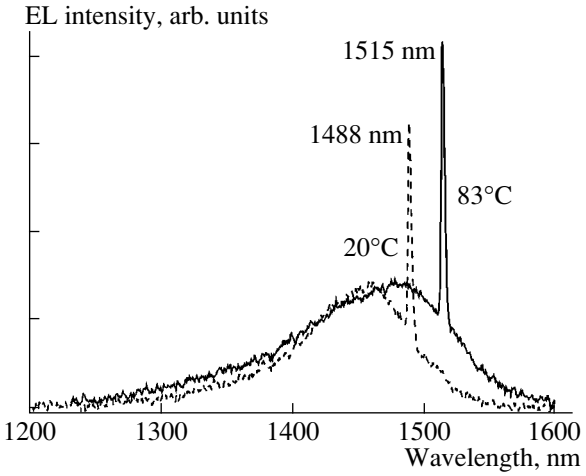

Fig. 2. Lasing spectra for a sample with four cleaved facets at 20 and 83°C. Size of the sample, 350 × 350 μm.

2. EXPERIMENT

The laser structures that we studied were grown by MBE on (100) n^+-GaAs substrates. Special modes of growth of the metamorphic InGaAs buffer layer allowed us to significantly reduce the density of dislocations propagating into the upper (active) layers. An $In_{0.2}Ga_{0.8}As$ layer was used as the laser waveguide; the emitters were $In_{0.2}Al_{0.3}Ga_{0.5}As$ layers. Ten layers of self-organized InAs/$In_{0.4}Ga_{0.6}As$ QDs separated by 45-nm-thick spacers were embedded in the middle of the waveguide layer. Special growth modes allowed us to prevent the formation of a high density of dislocations in the active region (Fig. 1). A more detailed description of the laser structure and modes of epitaxial growth was presented in [8].

Laser diodes were produced in a configuration with four cleaved facets and in a stripe configuration with a stripe width of 100 μm. The samples were soldered with In solder onto copper heat sinks, *p*-layer down. The laser characteristics were studied in pulsed mode (the duration of the driving current pulses was 300 ns; the repetition rate, 1 kHz).

3. RESULTS AND DISCUSSION

In determining the maximum possible wavelength of lasing and the minimum threshold current density in our structures, we used samples with four cleaved facets. The external loss in this configuration is negligible. The lower the external loss, the longer the wavelength and the lower the current density for the onset of lasing [9]. Growing structures on a metamorphic InGaAs buffer, which is designed to relieve stresses, makes it possible to reach a lasing wavelength of 1488 nm at room temperature (Fig. 2). It is significant that the threshold current density does not increase as the wavelength increases (see table). At a temperature of 83°C, the lasing wavelength is 1515 nm.

In a stripe laser at room temperature, the peak of the lasing spectrum lies at 1460 nm (Fig. 3a). The blue shift is related to the increase in external loss [9]. The temperature dependence of the peak wavelength in the lasing spectrum can be approximated by a linear dependence with a slope of 0.43 nm/K (Fig. 3b). The absence of a stepwise decrease in the lasing wavelength with increasing temperature means that the generation proceeds via the ground state of QDs at all temperatures.

Temperature dependences of the differential efficiency and the threshold current density are shown in Fig. 4. At 25–72°C, the increase in threshold current density is described by the characteristic temperature T_0 = 61 K. The differential efficiency is 50% at 25°C; it remains virtually unchanged up to 40°C and then decreases to 32% at 72°C. In a laser with a GaInNAsSb active region, T_0 equals 83 K in the temperature range 10–35°C [5], but at higher temperatures a sharp rise in the threshold current density was observed.

Figure 5 shows the light–current characteristic of a 1.5-mm-long laser in pulsed mode. No reflecting coatings were deposited onto the laser facets. The threshold current density J_{th} equals 2.0 kA/cm^2. The light–current

Threshold current density of long-wavelength lasers on GaAs substrates in relation to the lasing wavelength

Epitaxial structure no.	Lasing wavelength, nm	Threshold current density, A cm^{-2}
5–450	1445	880
5–451	1466	860
5–478	1480	800
5–449	1488	800

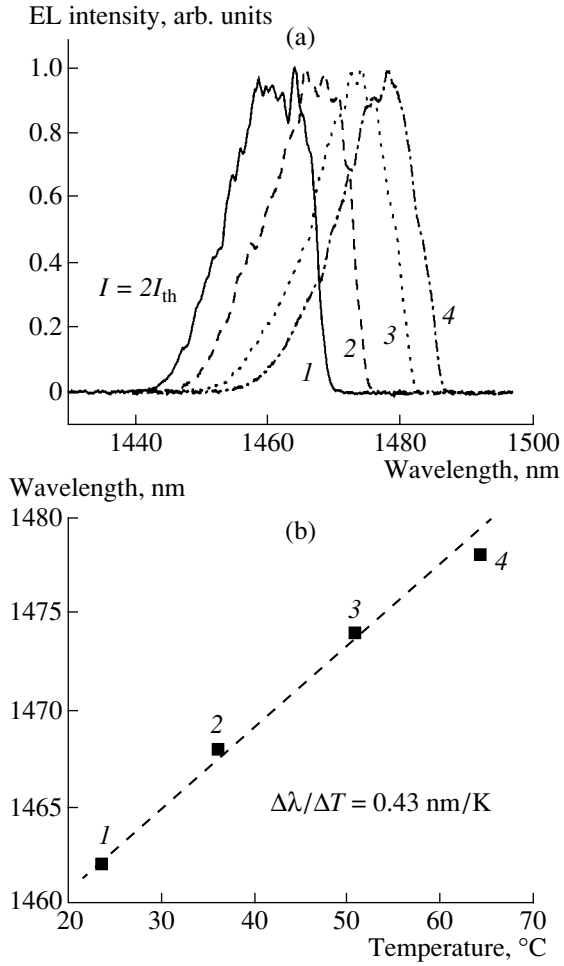

Fig. 3. (a) Lasing spectra at different temperatures and (b) temperature dependence of the lasing wavelength for a stripe laser. The stripe width is 100 μm; the length, 1500 μm. Temperature: (*1*) 23, (*2*) 36, (*3*) 51, and (*4*) 65°C.

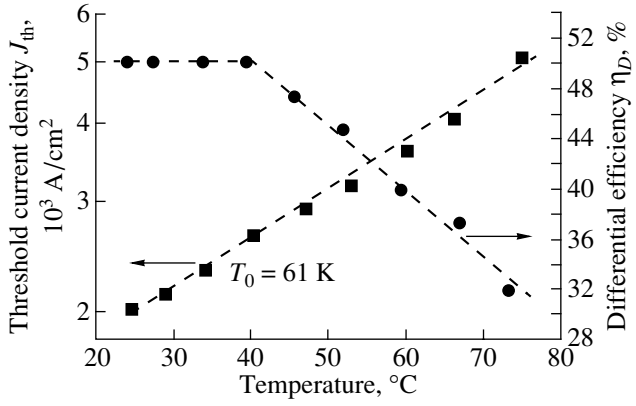

Fig. 4. Temperature dependences of the differential efficiency and threshold current density.

characteristic is nearly linear up to a current of 17 A, which indicates that the active region is not overheated. The differential efficiency η_D is 50%. The lasing spectra are shown in the inset of Fig. 5. The half-width of

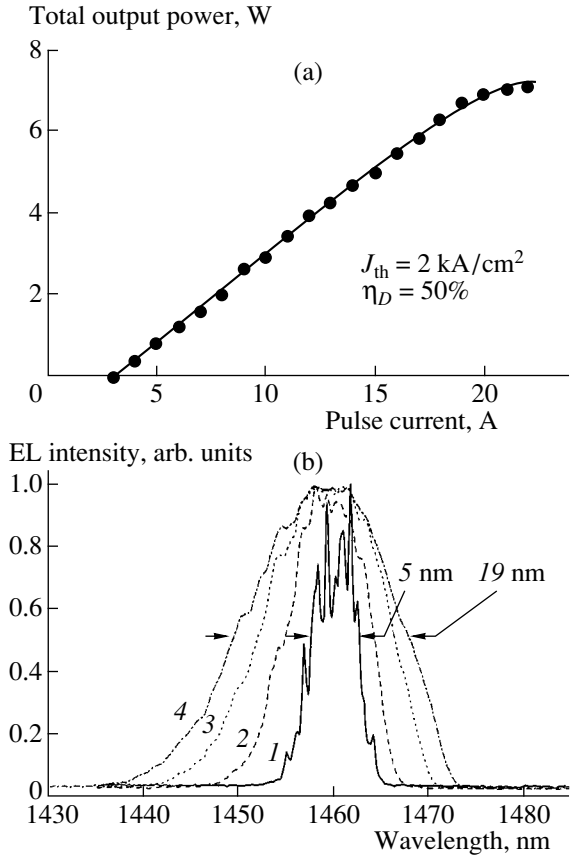

Fig. 5. (a) Output power for a sample with two cleaved facets as a function of the driving current in pulsed mode and (b) lasing spectra at different driving currents: (*1*) 3.3, (*2*) 6, (*3*) 10, and (*4*) 16 A.

the spectrum equals 5 nm at a current of 3 A. When the current increases to 16 A, the spectrum is broadened to 19 nm, but the peak position remains unchanged. Thus, generation proceeds via the ground state of QDs up to maximum power.

4. CONCLUSION

We have produced InAs–InGaAs QD lasers for the 1.4 to 1.5-μm range on GaAs substrates. The threshold current density and differential efficiency of lasers with a 1.5-mm-long cavity were, respectively, 2 kA/cm^2 and 50%. A high output power of 7 W at room temperature in pulsed mode is obtained. These results demonstrate the validity of the approach based on the concept of metamorphic growth in the design of long-wavelength light emitters on GaAs.

ACKNOWLEDGMENTS

This study was supported by a joint project of the Ioffe PTI, NSC-Nanosemiconductor GmbH (Germany), the Volkswagen Foundation, and INTAS.

REFERENCES

1. B. V. Volovik, D. S. Sizov, A. F. Tsatsul'nikov, *et al.*, Fiz. Tekh. Poluprovodn. (St. Petersburg) **34**, 1368 (2000) [Semiconductors **34**, 1316 (2000)].
2. A. E. Zhukov, B. V. Volovik, S. S. Mikhrin, *et al.*, Pis'ma Zh. Tekh. Fiz. **27** (17), 51 (2001) [Tech. Phys. Lett. **27**, 734 (2001)].
3. D. Gollub, M. Fisher, and A. Forchel, Electron. Lett. **38**, 1183 (2002).
4. W. Ha, V. Gambin, S. Bank, *et al.*, in *Abstracts of International Conference on Molecular Beam Epitaxy* (San Francisco, USA, 2002), p. 61.
5. L. H. Li, V. Sallet, G. Patriarche, *et al.*, Electron. Lett. **39**, 519 (2003).
6. S. S. Mikhrin, A. E. Zhukov, A. R. Kovsh, *et al.*, Fiz. Tekh. Poluprovodn. (St. Petersburg) **36**, 1400 (2002) [Semiconductors **36**, 1315 (2002)].
7. A. R. Kovsh, N. A. Maleev, A. E. Zhukov, *et al.*, Electron. Lett. **38**, 1104 (2002).
8. A. E. Zhukov, A. P. Vasil'ev, A. R. Kovsh, *et al.*, Fiz. Tekh. Poluprovodn. (St. Petersburg) **38** (2004) (in press).
9. L. V. Asryan, M. Grundmann, N. N. Ledentsov, *et al.*, IEEE J. Quantum Electron. **37**, 418 (2001).

Translated by D. Mashovets